

A SEARCH FOR LONG-LIVED, CHARGED,  
SUPERSYMMETRIC PARTICLES USING IONIZATION WITH  
THE ATLAS DETECTOR

by

BRADLEY AXEN

A dissertation submitted in partial satisfaction of the  
requirements for the degree of

Doctor of Philosophy  
in  
Physics  
in the  
Graduate Division  
of the  
University of California, Berkeley

Committee in charge:  
Professor Beate Heinemann, Chair  
Professor Yury Kolomensky  
Professor Karl van Bibber

Fall 2016



## ABSTRACT

---

A Search for Long-Lived, Charged, Supersymmetric Particles using Ionization  
with the ATLAS Detector

by

Bradley Axen

Doctor of Philosophy

University of California, Berkeley

Professor Beate Heinemann, Chair

Several extensions of the Standard Model predict the existence of charged, very massive, and long-lived particles. Because of their high masses these particles would propagate non-relativistically through the ATLAS pixel detector and would therefore be identifiable through a measurement of large specific energy loss. Measuring heavy, long-lived particles through their track parameters in the pixel detector allows sensitivity to particles with lifetimes in the nanosecond range and above. This dissertation presents an inner detector driven method for identifying such particles in proton-proton collisions at 13 TeV with the 2015 LHC dataset corresponding to an integrated luminosity of  $3.5 \text{ pb}^{-1}$ .

To be filled.

## ACKNOWLEDGEMENTS

---

To be filled.

## CONTENTS

---

1	INTRODUCTION	1
I	THEORETICAL CONTEXT	3
2	STANDARD MODEL	4
2.1	Action and the Lagrangian . . . . .	4
2.2	Gauge Invariance and Forces . . . . .	5
2.2.1	$SU(2) \times U(1)$ and the Electroweak Force . . . . .	7
2.2.2	$SU(3)$ and the Strong Force . . . . .	7
2.3	Noether's Theorem, Charges, and Matter . . . . .	8
2.3.1	Quarks . . . . .	8
2.3.2	Leptons . . . . .	9
2.3.3	Chirality . . . . .	10
2.4	Higgs Mechanism and Mass . . . . .	10
2.5	Phenomenology . . . . .	12
2.5.1	Standard Model Calculations . . . . .	12
2.5.2	Electroweak Physics . . . . .	14
2.5.3	Strong Physics . . . . .	14
2.5.4	Proton-Proton Collisions . . . . .	15
2.5.5	Simulation . . . . .	16
2.6	Limitations . . . . .	17
2.6.1	Theoretical Concerns . . . . .	17
2.6.2	Cosmological Observations . . . . .	18
3	SUPERSYMMETRY	20
3.1	Structure . . . . .	20
3.2	Motivation . . . . .	22
3.3	Simplified Models . . . . .	24
3.4	Long-Lived Particles . . . . .	25
II	EXPERIMENTAL STRUCTURE AND RECONSTRUCTION	27
4	THE LARGE HADRON COLLIDER	28
4.1	Injection Chain . . . . .	29
4.2	Design . . . . .	30
4.2.1	Layout . . . . .	30
4.2.2	Magnets . . . . .	31
4.2.3	Radio Frequency Cavities . . . . .	32
4.2.4	Beam . . . . .	34
4.3	Luminosity Parameters . . . . .	34
4.4	Delivered Luminosity . . . . .	36
5	THE ATLAS DETECTOR	38
5.1	Coordinate System . . . . .	40
5.2	Magnetic Field . . . . .	41
5.3	Inner Detector . . . . .	43

5.3.1	Pixel Detector . . . . .	46
5.3.2	Semiconductor Tracker . . . . .	48
5.3.3	Transition Radiation Tracker . . . . .	50
5.4	Calorimetry . . . . .	50
5.4.1	Electromagnetic Calorimeter . . . . .	52
5.4.2	Hadronic Calorimeters . . . . .	53
5.5	Muon Spectrometer . . . . .	55
5.5.1	Monitored Drift Tube . . . . .	57
5.5.2	Resistive Plate Chamber . . . . .	58
5.5.3	Cathode Strip Chamber . . . . .	58
5.5.4	Thin Gap Chamber . . . . .	58
5.6	Trigger . . . . .	60
6	EVENT RECONSTRUCTION	63
6.1	Charged Particles . . . . .	63
6.1.1	Pixel Neural Network . . . . .	66
6.1.2	Pixel dE/dx . . . . .	67
6.1.3	Vertex Reconstruction . . . . .	68
6.2	Electrons and Photons . . . . .	68
6.2.1	Photon Identification . . . . .	70
6.2.2	Electron Identification . . . . .	70
6.3	Muons . . . . .	70
6.3.1	Muon Identification . . . . .	71
6.4	Jets . . . . .	71
6.4.1	Topological Clustering . . . . .	72
6.4.2	Jet Algorithms . . . . .	73
6.4.3	Jet Energy Scale . . . . .	74
6.5	Missing Transverse Energy . . . . .	75
III	CALORIMETER RESPONSE	77
7	RESPONSE MEASUREMENT WITH SINGLE HADRONS	78
7.1	Dataset and Simulation . . . . .	79
7.1.1	Data Samples . . . . .	79
7.1.2	Simulated Samples . . . . .	79
7.1.3	Event Selection . . . . .	79
7.2	Inclusive Hadron Response . . . . .	80
7.2.1	E/p Distribution . . . . .	80
7.2.2	Zero Fraction . . . . .	81
7.2.3	Neutral Background Subtraction . . . . .	83
7.2.4	Corrected Response . . . . .	84
7.2.5	Additional Studies . . . . .	86
7.3	Identified Particle Response . . . . .	89
7.3.1	Decay Reconstruction . . . . .	90
7.3.2	Identified Response . . . . .	91
7.3.3	Additional Species in Simulation . . . . .	93
7.4	Summary . . . . .	93
8	JET ENERGY RESPONSE AND UNCERTAINTY	95

8.1	Motivation . . . . .	95
8.2	Uncertainty Estimate . . . . .	95
8.3	Summary . . . . .	98
<b>IV</b>	<b>SEARCH FOR LONG-LIVED PARTICLES</b>	<b>101</b>
9	LONG-LIVED PARTICLES IN ATLAS	102
9.1	Event Topology . . . . .	102
9.1.1	Detector Interactions . . . . .	103
9.1.2	Lifetime Dependence . . . . .	105
9.2	Simulation . . . . .	108
10	EVENT SELECTION	111
10.1	Trigger . . . . .	112
10.2	Kinematics and Isolation . . . . .	113
10.3	Particle Species Rejection . . . . .	117
10.4	Ionization . . . . .	121
10.4.1	Mass Estimation . . . . .	121
10.5	Event Selection . . . . .	123
11	BACKGROUND ESTIMATION	125
11.1	Background Sources . . . . .	125
11.2	Prediction Method . . . . .	126
11.3	Validation . . . . .	127
11.3.1	Closure in Simulation . . . . .	127
11.3.2	Validation Region in Data . . . . .	128
11.4	Expected Background . . . . .	129
12	SYSTEMATIC UNCERTAINTIES	131
12.1	Background Estimate . . . . .	131
12.1.1	Analytic Description of $dE/dx$ . . . . .	132
12.1.2	Muon Fraction . . . . .	132
12.1.3	IBL Corrections . . . . .	132
12.1.4	Normalization . . . . .	132
12.2	Signal Yield . . . . .	133
12.2.1	initial state radiation ( <b>ISR</b> ) Modeling . . . . .	133
12.2.2	Pileup Reweighting . . . . .	133
12.2.3	Trigger Efficiency Reweighting . . . . .	134
12.2.4	Missing Transverse Momentum Scale . . . . .	135
12.2.5	Momentum Parametrization . . . . .	135
12.2.6	Ionization Requirement . . . . .	136
12.2.7	Electron and Jet Rejection . . . . .	136
12.2.8	Muon Veto . . . . .	136
12.2.9	Luminosity . . . . .	137
12.2.10	Signal Cross Section . . . . .	137
13	RESULTS	139
13.1	Cross Section Limits . . . . .	139
13.2	Mass Limits . . . . .	142
14	SUMMARY AND OUTLOOK	146

CONTENTS

V APPENDIX	148
A EXPANDED R-HADRON YIELDS AND LIMITS	149
BIBLIOGRAPHY	155

## LIST OF FIGURES

---

Figure 1	A Feynman diagram representing the interaction of the $A$ field with a generic fermion, $f$ . . . . .	7
Figure 2	The particle content of the <b>SM</b> , including the names, masses, spins, and charges of each of the particles. . . . .	9
Figure 3	A feynman diagram for photon propagation including a loop of electrons. . . . .	13
Figure 4	An approximation of the running of the coupling constants in the <b>SM</b> up to the Planck scale [2]. . . . .	13
Figure 5	The Feynman diagrams representing the decays of the W and Z bosons to fermions. Here $f$ indicates a generic fermion, $\bar{f}$ its antiparticle, and $f'$ the partner of that fermion in the same generation. . . . .	14
Figure 6	The <b>PDFs</b> for proton-proton collisions at $Q^2 = 10 \text{ GeV}^2$ and $Q^2 = 10^4 \text{ GeV}^2$ . Each shows the fraction of particles which carry a fraction $x$ of the total proton energy at the specified scale [4]. The distribution for gluons is scaled by 0.1 to fit within the axis range. . . . .	16
Figure 7	The distribution of velocities of stars as a function of the radius from the center of the galaxy. The contributions to the velocity from the various components of matter in the galaxy are shown [8]. . . . .	19
Figure 8	The evolution of the masses of sparticles with the energy scale $Q$ [11]. . . . .	22
Figure 9	An approximation of the running of the coupling constants in the <b>MSSM</b> up to the Planck scale [2]. . . . .	23
Figure 10	Mass reach of ATLAS searches for Supersymmetry as of July 2015. Only a representative selection of the available results is shown [13]. . . . .	24
Figure 11	The decay of a gluino to quarks and an <b>LSP</b> , which precedes through a squark. . . . .	26
Figure 12	The four collision points and corresponding experiments of the <b>LHC</b> . The image includes the location of the nearby city of Geneva as well as the border of France and Switzerland [23]. . . . .	29
Figure 13	The cumulative luminosity over time delivered to the ATLAS experiment from high energy proton-proton collisions since 2011. The energies of the collisions are listed for each of the data-taking periods. The figure shows the delivered luminosity as of the conclusion of data collection in 2016 [24]. . . . .	30

Figure 14	The accelerator complex that builds up to the full design energies at the <a href="#">LHC</a> . The protons are passed in order to Linac 2, the <a href="#">PSB</a> , the <a href="#">PS</a> , the <a href="#">SPS</a> and then the <a href="#">LHC</a> [25]. . . . .	31
Figure 15	A schematic of the layout of the <a href="#">LHC</a> , not to scale. The arched and straight sections are illustrated at the bottom of the schematic, and all four crossing sites are indicated with their respective experiments [17]. . . . .	32
Figure 16	A cross section of the the cryodipole magnets which bend the flight path of protons around the circumference of the <a href="#">LHC</a> . The diagram includes both the superconducting coils which produce the magnetic field and the structural elements which keep the magnets precisely aligned [17]. . . . .	33
Figure 17	The arrangement of four <a href="#">RF</a> cavities within a cryomodule [17]. . . . .	33
Figure 18	The cumulative luminosity versus time delivered to ATLAS (green), recorded by ATLAS (yellow), and certified to be good quality data (blue) during stable beams for pp collisions at 13 TeV in 2015 [24]. . . . .	36
Figure 19	The luminosity-weighted distribution of the mean number of interactions per crossing for the 2015 pp collision data at 13 TeV [24]. . . . .	37
Figure 20	A cut-away schematic of the layout of the ATLAS detector. Each of the major subsystems is indicated [19]. .	39
Figure 21	A cross-sectional slice of the ATLAS experiment which illustrates how the various <a href="#">SM</a> particles interact with the detector systems. . . . .	39
Figure 22	The layout of the four superconducting magnets in the ATLAS detector [19]. . . . .	42
Figure 23	A quarter section of the ATLAS inner detector which shows the layout of each of the subdetectors in detail. The lower panel shows an enlarged view of the pixel detector. Example trajectories for a particle with $\eta = 1.0, 1.5, 2.0, 2.5$ are shown. The <a href="#">IBL</a> , which was added after the original detector commissioning, is not shown [19].	44
Figure 24	A computer generated three-dimensional view of the inner detector along the line of the beam axis. The subdetectors and their positions are labeled [19]. . . . .	45
Figure 25	An alternative computer generated three-dimensional view of the inner detector transverse to the beam axis. The subdetectors and their positions are labeled [19]. .	45

Figure 26	The integrated radiation lengths traversed by a particle at the exit of the ID envelope (outside of the <b>TRT</b> after 108.2 cm), including the services and thermal enclosures. The distribution is shown as a function of $ \eta $ and averaged over $\phi$ . The breakdown indicates the contributions of individual sub-detectors, including services in their active volume [19]. . . . .	46
Figure 27	A cut away image of the outer three layers of the pixel detector [19]. . . . .	47
Figure 28	An image of the insertion of the <b>IBL</b> into the current pixel detector [27]. . . . .	48
Figure 29	A three-dimensional computer-generated image of the geometry of the <b>IBL</b> with a view (a) mostly transverse to the beam pipe (b) mostly parallel to the beam pipe [26]. . . . .	49
Figure 30	An expanded view of the geometry of the <b>SCT</b> double layers in the barrel region [19]. . . . .	49
Figure 31	An overview of the ATLAS calorimeter systems [19]. . . . .	51
Figure 32	The depth of (a) the electromagnetic barrel calorimeter in radiation lengths and of (b) all calorimeters in interaction lengths as a function of pseudorapidity [19]. . . . .	52
Figure 33	A schematic of the <b>LAr</b> calorimeter in the barrel region, highlighting the accordion structure [19]. . . . .	52
Figure 34	A schematic of a hadronic tile module which shows the alternating layers of steel and plastic scintillator [19]. . . . .	54
Figure 35	The segmentation in depth and $\eta$ of the tile-calorimeter modules in the central (left) and extended (right) barrels [19]. . . . .	54
Figure 36	A cut-away diagram of the muon systems on ATLAS [19]. . . . .	55
Figure 37	A quarter view of the muon spectrometer which highlights the layout of each of the detecting elements. The BOL, BML, BIL, EOL, EML, and EIL are all <b>MDT</b> elements, where the acronyms encode their positions [19]. . . . .	56
Figure 38	A schematic of the cross-section of the muon spectrometer in the barrel region [19]. . . . .	56
Figure 39	A schematic of a single <b>MDT</b> chamber, which shows the multilayers of drift tubes as well as the alignment system [19]. . . . .	57
Figure 40	A schematic of the <b>CSC</b> endcap, showing the overlapping arrangement of the eight large and eight small chambers [19]. . . . .	59
Figure 41	A schematic of the <b>TGC</b> doublet and triplet layers [19]. . . . .	59
Figure 42	The <b>L1</b> Trigger rate broken down into the types of triggers as a function of the luminosity block for the 2015 data collection period [28]. . . . .	61

Figure 43	The HLT Trigger rate broken down into the types of triggers as a function of the luminosity block for the 2015 data collection period. . . . .	62
Figure 44	An illustration of the perigee representation of track parameters for an example track. The charge is not directly shown, but is indicated by the direction of curvature of the track [31]. . . . .	64
Figure 45	The $x$ and $y$ locations of the hits generated in a simulated $t\bar{t}$ event in the inner detector. The hits which belong to tracks formed using the inside-out algorithm are highlighted in red, while the hits which belong to tracks formed using the outside-in algorithm are circled in black. This figure does not include hits in the IBL. . . . .	65
Figure 46	The tracking reconstruction efficiency as a function of (a) $\eta$ and (b) $p_T$ [32]. . . . .	66
Figure 47	Examples of the clusters formed in a single layer of the pixel detector for (a) a single isolated particle, (b) two nearly-overlapping particles, and (c) a particle which emits a $\delta$ -ray [33]. . . . .	67
Figure 48	The vertex reconstruction efficiency as a function of the number of associated tracks [35]. . . . .	69
Figure 49	The total, fractional JES uncertainties estimated for 2015 data as a function of jet $p_T$ . . . . .	75
Figure 50	The $E/p$ distribution and ratio of simulation to data for isolated tracks with (a) $ \eta  < 0.6$ and $1.2 < p/\text{GeV} < 1.8$ and (b) $ \eta  < 0.6$ and $2.2 < p/\text{GeV} < 2.8$ . . . . .	81
Figure 51	The fraction of tracks as a function (a, b) of momentum, (c, d) of interaction lengths with $E \leq 0$ for tracks with positive (on the left) and negative (on the right) charge. . . . .	82
Figure 52	An illustration (a) of the geometry of energy deposits in the calorimeter. The red energy deposits come from the charged particle targeted for measurement, while the blue energy deposits are from nearby neutral particles and must be subtracted. The same diagram (b) for the neutral-background selection, described in Section 7.2.3. . . . .	83
Figure 53	$\langle E/p \rangle_{\text{BG}}$ as a function of the track momentum for tracks with (a) $ \eta  < 0.6$ , (b) $0.6 <  \eta  < 1.1$ , and as a function of the track pseudorapidity for tracks with (c) $1.2 < p/\text{GeV} < 1.8$ , (d) $1.8 < p/\text{GeV} < 2.2$ . . . . .	84
Figure 54	$\langle E/p \rangle_{\text{COR}}$ as a function of track momentum, for tracks with (a) $ \eta  < 0.6$ , (b) $0.6 <  \eta  < 1.1$ , (c) $1.8 <  \eta  < 1.9$ , and (d) $1.9 <  \eta  < 2.3$ . . . . .	85

Figure 55	$\langle E/p \rangle_{\text{COR}}$ calculated using LCW-calibrated topological clusters as a function of track momentum for tracks with (a) zero or more associated topological clusters or (b) one or more associated topological clusters. . . . .	86
Figure 56	Comparison of the $\langle E/p \rangle_{\text{COR}}$ for tracks with (a) less than and (b) greater than 20 hits in the TRT. . . . .	87
Figure 57	Comparison of the $\langle E/p \rangle_{\text{COR}}$ for (a) positive and (b) negative tracks as a function of track momentum for tracks with $ \eta  < 0.6$ . . . . .	88
Figure 58	Comparison of the $E/p$ distributions for (a) positive and (b) negative tracks with $0.8 < p/\text{GeV} < 1.2$ and $ \eta  < 0.6$ , in simulation with the FTFP_BERT and QGSP_BERT physics lists. . . . .	88
Figure 59	Comparison of the response of the hadronic calorimeter as a function of track momentum (a) at the EM-scale and (b) after the LCW calibration. . . . .	89
Figure 60	Comparison of the response of the EM calorimeter as a function of track momentum (a) at the EM-scale and (b) with the LCW calibration. . . . .	89
Figure 61	The reconstructed mass peaks of (a) $K_S^0$ , (b) $\Lambda$ , and (c) $\bar{\Lambda}$ candidates. . . . .	90
Figure 62	The $E/p$ distribution for isolated (a) $\pi^+$ , (b) $\pi^-$ , (c) proton, and (d) anti-proton tracks. . . . .	91
Figure 63	The fraction of tracks with $E \leq 0$ for identified (a) $\pi^+$ and $\pi^-$ , and (b) proton and anti-proton tracks . . . . .	92
Figure 64	The difference in $\langle E/p \rangle$ between (a) $\pi^+$ and $\pi^-$ (b) $p$ and $\pi^+$ , and (c) $\bar{p}$ and $\pi^-$ . . . . .	93
Figure 65	$\langle E/p \rangle_{\text{COR}}$ as a function of track momentum for (a) $\pi^+$ tracks and (b) $\pi^-$ tracks. . . . .	94
Figure 66	The ratio of the calorimeter response to single particles of various species to the calorimeter response to $\pi^+$ with the physics list FTFP_BERT. . . . .	94
Figure 67	The spectra of true particles inside anti- $k_t$ , $R = 0.4$ jets with (a) $90 < p_T/\text{GeV} < 100$ , (b) $400 < p_T/\text{GeV} < 500$ , and (c) $1800 < p_T/\text{GeV} < 2300$ . . . . .	96
Figure 68	The JES response uncertainty contributions, as well as the total JES uncertainty, as a function of jet $p_T$ for (a) $ \eta  < 0.6$ and (b) $0.6 <  \eta  < 1.1$ . . . . .	99
Figure 69	The correlations between bins of average reconstructed jet momentum as a function of jet $p_T$ and $ \eta $ for jets in the central region of the detector. . . . .	100
Figure 70	The processes which contribute to gluino pair production in the proton proton collisions, where the quarks and gluons are proton constituents. . . . .	103
Figure 71	The generated $p_T$ and $\beta$ distributions for R-Hadrons with $M = 1600 \text{ GeV}$ . . . . .	103

Figure 72	A schematic diagram of an R-Hadron event with a life-time around 0.01 ns. The diagram includes one charged R-Hadron (solid blue), one neutral R-Hadron (dashed blue), LSPs (dashed green) and charged hadrons (solid orange). The pixel detector, calorimeters, and muon system are illustrated but not to scale. . . . .	106
Figure 73	Schematic diagram of an R-Hadron event with a life-time around 5 ns, where the masses of the R-Hadron and LSP are nearly degenerate. The diagram includes charged R-Hadrons (solid blue), neutral R-Hadrons (dashed blue), LSPs (dashed green) and charged hadrons (solid orange). The pixel detector, calorimeters, and muon system are illustrated but not to scale. . . . .	107
Figure 74	Schematic diagram of an R-Hadron event with a life-time around 5 ns, where the masses of the R-Hadron and LSP are not degenerate. The diagram includes charged R-Hadrons (solid blue), neutral R-Hadrons (dashed blue), LSPs (dashed green) and charged hadrons (solid orange). The pixel detector, calorimeters, and muon system are illustrated but not to scale. . . . .	108
Figure 75	A schematic diagram of an R-Hadron event with a life-time around 20 ns. The diagram includes one charged R-Hadron (solid blue), one neutral R-Hadron (dashed blue), LSPs (dashed green) and charged hadrons (solid orange). The pixel detector, calorimeters, and muon system are illustrated but not to scale. . . . .	109
Figure 76	A schematic diagram of a VLL R-Hadron event. The diagram includes one charged R-Hadron (solid blue) and one neutral R-Hadron (dashed blue). The pixel detector, calorimeters, and muon system are illustrated but not to scale. . . . .	110
Figure 77	The distribution of (a) $E_T^{\text{miss}}$ and (b) Calorimeter $E_T^{\text{miss}}$ for simulated signal events before the trigger requirement. The final bin includes all events above the axis range. . . . .	113
Figure 78	The distribution of $E_T^{\text{miss}}$ for data and simulated signal events, after the trigger requirement. The final bin includes all events above the axis range. . . . .	114
Figure 79	The trigger efficiency for the HLT_xe70 trigger requirement as a function of (a) $E_T^{\text{miss}}$ and (b) Calorimeter $E_T^{\text{miss}}$ for simulated signal events. . . . .	115
Figure 80	The dependence of $dE/dx$ on $N_{\text{split}}$ in data after basic track hit requirements have been applied. . . . .	116
Figure 81	The distribution of $dE/dx$ with various selections applied in data and simulated signal events. The final bin includes all tracks above the axis range. . . . .	116

Figure 82	The distribution of track momentum for data and simulated signal events, after previous selection requirements have been applied. The final bin includes all tracks above the axis range. . . . .	117
Figure 83	The distribution of $M_T$ for data and simulated signal events, after previous selection requirements have been applied. The final bin includes all tracks above the axis range. . . . .	118
Figure 84	The distribution of summed tracked momentum within a cone of $\Delta R < 0.25$ around the candidate track for data and simulated signal events, after previous selection requirements have been applied. The final bin includes all tracks above the axis range. . . . .	119
Figure 85	The normalized, two-dimensional distribution of $E/p$ and $f_{\text{EM}}$ for simulated (a) 1200 GeV very long-lived (VLL) R-Hadron, and (b) 1200 GeV, 10 ns R-Hadron, (c) $Z \rightarrow ee$ , and (d) $Z \rightarrow \tau\tau$ events. . . . .	120
Figure 86	Two-dimensional distribution of $dE/dx$ versus charge signed momentum ( $qp$ ) for minimum-bias tracks. The fitted distributions of the most probable values for pions, kaons and protons are superimposed. . . . .	122
Figure 87	The distribution of mass estimated using $dE/dx$ for simulated VLL R-Hadrons with masses between 1000 and 1600 GeV. . . . .	122
Figure 88	The acceptance $\times$ efficiency as a function of R-Hadron (a) mass and (b) lifetime. (a) shows all of the combinations of mass and lifetime considered in this search, and (b) highlights the lifetime dependence for 1000 GeV and 1600 GeV R-Hadrons. . . . .	124
Figure 89	The distribution of (a) $dE/dx$ and (b) momentum for tracks in data and simulated signal after requiring the event level selection and the track selection on $p_T$ , hits, and $N_{\text{split}}$ . Each sub-figure shows the normalized distributions for tracks classified as hadrons, electrons, and muons in data and R-Hadrons in the simulated signal. . . . .	126
Figure 90	The distribution of $M_{dE/dx}$ (a) before and (b) after the ionization requirement for tracks in simulated W boson decays and for the randomly generated background estimate. . . . .	128
Figure 91	The distribution of $M_{dE/dx}$ (a) before and (b) after the ionization requirement for tracks in the validation region and for the randomly generated background estimate. . . . .	129

Figure 92	The trigger efficiency for the HLT_xe70 trigger requirement as a function of Calorimeter $E_T^{\text{miss}}$ for simulated data events with a W boson selection. Simulated signal events and simulated W boson events are also included. . . . .	134
Figure 93	The efficiency of the muon veto for R-hadrons of two different masses, as a function of $\frac{1}{\beta}$ for simulated R-Hadron tracks. . . . .	137
Figure 94	The average reconstructed MDT $\beta$ distribution for $Z \rightarrow \mu\mu$ events in which one of the muons has a late arrival time in the MDT, for both data and simulation. A gaussian fit is superimposed. . . . .	138
Figure 95	The observed mass distribution of events in data and the generated background distribution in (a) the VLL and (b) the LL signal region. A few example simulated signal distributions are superimposed. . . . .	140
Figure 96	The observed and expected cross section limits as a function of mass for the VLL simulated signal. The predicted cross section values for the corresponding signals are also shown. . . . .	142
Figure 97	The observed and expected cross section limits as a function of mass for each generated lifetime. The predicted cross section values for the corresponding signals are also shown. An example of Run 1 cross section limits and predicted cross sections are shown in (d) for comparison. . . . .	143
Figure 98	The excluded range of masses as a function of gluino lifetime. The expected lower limit (LL), with its experimental $\pm 1\sigma$ band, is given with respect to the nominal theoretical cross section. The observed 95% LL obtained at $\sqrt{s} = 8$ TeV [94] is also shown for comparison. . . . .	145
Figure 99	The constraints on the gluino mass as a function of lifetime for a split-supersymmetry model with the gluino R-Hadrons decaying into a gluon or light quarks and a neutralino with mass of 100 GeV. The solid lines indicate the observed limits, while the dashed lines indicate the expected limits. The area below the curves is excluded. The dots represent results for which the particle is assumed to be prompt or VLL. This curve representing this analysis is shown in orange. . . . .	147

## LIST OF TABLES

---

Table 1	The particles in the <b>SM</b> and their corresponding superpartners in the <b>MSSM</b> . . . . .	<b>21</b>
Table 2	The design parameters of the <b>LHC</b> beam that determines the energy of collisions and the luminosity, for both the injection of protons, at the nominal circulation, and during the 2015 data-taking period. . . . .	<b>35</b>
Table 3	The performance goals for each of the subsystems of the ATLAS detector. The $ \eta $ coverage specifies the range where the subsystem needs to be able to provide measurements with the specified resolution. The resolutions include a $p_T$ or $E$ dependence that is added in quadrature with a $p_T/E$ independent piece. . . . .	<b>40</b>
Table 4	A summary of the parameters of each of the three magnet systems on ATLAS. . . . .	<b>42</b>
Table 5	A summary of the parameters of the inner detector and each of the subdetectors [19]. . . . .	<b>47</b>
Table 6	A subset of the trigger menu for the 2015 data collection with $L = 5 \times 10^{33} \text{ cm}^{-2} \text{ s}^{-1}$ . Both the <b>L1</b> and <b>HLT</b> selection requirements and their trigger rates are shown measured at the specified luminosity are shown. The typical offline selections represent a typical set of offline requirements imposed after the trigger in an analysis [28]. . . . .	<b>61</b>
Table 7	The dominant sources of corrections and systematic uncertainties in the <b>JES</b> estimation technique, including typical values for the correcting shift ( $\Delta$ ) and the associated uncertainty ( $\sigma$ ). . . . .	<b>97</b>
Table 8	The radial distances of each of the subdetectors and example arrival times for an R-Hadron with $\eta = 0$ and the specified $\beta$ . . . . .	<b>104</b>
Table 9	The expected number of events at each level of the selection for long-lived ( <b>LL</b> ) 1600 GeV, 10 ns R-Hadrons, along with the number of events observed in data, for $3.2 \text{ fb}^{-1}$ . The simulated yields are shown with statistical uncertainties only. The total efficiency $\times$ acceptance is also shown for the signal and the rejection factor relative to initial track requirement is shown for data. . . . .	<b>123</b>
Table 10	The expected number of background events within each of the mass windows for the stable and metastable signal regions. . . . .	<b>130</b>

Table 11	A summary of the sources of systematic uncertainty for the data-driven background in the signal region. If the uncertainty depends on the mass, the maximum values are reported. . . . .	131
Table 12	A summary of the sources of systematic uncertainty for the simulated signal yield. The uncertainty depends on the mass and lifetime, and the maximum negative and positive values are reported in the table. . . . .	133
Table 13	Example of the contributing systematic variations to the total systematic for the $E_T^{\text{miss}}$ Scale, as measured in a 1200 GeV, <b>VLL</b> R-Hadron signal sample. . . . .	135
Table 14	The estimated number of background events and the number of observed events in data for the specified selection regions prior to the requirement on mass. The background estimates show statistical and systematic uncertainties. . . . .	139
Table 15	The left and right extremum of the mass window for each generated mass point with a 10 ns lifetime. . . . .	140
Table 16	The left and right extremum of the mass window used for each generated <b>VLL</b> mass point. . . . .	140
Table 17	The expected number of signal events, the expected number of background events, and the observed number of events in data with their respective statistical errors within the respective mass window for each generated <b>VLL</b> mass point . . . . .	141
Table 18	The expected number of signal events, the expected number of background events, and the observed number of events in data with their respective statistical errors within the respective mass window for each generated mass point with a lifetime of 10 ns. . . . .	141
Table 19	The observed and expected 95% CL lower limit on mass for gluino R-Hadrons for each considered lifetime. . . . .	144
Table 20	The left and right extremum of the mass window for each generated mass point with a 50 ns lifetime. . . . .	149
Table 21	The left and right extremum of the mass window for each generated mass point with a 30 ns lifetime. . . . .	149
Table 22	The left and right extremum of the mass window for each generated mass point with a 10 ns lifetime. . . . .	150
Table 23	The left and right extremum of the mass window used for each generated mass point with a lifetime of 3 ns. . . . .	150
Table 24	The left and right extremum of the mass window used for each mass point with a lifetime of 1 ns. . . . .	150
Table 25	The left and right extremum of the mass window for each generated mass point with a lifetime of 0.4 ns. . . . .	151
Table 26	The left and right extremum of the mass window used for each generated stable mass point. . . . .	151

Table 27	The expected number of signal events, the expected number of background events, and the observed number of events in data with their respective statistical errors within the respective mass window for each generated mass point with a lifetime of 50 ns. . . . .	151
Table 28	The expected number of signal events, the expected number of background events, and the observed number of events in data with their respective statistical errors within the respective mass window for each generated mass point with a lifetime of 30 ns. . . . .	152
Table 29	The expected number of signal events, the expected number of background events, and the observed number of events in data with their respective statistical errors within the respective mass window for each generated mass point with a lifetime of 10 ns. . . . .	152
Table 30	The expected number of signal events, the expected number of background events, and the observed number of events in data with their respective statistical errors within the respective mass window for each generated mass point with a lifetime of 3 ns. . . . .	153
Table 31	The expected number of signal events, the expected number of background events, and the observed number of events in data with their respective statistical errors within the respective mass window for each generated mass point with a lifetime of 1 ns. . . . .	153
Table 32	The expected number of signal events, the expected number of background events, and the observed number of events in data with their respective statistical errors within the respective mass window for each generated mass point with a lifetime of p4 ns. . . . .	154
Table 33	The expected number of signal events, the expected number of background events, and the observed number of events in data with their respective statistical errors within the respective mass window for each generated stable mass point . . . . .	154

## ACRONYMS

---

- SM Standard Model  
QCD quantum chromodynamics  
PDF parton distribution function  
NLO next-to-leading order  
NLL next-to-leading logarithmic  
BSM Beyond the Standard Model  
SUSY Supersymmetry  
MSSM Minimal Supersymmetric Model  
cMSSM Constrained MSSM  
pMSSM Phenomenological MSSM  
LSP Lightest Supersymmetric Particle  
WIMP Weakly Interacting Massive Particle  
LLP Long-Lived Particle  
CERN European Organization for Nuclear Research  
LHC Large Hadron Collider  
CMS Compact Muon Solenoid  
ALICE A Large Ion Collider Experiment  
LHCb Large Hadron Collider beauty experiment  
LEP the Large Electron Positron collider  
PS Proton Synchrotron  
PSB Proton Synchrotron Booster  
SPS Super Proton Synchrotron  
EPJC European Physical Journal C  
IBL Insertible B-Layer  
SCT silicon microstrip  
TRT Transition Radiation Tracker

LAr liquid argon  
EM electromagnetic  
RPC Resistive Plate Chamber  
TGC Thin Gap Chamber  
MDT Monitored Drift Tube  
CSC Cathode Strip Chamber  
ToT time over threshold  
RoI Region of Interest  
LCW local cluster weighted  
MIP minimally ionizing particle  
IP impact parameter  
JES jet energy scale  
MDT Monitored Drift Tube  
RF radiofrequency  
L1 Level 1  
HLT high level trigger  
LL long-lived  
VLL very long-lived  
CR Control Region  
LO leading order  
ISR initial state radiation  
RMS root mean square

## INTRODUCTION

---

As of 2012, with the discovery of the Higgs boson, the Standard Model ([SM](#)) provides a complete and validated description of the interactions of fundamental particles. It describes a remarkable range of phenomena given its simple foundation, and has been successful in explaining high energy physics in all experiments yet performed. However, it is clear that the picture is incomplete: without a description of gravity or an explanation for dark matter, an extension is necessary to describe new physics at higher energies. These deficiencies motivate a wide range of experiments that search for new physics. The Large Hadron Collider ([LHC](#)) provides the highest energy approach, seeking to discover unobserved particles or interactions in high energy proton collisions.

The experiments at the [LHC](#) have searched for a variety of new phenomena in the years since collisions began in 2010. A major focus of these searches has been on Supersymmetry ([SUSY](#)), an extension to the [SM](#) which has the potential to ameliorate many of its shortfalls. None of the searches have found evidence of new physics, and between them they have begun to rule out a number of models that would predict new particles at the TeV scale. This motivates searches for more exotic signals that may have been missed, using analysis techniques tuned specifically for those signals.

This dissertation presents a search for Long-Lived Particles ([LLPs](#)) using the 13 TeV collisions collected during 2015 at the [LHC](#). Charged [LLPs](#) are predicted to exist in a subset of [SUSY](#) models, and have dramatically different detector signatures than both [SM](#) processes and other [SUSY](#) models. This search focuses on isolating that unique signature using ionization measurements in the ATLAS detector.

Part I provides the theoretical context and motivation for a search for new physics in high energy collisions. Chapter 2 outlines the basic framework of the [SM](#) and describes its particles and interactions. It also discusses the limitations of the [SM](#) that motivate the existence of new physics. Chapter 3 discusses a possible solution to the shortcomings of the [SM](#), the theory of Supersymmetry, and the ways that it can generate [LLP](#).

Part II discusses the structure of the accelerator complex that provides collisions as well as the experiment that measures them. Chapter 4 summarizes the design and performance of the [LHC](#) and the features of the proton-proton collisions it produces. Chapter 5 then discusses the components of the ATLAS detector and how they can be used to measure the particles produced in [LHC](#) collisions. Chapter 6 describes the algorithms used to reconstruct physics particles and processes from the electronic signals in the detector.

Part III presents a measurement of calorimeter response, an important component of event reconstruction used in many physics analyses. Chapter 7 describes a direct, *in situ* measurement of calorimeter response using isolated hadrons, and

investigates the modeling of that response in simulation. Chapter 8 uses those measurements to construct a correction for the energy of jets in simulation, the jet energy scale (**JES**), and to estimate an uncertainty for that correction.

Part IV details the search for **LLPs**. It begins with a discussion of the simulation of **LLPs** in ATLAS, focusing on the detector signatures and how they vary with the properties of those particles in Chapter 9. Then Chapter 10 discusses the strategy of the search and the requirements used to select **LLPs** and to reject **SM** backgrounds. Chapter 11 explains a method for predicting the background from **SM** processes, and shows a validation of the technique. Chapter 12 describes the systematic uncertainties on both the selection efficiency for signal events and the background method. The results of the search are presented in Chapter 13. Chapter 14 concludes with a summary of the search and its context in the combined search for **LLP**, as well as an outlook for future searches.

PART I  
THEORETICAL CONTEXT

# 2

## STANDARD MODEL

---

The [SM](#) of particle physics seeks to explain the symmetries and interactions of fundamental particles. The [SM](#) provides predictions in particle physics for interactions up to the Planck scale ( $10^{19}$  GeV). It has been tested by several generations of experiments and has been remarkably successful; no significant deviations from its predictions have been found.

The theory itself is a quantum field theory grown from an underlying symmetry,  $SU(3) \times SU(2) \times U(1)$ , that generates all of the interactions consistent with experimental observations<sup>1</sup>. These interactions are referred to as the Strong, Weak, and Electromagnetic forces. Each postulated symmetry necessitates the existence of an associated conserved charge, which appear as properties of the observed particles in nature.

Although this model has been very predictive, the theory is incomplete; for example, it is not able to describe gravity or astronomically observed dark matter. These limitations suggest a need for an extension or new theory to describe physics at higher energies.

### 2.1 ACTION AND THE LAGRANGIAN

Originally, both action and the Lagrangian were constructed for an integral reformulation of the laws of classical mechanics, which is a purely mathematical step: any differential equation can be re-expressed in terms of an integral equation. The Lagrangian,  $\mathcal{L}$ , is classically given by the difference of kinetic energy and potential energy. The Lagrangian is defined this way so that the action,  $\mathcal{S}$ , given by

$$\mathcal{S}[\mathbf{q}(t)] = \int_{t_1}^{t_2} \mathcal{L}(\mathbf{q}, \dot{\mathbf{q}}, t) dt \quad (1)$$

returns the classical equations of motion when one requires it to be stationary in the path,  $\mathbf{q}(t)$ . This formulation of classical mechanics is extremely useful in calculations, and generalizes beautifully to cover all types of physics.

In particular, with the development of quantum mechanics in the twentieth century, the concepts of action and the Lagrangian were found to generalize to more complicated physics for which the classical laws do not hold. Quantum mechanics and quantum field theory can be constructed from the action, using the path integral formulation, by assuming that a particle undergoes all possible paths  $\mathbf{q}(t)$  with an imaginary phase given by  $e^{i\mathcal{S}[\mathbf{q}(t)]/\hbar}$ . This reduces to classical mechanics in the limit as  $\hbar$  goes to zero, as all paths for which the action is not stationary interfere with each other so as to cancel their contributions. Because

---

<sup>1</sup> excluding gravity

the wavefunction of a particle can be completely determined through the action and the action depends only on the Lagrangian, the Lagrangian itself is sufficient to describe the physics governing the particle.

So, in both classical and quantum mechanics, the Lagrangian of a system contains everything there is to know about the system, apart from initial conditions. Thus, the most natural way to express that a system has a certain symmetry is to require that the Lagrangian is invariant under a corresponding symmetry transformation. This makes the Lagrangian the central piece of the discussion of gauge invariance; the mathematical representation of gauge invariance is that a gauge transformation on the appropriate components of the Lagrangian returns an identical Lagrangian. That is,

$$\mathcal{L}(\psi, D^\mu) = \mathcal{L}(U\psi, D'^\mu) \quad (2)$$

where  $\psi$  is the wavefunction and  $D^\mu$  is the derivative operator, both of which may transform under a symmetry operation. There are a number of immediate and surprisingly powerful consequences of requiring that the Lagrangian is invariant under a symmetry operation.

## 2.2 GAUGE INVARIANCE AND FORCES

The simplest possible relativistic, quantum Lagrangian for matter particles is the free Dirac Lagrangian, which describes a relativistic fermion in a vacuum.

$$\mathcal{L} = i\bar{\psi}\not{d}\psi - m\bar{\psi}\psi \quad (3)$$

A fermion denotes a particle with spin-1/2, and the kinematic term ( $i\bar{\psi}\not{d}\psi$ ) is chosen to correctly describe the free propagation of a fermionic particle with mass  $m$ . This equation is invariant under a global  $U(1)$  transformation, that is changing  $\psi$  by a complex phase has no effect. The derivative operator commutes with a constant phase factor, and wherever  $\psi$  appears its complex conjugate also appears so as to cancel out the change of phase. However, the Lagrangian as written is not invariant under the local  $U(1)$  symmetry postulated for the SM, which can be written as  $U = e^{i\alpha(x)}$ . The piece of the Lagrangian involving a derivative will return an extra term that will break the invariance of the Lagrangian under this transformation:

$$\begin{aligned} \mathcal{L}' &= i(\bar{\psi}U^\dagger)\not{d}(U\psi) - m(\bar{\psi}U^\dagger)(U\psi) \\ &= i(\bar{\psi}U^\dagger)U(\not{d} - \gamma^\mu\partial_\mu\alpha(x))\psi - m(\bar{\psi}U^\dagger)(U\psi) \\ &= i\bar{\psi}\not{d}\psi - m\bar{\psi}\psi - i\gamma^\mu\partial_\mu\alpha(x)\bar{\psi}\psi \\ &= \mathcal{L} - i\gamma^\mu\partial_\mu\alpha(x)\bar{\psi}\psi \\ &\neq \mathcal{L} \end{aligned}$$

So, in order to enforce the required symmetry, the typical approach is to construct a covariant derivative, that is to add a term to the derivative operator

so that the unwanted term in  $\mathcal{L}'$  is exactly canceled. A generic form for such a derivative is given by

$$D^\mu = \partial^\mu - iqA^\mu$$

where at this point  $A^\mu$  is an arbitrary field that transforms under the  $U(1)$  operator and  $q$  is a scaling factor. Adding this component to the above Lagrangian gives

$$\mathcal{L}' = i(\bar{\psi}U^\dagger)U(\not{d} - \gamma^\mu\partial_\mu\alpha(x) - iq\gamma^\mu A'_\mu)\psi - m(\psi U^\dagger)(U\psi) \quad (4)$$

$$\mathcal{L}' = \mathcal{L} + \gamma^\mu(-i\partial_\mu\alpha(x) - iqA'_\mu + iqA_\mu)\bar{\psi}\psi \quad (5)$$

and because the transformation of  $A^\mu$  is unspecified,  $\mathcal{L} = \mathcal{L}'$  whenever

$$A'_\mu = A_\mu - \frac{1}{q}\partial_\mu\alpha(x)$$

The above procedure demonstrated that beginning with the Lagrangian for a free fermion and imposing a local  $U(1)$  symmetry required the existence of a vector field  $A^\mu$ , and specified its transformation under the  $U(1)$  gauge group. The additional term in the derivative can be expanded to form a completely separate term in the Lagrangian,

$$\mathcal{L} = i\bar{\psi}\not{d}\psi - m\bar{\psi}\psi - (q\bar{\psi}\gamma^\mu\psi)A^\mu \quad (6)$$

and in this form it is clear that the  $A^\mu$  term has the exact form of the electromagnetic interaction. That is, this is the Lagrangian which reproduces the relativistic form of Maxwell's equations for a particle interacting with an electromagnetic field. It is natural to also introduce a term to the Lagrangian at this point to describe the free propagation of the vector  $A$  field, where the propagation of a vector field has the form of

$$-\frac{1}{16\pi}F^{\mu\nu}F_{\mu\nu} \quad \text{with} \quad F_{\mu\nu} = \partial_\mu A_\nu - \partial_\nu A_\mu \quad (7)$$

This then also describes the electromagnetic interactions in a vacuum and the propagation of a photon. This component of the Lagrangian could also potentially include a mass term, but such a term would not be gauge invariant and so must be excluded. The photon is an example of a gauge boson, a spin-1 particle required to exist by a gauge symmetry of the Lagrangian and one that corresponds to a force. In summary, requiring the  $U(1)$  symmetry was enough to recover all of electromagnetism and to predict the existence of a photon in the SM.

The interaction term that was placed into the Lagrangian by this procedure can be conveniently summarized with Feynman diagrams, which diagrammatically represent a transition from an initial state to a final state. The contribution

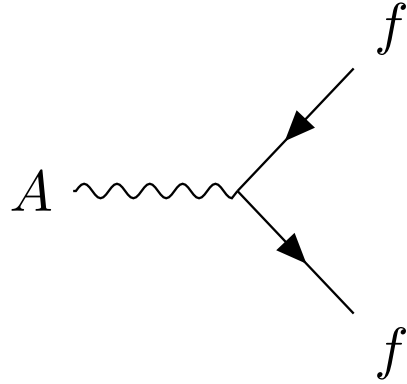


Figure 1: A Feynman diagram representing the interaction of the  $A$  field with a generic fermion,  $f$ .

of all diagrams that start with the same initial state and end with the same final state must be summed, but more complicated diagrams can be built by linking together the simplest versions. A diagram that corresponds to the above term,  $(q\bar{\psi}\gamma^\mu\psi)A^\mu$ , is shown in Figure 1, for an interaction with a generic fermion.

### 2.2.1 $SU(2) \times U(1)$ AND THE ELECTROWEAK FORCE

The full picture of the electroweak section of the SM is more complicated than the simplified explanation of the electromagnetic piece described above. In practice, it is necessary to consider the entire  $SU(2) \times U(1)$  symmetry together, but the procedure is the same. Enforcing the symmetry on the Lagrangian requires the introduction of a covariant derivative, this time with four total distinct terms, one for each of the generators of  $SU(2) \times U(1)$ . The result is a series of terms in the Lagrangian which describe the interaction of a fermion with four vector (spin-1) fields, the  $W_1$ ,  $W_2$ ,  $W_3$ , and  $B$  fields. These fields can mix in the quantum sense, and linear combinations form the  $W^+$ ,  $W^-$ ,  $Z$ , and  $A$  fields that are considered actual particles in the SM<sup>2</sup>.

### 2.2.2 $SU(3)$ AND THE STRONG FORCE

The same procedure can be applied starting with the  $SU(3)$  symmetry requirement, where eight additional fields must be introduced, one for each of the generators of  $SU(3)$ . The resulting Lagrangian describes quantum chromodynamics (QCD) and predicts the existence of eight massless gauge bosons known collectively as gluons. The complexity of the interactions of those eight gluons leads to surprising phenomena, discussed in Section 2.5.3.

---

<sup>2</sup> These states are the actual particles because they are mass eigenstates, but the full explanation of this will have to wait for the discussion of the Higgs mechanism in Section 2.4.

## 2.3 NOETHER'S THEOREM, CHARGES, AND MATTER

Another direct consequence of the symmetries stipulated in the SM are a series of conserved quantities, Noether charges, named after the mathematician and physicist Emmy Noether. The charges arise as a direct consequence of Noether's theorem, which can be informally stated as

*For every symmetry of the Lagrangian, there exists a corresponding physical quantity whose value is conserved in time.*

Or, stated another way, symmetries of the Lagrangian mathematically require the conservation of specific quantities taken from the Lagrangian. This relationship can also be thought of as operating in the other direction, the existence of a conserved charge can be shown to generate the symmetry in the Lagrangian. This theorem is actually quite striking in a somewhat unexpected relation between simple geometric symmetries and physically observable conservation laws. For example, the theorem connects the translation invariance of the Lagrangian in space to the conservation of momentum and the translation invariance in time to the conservation of energy.

In the context of the SM, the required symmetries of  $U(1) \times SU(2) \times SU(3)$  correspond to the charges that are considered properties of all elementary particles. The most familiar of these properties is the electric charge,  $Q$ , which is one of the conserved quantities of  $SU(2) \times U(1)$ . The remaining pieces of  $SU(2) \times U(1)$  correspond to weak isospin,  $T$  and  $T_3$ , where  $T$  has only non-negative values and  $T_3$  can be positive and negative.  $T$  is the magnitude of the full three vector of weak isospin,  $\mathbf{T}$ , and  $T_3$  is the projection along the third component that is the other conserved quantity derived from  $SU(2) \times U(1)$ . The  $SU(3)$  symmetry is generated by the three colors of QCD, red, green, and blue, each with a corresponding opposite color, anti-red, anti-green, and anti-blue. The color charges are also conserved in the SM.

The matter in the observable universe consists of a collection of particles which carry these charges, in addition to spin and mass. The matter particles are all fermions: particles with spin-1/2. All of the fermions belong to one of two groups, quarks and leptons, and one of three generations. Each of the generations have the same quantum numbers and charges but significantly different masses; the particles in higher generations have increasing mass. Quarks are distinguished from leptons in that they carry color charge, in addition to electric charge and weak isospin. The particles in the SM are summarized in Figure 2, and the matter particles are the twelve types of fermions displayed on the left side of the graphic.

### 2.3.1 QUARKS

The three generations of quarks each consist of a quark with electric charge +2/3 and one with charge -1/3. They are called up and down, charm and strange, and top and bottom respectively, and these are referred to as the quark flavors. Although Figure 2 only shows these six flavors, there is a unique particle for each

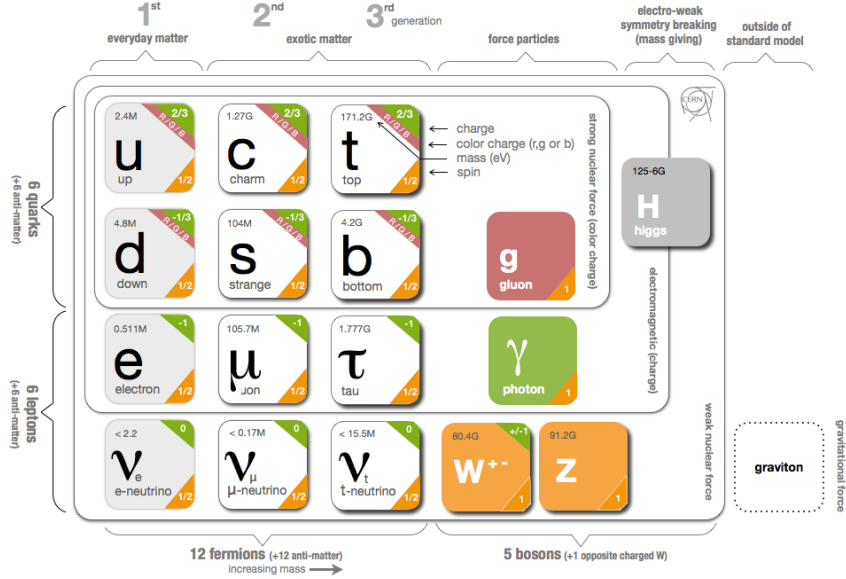


Figure 2: The particle content of the SM, including the names, masses, spins, and charges of each of the particles.

combination of the three colors and flavor. And each quark has an anti-particle with the opposite electric charge values.

However, individual quarks are never observed in nature, but instead form color-neutral bound states. This is a consequence of interaction of gluons with color charge called confinement, discussed in Section 2.5.3. One way to form a color neutral combination is a bound state of three quarks with three different color charges, called a baryon. Baryons are the most common type of quark configuration in conventional matter, and include protons and neutrons. The other common configuration is a bound state of a quark and an anti-quark, called a meson, where the two quarks have opposite colors. Although there is no direct conservation law resulting from the symmetries of the SM Lagrangian, an accidental symmetry results in the approximate conservation of baryon number,  $B$ , where baryons have  $B = 1$  and mesons have  $B = 0$ . That is, no interactions have been observed which directly alter baryon number.

### 2.3.2 LEPTONS

The remaining fermions, the leptons, do not carry color charge. Each generation contains an electrically charged lepton, the electron, muon, and tau, and an electrically neutral lepton called a neutrino. For the charged leptons, the flavors are mass eigenstates, with the masses listed in Figure 2. The flavors of the neutrinos, on the other hand, are not mass eigenstates: their propagation in quantum superpositions of flavor states leads to oscillations between different flavors. The absolute masses of the neutrinos are not currently known, but the phenomenon

of oscillations shows that they have three different mass values. Another accidental symmetry leads to an approximate conservation of lepton number  $L$ , the difference in the number of leptons and anti-leptons; again there are no interactions present in the SM which directly alter lepton number.

### 2.3.3 CHIRALITY

All of the fermions described above have two possible values of the magnitude of weak isospin,  $T$ , either 0 or 1/2. The fermions with  $T = 0$  are called right-handed, while those with  $T = 1/2$  are called left-handed. Because  $T$  is the charge corresponding to the weak force, right-handed particles do not interact with the weak gauge bosons in the same way that neutral particles do not interact with photons. For left-handed fermions, each of the quark and lepton generations have one particle with  $T_3 = -1/2$  and one with  $T_3 = +1/2$ . The neutrinos have  $T_3 = +1/2$ , while the charged leptons have  $T_3 = -1/2$ . Similarly, the positively charged quarks have  $T_3 = +1/2$  and the negatively charged quarks have  $T_3 = -1/2$ . Because the right-handed neutrinos would have no charge of any type, it is not clear if they exist at all.

## 2.4 HIGGS MECHANISM AND MASS

The description of the electroweak forces above left out an important part of the observed nature of the electroweak force. Many physical experiments observed phenomena corresponding to the interaction of the weak bosons that were best explained if they had significant masses. But as mentioned before, massive bosons would break the gauge invariance of the Lagrangian. A large mass for the W and Z bosons is necessary to explain the relative weakness of their interactions compared to the electromagnetic field. The Lagrangian's discussed above did not include a mass term for the gauge bosons, and in fact such a term would not be allowed by the requirement of gauge invariance. This was a significant problem for the SM, and the symmetry of the electroweak sector would have to be broken in order to allow for non zero masses for some of the gauge bosons.

One mechanism to allow for this symmetry breaking is the Higgs mechanism, which posits the existence of an additional scalar field. It begins with a  $SU(2) \times U(1)$  invariant Lagrangian of the form

$$\mathcal{L} = |D_\mu \phi|^2 - \frac{1}{2}\mu^2\phi^+\phi - \frac{1}{4}\lambda(\phi^+\phi)^2 \quad (8)$$

where  $\phi$  is the new scalar field with two components and, importantly,  $\mu^2$  is negative. This leads to a minimum value of the field at a non-zero value of  $\phi$ , specifically where

$$\langle\phi\rangle = \frac{1}{\sqrt{2}} \begin{pmatrix} 0 \\ v \end{pmatrix} \quad \text{with} \quad v = \frac{2\mu^2}{\lambda} \quad (9)$$

Expanding the original Lagrangian about its expectation value in terms of the perturbation  $H$ ,

$$\langle \phi \rangle = \frac{1}{\sqrt{2}} \begin{pmatrix} 0 \\ v + H \end{pmatrix} \quad (10)$$

gives potential terms in the Lagrangian like

$$\mathcal{L}_H = -\frac{1}{2} m_H^2 H^2 - \sqrt{\frac{\lambda}{2}} m_H H^3 - \frac{1}{4} \lambda H^4 \quad (11)$$

where  $m_H = \sqrt{2}\mu$ . The form of this Lagrangian shows that the non-zero expectation value of the  $\phi$  field has introduced a massive scalar field  $H$  with self interaction terms. It has an additional important consequence on the description of the gauge bosons, through the expansion of the term involving the covariant derivative:

$$|D_\mu \phi|^2 \supset \frac{1}{8} (g^2 (W_{1\mu} W_1^\mu + W_{2\mu} W_2^\mu) + (g' B_\mu - g W_3 \mu)^2) \quad (12)$$

where the  $W_i$  and  $B$  fields are the original  $SU(2) \times U(1)$  gauge fields mentioned previously. The above equation can be rearranged using linear combinations of the fields to form mass terms for the gauge bosons, and the mass eigenstates are exactly the  $W^\pm$ ,  $Z$ , and  $A$  fields. Only the  $A$  field, corresponding to the photon, results in a zero mass, and the remaining three particles have non-zero mass values. Because the previously introduced Lagrangian, written in terms of  $\phi$ , was clearly gauge invariant, this resulting configuration must also be gauge invariant.

This is the Higgs mechanism, where the introduction of a gauge invariant scalar field with a non-zero expectation value can generate masses for the gauge bosons without violating the underlying symmetries. The particle that is associated with the perturbations of this field,  $H$ , is called the Higgs boson, and is said to generate the masses of the remaining bosons because the vacuum expectation value introduces mass-like terms for each of the bosons. The resulting masses are listed in Figure 2. Because this mechanism was so successful in describing the observed properties of the  $W$  and  $Z$  bosons, it has been considered part of the SM for decades, although the actual Higgs boson was only recently observed in 2012, fully confirming the theory.

The Higgs mechanism is also responsible for generating the masses of the fermions. The original mass terms that were listed in the Lagrangian for fermions are replaced with Yukawa coupling terms, which introduce interactions between the  $\phi$  field and the fermions. Like with the gauge bosons, the non-zero expectation value of the field yields mass terms, and the expansion about that value introduces interaction terms between the fermions and the Higgs boson. The masses are different between each fermion because each has a different Yukawa coupling, which results in the masses listed in Figure 2.

## 2.5 PHENOMENOLOGY

The [SM](#) Lagrangian described above contains all of the information necessary to describe particle physics through the path integral formulation. However, a tremendous amount of complexity emerges from that description because of the diverse allowed interactions between the ensemble of particles in the [SM](#). A qualitative understanding of the phenomenology produced by those interactions is immensely helpful in understanding the analysis of particle physics.

### 2.5.1 STANDARD MODEL CALCULATIONS

The terms in the Lagrangian describing interactions of particles can be used to evaluate cross sections or decay widths through perturbation theory. A cross section quantifies the probability of a given process to result in a scattering of particles, measured as an effective area, while a decay width measures the width of the mass distribution of a particle, which is inversely proportional to its lifetime. Perturbation theory uses a diagrammatic expansion to approximate [SM](#) interactions as a series of feynman diagrams, each representing an amplitude for the transition between initial and final state. The feynman diagrams uniquely specify that transition amplitude through the feynman rules [1]. The transition amplitude includes a phase space component to account for the initial and final momenta, and an addition matrix element which describes the interaction. The complex amplitude for each process with the same initial and final state must be summed, and then the cross section or decay width is calculated as the square of the amplitude integrated over all valid final state momenta. For example, the decay rate for a particle of mass  $m_A$  to two final state particles with momenta  $\mathbf{p}_i$  and  $\mathbf{p}_j$  is given by

$$\Gamma = \int \frac{d^3 p_i d^3 p_j}{(2\pi)^6 4E_i E_j} (2\pi)^4 \delta^{(4)}(\mathbf{p}_A - \mathbf{p}_i - \mathbf{p}_j) |\mathcal{M}|^2$$

where the prefactor is the phase space term, the delta function enforces conservation of four-momentum, and  $\mathcal{M}$  is the matrix element. The matrix element includes dimensionless constant terms that describe the strength of the interaction, called coupling constants:  $\alpha$  for the photon,  $\alpha_W$  for the weak bosons, and  $\alpha_s$  for the gluons.

The sum over all diagrams with the same initial and final state leads to important consequences in the [SM](#). Most process have a small number of leading order diagrams, where leading order indicates the diagram with the fewest factors of the coupling constants. When the coupling constants are less than unity, the diagrams of higher order have diminishing contributions. This is called the perturbative regime, and allows for approximate calculations by using a set order, referred to as leading order ([LO](#)), next-to-leading order ([NLO](#)), and so on. A coupling constant greater than unity results in a non-perturbative regime, and requires other calculation techniques.

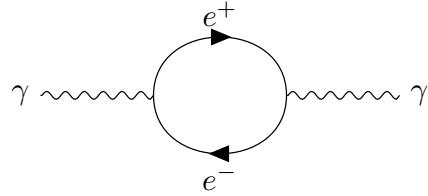


Figure 3: A feynman diagram for photon propagation including a loop of electrons.

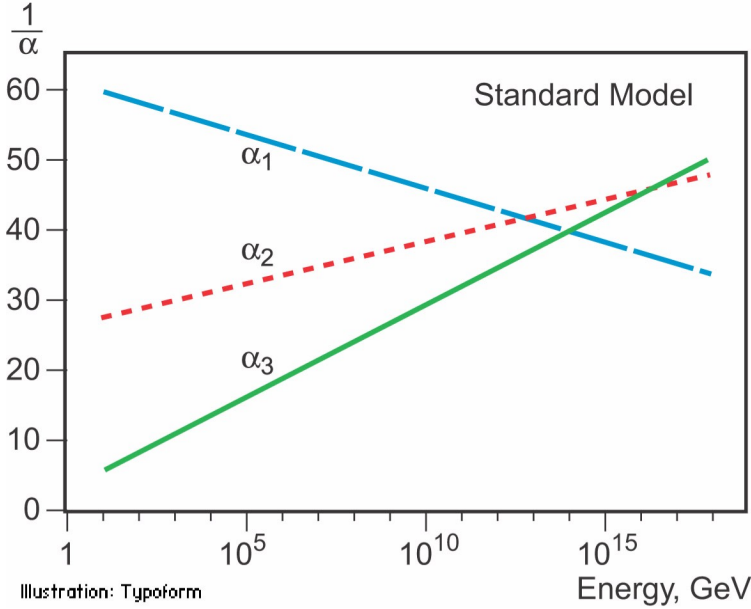


Figure 4: An approximation of the running of the coupling constants in the SM up to the Planck scale [2].

However, even in a perturbative theory, the sum over all diagrams in the amplitude includes loop diagrams; for example any photon line in a Feynman diagram can be replaced with the line in Figure 3 and still form a valid interaction. These and other types of loop diagrams introduce divergent contributions to SM processes, which would seem to make the theory inconsistent. The solution to this problem is to absorb those contributions into the coupling constants and charges in the Lagrangian, so that the combination of the bare value and the loop contributions gives the correct physical observables. This process is called renormalization, and a theory where the divergences can consistently be absorbed into the definition of the constants in the Lagrangian is called renormalizable.

Setting the renormalized coupling constants requires a measurement at a specific energy scale, and only at that scale are the contributions of the loop diagrams precisely cancelled. At a different energy the loop diagram contribution changes, and can be thought of as a modification to the coupling constant. The renormalization procedure thus predicts a variation of the coupling constants with the scale of the interaction, and specifies how they change with energy. The energy dependence is called the running of the coupling constants, and the effect on the three couplings in the SM is shown in Figure 4.

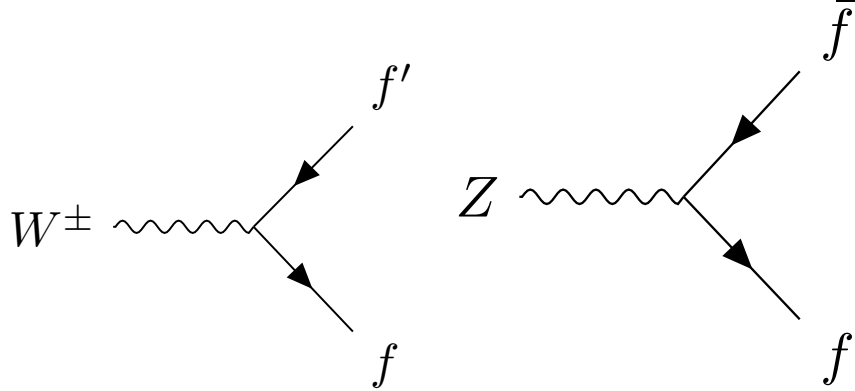


Figure 5: The Feynman diagrams representing the decays of the  $W$  and  $Z$  bosons to fermions. Here  $f$  indicates a generic fermion,  $\bar{f}$  its antiparticle, and  $f'$  the partner of that fermion in the same generation.

### 2.5.2 ELECTROWEAK PHYSICS

The masses of the  $W$  and  $Z$  bosons result in significantly different processes for the weak fields than the electromagnetic field, despite their interactions being similar before symmetry breaking. The massless photon is stable, and can propagate in a vacuum, resulting in the familiar long range interactions of electromagnetism. The  $W$  and  $Z$  bosons, however, are unstable, as they have large enough masses to decay to fermions, such as the decays shown in Figure 5. For this reason, photons can be observed directly, while the other bosons are sufficiently short-lived (with lifetimes around  $10^{-25}$  s) that they can only be measured from their decay products.

Because the electroweak bosons interact with both quarks and leptons, they are responsible for the production of leptons in proton-proton collisions.  $Z$  bosons and photons produce pairs of opposite sign, same flavor leptons.  $W$  bosons, on the other hand, produce a single lepton and the corresponding neutrino. The electroweak bosons also decay to hadrons by producing pairs of quarks, as shown in Figure 5. The  $Z$  boson decays to hadrons with a branching ratio of 69.9%, to neutrinos with 20.0%, and to charged leptons 10.1% of the time [3]. The  $W$  boson decays to hadrons with a branching ratio of 67.6% and to leptons 32.4% [3].

### 2.5.3 STRONG PHYSICS

The phenomenology of the strong sector differs significantly from the weak sector because the gluons are massless but color charged. Because of this, gluons can interact with each other, and contributions from multiple gluon interactions lead to a significant growth in the strength of the field at low energies. The dependence of the field strength on the energy scale is described by renormalization, and in QCD the coupling is only small at high energies. Below approximately 1

GeV, the strength of those interactions results in confinement: the interactions are so strong that when quark-antiquark pairs separate, the fields between them generate additional quarks to form color neutral bound states. Above around the GeV scale, the interactions of quarks become perturbative, similar to the electroweak fields; this phenomenon is known as asymptotic freedom.

At lower energies, however, the strength of the strong interaction is so significant that the interactions of color-charged particles create additional particles until they form neutral bound-states. This process is known as hadronization, and explains why no quarks are observed isolated in nature: they all form bound states of hadrons like protons, neutrons, and pions. The hadronization process can produce a significant number of particles, so that a single energetic quark recoiling against another quark can generate a cascade of dozens of hadrons. Because of the initial boost of such an energetic configuration, the resulting hadrons are collimated, and conical spray of particles often referred to as a jet.

#### 2.5.4 PROTON-PROTON COLLISIONS

Proton-proton collisions are a convenient way to generate high energy interactions to probe the SM and to search for new physics. At the energies that will be discussed in this analysis, the substructure of the protons is very important to the description of the resulting interactions. At lowest order, protons are composed of two up quarks and one down quark, but this description is incomplete. The actual bound state includes a chaotic sea of additional gluons and  $q\bar{q}$  pairs, each of which carries a variable fraction of the proton's energy. When a proton-proton collision takes place, it is these constituents that interact with each other, resulting in a highly variable collision energy even when the proton-proton energy is consistent.

The fraction of the energy carried by each constituent varies moment to moment, but can be modelled probabilistically by parton distribution functions (PDFs). These are difficult to predict theoretically, as the QCD calculations are non-perturbative, and instead are measured in hard-scattering experiments. They are usually represented by how often a given type of particle carries a fraction  $x$  of the total proton energy. Those fractions change significantly with the scale of the interaction,  $Q$ ; the PDFs of proton-proton collisions at both  $Q^2 = 10 \text{ GeV}^2$  and  $Q^2 = 10^4 \text{ GeV}^2$  are shown in Figure 6.

The underlying PDFs of protons has important effects on the calculation of cross sections in proton-proton collisions. Instead of specifying an exact initial momentum for the cross section calculation, in a proton-proton collision it is necessary to integrate over the contribution to a given process from the PDFs for all possible constituent particles. The constituents are unlikely to carry the entire momentum of the proton, so the cross section for processes involving massive particle are suppressed.

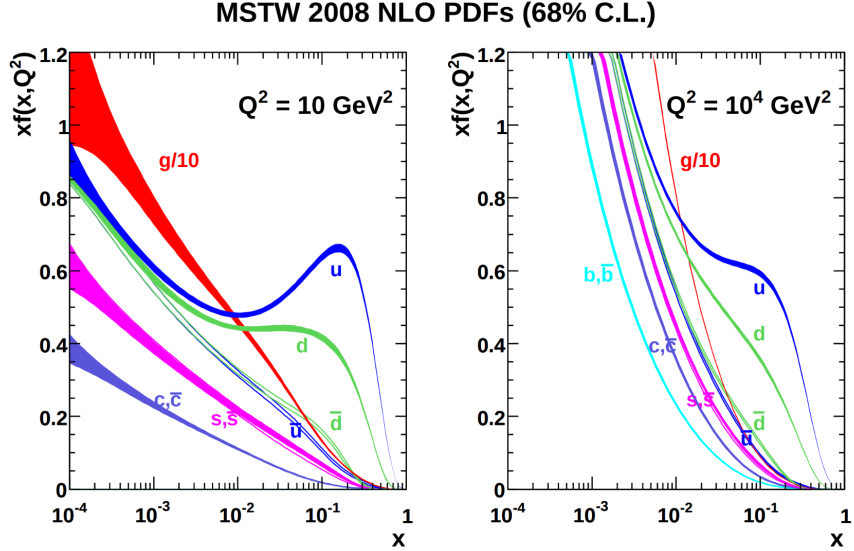


Figure 6: The PDFs for proton-proton collisions at  $Q^2 = 10 \text{ GeV}^2$  and  $Q^2 = 10^4 \text{ GeV}^2$ . Each shows the fraction of particles which carry a fraction  $x$  of the total proton energy at the specified scale [4]. The distribution for gluons is scaled by 0.1 to fit within the axis range.

### 2.5.5 SIMULATION

Although the SM provides the necessary components to model the proton-proton collisions at the LHC, the complexity of the processes make direct predictions difficult. The LHC experiments rely on simulations that break down the collisions and resulting detector interactions into several steps in order to predict expected SM and even Beyond the Standard Model (BSM) events. The simulation begins with a selection of two proton constituents to collide from the PDFs described in Section 2.5.4, which fully specify the particle types and their momenta. The initial momenta are then fed into an event generator, which calculates the cross section and predicts the final momentum using the matrix element formulation described in Section 2.5.1. This analysis uses both the Pythia 6.4.27 [5] and MG5\_aMC@NLO [6] generators in simulated events. The next step calculates additional processes that occur during the primary interaction, including hadronization, fragmentation, and initial state radiation. The result of this intial event generation is a series of particles and momentum that were produced in the collision. These initial particle states are recorded for simulation studies, and are often referred to as truth.

These particles must then be propagated through a simulated detector geometry, where the signal they produce in the detector models can be modeled. Geant4 [7] provides a toolbox that describes the propagation of particles in the magnetic field as well as their interactions with the detector material. It also simulates secondary interactions where additional particles may be produced, such as a photon interacting with the detector material and converting to two electrons. Each particle is tracked until its energy is lost or it exits the volume of the

detector, and the signals it generates in the active regions of the detector simulation are recorded. Those signal are then converted into the expected electronic outputs of the detector in a process called digitization. The result of this step has precisely the same format as collected data, so that both can be fed into the same reconstruction algorithms for analysis.

## 2.6 LIMITATIONS

Despite the great success of the relatively simple [SM](#) in describing such a broad range of emergent phenomena, it is clear that the picture it presents of the interactions of fundamental particles is incomplete. The [SM](#) contains concerning coincidences that suggest a more ordered underlying substructure that is not expressed in the current form. It also fails to explain a number of cosmological measurements of the nature of matter in the universe. These limitations suggest the need for new, [BSM](#) physics that would provide a more complete description at higher energies.

### 2.6.1 THEORETICAL CONCERNS

There have been no successful integrations of the [SM](#)'s description of the electroweak and strong forces with the description of gravity, and it is still unclear how to account for the effects of gravity at the Planck scale of approximately  $10^{19}$  GeV, where its interactions are as strong as the remaining forces. The Planck scale is an important cutoff for the [SM](#), as it is clear that the [SM](#) must break down somewhere between the current highest energy tests of the [SM](#), around 1 TeV, and the Planck scale.

One example of this is the Higgs mass, which is determined by a sum of its bare mass and the interactions in the vacuum with all massive particles. As there must be new physics at the Planck scale to describe gravity, some of those corrections would include contributions at a scale seventeen orders of magnitude above the mass of the Higgs. Either the bare mass of the Higgs boson precisely cancels those contributions to leave a remainder seventeen orders of magnitudes smaller, or a new theory exists at a lower scale the shields the Higgs mass from those terms. A theory where such a unlikely cancellation of free parameters occurs is called fine-tuned, and one that is free from such cancellations is called natural. Theories where the mass of the Higgs is natural are usually preferred, as they suggest an underlying, coherent structure. The enormous difference in scales between the weak scale (including the Higgs mass), and the Planck scale, is often referred to as the hierarchy problem.

There is also a compelling argument that the  $SU(3) \times SU(2) \times U(1)$  gauge structure of the [SM](#) might originate from a single, unified gauge theory. For example, it is possible to represent that gauge structure as a  $SU(5)$  gauge group with only a few inconsistencies with the current implementation. This unification is suggested by the scaling of the coupling constants for each of the forces under renormalization; they come close to converging to a single value at higher energies, as seen in Figure 4. An additional correction to the scaling of the cou-

pling constants from new physics above the TeV scale could cause them to merge into a single value at high energies.

## 2.6.2 COSMOLOGICAL OBSERVATIONS

The [SM](#) contains a symmetry in the description of matter and antimatter that is not reflected in cosmological observations. The processes of the standard model create or remove matter and antimatter in equal amounts, so a universe that begins with an equal quantity of each should result in a universe with an approximate<sup>3</sup> balance of matter and antimatter. However, cosmological observations of the relative amount of each type clearly show that the directly observable mass of the universe is overwhelmingly made of matter. As this difference is largely a difference in the generation of baryons and anti-baryons, this discrepancy is often referred to as the baryogenesis problem.

A number of astrophysical observations of large scale gravitational interactions suggest the presence of a significant amount of non-luminous matter that interacts with the normal matter only gravitationally. The first evidence of this came from the observation of galactic rotation curves, the velocities of stars as a function of the radius from the center of a galaxy. These can be directly predicted from the amount of matter contained within the sphere up to the radius of the star. An estimate of velocity based only on the luminous matter in the galaxies would predict a dependence that falls off with the radius, but the observed curves show a mostly constant distribution of velocities [8], as seen in Figure 7. The higher velocities than predicted by the luminous matter can be explained by a halo of dark matter that extends significantly outside the galactic disk.

This dark matter accounts for a majority of the matter in the universe, and is incompatible with the matter particles predicted by the [SM](#). Many observations support its existence, but there have been no direct detections of a particle which could account for the large quantity of gravitationally interacting dark matter. The [SM](#) would have to require a significant extension to include the particles needed to explain dark matter and the processes needed to explain the observed matter-antimatter asymmetry.

---

<sup>3</sup> There are some processes in the standard model which can result in a small imbalance of matter and antimatter, but not at the scale observed cosmologically.

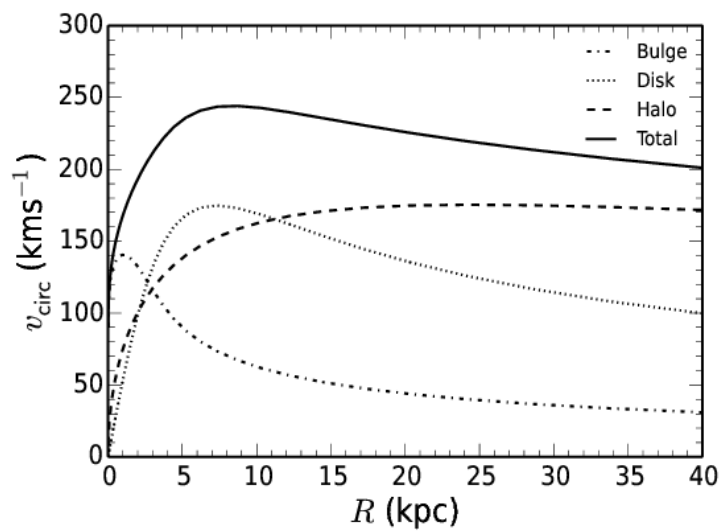


Figure 7: The distribution of velocities of stars as a function of the radius from the center of the galaxy. The contributions to the velocity from the various components of matter in the galaxy are shown [8].

# 3

## SUPERSYMMETRY

---

The theory of [SUSY](#) presents an extension to the [SM](#) that solves a number of the outstanding issues. It is based on another proposed symmetry, one which introduces an equality between the fermionic particles and proposed bosonic partners and also between bosonic particles and their proposed fermionic partners. The symmetry is defined by extending spacetime into a superspace, which includes one dimension that describes a particle's spin: a transformation in this space moves a fermion with spin-1/2 to a boson with spin-0 or vice-versa. Requiring the [SM](#) to be symmetrical under these transformations requires the existence of a bosonic partner for every current matter fermion in the [SM](#) and a fermionic partner for every boson. The partners are called superparticles (sparticles), where quarks partner with squarks and leptons partner with sleptons, and each boson has a fermionic partner called a gaugino. The superpartners, in the original form of the theory, should be identical to the original particle in every way except for spin; that is they would have the same quantum charges and the same mass.

However, the simplest version of the theory, where the symmetry is unbroken, is incompatible with current observations of physics in a number of systems. The most striking example comes from the electron, as the superpartner of an electron would introduce a stable, negatively charged, and bosonic particle. Such a particle would drastically alter atomic properties by providing a way to create atoms without the valence structure of electrons that results from the Pauli exclusion principle for fermions. Various high energy physics measurements have also confirmed the spin of the W and Z bosons, for example, and a fermionic gaugino has never been produced at those masses. The solution to this incompatibility with observation is to conjecture that the symmetry exists but is spontaneously broken, where the masses of the supersymmetric particles are significantly larger than those of the current [SM](#) particles. Like the spontaneous symmetry breaking of the electroweak system, this symmetry breaking can be accomplished by introducing an additional Higgs mechanism.

### 3.1 STRUCTURE

There are a number of ways to model the particulars of [SUSY](#), but many of the resulting phenomena are similar, and a discussion of an example is sufficient to describe the structure and results of the theory. The Minimal Supersymmetric Model ([MSSM](#)) is one example of a complete description that includes the necessary symmetry breaking to result in the different masses between particles and sparticles [9]. It is called minimal because it is designed to use the simplest possible extension to the Higgs sector of the [SM](#) that results in the split scale between [SM](#) and [SUSY](#) particles. However even a minimal version includes a remarkable number of free parameters, over 100, and the [MSSM](#) is often further con-

Sector	Particles	Sparticles
Baryonic Matter	$(u, d)$	$(\tilde{u}, \tilde{d})$
	$(c, s)$	$(\tilde{c}, \tilde{s})$
	$(t, b)$	$(\tilde{t}, \tilde{b})$
Leptonic Matter	$(\nu_e, e)$	$(\tilde{\nu}_e, \tilde{e})$
	$(\nu_\mu, \mu)$	$(\tilde{\nu}_m u, \tilde{\mu})$
	$(\nu_\tau, \tau)$	$(\tilde{\nu}_\tau, \tilde{\tau})$
Higgs	$(H_u^+, H_u^0)$	$(\tilde{H}_u^+, \tilde{H}_u^0)$
	$(H_d^0, H_d^-)$	$(\tilde{H}_d^0, \tilde{H}_d^-)$
Strong	$g$	$\tilde{g}$
Electroweak	$(W^\pm, W^0)$	$(\tilde{W}^\pm, \tilde{W}^0)$
	$B^0$	$\tilde{B}^0$

Table 1: The particles in the [SM](#) and their corresponding superpartners in the [MSSM](#).

strained to include fewer parameters in models such as the Phenomenological [MSSM](#) ([pMSSM](#)) and the Constrained [MSSM](#) ([cMSSM](#)) [10].

The theory includes a sparticle partner for every [SM](#) particle, which are listed in Table 1. To then provide the different masses for those sparticles, the [MSSM](#) introduces a second Higgs interaction. The resulting scalar field, along with the original Higgs field, generates five total particles,  $h^0$ , the original Higgs boson,  $A^0$ ,  $H^0$ , and  $H^\pm$ , where the last two are electrically charged. These Higgs bosons can mix with the supersymmetric gauginos to form a series of mass eigenstates. These are usually referred to by the order of their masses, where the neutral gauginos (neutralinos) are labeled  $\tilde{\chi}_1^0$ ,  $\tilde{\chi}_2^0$ ,  $\tilde{\chi}_3^0$ , and  $\tilde{\chi}_4^0$ . The charged gauginos (charginos) are similarly labeled  $\tilde{\chi}_1^\pm$  and  $\tilde{\chi}_2^\pm$ . Table 1, lists the gauginos which are direct partners of the original gauge bosons in the [SM](#) rather than these resulting mass eigenstates.

The minimal extension of the Higgs sector in the [MSSM](#) predicts relationships between the masses of the sparticles [11]. For example, to leading order the mass of the gluino is three times larger than the mass of the wino and six times larger than the mass of the bino. These mass parameters, like the gauge couplings in the [SM](#), run under renormalization and predict the variation of the mass of the sparticles with the energy scale  $Q$ . An example of the running of the masses is shown in Figure 8 [11], which includes both scalar and gaugino sparticles. The result requires the selection of a specific set of parameters, and is intended to illustrate the overall trends rather than to predict actual mass values.

In addition to the new particle content, the [MSSM](#) introduces new interactions for the gauge bosons and gauginos. All interaction terms are added to the Lagrangian which describe the interaction of a gauge boson or gaugino with a particle or sparticle with the appropriate charge. Such terms include a few interactions which would violate the observed  $B - L$  symmetry that prevents proton decay. Either the couplings on these terms must be extremely small to match the experimental limits on those decays, or an additional symmetry must be im-

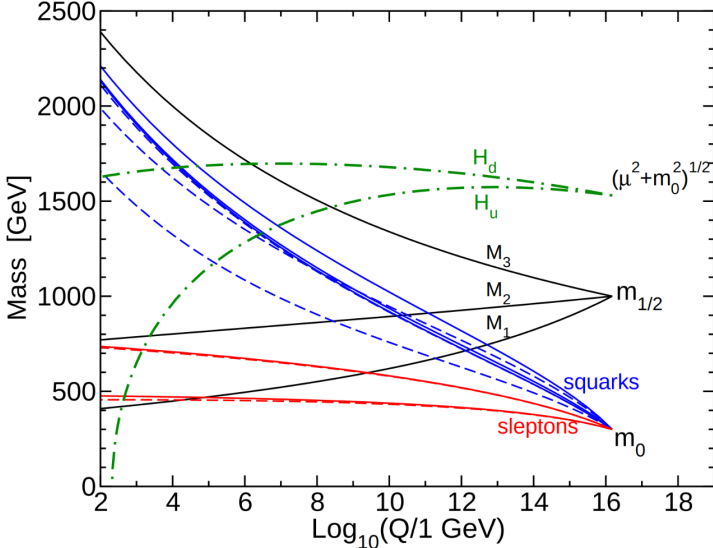


Figure 8: The evolution of the masses of sparticles with the energy scale  $Q$  [11].

posed to exclude the terms. The **MSSM** and several other **SUSY** models choose to introduce a new symmetry known as R-parity, where the conserved quantity,  $P_R$  is defined as

$$P_R = (-1)^{2s+3(B-L)}$$

with  $s$  as the spin of the particle. Sparticles are R-parity odd while **SM** particles are R-parity even. And by requiring that each term in the supersymmetric Lagrangian conserves R-parity, it is enforced that sparticles are produced in pairs.

The conservation of R-parity removes the  $B - L$  violating terms from the Lagrangian. The remaining terms include all of the interactions of the **SM** where two of the particles are replaced with their **SUSY** partners, so that R-parity is conserved in the interactions. This also has an important significance in making the Lightest Supersymmetric Particle (**LSP**), the  $\tilde{\chi}_1^0$ , stable, as it cannot decay to only **SM** particles without violating the conservation of R-parity. The heavier sparticles then decay in chains, emitting an **SM** particle in each step, and leave behind the **LSP** at the end of the chain.

### 3.2 MOTIVATION

**SUSY** models, including the **MSSM**, ameliorate many of the issues in the **SM** discussed in Section 2.6. **SUSY** is particularly well motivated as a natural extension to the **SM** because the simple underlying assumption solves three major, seemingly unrelated concerns. And these benefits are all consistent with the existence of sparticles at the TeV scale, within the reach of modern collider experiments [12].

The first, a solution to the hierarchy problem, comes as a direct consequence of the introduction of massive superpartners for each **SM** particle. The contributions to the Higgs mass from the much higher energy Planck scale come from a

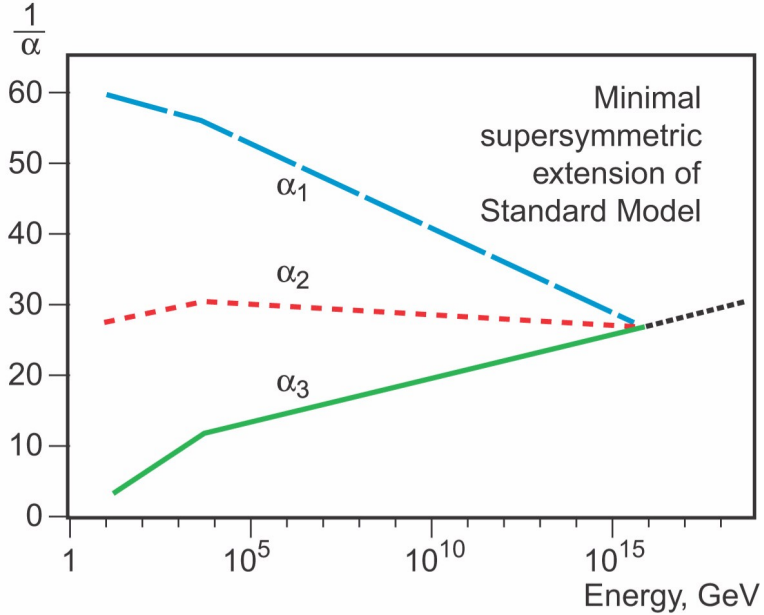


Figure 9: An approximation of the running of the coupling constants in the [MSSM](#) up to the Planck scale [2].

series of loop diagrams in the [SM](#), where each massive [SM](#) particle has a loop contribution. The introduction of superpartners generates a series of corresponding diagrams for correction to the Higgs mass, with opposite sign contributions because the superpartners have different spins. Those opposite sign contributions cancel the divergences from the original loop diagrams at high energies, leaving behind a correction to the Higgs mass that is at the same scale as the masses of the superpartners. If the superpartners exist at the TeV scale, then the Higgs mass of 125 GeV can be explained without significant fine-tuning, and the theory becomes natural [12].

[SUSY](#) also has the potential to precisely enable the unification of the coupling constants at high energy. Without supersymmetric contributions, the coupling constants come close to a single value near the Planck scale suggesting an underlying trend, as shown in Figure 4, but they do not exactly merge. With the addition of the [MSSM](#), they can join almost exactly at a single point, enabling a unification into a single gauge theory at high energy, as shown in Figure 9. This precise unification, like the naturalness argument, also requires that the masses of the superpartners be near the TeV scale [12].

The presence of R-parity in a [SUSY](#) model also provides an explanation for dark matter. The [LSP](#), as discussed in Section 3.1, is a massive, neutral, and stable particle as long as R-parity is conserved. In the early universe, when the energy density was extremely high, [LSPs](#) could be spontaneously produced just as often as other particles like photons, and would result in a thermal equilibrium. Then, as the universe cooled, the average energy would be too low to create additional [LSPs](#), and they would be left behind and only interact with the remaining matter gravitationally, a process called freeze out. Since those particles are stable, they would remain indefinitely. A Weakly Interacting Massive Particle ([WIMP](#)) at the

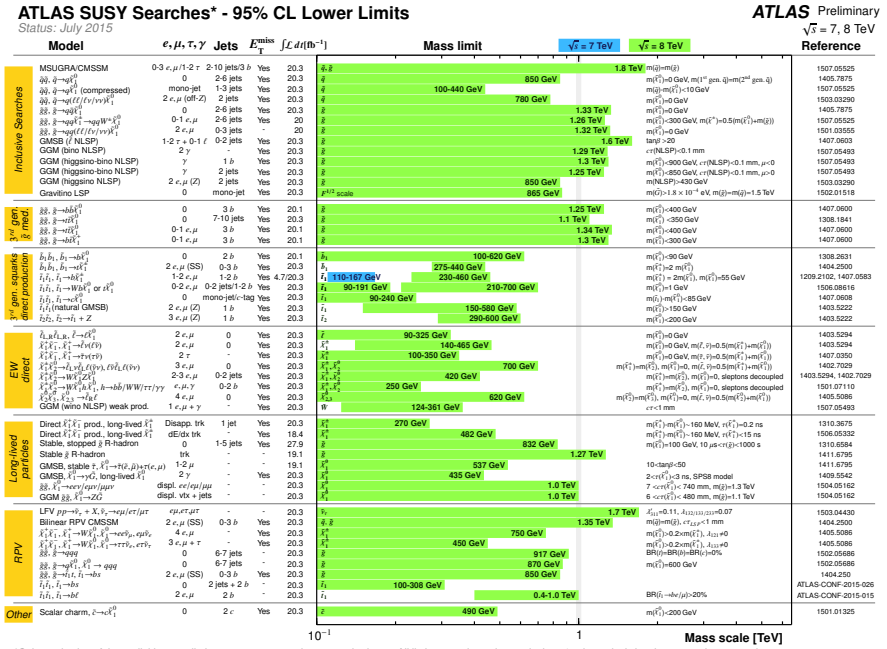


Figure 10: Mass reach of ATLAS searches for Supersymmetry as of July 2015. Only a portion of the available results is shown [12].

TeV scale provides the correct interaction rate to predict the currently observed ratio of dark matter to baryonic matter. A **WIMP** is a massive particle that interacts only weakly and gravitationally, not strongly or electromagnetically, such as what is proposed in the **LSP**. Therefore **SUSY** can explain the observed amount of dark matter in the universe.

Together, this variety of solutions to existing problems provides strong theoretical support for the existence of SUSY near the TeV scale. The LHC is the first collider experiment to be able to probe into TeV scale interactions, providing a new opportunity to search for this extension to the SM. The mass limits of various SUSY searches using data from the first run of the LHC on the ATLAS experiment are shown in Figure 10. A range of models have begun to be excluded with masses above 1 TeV [3], leading to a motivation to explore a wider variety of models with phenomena that may have been missed by the most direct search strategies.

### 3.3 SIMPLIFIED MODELS

There are a large suite of full SUSY models that produce similar results. Each of those models can have hundreds of individual parameters that ultimately determine the masses and interactions of the supersymmetric particles. To avoid this complexity in making experimental measurements, the analyses of high energy collisions often rely on simplified models. These models focus on a single process predicted by a theory, but are not full theoretical descriptions. They focus on the observable parameters such as the mass of the particles and their lifetimes,

which are controlled directly rather than derived from underlying parameters. Unlike an actual model for [SUSY](#), simplified models only include particles and interactions relevant for a specific search and do not assume any relationships between the masses of the particles involved. This allows straightforward simulation of a specific event topology with control over the parameters that most directly influence the experimental signatures.

Experimental analyses use these models to search for new physics and to set limits on the production rates for a given type of process with working points of a few observable parameters. As one example, a simplified model may specify pair production of gluinos where the free parameters are the mass of the gluino and the types and masses of the particles it can decay into. The small number of parameters allows the phase space to be searched in a grid by simulating events with a few examples for the parameters and interpolating between them. The resulting analysis can set cross sectional limits as a function of the simplified parameters, and this allows for an easy interpretation of the result in a number of [SUSY](#) models.

### 3.4 LONG-LIVED PARTICLES

Some proposed [SUSY](#) models can produce [LLPs](#) other than just the [LSP](#). The most direct search strategies for [SUSY](#) often assume that the various non-stable sparticles decay promptly, rather than propagating through some fraction of the detector. Although the processes involved are very similar, the long-lifetime of the produced particles can lead to very different experimental signatures, and often require separate dedicated searches. It is important to design and execute search strategies for [LLPs](#) in order to completely cover possible production of new physics.

There are several ways to generate long lifetimes for the massive [SUSY](#) particles, depending on the specific model. In examples like Split Supersymmetry [14, 15] and Spread Supersymmetry [16], the introduction of a split between two mass scales suppresses the decay of gluinos. In these and similar models, the squarks are much heavier than the gluino, where the mass scale of the squarks is roughly  $10^6$  GeV while the mass scale of the gluinos is roughly  $10^3$  GeV. The gluino must decay through the production of a virtual squark, as shown in the diagram of Figure 11. The large mass of the squarks in the split models suppresses the decay rate, and can result in lifetimes of the order of 1 ns [16].

Nearly degenerate particles can also result in long lifetimes, again by suppressing decay rates. When a particle must decay to another particle with nearly the same mass, the phase space factor in the decay results in a low decay rate. For example, a neutron has a lifetime of roughly fifteen minutes because its mass is so close to the proton. Models which result in a nearly degenerate chargino and [LSP](#) provide a long-lived chargino as well.

Again, because of the wide variety of models which can produce [LLPs](#) and the large number of parameters which determine their masses and lifetimes, the analysis presented here focuses on simplified models rather than assuming any particular underlying theory. The models directly specify the decay mode of the

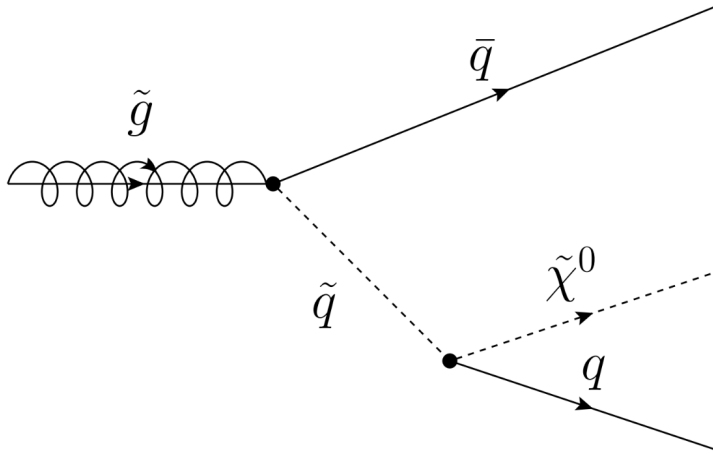


Figure 11: The decay of a gluino to quarks and an LSP, which precedes through a squark.

LLPs as well as their masses and lifetimes, using a grid of values. The results of searches using these simplified models can be interpreted over a very wide range of models that predict LLPs, even including non-supersymmetric extensions to the SM.

PART II  
EXPERIMENTAL STRUCTURE AND RECONSTRUCTION

# 4

## THE LARGE HADRON COLLIDER

---

The [LHC](#), a two-ring superconducting hadron accelerator, provides high energy proton-proton collisions for several large experiments at European Organization for Nuclear Research ([CERN](#)) in Geneva, Switzerland [17, 18]. It is the largest, highest-luminosity, and highest-energy proton collider ever built, and was constructed by a collaboration of more than 10,000 scientists and engineers from the more than 100 countries that contribute to [CERN](#). The original design of the [LHC](#) focused on providing collision energies of up to 14 TeV and generating enough collisions to reveal physics beyond the [SM](#) which is predicted to exist at higher energy scales.

The [LHC](#) was installed in an existing 27 km tunnel at [CERN](#) which was originally designed to house the Large Electron Positron collider ([LEP](#)) [17]. This allows the collider to use existing accelerators at the same complex to provide the initial acceleration of protons up to 450 GeV before injecting into [LHC](#). The injected hadrons are accelerated up to as much as 14 TeV while being focused into two beams traveling in opposite directions. During this process the protons circulate around the tunnel millions of times, while the beams are intermittently crossed at the four locations of the experiments to provide collisions. These collision points correspond to the four major [LHC](#) experiments: ATLAS, Compact Muon Solenoid ([CMS](#)), Large Hadron Collider beauty experiment ([LHCb](#)), and A Large Ion Collider Experiment ([ALICE](#)), and Figure 12 shows the layout of the experiments both on the surface and below. ATLAS and [CMS](#) are both general purpose, high-luminosity detectors which search for a wide range of new types of physics [19, 20]. [LHCb](#) studies the interactions of b-hadrons to explore the asymmetry between matter and antimatter [21]. [ALICE](#) focuses on the collisions of lead ions, which the [LHC](#) also provides for about one month per year, in order to study the properties of quark-gluon plasma [22].

During the first five years of continued operation, after the [LHC](#) turned on in 2010, the [LHC](#) has provided four major data collecting periods. In 2010 the [LHC](#) generated collisions at several energies, starting at 900 GeV. It increased the energy from 900 GeV to 2.76 TeV and then subsequently to 7 TeV, with a peak luminosity of  $2 \times 10^{32} \text{ cm}^{-2}\text{s}^{-1}$ , and a total delivered luminosity of  $50 \text{ pb}^{-1}$ . The next run, during 2011, continued the operation at 7 TeV and provided an additional  $5 \text{ fb}^{-1}$  with a peak luminosity of  $4 \times 10^{33} \text{ cm}^{-2}\text{s}^{-1}$ . The energy was then increased to 8 TeV for the data collection during 2012, which provided  $23 \text{ fb}^{-1}$  with a peak luminosity of  $7.7 \times 10^{33} \text{ cm}^{-2}\text{s}^{-1}$ . After the first long shutdown for 2013 and 2014, the [LHC](#) resumed operation and increased the energy to 13 TeV in 2015, where it delivered  $4.2 \text{ fb}^{-1}$  with a peak luminosity of  $5.5 \times 10^{33} \text{ cm}^{-2}\text{s}^{-1}$ . The [LHC](#) is currently providing additional 13 TeV collisions in 2016 with higher luminosities than during any previous data collection periods. These running periods are summarized in Figure 13, which shows the total delivered

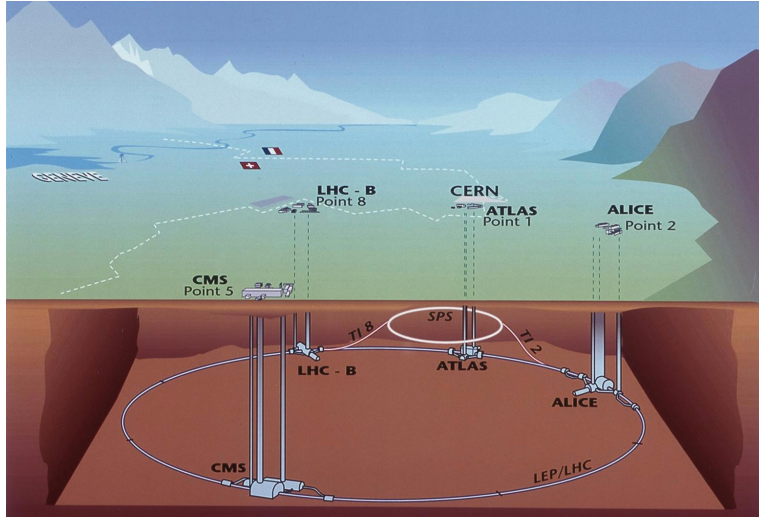


Figure 12: The four collision points and corresponding experiments of the [LHC](#). The image includes the location of the nearby city of Geneva as well as the border of France and Switzerland [23].

luminosity over time for the ATLAS experiment during each of the four years of data collection since 2011. The full design energy of 14 TeV can only be reached after further magnet training that is scheduled for the long shutdown over 2019-2020.

#### 4.1 INJECTION CHAIN

The [LHC](#) takes advantage of the presence of previously built accelerators at [CERN](#) to work up to the target energy in consecutive stages. The series of accelerators that feed into the [LHC](#) are known collectively as the injection chain, and together with the [LHC](#) form the accelerator complex. The full complex is illustrated in Figure 14, which details the complex series required to reach high energy collisions in the [LHC](#) experiments.

Protons at the [LHC](#) begin as hydrogen atoms in the Linac 2, a linear accelerator which replaced Linac 1 as the primary proton accelerator at [CERN](#) in 1978. In Linac 2, the hydrogen atoms are stripped of their electrons by a strong magnetic field, and the resulting protons are accelerated up to 50 MeV by cylindrical conductors charged by radio frequency cavities. The protons are then transferred to the Proton Synchrotron Booster ([PSB](#)), which uses a stack of four synchrotron rings to accelerate the protons up to 1.4 GeV. Then the protons are injected into the Proton Synchrotron ([PS](#)) which again uses synchrotron rings to bring the energy up to 25 GeV. The intermediate step between Linac 2 and the [PS](#) is not directly necessary, as the [PS](#) can accelerate protons starting from as low as 50 MeV. The inclusion of the [PSB](#) allows the [PS](#) to accept a higher intensity of injection and so increases the deliverable luminosity in the [LHC](#). The penultimate stage of acceleration is provided by the Super Proton Synchrotron ([SPS](#)), a large synchrotron with a 7 km circumference that was commissioned at [CERN](#)

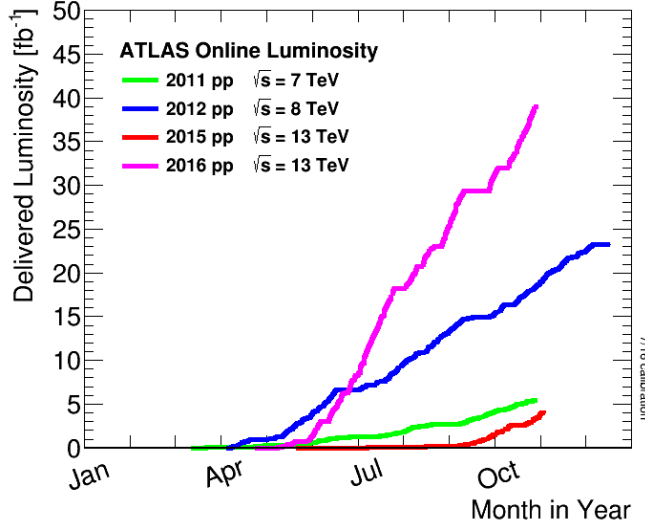


Figure 13: The cumulative luminosity over time delivered to the ATLAS experiment from high energy proton-proton collisions since 2011. The energies of the collisions are listed for each of the data-taking periods. The figure shows the delivered luminosity as of the conclusion of data collection in 2016 [24].

in 1976. During this step the protons increase in energy to 450 GeV, after which they can be directly injected into the [LHC](#).

The final step is the [LHC](#) itself, which receives protons from the [SPS](#) into two separate beam pipes which circulate in opposite directions. The filling process at this steps takes approximately 4 minutes, and the subsequent acceleration to the final energy (6.5 TeV during 2015 and up to 7 TeV by design) takes approximately half an hour. At this point the protons circulate around the circumference tens of thousands of times a second and continue for up to two hours.

## 4.2 DESIGN

### 4.2.1 LAYOUT

Many of the aspects of the [LHC](#) design are driven by the use of the existing [LEP](#) tunnel. This tunnel slopes gradually, with a 1.4% decline, with 90% of its length built into molasse rock which is particularly well suited to the application. The circumference is composed of eight 2987 meter arcs and eight 528 meter straight sections which connect them; this configuration is illustrated in Figure 15. The tunnel diameter is 3.7 m throughout its length.

The design energy is directly limited by the size of this tunnel, with its radius of curvature of 2804 m. A significant magnetic field is required to curve the protons around that radius of curvature; the relationship is given by

$$p \simeq 0.3BR \quad (13)$$

where  $p$  is the momentum of the particle in GeV,  $B$  is the magnetic field in Tesla, and  $R$  is the radius of curvature in meters. From the target design energy of

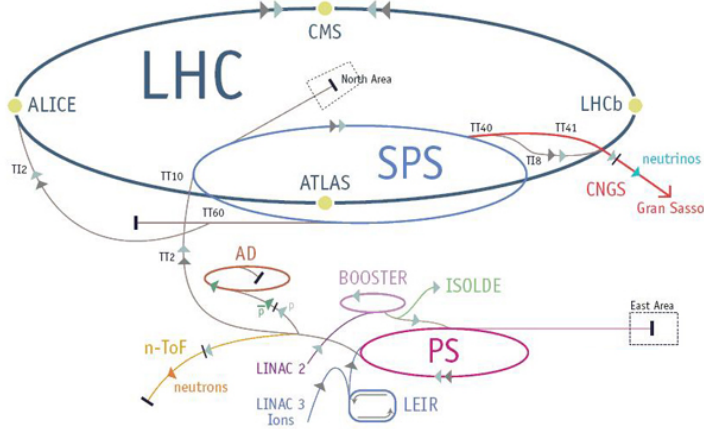


Figure 14: The accelerator complex that builds up to the full design energies at the LHC. The protons are passed in order to Linac 2, the PSB, the PS, the SPS and then the LHC [25].

14 TeV, or 7 TeV of momentum for protons in each beam, the required magnetic field is 8.33 Tesla. This is too large a field strength to be practical with iron electromagnets, because of the enormous power required and the resulting requirements for cooling. Because of these constraints, the LHC uses superconducting magnets which can maintain that field strength with significantly less power consumption.

#### 4.2.2 MAGNETS

The magnets chosen were made of Niobium and Titanium (NbTi) which allow for field strengths as high as 10 Tesla when cooled down to 1.9 K. Reaching the target temperature of 1.9 K for all of the magnets requires superfluid helium and a large cryogenic system along the entire length of the tunnel. During normal operation, the LHC uses 120 tonnes of helium within the magnets, and the entire system is cooled by eight cryogenic helium refrigerators. The temperature increase that occurs during transit from the refrigerator along the beam necessitates that the refrigerators cool the helium down to 1.8 K. Any significant increase above this temperature range can remove the superconductive properties of the magnets, which in turn generates drastically larger heat losses from the current within the magnets and causes a rapid rise in temperature called a quench.

There are approximately 8000 superconducting magnets distributed around the LHC. The 1232 bending magnets, which keep the protons curving along the length of the beam, are twin bore cryodipoles, which allow both proton beams to be accommodated by one magnet and all of the associated cooling structure. Figure 16 shows the cross section of the design for these dipoles. The magnets are very large, 16.5 m long with a diameter of 0.57 meters and a total weight of 28 tonnes. They are slightly curved, with an angle of 5.1 mrad, in order to carefully match the beam path. The twin bore accommodates both magnets inside the

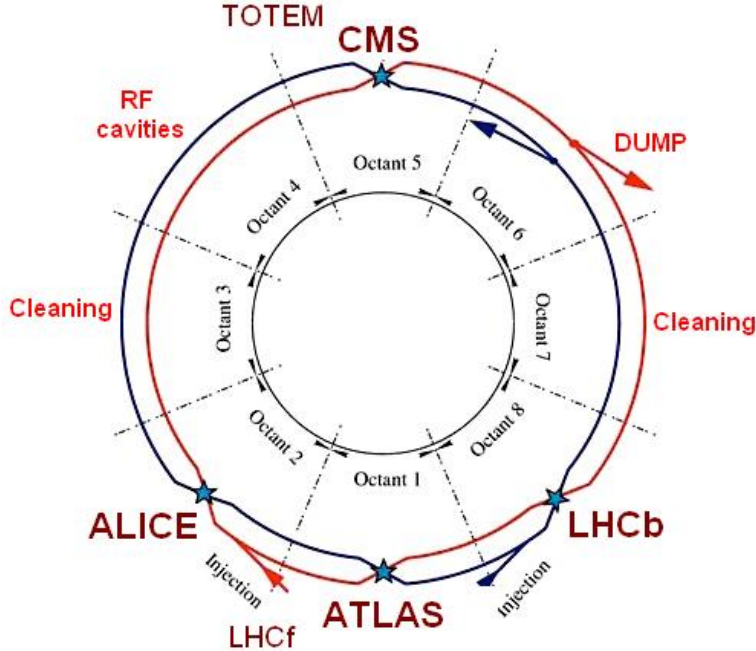


Figure 15: A schematic of the layout of the LHC, not to scale. The arched and straight sections are illustrated at the bottom of the schematic, and all four crossing sites are indicated with their respective experiments [17].

two 5 cm diameter holes which are surrounded by the superconducting coils. The coils require 12 kA of current in order to produce the required magnetic field. These coils are comprised of NbTi cable wound in two layers; the wire in the inner layer has a diameter of 1.065 mm while the wire in the outer layer has a diameter of 0.825 mm.

The large currents in the wires, along with the magnetic field produced, result in forces on the magnets which would tend to push them apart with over 10,000 Newtons per meter. Constraining the magnets requires a significant amount of structure including non-magnetic stainless steel collars. Both the presence of these electromagnetic forces and the varying thermal contraction coefficient of the pieces of the magnet produce significant forces on the cold mass structure. The cold mass is carefully engineered to so that these stresses do not significantly alter the magnetic field shape, which must be maintained between magnets to a precision of approximately  $10^{-4}$  for successful operation.

The remaining 6800 magnets are a variety of quadrupole, sextapole, octopole, and single bore dipole magnets. These are used to damp oscillations, correct beam trajectories, focus the beams during circulation, and to focus the beams before collisions.

#### 4.2.3 RADIO FREQUENCY CAVITIES

Sixteen radiofrequency (RF) cavities produce the actual acceleration of the proton beam up to the design energy. These RF cavities are tuned to operate at 400 MHz, and are powered by high-powered electron beams modulated at the same

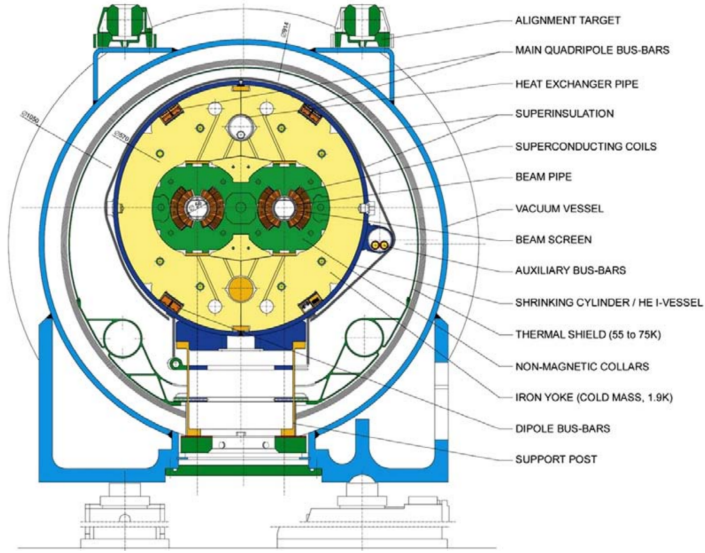


Figure 16: A cross section of the the cryodipole magnets which bend the flight path of protons around the circumference of the LHC. The diagram includes both the superconducting coils which produce the magnetic field and the structural elements which keep the magnets precisely aligned [17].

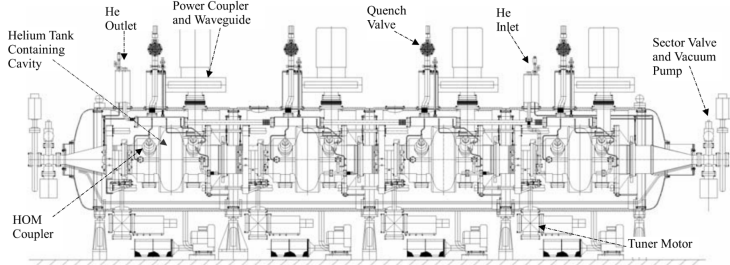


Figure 17: The arrangement of four RF cavities within a cryomodule [17].

frequency, called klystrons. The resonance within the cavity with the oscillating electric field establishes a voltage differential of 2 MV per cavity. The sixteen cavities are split between the two beams, so combined the cavities provide 16 MV per beam, which accelerate the protons on each consecutive pass through the cavity. This acceleration is also necessary during circulation even after the target energy has been reach in order to compensate for losses from synchrotron radiation.

The cavities are arranged in cryomodules which contain four cavities, with two cryomodules per beam; this arrangement is illustrated in Figure 17. These cryomodules are necessary to maintain the superconducting state of the cavities, which are also constructed from niobium. The RF cavities use niobium along with copper to allow for low power losses in the superconductors. The copper provides a reduced susceptibility to quenching, as it rapidly conducts away heat generated by imperfections in the niobium, as well as natural shielding from the earth's magnetic field which can interfere with the RF system.

The nature of the radio frequency oscillations tends to group protons together into buckets. A proton traveling exactly in phase with the RF oscillations will not be displaced at all during a single circulation, and those slightly ahead or behind of that phase will slightly decelerate or accelerate, respectively. This produces separate clusters of protons which arrive in phase to the cavities every 2.5 ns, corresponding to the 400 MHz frequency.

#### 4.2.4 BEAM

The beams of protons circulate within 27 km of 5 cm diameter beam pipe. This entire structure is kept under vacuum at 1.9 K to prevent interactions between the beam pipe and the magnets as well as to prevent any interactions between the circulating protons and gas in the pipe. The vacuum within the pipe establishes a pressure as low as  $10^{-9}$  mbar before the protons are introduced.

Because of the very high energies of the circulating protons, synchrotron radiation is not negligible in the bending regions. The protons are expected to radiate 3.9 kW per beam at 14 TeV, with 0.22 W/m, which is enough power to heat the liquid helium and cause a quench were it absorbed by the magnets. To prevent this, a copper screen is placed within the vacuum tube that absorb the emitted photons. This screen is kept between 5 and 20 K by the liquid helium cooling system.

### 4.3 LUMINOSITY PARAMETERS

In addition to the high energy of the collisions, the rate of collisions is extremely important to enabling the discovery of new physics. Many measurements and searches require a large number of events in order to be able to make statistically significant conclusions. The rate of collisions is measured using luminosity, the number of collisions per unit time and unit cross section for the proton-proton collisions. From the beam parameters, luminosity is given by

$$\mathcal{L} = \frac{N_b^2 n_b f_{rev} \gamma}{4\pi \epsilon_n \beta^*} F \quad (14)$$

where  $N_b$  is the number of protons per bunch,  $n_b$  is the number of bunches colliding,  $f_{rev}$  is the frequency of revolution,  $\gamma$  is the Lorentz factor for the protons at the circulating energy,  $\epsilon_n$  is the emittance,  $\beta^*$  is the amplitude function at the collision point, and  $F$  is a geometric factor that accounts for the crossing angle of the beams at the collision point. The emittance measures the average spread of particles in both position and momentum space, while the amplitude function is a beam parameter which measures how much the beam has been squeezed. Together  $\epsilon_n$  and  $\beta^*$  give the size of the beam in the transverse direction,  $\sigma = \sqrt{\epsilon \beta^*}$ .  $\beta$  changes over the length of the beam as the accessory magnets shape the distribution of protons, but only the value at the point of collisions,  $\beta^*$ , affects the luminosity.

The luminosity is maximized to the extent possible by tuning the parameters in Equation 14. A number of these are constrained by the design decisions. The

Parameter	Unit	Injection	Nominal	2015
Beam Energy	TeV	0.450	7	6.5
Peak Instantaneous Luminosity	$\text{cm}^{-2}\text{s}^{-1}$	-	$10^{34}$	$5 \times 10^{33}$
Bunch Spacing	ns	25	25	25
Number of Filled Bunches	-	2808	2808	2240
Normalized Transverse Emittance	$\mu\text{m}$	3.75	3.75	-
Frequency	MHz	400.789	400.790	-
RF Voltage/Beam	MV	8	16	-
Stored Energy	MJ	-	362	-
Magnetic Field	T	0.54	8.33	-
Operating Temperature	K	1.9	1.9	1.9

Table 2: The design parameters of the [LHC](#) beam that determines the energy of collisions and the luminosity, for both the injection of protons, at the nominal circulation, and during the 2015 data-taking period.

revolution frequency is determined entirely by the length of the tunnel, as the protons travel at very close to the speed of light. The geometric factor  $F$  is determined by the crossing angle of the beams at the collision points, a tunable component of the tunnel design; this angle is already very small at  $285 \mu\text{rad}$ , which helps to maximize the geometric factor.

The major pieces that can be adjusted are the number of protons per bunch,  $N_b$ , the number of bunches in the beam,  $n_b$ , and the amplitude function  $\beta$ . Increasing either  $N_b$  or  $n_b$  increases the amount of energy stored in the beam, which presents a danger if control of the beam is lost. At design specifications, the beam stores 362 MJ, which is enough energy to damage the detectors or accelerator if the beam were to wander out of the beam pipe. So, the luminosity is primarily controlled at the [LHC](#) by adjusting  $\beta^*$ , where lowering  $\beta^*$  increases the luminosity.  $\beta^*$  is tuned to provide the various values of luminosity used at the [LHC](#) which can be raised to as much as  $1.4 \times 10^{34} \text{ cm}^{-2}\text{s}^{-1}$ .

The nominal bunch structure consists of 3654 bunches, each holding  $10^{11}$  protons, which cross a collision point in 25 ns. These are further subdivided into the buckets mentioned in Section 4.2.3 by the clustering properties of the [RF](#) cavities. In 2015, the bunches are further grouped into trains of 72 bunches which are separated by a gap which would otherwise hold 12 bunches. At nominal operation 2808 of the bunches will actually be filled with protons, while the remainder are left empty to form an abort gap that can be used in case the beam needs to be dumped.

The various beam parameters are summarized in Table 2 for the designed operation. In practice, the beam has operated at lower energies and lower luminosities than the design values for the majority of its lifetime, but the [LHC](#) has begun to operate at full design values during Run 2.

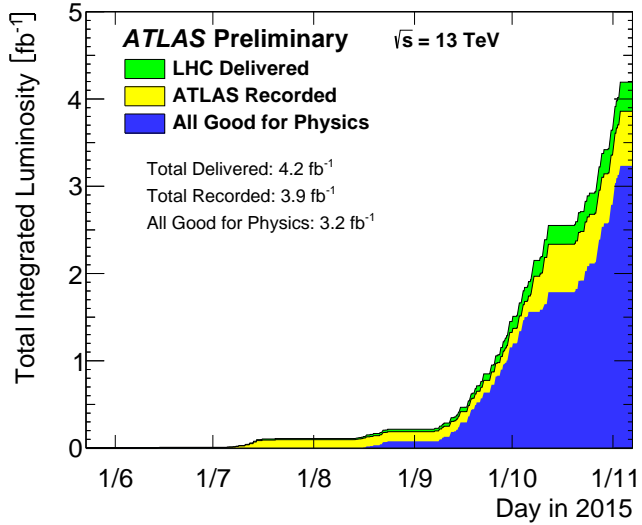


Figure 18: The cumulative luminosity versus time delivered to ATLAS (green), recorded by ATLAS (yellow), and certified to be good quality data (blue) during stable beams for pp collisions at 13 TeV in 2015 [24].

#### 4.4 DELIVERED LUMINOSITY

During the data collection of 2015, the LHC operated at luminosities as large as  $5 \times 10^{33} \text{ cm}^{-2}\text{s}^{-1}$ . It is convenient to refer to the integrated luminosity, the integral of the instantaneous luminosity, which corresponds directly to the number of delivered events for a given process.

$$N = \sigma \times \int \mathcal{L}(t) dt$$

where  $\sigma$  is the cross section for the process of interest. The integrated luminosity over time is shown in Figure 18. This includes the luminosity delivered by the LHC as well as the luminosity that was recorded by ATLAS. ATLAS only records collisions when the LHC reports that the beam conditions are stable, so some of the delivered luminosity is not recorded. The figure also includes the amount of luminosity marked as good for physics, which includes additional requirements on the operation of the detector during data collection that are necessary for precise measurements.

Because the beam circulates and collides bunches of protons, it is possible for a single crossing to produce multiple proton-proton collisions. As the instantaneous luminosity is increased, the average number of collisions generated per bunch crossing increases. An event refers to the entire collection of interactions during a single bunch crossing, while interactions refer to the individual proton-proton collisions. The additional interactions produced during each bunch crossing are referred to as pileup, which can be more precisely defined quantified using the average number of additional proton-proton interactions per crossing, often denoted  $\mu$ . Figure 19 shows the luminosity-weighted distribution of the mean number of interactions for events collected in 2015. The presence of as many as twenty interactions in a single collision provides a sig-

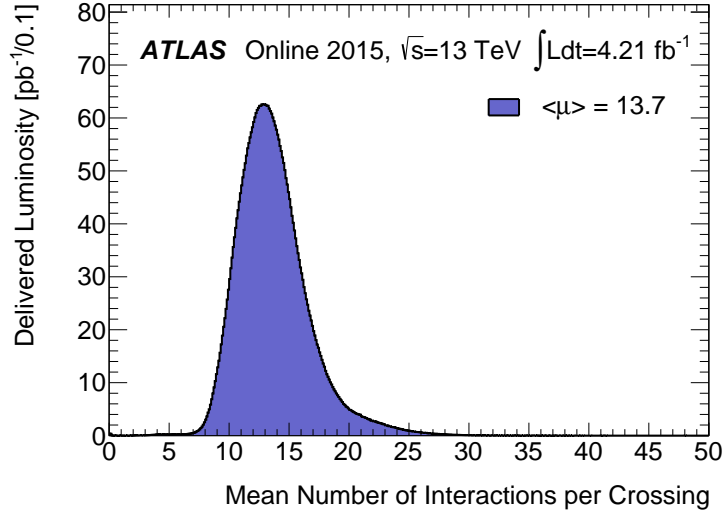


Figure 19: The luminosity-weighted distribution of the mean number of interactions per crossing for the 2015 pp collision data at 13 TeV [24].

nificant challenge in reconstructing events and isolating the targeted physical processes.

## THE ATLAS DETECTOR

---

The four major LHC experiments at CERN seek to use the never before matched energies and luminosities of the new collider to explore the boundaries of particle physics and to gain insight into the fundamental forces of nature. Two of these experiments, ATLAS and CMS, are general purpose detectors that seek to measure a variety of processes in the up to 13 TeV proton-proton collisions that occur as much as 800 million times per second at the LHC at the design luminosity of  $10^{34} \text{ cm}^{-2}\text{s}^{-1}$ . ATLAS employs a hermetic detector design, one which encloses the particle collisions as completely as possible with detecting elements, that allows it to study a wide range of physics from SM precision measurements to searches for new physics in models like SUSY [19].

Accommodating this wide variety of goals is a challenge for the design of the detector. The wide range of energies involved requires high measurement precision over several orders of magnitude, and the numerous physics processes require an ability to measure a variety of particle types. At the time of the construction of ATLAS, the Higgs boson had yet to be discovered, but the diphoton decay mode was (correctly) expected to be important and necessitated a high resolution photon measurement. The potential for decays of new heavy gauge bosons,  $W'$  and  $Z'$ , required a similarly high momentum resolution for leptons with momentum up to several TeV. Hadronic decay modes of several possible new high energy particles could result in very energetic jets, again up to several TeV, and reconstructing the decay resonances would again require good energy resolution. Several models, such as SUSY or Extra Dimensions, predict the existence of particles which would not interact with traditional detecting elements. However these particles can still be observed in a hermetic detector by accurately measuring the remaining event constituents to observe an imbalance in energy called missing energy or  $E_T^{\text{miss}}$ . Measuring  $E_T^{\text{miss}}$  implicitly requires a good resolution on all SM particles that can be produced. And at the lower end of the energy spectrum, precision SM measurements would require good resolution of a variety of particle types at energies as low as a few GeV, so the design needs to accommodate roughly three orders of magnitude.

This broad spectrum of measurements requires a variety of detector systems working together to form a cohesive picture of each collision. Two large magnet systems produce magnetic fields that provide a curvature to the propagation of charged particles and allows for precision momentum measurements in the subdetectors. The inner detector uses a combination of detector technologies to reconstruct particle trajectories and vertices for charged particles. A variety of calorimeters measure the energies of hadrons, electrons, and photons over a large solid angle. A large muon spectrometer identifies muons and uses the second magnet system to provide an independent measurement of their momentum

from the inner detector and improve the resolution. The layout of all of these systems is shown in Figure 20.

The performance goals needed to achieve the various targeted measurements and searches discussed above can be summarized as resolution and coverage requirements on each of these systems. Those requirements are listed in Table 3.

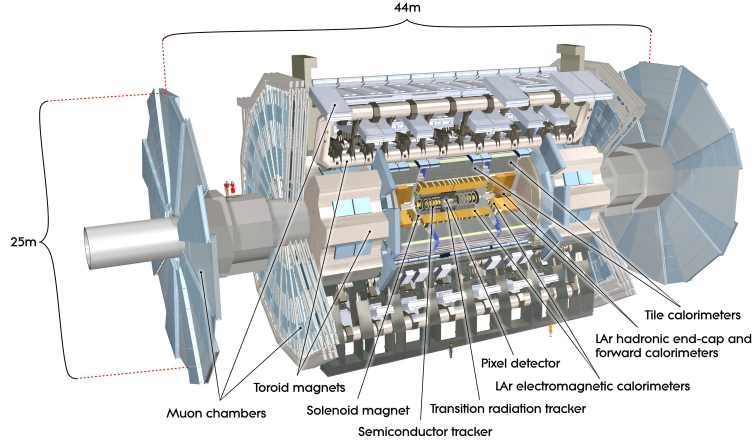


Figure 20: A cut-away schematic of the layout of the ATLAS detector. Each of the major subsystems is indicated [19].

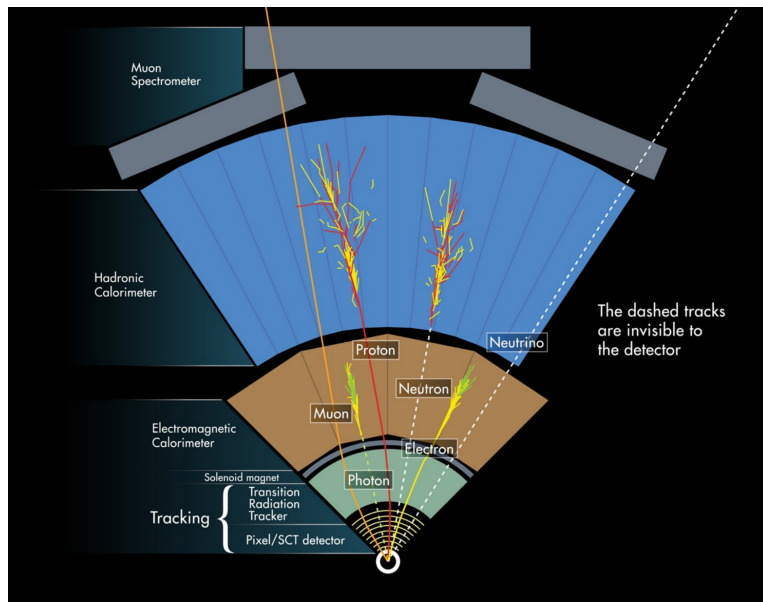


Figure 21: A cross-sectional slice of the ATLAS experiment which illustrates how the various SM particles interact with the detector systems.

Incorporating these various pieces into a single detector is a significant technical challenge. The resulting detector has a diameter of 22 m, is 46 m long, and weighs 7,000 tons; it is the largest volume particle detector ever constructed. The various detector elements need to be constructed and assembled with precision as low as micrometers. These systems all need to function well even after exposure to the significant radiation dose from the collisions. Designing, con-

Detector Component	Required Resolution	$ \eta $ Coverage	
		Measurement	Trigger
Tracking	$\sigma_{p_T}/p_T = 0.05\% p_T \oplus 1\%$	2.5	-
EM Calorimetry	$\sigma_E/E = 10\%/\sqrt{E} \oplus 0.7\%$	3.2	2.5
Hadronic Calorimetry			
Barrel and Endcap	$\sigma_E/E = 50\%/\sqrt{E} \oplus 3\%$	3.2	3.2
Forward	$\sigma_E/E = 100\%/\sqrt{E} \oplus 10\%$	3.1 – 4.9	3.1 – 4.9
Muon Spectrometer	$\sigma_{p_T}/p_T \leq 10\% \text{ for } p_T \leq 1 \text{ TeV}$	2.7	2.4

Table 3: The performance goals for each of the subsystems of the ATLAS detector. The  $|\eta|$  coverage specifies the range where the subsystem needs to be able to provide measurements with the specified resolution. The resolutions include a  $p_T$  or  $E$  dependence that is added in quadrature with a  $p_T/E$  independent piece.

structing, and installing the detector took the combined effort of more than 3000 scientists from 38 countries over almost two decades.

## 5.1 COORDINATE SYSTEM

The coordinate system defined for the ATLAS detector is used throughout all of the sections of this thesis. The system begins with the choice of a  $z$  axis along the beamline. The positive  $z$  side of the detector is commonly referred to as the *A*-side, and the negative  $z$  side is referred to as the *C*-side. The  $x - y$  plane is then the plane transverse to the beam direction, with the  $x$  direction defined as pointing from the interaction point to the center of the LHC ring and the  $y$  direction defined as pointing upwards. The nominal interaction point is the origin of this system.

It is more convenient in practice to use a cylindrical coordinate system; this choice of coordinate system reflects the cylindrical symmetry of the ATLAS detector. The distance from the beamline is the radius,  $r'$ , and the angle from the  $z$ -axis is  $\theta$ . The azimuthal angle,  $\phi$ , runs around the  $z$ -axis with  $\phi = 0$  corresponding to the  $x$ -axis. Many aspects of the detector are independent of this coordinate to first order; the detector is symmetric in  $\phi$ . The  $\theta$  direction is typically specified using rapidity or pseudorapidity, where rapidity is defined as

$$y = \frac{1}{2} \ln \frac{E + p_z}{E - p_z} \quad (15)$$

Rapidity is particularly useful to indicate the component along the  $z$  direction because differences in rapidity are invariant to boosts along the  $z$ -direction. A similar quantity which depends only on the  $\theta$  is the pseudorapidity,

$$\eta = -\ln \tan \frac{\theta}{2} \quad (16)$$

which approaches rapidity in the limit where the energy is much larger than the particle's mass and is identical for massless particles. It is often useful to refer to differences in solid angle using the pseudorapidity and the azimuthal angle:

$$\Delta R = \sqrt{\Delta\phi^2 + \Delta\eta^2} \quad (17)$$

The pseudorapidity is also invariant to boosts along the  $z$ -axis for high momentum particles, and is preferable to rapidity because it does not depend on the specific choice of particle. Pseudorapidity is also preferable to  $\theta$  because particle production is roughly uniform in equal-width intervals of  $\eta$  up to about  $\eta = 5.0$ . A particle traveling along the beampipe has  $\eta = \infty$  and a particle traveling perpendicular to the beampipe has  $\eta = 0$ . The extent of the tracker,  $|\eta| < 2.5$ , corresponds to approximately  $0.05\pi < \theta[\text{rad}] < 0.95\pi$  and the extent of the calorimeters,  $|\eta| < 4.9$  corresponds to approximately  $0.005\pi < \theta[\text{rad}] < 0.995\pi$ . Many detector components are broken into multiple subsystems to provide coverage at greater  $|\eta|$ . The lower  $|\eta|$  region is referred to as the barrel, typically with  $|\eta| \lesssim 1.4$ , and the greater  $|\eta|$  region is often referred to as the endcap.

The initial momentum along the  $z$  direction of the constituents in a proton-proton collision is unknown in hadron colliders because the constituent momenta vary between collisions (Section 2.5.4). Along the transverse plane, however, the vector sum of momentum will be zero. For this reason, many physical quantities are quantified in terms of their projection onto the transverse plan, such as  $p_T$  or  $E_T$ . In addition,  $p_T$  alone determines the amount of curvature in the magnetic field, and can be measured independently by measuring the curvature of a particle's propagation.

## 5.2 MAGNETIC FIELD

The magnet system used in ATLAS is designed to provide a substantial magnetic field in the two regions where the trajectory of particles is measured, the inner detector and the muon spectrometer. The magnetic field generates a Lorentz force that curves the trajectory of charged particles, following Equation 13. This allows the precision tracking elements to make high resolutions measurements of  $p_T$ . To provide a magnetic field in these regions, ATLAS uses a hybrid system with four separate, superconducting magnets. A single solenoid provides a 2 T axial, uniform magnetic field for the inner detector, while a barrel toroid and two endcap toroids produce a non-uniform magnetic field of 0.5 and 1 T, respectively, for the muon detectors. This geometry is illustrated in Figure 22, and the parameters of the three magnet systems are summarized in Table 4.

The central solenoid uses a single-layer coil with a current of 7.730 kA to generate the 2 T axial field at the center of the magnet. The single-layer coil design enables a minimal amount of material to be used in the solenoid's construction, which is important because the solenoid is placed between the inner detector and the calorimeters. At normal incidence the magnet has only 0.66 radiation lengths worth of material, where one radiation length is the mean distance over

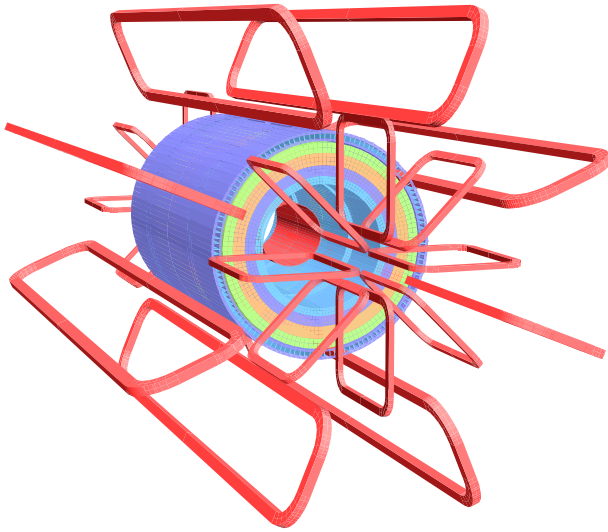


Figure 22: The layout of the four superconducting magnets in the ATLAS detector [19].

Parameter	Unit	Solenoid	Barrel Toroid	Endcap Toroids
Inner Diameter	m	2.4	9.4	1.7
Outer Diameter	m	2.6	20.1	10.7
Axial Length	m	5.3	25.3	5.0
Weight	tons	5.7	830	239
Conductor Size	mm <sup>2</sup>	30×4.25	57×12	41×4.25
Peak Field	T	2.6	3.9	4.1
Heat Load	W	130	990	330
Current	kA	7.7	20.5	20.0
Stored Energy	MJ	38	1080	206

Table 4: A summary of the parameters of each of the three magnet systems on ATLAS.

which a high-energy electron loses all but  $1/e$  of its energy through material interactions [3]. The coil is made of a high-strength aluminum stabilized NbTi superconductor which was optimized to achieve a high field with minimal thickness. The axial magnetic field produced by the solenoid bends charged particles in the  $\phi$  direction, following a circular path with a radius specified by Maxwell's equations (see Equation 13).

The barrel toroid consists of eight coils which generate a 0.5 T magnetic field, on average, in the cylindrical region around the calorimeters with an approximately 20 kA current. The coils are separated only by air to reduce the scattering of muons as they propagate through the region. The coils are made of an aluminum stabilized NbTiCu superconductor and each is separately housed in a vacuum and cold chamber. This magnetic configuration produces a field in the  $\phi$  and so curves muons traversing the volume primarily in the  $\eta$  direction.

The endcap toroids follow a similar design to the barrel toroid and produce a 1.0 T magnetic field, on average. Each has eight separate NbTiCu coils, and in this case all eight are housed within a single cold mass. This extra structure is necessary to withstand the Lorentz forces exerted by the magnets. These magnets are rotated 22.5% relative to the barrel toroid to provide a uniform field in the transition between the two systems. The endcap toroids also produce a field in the  $\phi$  direction and curve muons primarily in the  $\eta$  direction.

### 5.3 INNER DETECTOR

The ATLAS inner detector provides excellent momentum resolution as well as accurate primary and secondary vertex measurements through robust pattern recognition that identifies tracks left by charged particles. These tracks fulfill a number of important roles in the ATLAS measurement system: they measure the momentum of charged particles including electrons and muons, they can identify electrons, they assign particles to different vertices, and they provide a correction to  $E_T^{\text{miss}}$  measurements from low energy particles. The system has to be accurate enough to separate tracks from dozens of vertices, to resolve each vertex individually, and to measure the  $p_T$  of very high momentum tracks which curve very little even in the large magnetic field. This is accomplished by several independent layers of tracking systems. Closest to the interaction point is the very high granularity Pixel detector, including the newly added Insertible B-Layer ([IBL](#)), which is followed by the silicon microstrip ([SCT](#)) layers. These silicon subdetectors both use discrete space-points to reconstruct track patterns. The final layer, the Transition Radiation Tracker ([TRT](#)), uses many layers of straw tube elements interleaved with transition radiation material to provide continuous hits in the transverse plane. To provide the desired hermetic coverage, the subdetectors are divided into barrel and endcap geometries. Figure 23 shows the layout of the subdetectors in more detail, and illustrates how tracks at various pseudorapidities can traverse the subdetectors; tracks with  $\eta > 1.1$  begin to traverse the endcap subdetectors rather than those in the barrel, and tracks with  $\eta > 1.7$  use primarily endcap elements. The [IBL](#) was not present during the original commissioning of the inner detector and is not shown in this figure.

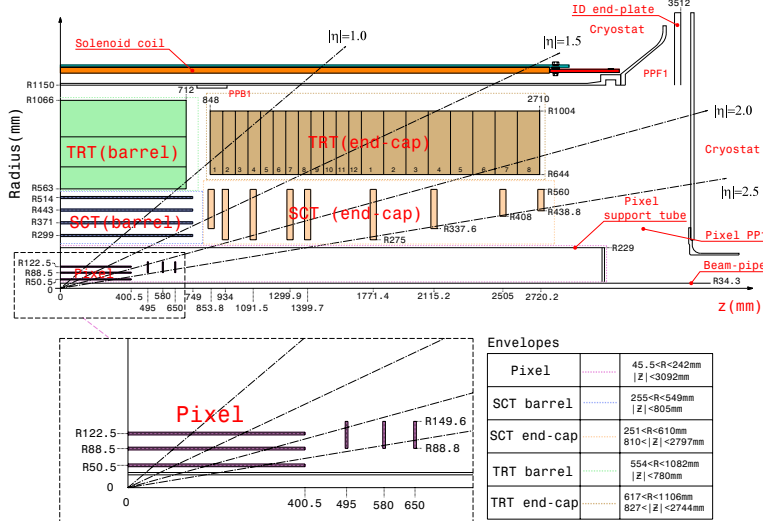


Figure 23: A quarter section of the ATLAS inner detector which shows the layout of each of the subdetectors in detail. The lower panel shows an enlarged view of the pixel detector. Example trajectories for a particle with  $\eta = 1.0, 1.5, 2.0, 2.5$  are shown. The IBL, which was added after the original detector commissioning, is not shown [19].

Figure 24 shows a computer generated three-dimensional view of the inner detector along the beam axis, which emphasizes the straw tube structure of the TRT as well as the overlapping geometry of the SCT. This figure also includes the IBL, which was added during the long shutdown and provides an additional measurement layer in the Pixel detector as of the beginning of Run 2. Figure 25 shows an alternative computer generated three-dimensional view transverse to the beam axis which emphasizes the endcap structures of the SCT and TRT.

As the closest system to the interaction point, it is crucial for the inner detector to use as little material as possible to avoid scattering of charged particles before they reach the remaining subdetectors. The various components, including the readout electronics, cooling infrastructure, gas volumes, and support structures, were designed to accommodate this need for minimal components. Even with these optimizations, the combination of stringent performance requirements and the harsh radiation environment in the inner detector requires a significant amount of material. This material causes many electrons to lose most of their energy before reaching the electromagnetic calorimeter and approximately 40% of photons convert into an electron-positron pair while traversing the inner detector. Figure 26 shows the integrated radiation lengths traversed by a straight track in the inner detector as a function of  $\eta$ , grouped by subdetector. There is a large increase in the amount of material for support structures around  $|\eta| = 1.7$ , where the inner detector transitions from barrel to endcap.

The inner detector is designed to work as a cohesive unit to provide complete tracking information for charged particles. Table 5 summarizes the parameters of each of the subdetectors as well as the parameters of the combined inner detector.

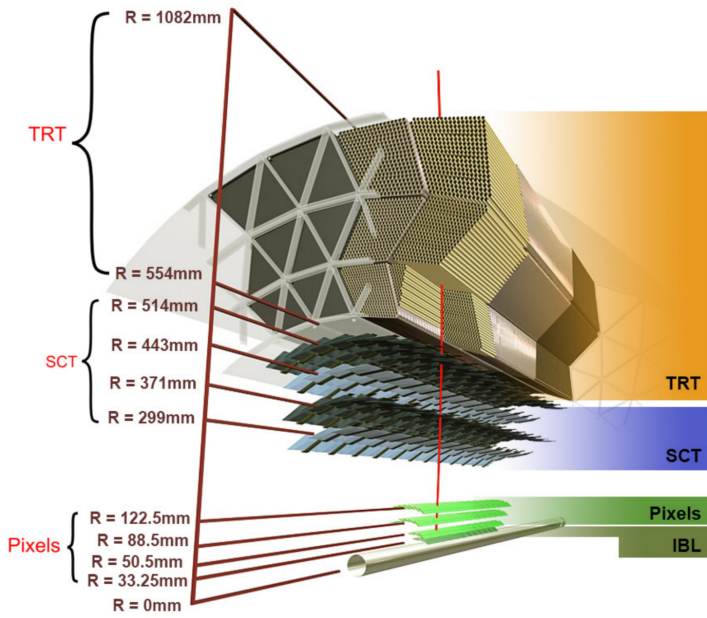


Figure 24: A computer generated three-dimensional view of the inner detector along the line of the beam axis. The subdetectors and their positions are labeled [19].

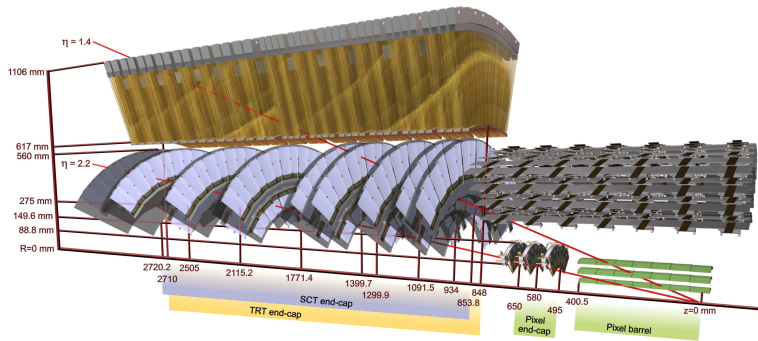


Figure 25: An alternative computer generated three-dimensional view of the inner detector transverse to the beam axis. The subdetectors and their positions are labeled [19].

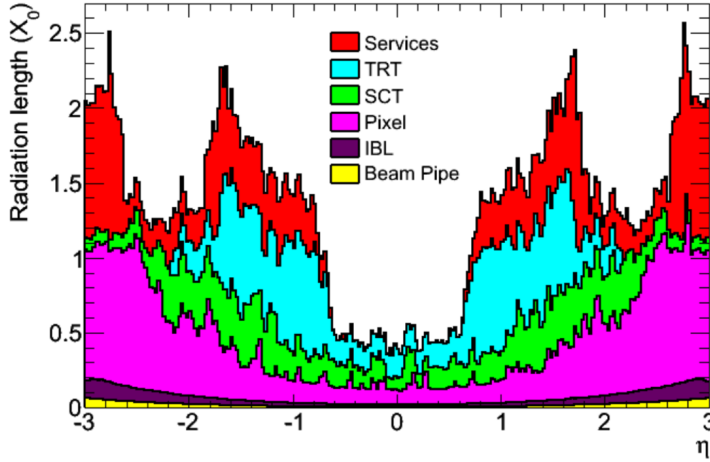


Figure 26: The integrated radiation lengths traversed by a particle at the exit of the ID envelope (outside of the [TRT](#) after 108.2 cm), including the services and thermal enclosures. The distribution is shown as a function of  $|\eta|$  and averaged over  $\phi$ . The breakdown indicates the contributions of individual sub-detectors, including services in their active volume [19].

### 5.3.1 PIXEL DETECTOR

The Pixel detector is the closest detector to the interaction point and therefore is designed to provide high granularity while simultaneously handling a large dose of radiation from collisions. It consists of four layers of silicon pixel modules, each of which provides a precision measurement on the trajectory of any charged particle. In the barrel region, the four layers are located at radial distances of 33 mm, 50.5 mm, 88.5 mm, and 122.5 mm. The three outer layers also include endcap elements, illustrated in Figure 23, which are located at  $z = 495$  mm,  $z = 580$  mm, and  $z = 650$  mm away from the interaction point.

The pixel sensor technology uses a p-n junction of n-type bulk that contains both p<sup>+</sup> and n<sup>+</sup> impurities. This combination is crucial in maintaining performance after a significant radiation dose, as the n<sup>+</sup> implants allow the sensor to continue function after the n-type bulk has been converted to a p-type bulk by the accumulation of radiation. In either configuration, when a charged particle passes through the bulk, it ionizes thousands of electron-hole pairs. The electrons and holes are pulled in opposite directions by the electric field established between the anode and cathode of the junction, which then produces a current that can be measured and recorded by readout electronics.

The size of the pixels in the original three layers are 50  $\mu\text{m}$  x 400  $\mu\text{m}$  in the  $r - \phi$  and  $z$  directions, respectively. Those pixels are bump-bonded to front-end readout chips, the FE-I3, which contains a total of 2880 pixels per chip. In the three original pixel layers, the chips are grouped into modules composed of 16 chips each with 46,080 pixels per module and a total size of 20 mm x 60 mm x 250  $\mu\text{m}$ . The modules are further arranged into long rectangular structures that run parallel to the beamline called staves. By tiling several staves with an offset of 20°, the stave geometry provides full azimuthal coverage in the barrel

Parameter	Inner Detector	Pixel	SCT	TRT
Inner Radius	3.3 cm	3.3 cm	30 cm	56 cm
$ \eta $ Coverage	-	2.5	2.5	2.0
Cell Width	-	50 $\mu\text{m}$	80 $\mu\text{m}$	4 mm
Cell Length	-	400 $\mu\text{m}$	12 cm	70 cm
Material at $ \eta  = 0.0$	0.3 $X/X_0$			
Material at $ \eta  = 1.7$	1.2 $X/X_0$			
Material at $ \eta  = 2.5$	0.5 $X/X_0$			
Number of Hits	48	4	8	36
Channels	99 M	92 M	6.3 M	350 k

Table 5: A summary of the parameters of the inner detector and each of the subdetectors [19].

region while accommodating the readout and cable systems. The endcap regions are instead arranged into petals and then into wheels. This arrangement can be seen in Figure 27 which shows a computer-generated, cut-away image of the outer three layers of the pixel detector. Together these three layers contain 1744 modules between the barrel and two endcap sections.

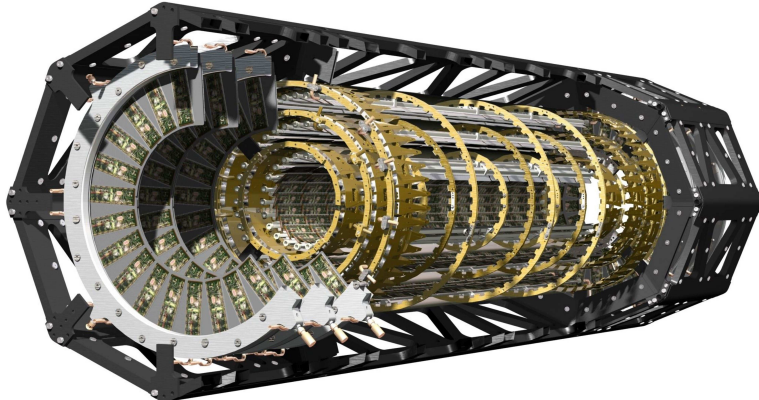


Figure 27: A cut away image of the outer three layers of the pixel detector [19].

The innermost layer, the IBL, was added during the long shutdown before Run 2, and provides the fourth track measurement. It was inserted directly into the existing pixel detector by removing the existing beam pipe and replacing it with a significantly smaller version. This insertion can be seen in action in Figure 28, which emphasizes the extreme precision required to place the the 70 cm long layer with only 2 mm of clearance. The IBL was commissioned to provide continued tracking robustness and high precision in the higher luminosity environment of Run 2 [26]. The proximity of this layer to the collisions necessitated an even higher granularity and better radiation hardness than the other pixel layers. And the strict space requirements to add an active sensing layer so close to the interaction point required a sensor chip with a much higher active area and a larger overall area per chip. These requirements led to the development of a

new chip type, the FE-I4 (compared to the FE-I3 chips used in the original pixel detector) with improved radiation hardness and a larger active area. The **IBL** is comprised of 448 of these individual chips arranged in 14 staves, with 26,880 pixels per chip and a chip size of 18.5 mm x 41.3 mm x 200  $\mu\text{m}$ . The staves, like in the other layers of the pixel detector, are offset by 14° to provide full azimuthal coverage. This arrangement can be seen in Figure 29, which shows two computer-generated images of the **IBL** geometry and includes the some of the remaining pixel layers.



Figure 28: An image of the insertion of the **IBL** into the current pixel detector [27].

### 5.3.2 SEMICONDUCTOR TRACKER

The **SCT**, the subdetector which immediately surrounds the Pixel detector, provides additional discrete measurements of the trajectory of a charged particle. Because the **SCT** is further away from the interaction point, the spatial resolution does not need to be as high as in the pixel detector, and so the **SCT** uses micro-strips instead of pixels. Although pixels provide a more accurate measurement, the number of pixels and readout channels required to cover the cylindrical area at the radius of the **SCT** layers would be prohibitively complicated and expensive.

Each individual silicon strip sensor contains 768 individual readout strips with a total area of 6.36 cm x 6.40 cm and a pitch of 80  $\mu\text{m}$ . Pairs of these sensors are then bonded together to form a combined strip with a length of 12.8 cm. Two of these combined strips are then placed back to back with a relative tilt of 40 mrad. This geometry is illustrated in an expanded view in Figure 30. The purpose of angular offset of the consecutive layers is to allow the strip sensor areas to more accurately measure the position of a particle in the  $z$  direction by comparing the overlap of the two strips which were traversed by a track.

Four of these double layers are placed in the barrel region, with radii of 299 mm, 371 mm, 443 mm, and 514 mm. Together these layers provide eight additional measurements for each track that traverses the central  $|\eta|$  region. In the endcap region, the layers are arranged in wheels, with the double layers simi-

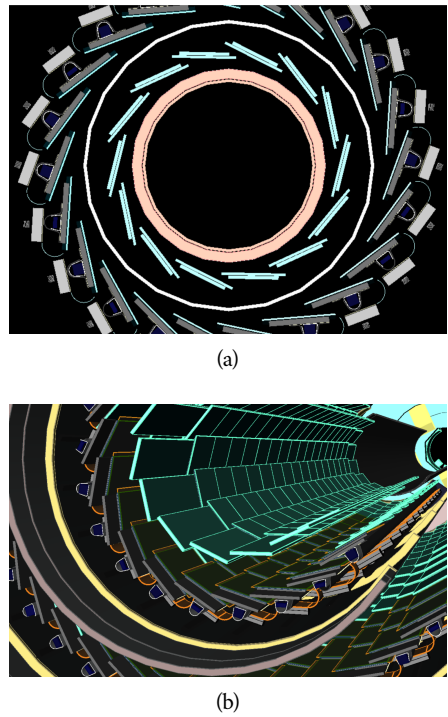


Figure 29: A three-dimensional computer-generated image of the geometry of the **IBL** with a view (a) mostly transverse to the beam pipe (b) mostly parallel to the beam pipe [26].

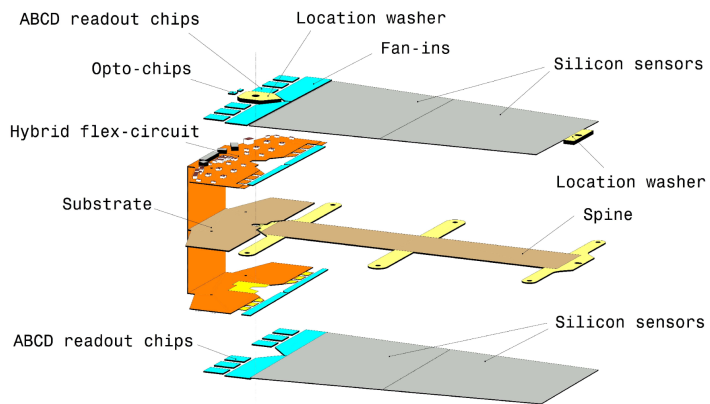


Figure 30: An expanded view of the geometry of the **SCT** double layers in the barrel region [19].

larly offset to provide improved resolution. With these configurations, the [SCT](#) achieves a spatial resolution of  $17\ \mu\text{m}$  in the  $r - \phi$  direction and  $580\ \mu\text{m}$  in the  $z$  direction.

### 5.3.3 TRANSITION RADIATION TRACKER

The final component of the inner detector, the [TRT](#), provides continuous tracking using straw drift tubes. The tubes are made of Kapton and aluminum with a diameter of 4 mm and are filled with a gas mixture of 70% Xe, 27% CO<sub>2</sub>, and 3% O<sub>2</sub>. At the center of each tube is a gold-plated anode tungsten wire which is  $30\ \mu\text{m}$  in diameter. When a charged particle passes through these tubes, it ionizes the gas within. The ions produced drift in the electric field established between the wire and the tube wall, and the large electric field near the wire produces avalanche multiplication and results in an electric current on the wire that is read out by the electronics and provides a track measurement. The time it takes the ionization to drift to the wire can be used to estimate the distance from the wire that the particle passed through the tube; this gives a resolution on the distance of approximately  $130\ \mu\text{m}$ . Combining several such measurements between consecutive hits in the [TRT](#) tubes allows the trajectory of the particle to be reconstructed with much better resolution than is available in each individual tube.

In addition to the continuous tracking, the detector can use transition radiation produced when a particle passes between the layers to distinguish between electrons and heavier charged particles. The space between the tubes is filled with CO<sub>2</sub>, and so has a different dielectric constant than the gas within the tubes which contains Xe. At the transition between those media, a relativistic particle emits radiation proportional to  $\gamma$ , so inversely proportional to mass at a fixed momentum. The photons produced in this transition then produces an ionization cascade which is significantly larger than the signal for the minimally-ionizing charged particles. To distinguish between these two cases, the [TRT](#) defines two signal thresholds, a low threshold for the typical signal produced by a minimally ionizing particle ([MIP](#)) and a high threshold for the signal produced by transition radiation. A high momentum electron is expected to produce approximately 7 to 10 high threshold hits as it traverses the [TRT](#), and thus these hits provide a way to distinguish electrons from other charged particles.

The [TRT](#) contains 351,000 tubes in total, divided between the barrel and endcap regions. In the barrel region, the tubes are 144 cm long and arranged in 73 layers parallel to the beampipe. In the endcap region, the tubes are 37 cm long and arranged in 160 layers transverse to the beampipe. These configurations can be seen in Figure 24 and Figure 25. With this geometry the [TRT](#) achieves a resolution of  $130\ \mu\text{m}$  in the  $r - \phi$  direction.

## 5.4 CALORIMETRY

The combination of calorimeter systems used in ATLAS can measure the energy of electrons, photons, hadrons, and hadronic jets with complete coverage up to

$|\eta| < 4.9$  and across  $\phi$ . Unlike the inner detector, the calorimeters are capable of measuring neutral particles. To accomplish precision measurements of these particle types, the ATLAS calorimeter system uses four individual calorimeters, a liquid argon ([LAr](#)) electromagnetic calorimeter in the barrel region, a tile hadronic calorimeter in the barrel region, a [LAr](#) hadronic endcap calorimeter, and a [LAr](#) forward calorimeter. Together these provide hermetic coverage for the ATLAS detector. The configuration of these calorimeters is illustrated in Figure 31.

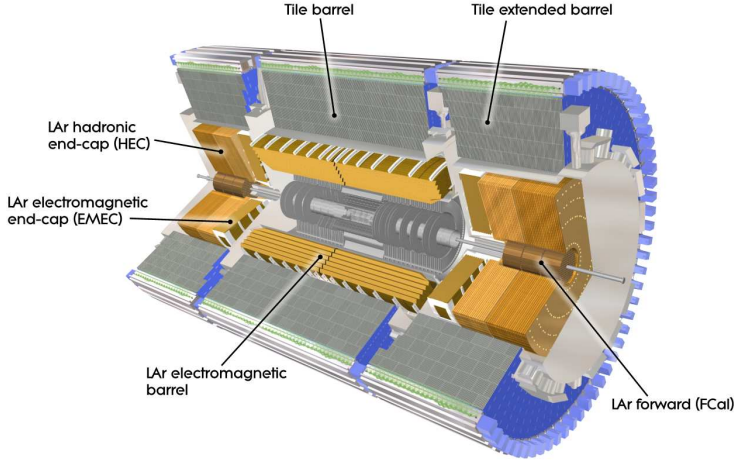


Figure 31: An overview of the ATLAS calorimeter systems [19].

The calorimeters are designed to absorb and measure the energy carried by a particle, and completely stop the particle's propagation in the process. This requires a significant amount of material to provide interactions. These interactions then produce secondary particles, which can produce tertiary particles in turn, and thus form a cascade of particles called an electromagnetic ([EM](#)) or hadronic shower, depending on the governing mechanism. Electromagnetic and hadronic showers have very different properties and require different technologies to measure them accurately. All of the calorimeters in the ATLAS calorimeter system are sampling calorimeters: they use alternating layers of absorbing and active material. The dense absorbing layers initiate the showers while the active layers measure the energy of the produced particles. A fraction of the energy is lost in the inactive layers, so the energy measurement from the active layers has to be corrected to estimate the actual energy of the particle.

The [EM](#) calorimeter provides around 20 radiation lengths ( $X_0$ ) while the hadronic calorimeter provides around 10 interaction lengths ( $\lambda$ ). As mentioned previously, radiation lengths measure the distance over which an electromagnetically interacting particle loses a characteristic fraction of its energy. Interaction lengths, on the other hand, measure the mean distance traveled by a hadronic particle before undergoing a nuclear interaction [3]. Figure 32 show the radiation lengths in the layers of the [EM](#) calorimeter in the barrel region as well as the interaction lengths for all calorimeters.

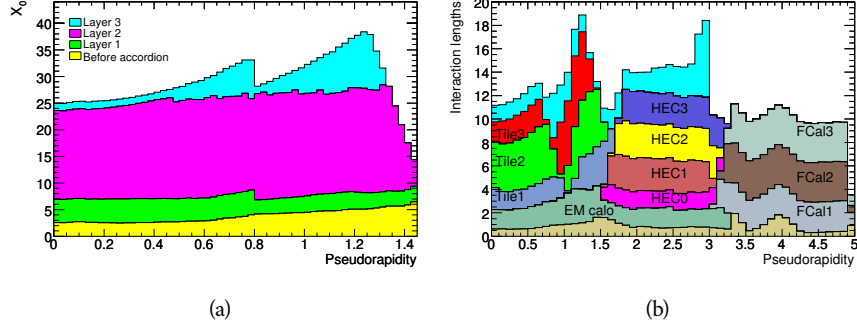


Figure 32: The depth of (a) the electromagnetic barrel calorimeter in radiation lengths and of (b) all calorimeters in interaction lengths as a function of pseudorapidity [19].

#### 5.4.1 ELECTROMAGNETIC CALORIMETER

The electromagnetic calorimeters use alternating layers of liquid argon and lead in an accordion shape. The accordion shape provides complete coverage in the  $\phi$  direction while also providing many alternating layers for a particle to pass through. The configuration is detailed in Figure 33. When an electron or a photon passes through the lead, it produces an electromagnetic shower. The particles produced in those showers then pass into and ionize the liquid argon; the ions produced can then be collected by an electrode in the liquid argon layer to provide the actual energy measurement.

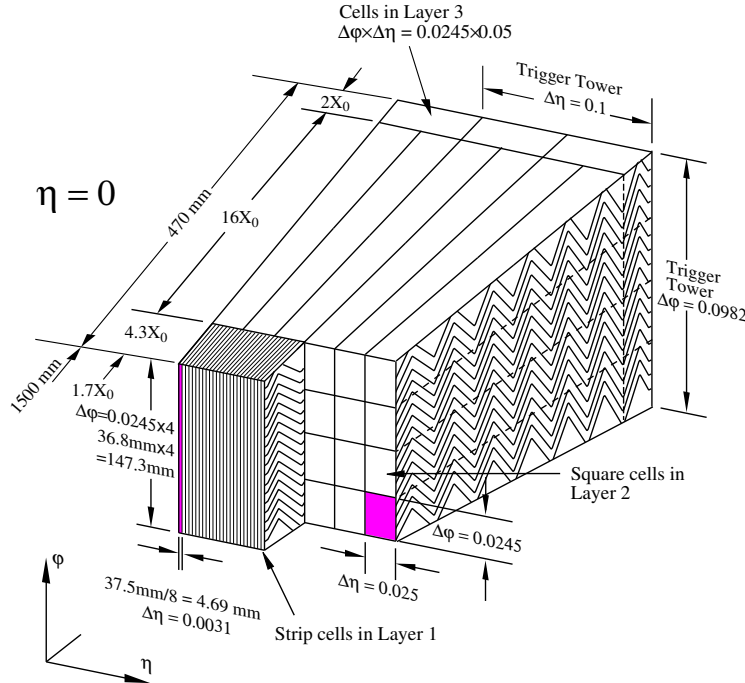


Figure 33: A schematic of the LAr calorimeter in the barrel region, highlighting the accordion structure [19].

The barrel region is covered by a presampler and three separate sampling layers with decreasing segmentation. The presampler is a thin layer of liquid argon which measures the energy of any electromagnetic showers which are initiated before the particle reaches the calorimeter due to interactions with the detector material. The first layer is the strip layer, which has fine segmentation in  $\eta$  to enhance the identification of shower shapes and to provide a precise  $\eta$  measurement for reconstructing photons and electrons. The strip layer has only 4 radiation lengths worth of material, and has a segmentation of  $\Delta\eta = 0.003$  and  $\Delta\phi = 0.1$ . The second layer is also finely segmented, with a segmentation of  $\Delta\eta = 0.025$  and  $\Delta\phi = 0.025$ , and a thickness of  $16 X_0$ . This layer is designed to contain an electromagnetic shower and to measure the majority of the energy for photons and electrons. The third layer is only  $2 X_0$  thick and measures the energy of electromagnetic showers which leak out of the second layer, and helps to separate electromagnetic showers from hadronic showers. The structure of the LAr endcap calorimeter is similar except that the layers are arranged parallel to the beampipe to measure energy deposits from high  $\eta$  particles.

## 5.4.2 HADRONIC CALORIMETERS

The hadronic calorimeters use a few different technologies to satisfy the resolution demands in the different areas of the detector, and together they cover the region  $|\eta| < 2.7$ . In the barrel region, for  $|\eta| < 1.7$ , the hadronic calorimeters are constructed of alternating tiles of steel and plastic scintillator. Like in the electromagnetic calorimeter, the dense layer initiates a shower (in this case the dense layer is the steel and the shower is hadronic) of particles which pass into and ionize the following layer. The ionization in the plastic scintillator instead produces a light signal proportional to the amount of ionization produced by the shower, and this signal is measured using photomultipliers and provides the actual energy measurement. The construction of a tile in the calorimeter is shown Figure 34, which highlights the alternating layers of steel and scintillator.

This tile calorimeter, as well as the remaining hadronic calorimeters, have a much coarser granularity than the electromagnetic calorimeters. The high granularity is not needed for an accurate energy measurement, and the hadronic calorimeters are not designed to distinguish particle types like the electromagnetic calorimeters. The tile granularity is approximately  $\Delta\eta = 0.1$  and  $\Delta\phi = 0.1$ , and the segmentation in depth and  $\eta$  is shown in Figure 35.

The remaining hadronic calorimeters all use the same alternating, sampling structure but with different active and inactive materials. The hadronic endcap calorimeter covers the range of  $1.5 < |\eta| < 3.2$  and uses an inactive layer of copper and an active layer of liquid argon. The forward calorimeter covers the range of  $3.1 < |\eta| < 4.9$  and uses a dense matrix of copper and tungsten filled with liquid argon. Particles propagating through the sampling layers ionize the liquid argon, and the ionization is collected at an electrode to provide a signal.

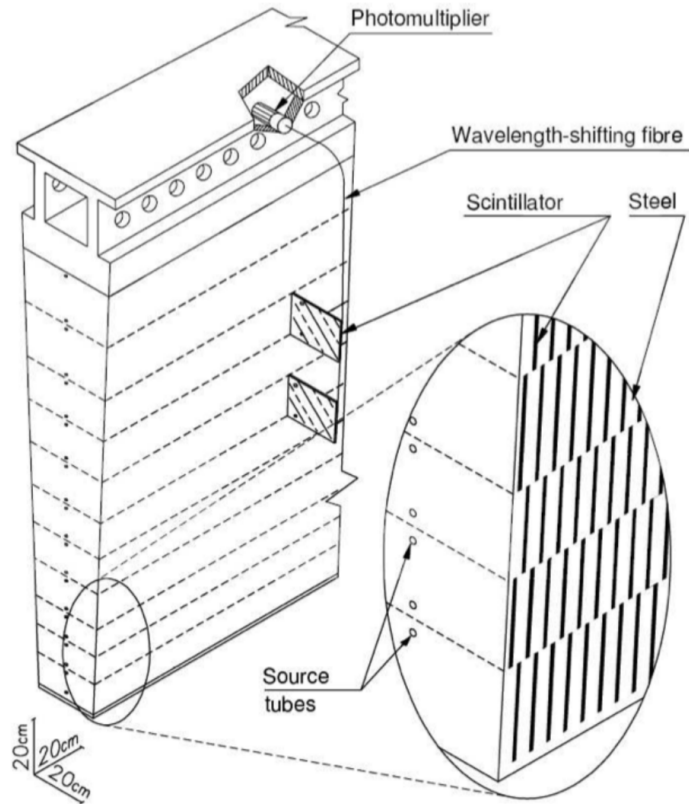


Figure 34: A schematic of a hadronic tile module which shows the alternating layers of steel and plastic scintillator [19].

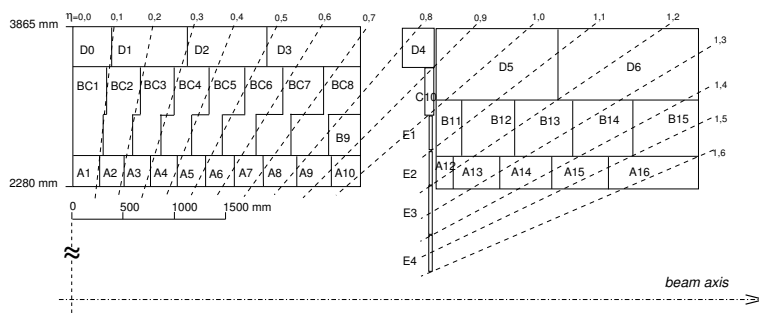


Figure 35: The segmentation in depth and  $\eta$  of the tile-calorimeter modules in the central (left) and extended (right) barrels [19].

## 5.5 MUON SPECTROMETER

Among SM particles, only muons and neutrinos consistently pass through the calorimeters. Because the neutrinos are also electrically neutral, there is no feasible option to measure them directly in ATLAS. The muons, on the other hand, are charged and are thus already measured as a track in the inner detector. The muon spectrometer provides a way to consistently identify muon tracks and also a way to provide an additional measurement of their momentum.

The muon spectrometer contains four subdetectors that cover the barrel and endcap regions. In the barrel region, the muon spectrometer uses a combination of Resistive Plate Chambers (RPCs) and Monitored Drift Tubes (MDTs) to provide both a coarse, fast measurement for triggering and a precise momentum measurement for offline event reconstruction. Similarly, in the endcap region, the Thin Gap Chambers (TGCs), MDTs, and Cathode Strip Chambers (CSCs) allow for both triggering and precise measurements. The CSCs are used only in the innermost layer of the endcap region between  $2.0 < |\eta| < 2.7$  where the particle flux is too large for the MDTs to provide accurate measurements. The overall layout of the muon systems are shown in the cut-away diagram in Figure 36, and Figure 37 shows a precise schematic of the layout of each of the detecting elements. The geometric arrangement shown provides consistent coverage for muons produced up to  $|\eta| < 2.7$ , and takes full advantage of the bending of the muons in the toroidal magnetic field, described in Section 5.2, to measure their momentum. Figure 38 shows a cross-section of the arrangement of the muon spectrometer in the barrel; the layers are divided into eight small and eight large chambers that are overlapped to provide complete coverage in  $\phi$ .

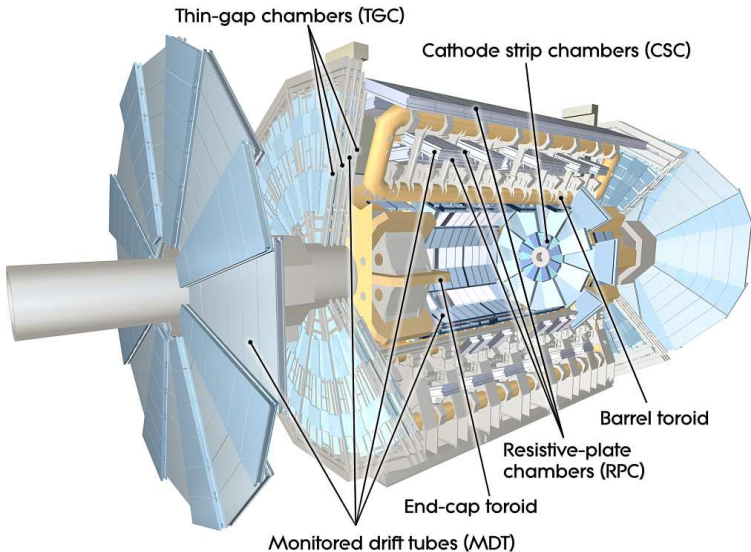


Figure 36: A cut-away diagram of the muon systems on ATLAS [19].

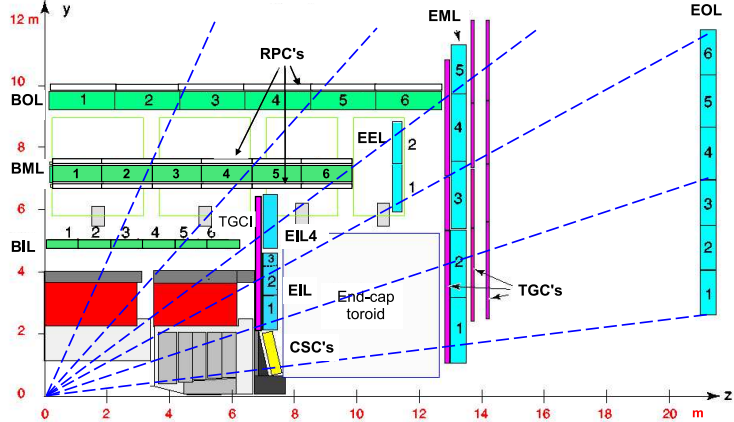


Figure 37: A quarter view of the muon spectrometer which highlights the layout of each of the detecting elements. The BOL, BML, BIL, EOL, EML, and EIL are all MDT elements, where the acronyms encode their positions [19].

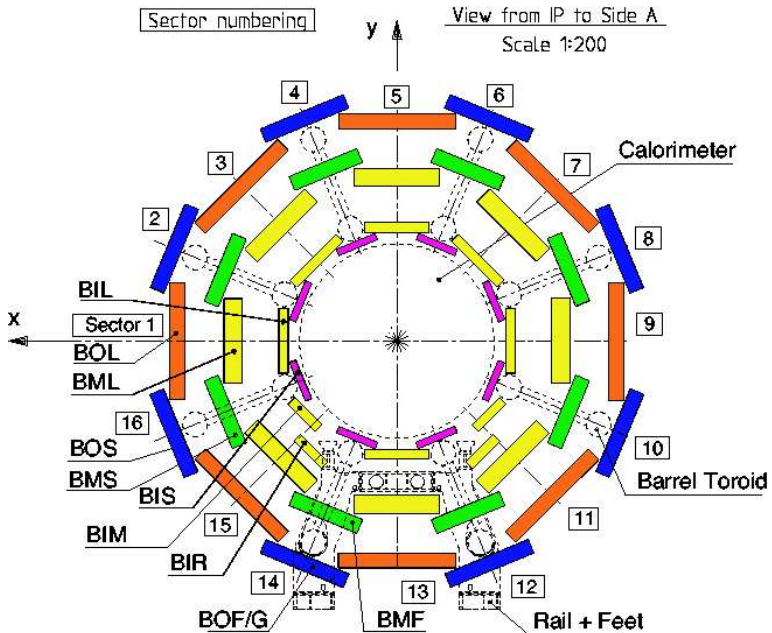


Figure 38: A schematic of the cross-section of the muon spectrometer in the barrel region [19].

## 5.5.1 MONITORED DRIFT TUBE

The momentum measurements in the barrel region are provided by three consecutive layers of MDT elements, located at approximately 5 m, 7 m, and 9 m from the interaction point. Each of these layers is a composite of two multilayers of drift tubes: two layers of three to four layers of tubes, as shown in Figure 39. These aluminum tubes are 3 cm in diameter, with lengths between 0.9 and 6.2 m, and are filled with a mixture of ArCO<sub>2</sub> kept at 3 bar absolute pressure. A central tungsten-rhenium wire with a diameter of 50  $\mu\text{m}$  runs along the length of the tube, and is kept at a potential of 3080 V.

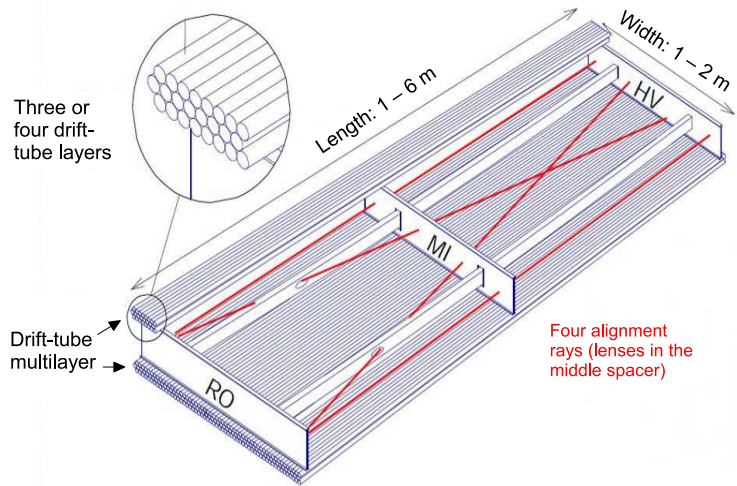


Figure 39: A schematic of a single MDT chamber, which shows the multilayers of drift tubes as well as the alignment system [19].

A muon traversing these tubes ionizes the gas, and the ionization electrons then drift in the electric field toward the central wire. Close to the wire, the electric field is strong enough to cause the original ionization electrons to ionize additional electrons, producing an avalanche that can be measured as a current along the wire. The time of arrival of that current depends on how far the muon entered from the wire, and can be used to achieve a position resolution of 80  $\mu\text{m}$  in an individual tube. The combination of the measurements in the consecutive layers of tubes improves this position resolution to 35  $\mu\text{m}$  transverse to the tubes, with a resolution of 1 m along the tube direction.

To achieve a good resolution over the entire length of a muon track, the relative positions of the tubes of the muon spectrometer must be known to an accuracy of 30  $\mu\text{m}$ . This is achieved by an optical laser alignment system placed in each of the individual chambers and throughout the cavern. These monitor any changes in position or alignment due to effects like gravitational sag, temperature shifts, and the magnetic field. The configuration of the alignment system within an individual chamber is also shown in Figure 38.

### 5.5.2 RESISTIVE PLATE CHAMBER

The **RPC** is the provides a fast measurement of the  $\phi$  position of muons for triggering in the barrel region. The system has a lower spatial resolution than the **MDTs** but has a faster measurement with a time resolution of just a few tens of nanoseconds. There are three **RPCs** layers in the muon spectrometer, two located on either side of the central **MDT** layer and one located outside the final **MDT** layer, as shown in Figure 37. The **RPCs** consist of two layers of parallel plates filled with a gas mixture of  $C_2H_2F_4$ . A muon passing through these systems ionizes the gas, like in the **MDT**, which causes an avalanche of ionization electrons in the electric field maintained between the plates. Metal strips on the outside of the chamber capacitively couple to the accumulated charge, and are read out to measure the  $\eta$  and  $\phi$  positions of the muon track.

### 5.5.3 CATHODE STRIP CHAMBER

The majority of the momentum measurements in the endcap region are provided by the **MDTs**. In the most forward region of the muon spectrometer, between  $2.0 < \eta < 2.7$ , the particle flux is very high due to contributions from low energy photons and neutrons. The **MDT** can only sustain a hit rate of approximately 150 Hz/cm<sup>2</sup> because of limitations in the drift times of the gas and the capacity of the readout electronics. The **CSCs** were designed to handle higher hit rates, up to 1000 Hz/cm<sup>2</sup>, and provide the necessary coverage in that high flux region.

The **CSC** consists of several multiwire proportional chambers, where the wires are oriented in the radial direction out from the beampipe. There are eight large and eight small chambers, arranged to partially overlap in the  $\phi$  direction, as shown in Figure 40. Like in the **MDT**, a muon traversing the system produces ionization in the gas; here, however, the ionization is collected on a number of wires. These wires couple to cathodes on the chambers which are segmented into strips in two directions. The relative amount of charge on each of the neighboring strips can be used to interpolate to the position of the muon in both  $\eta$  and  $\phi$ .

### 5.5.4 THIN GAP CHAMBER

Like in the barrel region, a separate, fast detector is required to provide position measurements of muons for trigger in the endcap region. This is provided by the **TGC** which consists of seven layers in the middle station of the endcap, two doublet layers and one triplet layer, and a single doublet layer in the inner endcap station. Figure 41 shows the arrangement of the triple and doublet layers of the **TGCs**.

Like the **CSCs**, the **TGCs** are multiwire proportional chambers with a wire-to-cathode distance of 1.4 mm and a wire-to-wire distance of 1.8 mm. Readout strips on the outside of the chambers run perpendicular to the wires, and couple to the charge collected on the wires to provide a position measurement in the  $\eta$  direction. The current induced on the wires is also readout to provide a position

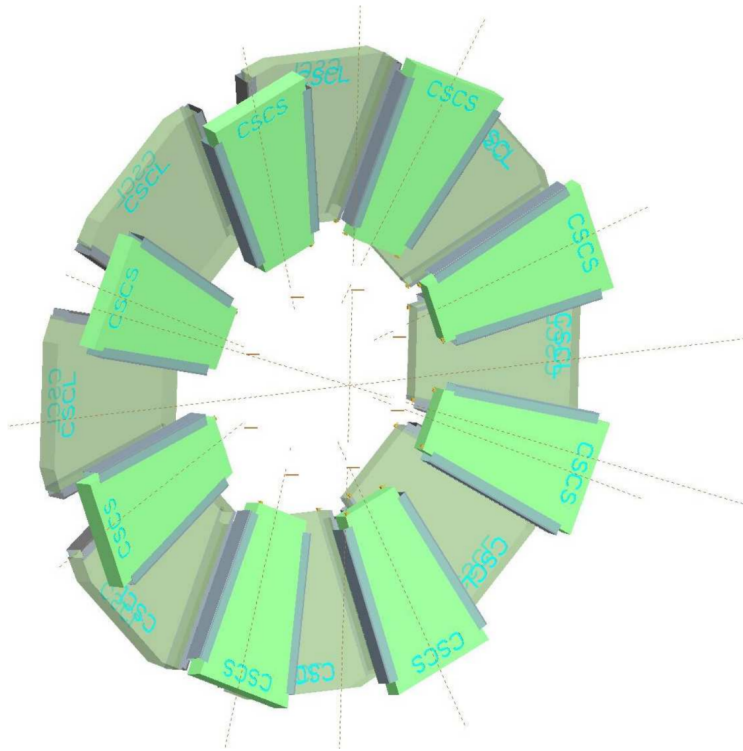


Figure 40: A schematic of the **CSC** endcap, showing the overlapping arrangement of the eight large and eight small chambers [19].

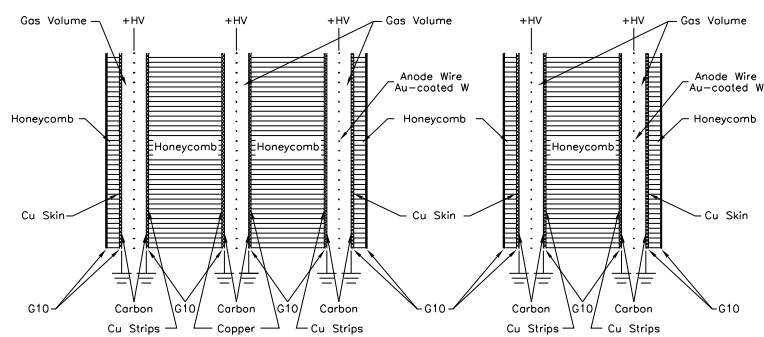


Figure 41: A schematic of the **TGC** doublet and triplet layers [19].

measurement in the  $\phi$  direction. The high electric field and small wire-to-wire distance give it the required good time resolution to be used for triggering events.

## 5.6 TRIGGER

It is not possible for the detector and the associated computing systems to record the 80 TB of data that the 40 MHz event rate produces every second. Instead, a small fraction of these events are selected by the trigger system to be recorded and later analyzed. Selecting interesting events at such a high rate poses a significant challenge for both the detector design and the implementation of a trigger decision and data acquisition system. The trigger must balance the time needed to decide to keep an event, to avoid losing information, with the filtering accuracy to consistently select a full menu of physics events that can be used for the wide array of searches and measurements targeted by ATLAS.

The ATLAS trigger system, as of Run 2, consists of two levels of decision making. The first level, referred to as Level 1 ([L1](#)), is hardware based and uses inputs from a subset of the detector elements to reduce the considered event rate from the original 40 MHz down to 100 kHz. The 100 kHz rate is the maximal rate that the event information can be transferred from the detector. The [L1](#) trigger decisions must be made with  $2.5 \mu\text{s}$ , or else the information stored from the event is still available to be read out to the next step. The second, software-based level, referred to as the high level trigger ([HLT](#)), makes the final decisions on which events to keep for analysis and selects a rate of around 1 kHz. The collection of selection criteria used to make the [L1](#) decisions feed into subsequent selection criteria in the [HLT](#), and the set of these combinations of [L1](#) and [HLT](#) criteria from the trigger menu which defines exactly what events are recorded on ATLAS. A subset of the trigger menu used for 2015 data collection is shown in Table 6, which summarizes the selection requirements at both levels and additionally shows the peak measured rates contributed by each.

At [L1](#), the trigger system uses information primarily from the calorimeters and muon spectrometer to select high  $p_{\text{T}}$  jets, electrons, photons, and muons. The electromagnetic calorimeter uses reduced granularity energy measurements as well as isolation requirements to select electrons and photons. The hadronic calorimeter also uses a combination of reduced granularity energy measurements and isolation to select high momentum jets and hadronically decaying tau leptons. The calorimeters are also used to provide triggers based on missing energy: the coarse granularity energy measurements are used to calculate a directional sum of energies and to trigger on a significant imbalance. The analysis discussed here uses the  $E_T^{\text{miss}}$  trigger shown in Table 6, with a [L1](#) rate of 0.7 kHz and an [HLT](#) rate of 55 Hz.

Only the [RPCs](#) and [TGCs](#) muon subdetectors contribute to the decision at [L1](#), and are used to identify high momentum muons. The contributions to the triggering rate of the various types of [L1](#) triggers are shown in Figure 42. The total rate is indicated in black and is lower than the sum of individual rates because there is significant overlap between different trigger channels. The majority of the rate comes from lepton and photon triggers.

Trigger	Typical offline selection	Trigger Selection		Level-1 Peak Rate (kHz)	HLT Peak Rate (Hz)
		Level-1 (GeV)	HLT (GeV)		
Single leptons	Single iso $\mu$ , $p_T > 21$ GeV	15	20	7	130
	Single $e$ , $p_T > 25$ GeV	20	24	18	139
	Single $\mu$ , $p_T > 42$ GeV	20	40	5	33
	Single $\tau$ , $p_T > 90$ GeV	60	80	2	41
Two leptons	Two $\mu$ 's, each $p_T > 11$ GeV	$2 \times 10$	$2 \times 10$	0.8	19
	Two $\mu$ 's, $p_T > 19, 10$ GeV	15	18, 8	7	18
	Two loose $e$ 's, each $p_T > 15$ GeV	$2 \times 10$	$2 \times 12$	10	5
	One $e$ & one $\mu$ , $p_T > 10, 26$ GeV	20 ( $\mu$ )	7, 24	5	1
	One loose $e$ & one $\mu$ , $p_T > 19, 15$ GeV	15, 10	17, 14	0.4	2
	Two $\tau$ 's, $p_T > 40, 30$ GeV	20, 12	35, 25	2	22
	One $\tau$ , one $\mu$ , $p_T > 30, 15$ GeV	12, 10 (+jets)	25, 14	0.5	10
Three leptons	One $\tau$ , one $e$ , $p_T > 30, 19$ GeV	12, 15 (+jets)	25, 17	1	3.9
	Three loose $e$ 's, $p_T > 19, 11, 11$ GeV	15, 2 $\times$ 7	17, 2 $\times$ 9	3	< 0.1
	Three $\mu$ 's, each $p_T > 8$ GeV	3 $\times$ 6	3 $\times$ 6	< 0.1	4
	Three $\mu$ 's, $p_T > 19, 2 \times 6$ GeV	15	18, 2 $\times$ 4	7	2
	Two $\mu$ 's & one $e$ , $p_T > 2 \times 11, 14$ GeV	$2 \times 10$ ( $\mu$ 's)	$2 \times 10, 12$	0.8	0.2
One photon	Two loose $e$ 's & one $\mu$ , $p_T > 2 \times 11, 11$ GeV	$2 \times 8, 10$	$2 \times 12, 10$	0.3	< 0.1
	one $\gamma$ , $p_T > 125$ GeV	22	120	8	20
Two photons	Two loose $\gamma$ 's, $p_T > 40, 30$ GeV	$2 \times 15$	35, 25	1.5	12
	Two tight $\gamma$ 's, $p_T > 25, 25$ GeV	$2 \times 15$	$2 \times 20$	1.5	7
Single jet	Jet ( $R = 0.4$ ), $p_T > 400$ GeV	100	360	0.9	18
	Jet ( $R = 1.0$ ), $p_T > 400$ GeV	100	360	0.9	23
$E_T^{\text{miss}}$	$E_T^{\text{miss}} > 180$ GeV	50	70	0.7	55
Multi-jets	Four jets, each $p_T > 95$ GeV	$3 \times 40$	$4 \times 85$	0.3	20
	Five jets, each $p_T > 70$ GeV	$4 \times 20$	$5 \times 60$	0.4	15
	Six jets, each $p_T > 55$ GeV	$4 \times 15$	$6 \times 45$	1.0	12
$b$ -jets	One loose $b$ , $p_T > 235$ GeV	100	225	0.9	35
	Two medium $b$ 's, $p_T > 160, 60$ GeV	100	150, 50	0.9	9
	One $b$ & three jets, each $p_T > 75$ GeV	$3 \times 25$	$4 \times 65$	0.9	11
	Two $b$ & two jets, each $p_T > 45$ GeV	$3 \times 25$	$4 \times 35$	0.9	9
$b$ -physics	Two $\mu$ 's, $p_T > 6, 4$ GeV plus dedicated $b$ -physics selections	6, 4	6, 4	8	52
Total				70	1400

Table 6: A subset of the trigger menu for the 2015 data collection with  $L = 5 \times 10^{33} \text{ cm}^{-2} \text{s}^{-1}$ . Both the L1 and HLT selection requirements and their trigger rates are shown measured at the specified luminosity are shown. The typical offline selections represent a typical set of offline requirements imposed after the trigger in an analysis [28].

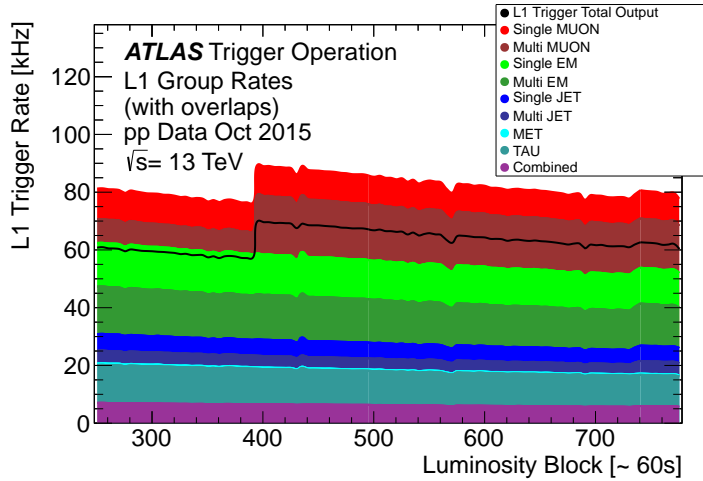


Figure 42: The L1 Trigger rate broken down into the types of triggers as a function of the luminosity block for the 2015 data collection period [28].

After an event is chosen by the [L1](#) trigger, the detector measurements from the bunch crossing which fired the trigger is read out from the front-end electronics and stored on read-out boards. This inclusive information is necessary to make more the more precise event selections than is possible with the reduced information at [L1](#). The [HLT](#) then uses this information with software algorithms to decide whether or not to permanently record the event. The [L1](#) trigger also forwards which decision was made and Region of Interests ([RoIs](#)) to the [HLT](#), which allows the [HLT](#) to focus on particular algorithms and particular sections of the detector to greatly improve the algorithmic selection speed. The additional information available to the [HLT](#) allows it to use full offline reconstruction algorithms (Chapter 6) to implement additional trigger targets, such as identified jets from the decays of b-hadrons. The contributions to the triggering rate of the various types of [HLT](#) triggers are shown in Figure 43.

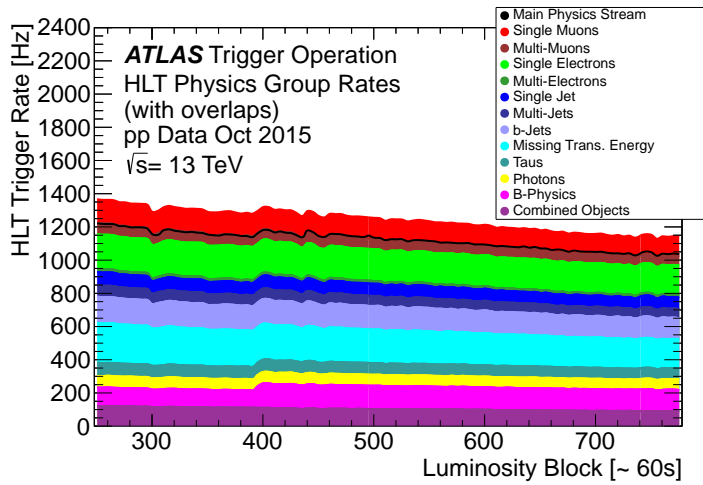


Figure 43: The [HLT](#) Trigger rate broken down into the types of triggers as a function of the luminosity block for the 2015 data collection period.

## EVENT RECONSTRUCTION

---

The ATLAS experiment combines measurements in the subdetectors to form a cohesive picture of each physics event. The majority of particles that traverse the detector leave behind some combination of ionization hits in the tracking detectors or energy deposits in the calorimeters, and these measurements can be used to reconstruct physical quantities like the particle’s energy, momentum, or trajectory. Even the type of the particle can be distinguished by comparing the various ways that different species of stable particles interact with the subdetectors. Reconstruction is the series of algorithms which take the electronic outputs of the detector and assigns them into individual physics objects. The physics objects summarize the properties of particles produced by the collision or subsequent decays, either for individual isolated particles like leptons, or for a collection of the cascade of products produced in the decay of an energetic hadron, called a jet. These are the objects and quantities most often used in analysis to make measurements of SM processes or to search for new physics.

### 6.1 CHARGED PARTICLES

As described in Section 5.3, charged particles that traverse the inner detector leave behind hits in the subdetectors. Each of these hits translates into a position measurement along the trajectory of that particle, with position resolutions depending on the subdetector that provided the measurement. Track reconstruction uses these position measurements to collect hits in consecutive layers of the detector into a trajectory consistent with a particle curving in a magnetic field [29, 30]. This reconstructed trajectory is called a track. The number of hits in the inner detector for each event makes a combinatorial method completely infeasible: the algorithms that form tracks must be significantly more intelligent so that event reconstruction does not exhaust computing resources.

The first and primary algorithm employed in track reconstruction is called the inside-out method, which begins with the assumption that the track originated from the interaction point. Its purpose is to identify primary particles, those which originate in the proton-proton collisions and with a lifetime long enough to reach the inner detector. Combinations of three hits are considered from measurements in the Pixel detector and the SCT, and form the seed for a track. Specifically, the seeding algorithm looks for a seed using three pixel hits, two pixel hits and one SCT hit, or three SCT hits. The seed is then extrapolated forwards and backwards into the Pixel and SCT detectors depending on the seed location, and hits in each layer are considered to be added to the track using a combinatorial Kalman filter [30]. After all of the silicon layers have been considered, tracks are filtered to reduce ambiguities from other nearby tracks or from combinatorial coincidences. Then the tracks are extended outwards into

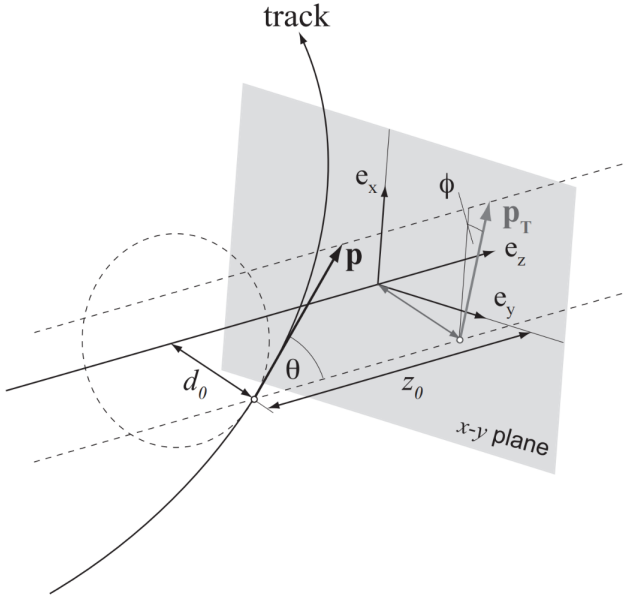


Figure 44: An illustration of the perigee representation of track parameters for an example track. The charge is not directly shown, but is indicated by the direction of curvature of the track [31].

the [TRT](#) in the same way. The result of this clustering algorithm is a collection of hits identified to belong to a single track. Once the hits are collected, a fitting algorithm calculates the track parameters which best model the locations of the hits and their resolutions. The fitting uses five parameters,  $(d_0, z_0, \phi, \theta, q/p)$ , to specify a track in a perigee representation:  $d_0$  and  $z_0$  are the transverse and longitudinal impact parameters at the closest approach to the nominal beam axis,  $\phi$  and  $\theta$  are the usual angular coordinates, and  $q/p$  is the charge divided by the curvature. These parameters are illustrated in Figure 44. Those parameters directly determine the direction and momentum of the particle which produced the track.

This inside-out algorithm is complemented by an outside-in algorithm, which is used to find tracks from secondary particles, those produced in the decays or interactions of the primary particles inside the detector. As the name indicates, the outside-in algorithm begins by seeding tracks in the outermost layers of the inner detector, in the [TRT](#). The seed in this case is formed by a segment in the [TRT](#), and the track is propagated backwards into the [SCT](#) before being refitted to use all the included points. Some tracks are found with [TRT](#) segments only, which can result from interactions with the detector following the [SCT](#). Figure 45 shows an example of the geometry of tracks formed by both algorithms, where the hits belonging to tracks found using the inside-out algorithm are highlighted in red, and the hits belonging to the tracks found using the outside-in algorithm are circled in black. The figure highlights the presence of a large number of both primary and secondary tracks in a single event, as well as the overall large number of hits present in the inner detector.

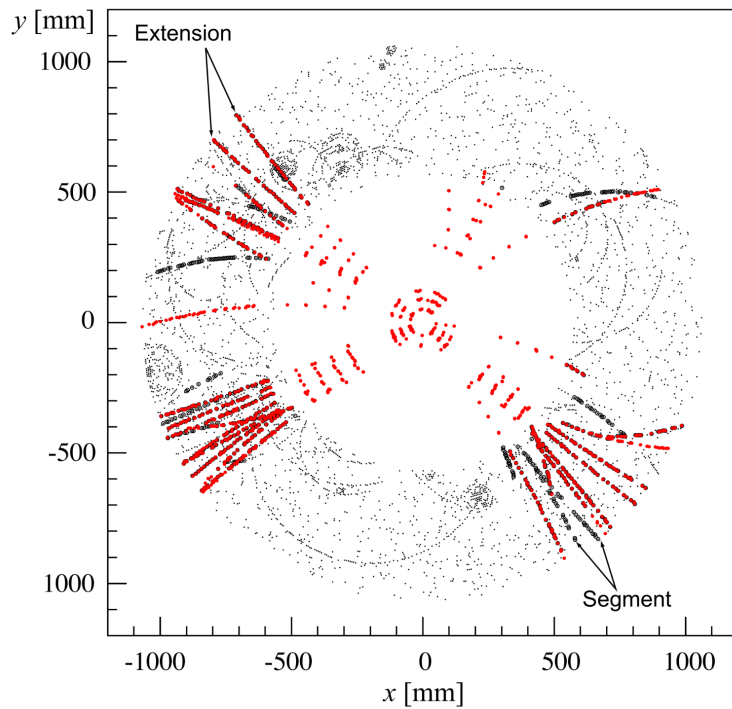


Figure 45: The  $x$  and  $y$  locations of the hits generated in a simulated  $t\bar{t}$  event in the inner detector. The hits which belong to tracks formed using the inside-out algorithm are highlighted in red, while the hits which belong to tracks formed using the outside-in algorithm are circled in black. This figure does not include hits in the IBL.

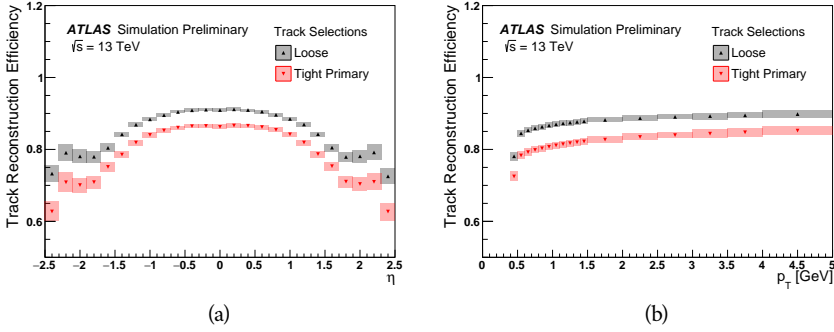


Figure 46: The tracking reconstruction efficiency as a function of (a)  $\eta$  and (b)  $p_T$  [32].

The tracks resulting from these algorithms can be contaminated by nearby particles confusing the tracking algorithm in a high luminosity environment. For example, enough hits present in the inner detector can lead to fake tracks from combinations of hits from multiple individual tracks. Therefore, after the tracks are formed and fitted, additional quality requirements are imposed in order to reduce such backgrounds. Most tracking applications require at least seven silicon hits, that is, seven hits between the Pixel detector and **SCT**. Then the tracks are required to have at most two holes in the Pixel detector, where holes are non-existing but expected measurements in a layer of the subdetector. If the missing hit corresponds to an inactive module, however, it is not counted as a hole but instead as a hit for tracking as the lack of a measurement is expected in that case. With these requirements, the inner detector achieves the reconstruction efficiencies shown in Figure 46 as a function of  $p_T$  and  $\eta$ . The efficiency ranges between 80% and 90% for the tight primary selection described above, and is maximized at high  $p_T$  and low  $|\eta|$ .

### 6.1.1 PIXEL NEURAL NETWORK

The hits in the Pixel detector are not typically confined to a single pixel, but rather the charge is spread over several pixels per layer which are grouped together into clusters. The clustering of these pixels for isolated tracks is relatively straightforward; a connected component analysis identifies groups of neighboring pixels above the readout threshold [33]. Complications can arise in the high occupancy environment where hits from multiple particles can overlap in a single cluster. Figure 47 shows examples of clusters generated by a single isolated particle, two nearly overlapping particles, and a particle which emits a  $\delta$ -ray. A  $\delta$ -ray is a secondary electron which is generated with enough energy to escape a significant distance away from the original particle and to generate additional ionization.

A series of neural-networks analyzes the shape of the clusters to determine how many particles produced the cluster and to estimate the positions of each of the particles within the cluster. These allow for an identification of clusters caused by more than one particle or by a particle that emits a  $\delta$ -ray. In a high-

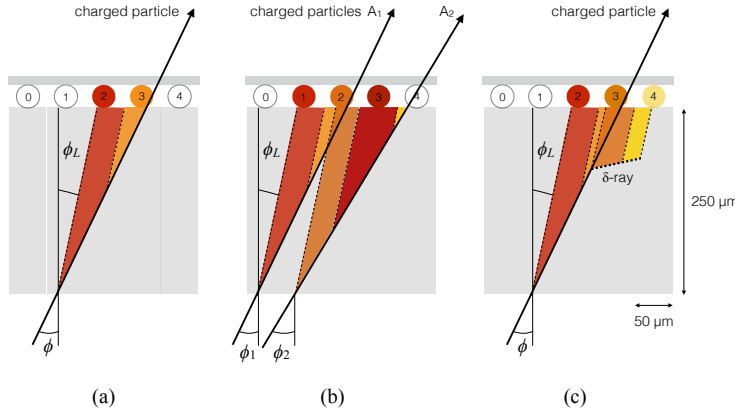


Figure 47: Examples of the clusters formed in a single layer of the pixel detector for (a) a single isolated particle, (b) two nearly-overlapping particles, and (c) a particle which emits a  $\delta$ -ray [33].

density tracking environment, the multiple position outputs can be used as the locations of individual hits to allow reconstruction of tracks which almost overlap and with a much better separation than is possible without the splitting of individual clusters.

### 6.1.2 PIXEL DE/DX

A hit in the Pixel detector corresponds to the voltage generated from ionization current rising above a threshold value that is tuned to consistently record the passing of MIPs. A larger amount of charge deposited results in a larger voltage, and a larger signal remains above the threshold for a longer period of time. The time over threshold (ToT) is read out of the Pixel detector, and can be used to provide a measurement of the charge deposited in each pixel. The charge measurements from each of the pixels included in a pixel cluster are summed to form one charge measurement per layer of the pixel detector. That charge measurement, combined with the angle of incidence of the track and the known sizes of each detector element, can be converted into a measurement of  $dE/dx$ , the ionization energy deposited per unit distance, measured in  $\text{MeVg}^{-1}\text{cm}^2$ . The IBL only has sixteen available values (4 bits) of ToT to readout, compared to the 256 available values (8 bits) in the remaining pixel layers. To help alleviate this lack of range, the IBL also records if it is in overflow: when the ionization is sufficient to generate a ToT above the largest value that can be recorded in the 4 bits. In the remaining layers, the charge value is lost if the hit is in overflow; however the significantly larger range of values makes this very rare in those layers.

The measurements across multiple layers are combined to form an average value of  $dE/dx$  for the track as a whole. Depending on where a charged particle is produced, it will traverse four Pixel layers and create four clusters on average. It can produce as few as two clusters in the Pixel detector if it passes through inactive modules, and as many as five if it is in a region of the detector where multiple

modules overlap. To reduce the influence of the typical long Landau tails of the distribution of  $dE/dx$  deposits [3], the average is calculated as a truncated mean of these clusters. The value measured in the IBL is removed if it is in overflow, as the measured value is not reliable in that case. If a track has five measurements in the pixel detector, the two highest cluster values are removed. If a track has two, three, or four measurements in the pixel detector, only the single highest cluster value is removed. The remaining values are averaged to form the pixel  $dE/dx$ .

### 6.1.3 VERTEX RECONSTRUCTION

A vertex represents the intersection of multiple tracks and corresponds to the location of an interaction. If at least two charged particles result from the interaction, the intersection of their resulting tracks reveals its position with high precision. Vertices are divided into two groups, primary vertices which correspond to the actual proton-proton collisions, and secondary vertices which correspond to decays of short-lived particles or interactions with the detector. Primary vertices are particularly important, as they can provide a precise location for the interaction which generated the observed particles. Understanding that location is crucial in understanding the geometry of the event.

Primary vertices are reconstructed by iteratively identifying seeds from reconstructed tracks [34]. Each track's extrapolated  $z$  position at the beamline forms a seed, and nearby tracks are fitted using that position as a point along their trajectory. The goodness of fit with that vertex is considered for each track, measured in  $\chi^2$ . The final position of the vertex is determined by a fit to all of the considered tracks, where the contribution from each track is weighted according to the  $\chi^2$  compatibility with that vertex and by the error on its position. Any tracks that are displaced by more than  $7\sigma$  from that vertex are removed from the fit and used to seed a new vertex. This procedure is iterated until no additional vertices can be found.

This procedure is typically performed twice. The first set of vertices is used to fit a profile for the beamspot, which indicates the position of the intersection of beams in that particular bunch crossing. The fitted beamspot then provides a constraint for the second attempt to locate primary vertices, where both the track fitting and seeding of vertices are required to be consistent with interactions occurring within the beamspot. The vertex reconstruction algorithm achieves the efficiency shown in Figure 48, increasing from 83% for vertices with two associated tracks and up to nearly 100% for vertices with four or more associated tracks.

## 6.2 ELECTRONS AND PHOTONS

Electrons are measured as both a charged particle track and energy deposits in the electromagnetic calorimeter. Photons, on the other hand, leave energy deposits in the electromagnetic calorimeter but do not produce a corresponding track. Because the electromagnetic interactions with the calorimeter of both

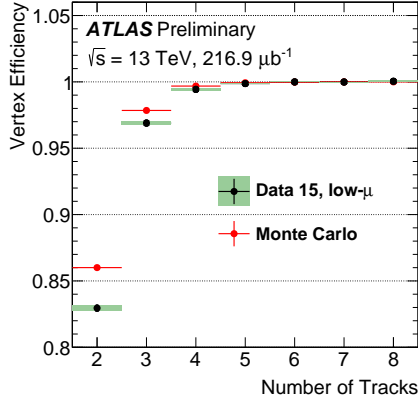


Figure 48: The vertex reconstruction efficiency as a function of the number of associated tracks [35].

photons and electrons produces more photons and electrons, the behavior in the calorimeter is very similar and there is significant overlap in the reconstruction techniques for each.

The reconstruction of a photon or an electron in the calorimeter is based on clustering algorithms which identify groups of energy deposits [36–38]. For this purpose, the entire electromagnetic calorimeter is subdivided into a grid of 200 by 256 towers in the  $\eta$  and  $\phi$  directions, respectively, where the individual grid units have a size of  $\Delta\eta = 0.025$  and  $\Delta\phi = 0.025$ . These towers correspond to individual cells in the middle, coarsest layer of the EM calorimeter, and in the remaining layers the cells are grouped together cover the same area in  $\eta - \phi$  space. The clustering begins by finding seeds with a sliding-window algorithm based on the towers: a window of 3 by 5 towers is formed and translated until the sum of the energy within the window is maximized. If that energy is above 2.5 GeV, then that region becomes a seed. The choice of 2.5 GeV was chosen to compromise between maximizing reconstruction efficiency while minimizing fake electron seeds from electronic noise or soft hadrons from additional interactions. The seeds are rejected if the energy measured in the hadronic calorimeter behind the seed is large, as this typically indicates a hadron rather than an electron or photon.

Next, the inner detector tracks within a cone of  $\Delta R = 0.3$  are compared to the location and energy of the seed. Tracks are matched to the cluster if the extrapolation of the track to the energy-weighted center in the middle layer of the EM calorimeter falls within  $\Delta\phi < 0.2$  in the direction of the curvature of the track or  $\Delta\phi < 0.05$  in the direction opposite of the curvature of the track. If the seed matches with a track that originated from a primary vertex, the combination of track and electromagnetic cluster is reconstructed as an electron. If the seed matches with a track that did not originate from a primary vertex, then the electromagnetic cluster is reconstructed as a converted photon. And if there is no corresponding track in the inner detector, then the cluster is reconstructed as a photon.

After classification, the final clustering of the energy in the [EM](#) calorimeter calorimeter is performed. The classification must be done first, as the expected size of the energy deposits in the calorimeter are different for electrons and photons. In the barrel region, the final clusters for electrons are formed in rectangles of 3 towers in the  $\eta$ -direction and 7 towers in the  $\phi$ -direction. This asymmetric window accounts for the curving of the charged particles only in the  $\phi$  direction. For photons, the size of the rectangle is 3 towers by 5 towers. In the endcap region, all object types are clustered in rectangles of 5 towers by 5 towers, as the effect of the magnetic field curvature is less pronounced in this region. The sum of the energies in these clusters provide the final energy measurement for the electron or photon.

### 6.2.1 PHOTON IDENTIFICATION

The original requirement for constructing a photon cluster, a significant energy deposit in the electromagnetic calorimeter without a corresponding track or energy deposits in the hadronic calorimeter, is already effective in identifying photons. However, there is a significant background for prompt photon production from the decays of pions,  $\pi^0 \rightarrow \gamma\gamma$ . These can be identified using the shape of the cluster in the narrow  $\eta$  granularity in the first layer of the [EM](#) calorimeter.

### 6.2.2 ELECTRON IDENTIFICATION

Prompt electrons have a number of backgrounds, such as secondary electrons from hadron decays or misidentified hadronic jets, that can be rejected using additional information from the [EM](#) calorimeter and the inner detector. The most basic level of electron identification, referred to as Loose, makes requirements on the shower shapes in the high granularity first layer of the [EM](#) calorimeter as well as the quality of the inner detector track. It also requires a good match between the track and the calorimeter energy deposits and a small fraction of energy in the hadronic calorimeter behind the electromagnetic cluster. ATLAS defines several additional working points, including MediumLL and TightLL, which provide progressively lower background rates for electrons by imposing additionally strict requirements on the above variables as well as new requirements like the impact parameter of the inner detector track or the comparison of the cluster energy to the momentum in the inner detector. The LL designates that the requirement is based on a threshold on the output of a likelihood function using the above quantities as an input [37].

## 6.3 MUONS

Muons produced in ATLAS first traverse the inner detector and leave behind a track as described in Section 6.1. The muon then passes through the calorimeter, leaving behind a small, characteristic amount of energy, and then passes through the muon spectrometer where it produces hits in the [MDTs](#) or [CSCs](#). Muon tracks

are formed from local segments of hits in each layer of the MDTs or CSCs, and then the final muon spectrometer track is formed by combining the two local segments [39]. When a track is reconstructed in both the inner detector and the muon spectrometer, the track is refitted to include the hits in both the inner detector and the muon spectrometer, and forms a combined muon.

In a few regions of the detector, a muon may fail to leave behind both a complete inner detector and muon system track. For a very small fraction of the acceptance of the muon system, there is only one layer of muon chambers and a global muon system track is not formed. In this case, as long as the track in the inner detector exists and geometrically matches to a segment, a segment-tagged muon is formed using momentum measurements from the inner detector. In the region where the muon system has coverage but the inner detector does not,  $2.5 < |\eta| < 2.7$ , a stand-alone muon is formed which uses only information from the muon system. And for muons produced within one of the few holes in the muon system, including  $|\eta| < 0.1$ , the characteristic energy deposits in the calorimeter can be used to tag an inner detector track as a calo-tag muon. These additional categories are used to achieve high efficiency over a larger range of acceptance, but the combined muons are the most reliable.

### 6.3.1 MUON IDENTIFICATION

The various types of muons are incorporated into three working points: Loose, Medium, and Tight, which reflect the increasing muon purity for each of the selections definitions. Tight muons include only combined muons with a good track fit quality and momentum resolution and at least two hits in a precision muon system layer. Medium muons include those in tight as well as combined muons with one precision hit and one precision hole, where hole is defined in the same way as in Section 6.1. The medium working point also includes stand-alone muons with  $|\eta| > 2.5$  and at least two hits in precision layers. And finally the loose working point includes both medium and tight muons, but additional includes segment-tagged and calo-tagged muons in the region  $|\eta| < 0.1$ . The reconstruction efficiencies for muons with  $p_T > 20$  GeV range from 91.8% for tight muons and up to 98.1% for loose muons [39].

## 6.4 JETS

A jet does not directly correspond to a physical particle, unlike all of the reconstructed objects described above, but instead tries to capture the conical cascade of particles produced in the hadronization of a quark or gluon from the proton-proton collision. The hadronization process creates a very large number of collimated particles, with a high enough density that individually reconstructing all of the produced particles in the calorimeter is not possible within ATLAS. However most analyses are interested only in the kinematics of the particle which produced the cascade, rather than the individual products. Therefore, jets are a useful tool to measure the combined energy and direction of the ensemble of products and thus represents the kinematics of the original. Jet algorithms are

very generic and can be used to group together a number of types of objects to form aggregate representations. For example, truth particles in simulation can be grouped in truth jets, or tracks from the inner detector can be grouped together to form track jets. This section, however, will focus on calorimeter jets which take topoclusters of energy deposits in the calorimeter as inputs and produce a combined object which represents the energy measured by the calorimeter and the location where it was deposited.

#### 6.4.1 TOPOLOGICAL CLUSTERING

Hadrons often deposit their energy into multiple individual cells in both the electromagnetic and hadronic calorimeters. The purpose of topological clustering is to group cells in all three dimensions into clusters that represent a single energy deposit. The procedure must be robust enough to reject noise fluctuations in the cell energy measurements that can come from both electronic noise and additional low energy particles produced in pileup activity. The background level of calorimeter noise is called  $\sigma_{\text{noise}}$ , and is an important component of the topological clustering.

The topological clusters are formed in a three step process called the 4-2-0 threshold scheme, which uses three energy thresholds to build up a cluster from cells [40]. First, any cells with a measured energy above  $4\sigma_{\text{noise}}$  are identified as seed cells. The cells adjacent to the seed cells with a measured energy above  $2\sigma_{\text{noise}}$  are called secondary cells. All of the cells which are adjacent to a secondary cell with  $E_{\text{cell}} > 2\sigma_{\text{noise}}$  are also labeled secondary cells. Tertiary cells are those immediately adjacent to a seed or secondary cell with a measured energy above zero. Adjacency in this sense is defined in three dimensions, cells are adjacent if they are neighbors within a layer but also if they have the same  $\eta - \phi$  coordinates but are in adjacent layers or even in an adjacent layer in another calorimeter.

From these definitions, clusters are built by resolving the seeds in order of significance, the ratio  $E_{\text{cell}}/\sigma_{\text{noise}}$ . All adjacent secondary cells to the highest significance seed are added to that seed's topocluster, and any of those cells which would also have qualified as seeds are removed from the list of seeds. Once all of the secondary cells have been added, the tertiary cells are then added to that cluster as well. This procedure is then iterated until no seeds remain, forming the first round of topoclusters.

It is also useful to split topoclusters into multiples if local maxima are present within the topocluster, as clusters produced by multiple nearby particles can merge. The splitting process begins by finding local maxima cells in the middle layer of the calorimeters with a minimum energy of 500 MeV and at least four neighboring secondary cells. These requirements reduce the likelihood to split a cluster due to random fluctuations, as the middle layers provide the most reliable energy measurements. Cells between two local maxima can then be shared between two clusters to account for overlapping contributions from two particles. The energy sharing is weighted by the energy of each cluster as well as the distance of the cell to the centroid of that cluster.

The energies of all the cells in the cluster are then summed together to form the energy of that cluster. The energy needs to be corrected for the various losses expected in the calorimeter, as described in Section 5.4. The simplest correction, scaling the measured energy by the sampling fraction, brings the cluster energies to the EM scale. It is called the EM scale because it accurately describes the energy of electromagnetic showers.

Another scale is defined to improve accuracy for hadronic processes, the local cluster weighted (LCW) scale, that helps to correct for the expected variations in hadronic energy deposits. The LCW correction first determines if the shower is hadronic or electromagnetic, based on the depth of the shower and the cluster energy density. For hadronic showers, the energy is corrected for calorimeter non-compensation, an effect which reduces the measured energy of hadronic showers because some of the energy goes into invisible processes like the break up of nuclei. All clusters are then corrected for energy that may be deposited in uninstrumented regions in that cluster’s location in the calorimeter, and they are also corrected with an estimate of how much energy falls outside the extent of the cluster based on its shape and the deposit type.

#### 6.4.2 JET ALGORITHMS

Using the topological clusters as inputs, a jet algorithm groups them together into a collection of adjacent energy deposits that is intended to correspond to a single process [41]. Jet algorithms need a few key characteristics to be usable for physics analysis. First, the jets produced by the algorithm should have little dependence on the addition of soft particles to the event (infrared safety), as a negligible addition of energy should not significantly modify the event topology. The jets produced by the algorithm should also be collinear safe: a single quark replaced by two, parallel quarks with half the original’s momentum should not change the resulting jets. This requirement is important as the jets are intended to capture only the properties of the aggregate and not those of individual particles. And finally the algorithm needs to be sufficiently simple and fast to be used for the large rate of collected proton-proton collisions on ATLAS.

The most commonly used algorithm on ATLAS that satisfies these requirements is called the anti- $k_t$  algorithm [42]. The anti- $k_t$ , in brief, relies on iteratively combining the input objects that are closest together, where closest is defined by a particular distance metric,  $d_{i,j}$ , where the index  $i$  represents the combination constructed so far and  $j$  is an additional object being considered. The combinations stop when the closest remaining object is the beam itself, where the distance to the beam is called  $d_{i,B}$ . An entire class of algorithms follows this procedure with the following distance metrics

$$d_{i,j} = \min(k_{ti}^{2p}, k_{tj}^{2p}) \frac{\Delta_{ij}^2}{R^2} \quad (18)$$

$$d_{i,B} = k_{ti}^{2p} \quad (19)$$

where  $\Delta_{i,j} = (y_i - y_j)^2 + (\phi_i - \phi_j)^2$ ,  $k_{ti}$  is the transverse momentum of the object,  $y$  is the rapidity, and  $p$  is a parameter of the algorithm. Anti- $k_t$  is the particular case where  $p = -1$ , and is a choice that results in an algorithm that is both infrared and collinear safe.

The algorithm is repeated until there are no input objects remaining, which results in a series of jets. Each jet has a complete four momentum from the combination of its input clusters, where the combinations assume a mass of zero. The jet energies then need to be calibrated to attempt to match the energy of the object which produced the jet.

### 6.4.3 JET ENERGY SCALE

Though the [LCW](#) scheme attempts to correct the topoclusters to reflect the true deposited energy, the correction does not fully account for energy lost within the calorimeters. Because of these effects, the original reconstructed jet energy does not reflect the true energy of the particle which initiated the jet. Therefore it is necessary to additionally correct the reconstructed jet itself, in addition to the corrections on the inputs. This correction is referred to as the [JES](#), which combines several individual steps of calibration [43].

The first calibration step corrections the direction of the jet to ensure that it points back to the primary vertex. Next, the energy of the jet is corrected for pileup by subtracting the expected contribution from pileup based on the momentum,  $\eta$ , and area of the jet as well as the number of reconstructed vertices and the expected number of interactions per crossing,  $\mu$ . The largest single correction adjusts the jet energy and pseudorapidity to attempt to match the energy and pseudorapidity of the parton which produced it. This correction is measured in simulation by comparing the reconstructed jet energies to the energy of the truth particle which produced it. However the simulation is not relied on alone to estimate this correction, and an additional step applies an additional energy correction based on in-situ measurements in data. These corrections come from various techniques which measure jet energies indirectly by balancing them with other, well-measured objects. In the central region ( $|\eta| < 1.2$ ), jets are balanced against photons and the leptonic decays of Z bosons and high momentum jets ( $p_T > 210$  GeV) are also balanced against multiple smaller jets in multijet events. Jets at larger pseudorapidities, above  $|\eta| = 1.2$ , are calibrated by balancing with lower pseudorapidity jets.

These steps introduce a number of systematic uncertainties, referred to as the [JES](#) uncertainty. The largest of these comes from the in-situ measurements, which are statistically limited in measuring high momentum and high pseudorapidity jets. The total, fractional [JES](#) uncertainty is shown as a function of  $p_T$  in Figure 49. The uncertainty falls to a minimum value of just over 1.0% around a few hundred GeV, and rises again at high momentum because of the difficulty of measuring jet balance in data above 2-3 TeV. The uncertainty is also minimized at low  $|\eta|$ , and grows at large  $|\eta|$  again where making in-situ measurements is difficult. This technique does not actually provide a measurement of the uncertainty for the highest energy jets, above 3 TeV, because there are not enough

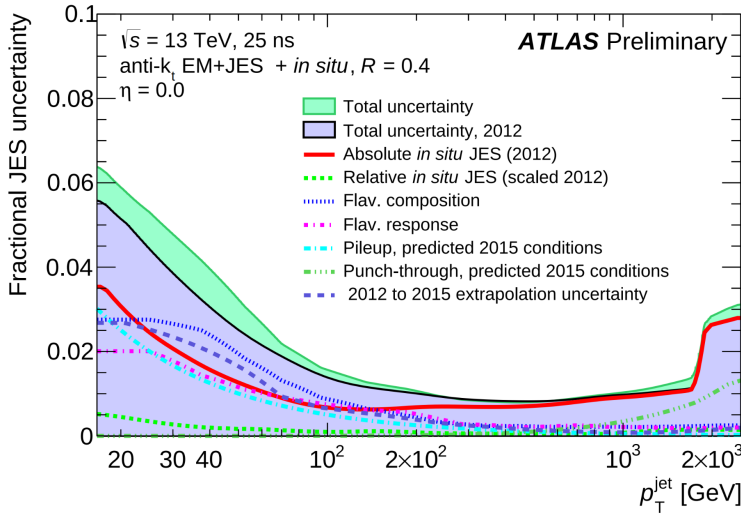


Figure 49: The total, fractional JES uncertainties estimated for 2015 data as a function of jet  $p_T$ .

measured data events to provide them. An alternative method for deriving the JES and JES uncertainty that can be used even for very high  $p_T$  jets will be discussed in Chapter 8.

## 6.5 MISSING TRANSVERSE ENERGY

Among stable SM particles, only the neutrino cannot be directly measured in the ATLAS detector. Because the neutrino carries neither electric nor color charge, it is very unlikely to interact with the tracking detectors or the calorimeters, and instead passes through the detector completely unobserved. Some particles which have been conjectured to exist, like the LSP in many SUSY models, would also have the same behavior. Therefore, it is important for ATLAS to provide some way to assess the momentum carried away by a neutral, colorless particle. This can be accomplished through a measurement of missing energy in the transverse direction, or  $E_T^{\text{miss}}$ , which quantifies the momentum imbalance of the observed particles. From the conservation of momentum and the lack of the initial momentum in the transverse plane in the proton-proton collisions, any imbalance of momentum can be inferred to be carried away by an unmeasured particle.

$E_T^{\text{miss}}$  is more precisely defined as the magnitude of the vector sum of the  $(p_x, p_y)$  components of each observed object's momentum. The definition is simple, but there can be significant complexity in defining the inputs. As of Run 2, ATLAS uses a common algorithmic approach to carefully calculate missing energy, but each analysis is free to define its own inputs. For the analysis discussed throughout this thesis, the missing energy inputs consist of the electrons, photons, muons, and jets discussed in the previous sections, in addition to a track-based term that accounts for the contribution of low  $p_T$  particles (soft term).

To produce the most precise measurement of  $E_T^{\text{miss}}$ , it is important to use the best representation of the momentum of each of the input objects, which can often be reconstructed as multiple different types in a single event. For example, an electron can be reconstructed separately as an electron (Section 6.2) and a jet (Section 6.4), but the electron representation has the highest precision for reconstructing the true electron momentum. To ensure no duplications in the  $E_T^{\text{miss}}$  definition, the inputs are collectively considered for overlap removal. Only the most precise object type is kept for objects that fall within a cone of  $\Delta R < 0.2$  for pairs of electrons and jets and a cone of  $\Delta R < 0.4$  for other pair types.

The fully reconstructed objects do not include all of the energy within the events, as some clusters do not enter into a jet and some tracks are not classified as electrons or muons. These momentum carried by these objects is accounted for in a soft-term, which tallies all of the energy carried by the particles too soft to form separate objects. The track soft term uses only tracking information to estimate the contribution of soft objects, and does so by vectorially summing the momentum of all well-reconstructed tracks with momentum above 400 MeV that are not associated to other objects.

All of these contributions together give a single  $E_T^{\text{miss}}$  value for a given event. The direction of that missing energy is taken as opposite the vector sum of all the constituents, to correspond to the momentum an invisible particle would have to have to make the event balanced. Depending on the context, this missing energy can be considered the energy of a neutrino or an LSP, with a large missing energy being a common signal criteria for searches for new physics.

PART III  
CALORIMETER RESPONSE

## RESPONSE MEASUREMENT WITH SINGLE HADRONS

---

As discussed in Section 6.4, colored particles produced in collisions hadronize into jets of multiple hadrons. One approach to understanding jet energy measurements in the ATLAS calorimeters is to evaluate the calorimeter response to those individual hadrons; measurements of individual hadrons can be used to build up an understanding of the jets that they form. The redundancy of the momentum provided by the tracking system and the energy provided by the calorimeter provides an opportunity to study calorimeter response using real collisions, as described further in Section 7.2.

Calorimeter response includes a number of physical effects that can be extracted to provide insight into many aspects of jet modeling. First, many charged hadrons interact with the material of the detector prior to reaching the calorimeters and thus do not deposit any energy. Comparing this effect in data and simulation is a powerful tool in validating the interactions of particles with the material of the detector and the model of the detector geometry in simulation, see Section 7.2.2. The particles which do reach the calorimeter deposit their energy into several adjacent cells, which are then clustered together. The energy of the cluster is then the total energy deposited by that particle. Comparing the response of hadrons in data to that of simulated hadrons provides a direct evaluation of the showering of hadronic particles and the energy deposited by particles in matter (Section 7.2.4).

The above studies all use an inclusive selection of charged particles, which are comprised predominantly of pions, kaons, and (anti)protons. It is also possible to measure the response to various identified particle types separately to evaluate the simulated interactions of each particle, particularly at low energies where differences between species are very relevant. Pions and (anti)protons can be identified through decays of long-lived particles, in particular  $\Lambda$ ,  $\bar{\Lambda}$ , and  $K_S^0$ , and then used to measure response as described above. This is discussed in detail in Section 7.3.

The results in this chapter use data collected at 7 and 8 TeV collected in 2010 and 2012, respectively. Both are included as the calorimeter was repaired and recalibrated between those two data-taking periods. Both sets of data are compared to an updated simulation that includes new physics models provided by Geant4 [7] and improvements in the detector description [44, 45]. The present results are published in European Physical Journal C (EPJC) [46] and can be compared to a similar measurement performed in 2009 and 2010 [47], which used the previous version of the simulation framework [48].

## 7.1 DATASET AND SIMULATION

### 7.1.1 DATA SAMPLES

The two datasets used in this chapter are taken from dedicated low-pileup runs where the fraction of events with multiple interactions was negligible. These datasets are used rather than those containing full-pileup events to facilitate measurement of isolated hadrons. The 2012 dataset at  $\sqrt{s} = 8$  TeV contains 8 million events and corresponds to an integrated luminosity of  $0.1 \text{ nb}^{-1}$ . The 2010 dataset at  $\sqrt{s} = 7$  TeV contains 3 million events and corresponds to an integrated luminosity of  $3.2 \text{ nb}^{-1}$ . The latter dataset was also used for the 2010 results [47], but it has since been reanalyzed with an updated reconstruction including the final, best understanding of the detector description for the material and alignment from Run 1.

### 7.1.2 SIMULATED SAMPLES

The two datasets above are compared to simulated single-, double-, and non-diffractive events generated with Pythia8 [49] using the A2 configuration of hadronization [50] and the MSTW 2008 parton-distribution function set [51, 52]. The admixture of the single-, double-, and non-diffractive events uses the default relative contributions from Pythia8. The conditions and energies for the two simulations are chosen so that they match those of the corresponding dataset.

To evaluate the interaction of hadrons with detector material, the simulation uses two different collections of hadronic physics models, called physics lists, in Geant4 9.4 [53]. The first, QGSP\_BERT, combines the Bertini intra-nuclear cascade [54–56] below 9.9 GeV, a parametrized proton inelastic model from 9.5 to 25 GeV [57], and a quark-gluon string model above 12 GeV [58–62]. The second, FTFP\_BERT, combines the Bertini intra-nuclear cascade [54–56] below 5 GeV and the Fritiof model [63–66] above 4 GeV. In either list, Geant4 enforces a smooth transition between models where multiple models overlap.

### 7.1.3 EVENT SELECTION

The event selection for this study is minimal, as the only requirement is selecting good-quality events with an isolated track. Such events are triggered by requiring at least two hits in the minimum-bias trigger scintillators. After trigger, each event is required to have exactly one reconstructed vertex, and that vertex is required to have four or more associated tracks.

The particles which are selected for the response measurements are first identified as tracks in the inner detector. The tracks are required to have at least 500 MeV of transverse momentum. To ensure a reliable momentum measurement, these tracks are required to have at least one hit in the pixel detector, six hits in the SCT, and small longitudinal and transverse impact parameters with respect to the primary vertex [47]. For the majority of the measurements in this chapter,

the track is additionally required to have 20 hits in the TRT, which significantly reduces the contribution from tracks which undergo nuclear interactions. This requirement and its effect is discussed in more detail in Section 7.2.5. In addition, tracks are rejected if there is any other reconstructed track which extrapolates to the calorimeter within a cone of  $\Delta R = \sqrt{(\Delta\phi)^2 + (\Delta\eta)^2} < 0.4$ . This requirement guarantees that the contamination of energy from nearby charged particles is negligible [47].

## 7.2 INCLUSIVE HADRON RESPONSE

The calorimeter response is more precisely defined as the ratio of the measured calorimeter energy to the true energy carried by the particle, although this true energy is unknown. For charged particles, however, the inner detector provides a very precise measurement of momentum (with uncertainty less than 1%) that can be used as a proxy for true energy. The ratio of the energy deposited by the charged particle in the calorimeter,  $E$ , to its momentum measured in the inner detector  $p$ , forms the calorimeter response measure called  $E/p$ . Though the distribution of  $E/p$  contains a number of physical features, this study focuses on the trends in two aggregated quantities:  $\langle E/p \rangle$ , the average of  $E/p$  for the selected tracks, and the zero fraction, the fraction of tracks with no associated energy in the calorimeter for those tracks.

The calorimeter energy assigned to a track is defined using clusters. The clusters are formed using a 4–2–0 algorithm [67] that begins with seeds requiring at least 4 times the average calorimeter cell noise. The neighboring cells with at least twice that noise threshold are then added to the cluster, and all bounding cells are then added with no requirement. This algorithm minimizes noise contributions through its seeding process, and including the bounding cells improves the energy resolution [68]. The clusters are associated to a given track if they fall within a cone of  $\Delta R = 0.2$  of the extrapolated position of the track, which includes about 90% of the energy on average [47].

### 7.2.1 E/P DISTRIBUTION

The  $E/p$  distributions measured in both data and simulation are shown in Figure 50 for two example bins of track momentum and for tracks in the central region of the detector. These distributions show several important features of the  $E/p$  observable. The large content in the bin at  $E = 0$  comes from tracks that have no associated cluster, which occurs due to interactions with detector material prior to reaching the calorimeter or the energy deposit being insufficiently large to generate a seed, and are discussed in Section 7.2.2. The small negative tail also comes from tracks that do not deposit any energy in the calorimeter but are randomly associated to a cluster with an energy below the noise threshold. The long positive tail above 1.0 comes from the contribution of neutral particles. Nearby neutral particles deposit (sometimes large) additional energy in the calorimeter but do not produce tracks in the inner detector, so they cannot be rejected by the track isolation requirement. Additionally the peak and mean of

the distribution falls below 1.0 because of the loss of energy not found within the cone as well as the non-compensation of the calorimeter.

The data and simulation share the same features, but the high and low tails are significantly different. The simulated events tend to overestimate the contribution of neutral particles to the long tail, an effect which can be isolated and removed as discussed in Section 7.2.3. Additionally, the simulated clusters have less noise on average, although this is a small effect on the overall response.

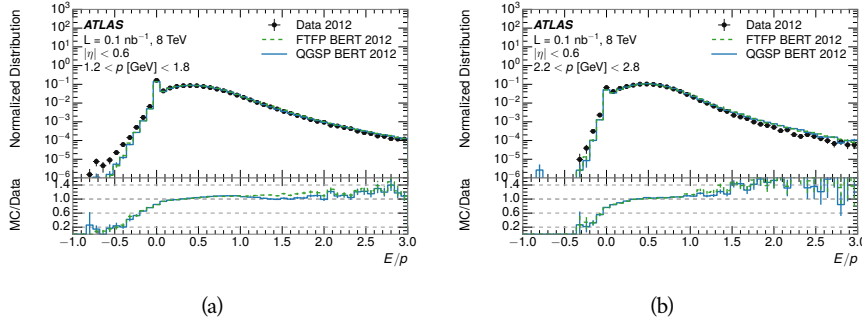


Figure 50: The  $E/p$  distribution and ratio of simulation to data for isolated tracks with (a)  $|\eta| < 0.6$  and  $1.2 < p/\text{GeV} < 1.8$  and (b)  $|\eta| < 0.6$  and  $2.2 < p/\text{GeV} < 2.8$ .

## 7.2.2 ZERO FRACTION

The fraction of particles with no associated clusters, or similarly those with  $E \leq 0$ , reflects the modeling of both the detector geometry and hadronic interactions. The zero fraction is expected to rise as the amount of material a particle traverses increases, while it is expected to decrease as the particle energy increases. This dependence can be seen in Figure 51, where the zero fraction in data and simulation is shown as a function of momentum and the amount of material measured in interaction lengths. The trends are similar between 2010 and 2012 and for positively and negatively charged particles. The zero fraction decreases with energy as expected. The absolute discrepancy in zero fraction between data and simulation decreases with momentum from 5% to less than 1%, but this becomes more pronounced in the ratio as the zero fraction shrinks quickly with increasing momentum. The amount of material in the detector increases with  $\eta$ , which is used to obtain results for interaction lengths ranging between 0.1 and 0.65  $\lambda$ . As the data and simulation have significant disagreement in the zero fraction over a number of interaction lengths, the difference must be primarily from the modeling of hadronic interactions with detector material and not just the detector geometry. Although two different hadronic interaction models are shown in the figure, they have very similar discrepancies to data because both use the same description (the BERT model) at low momentum.

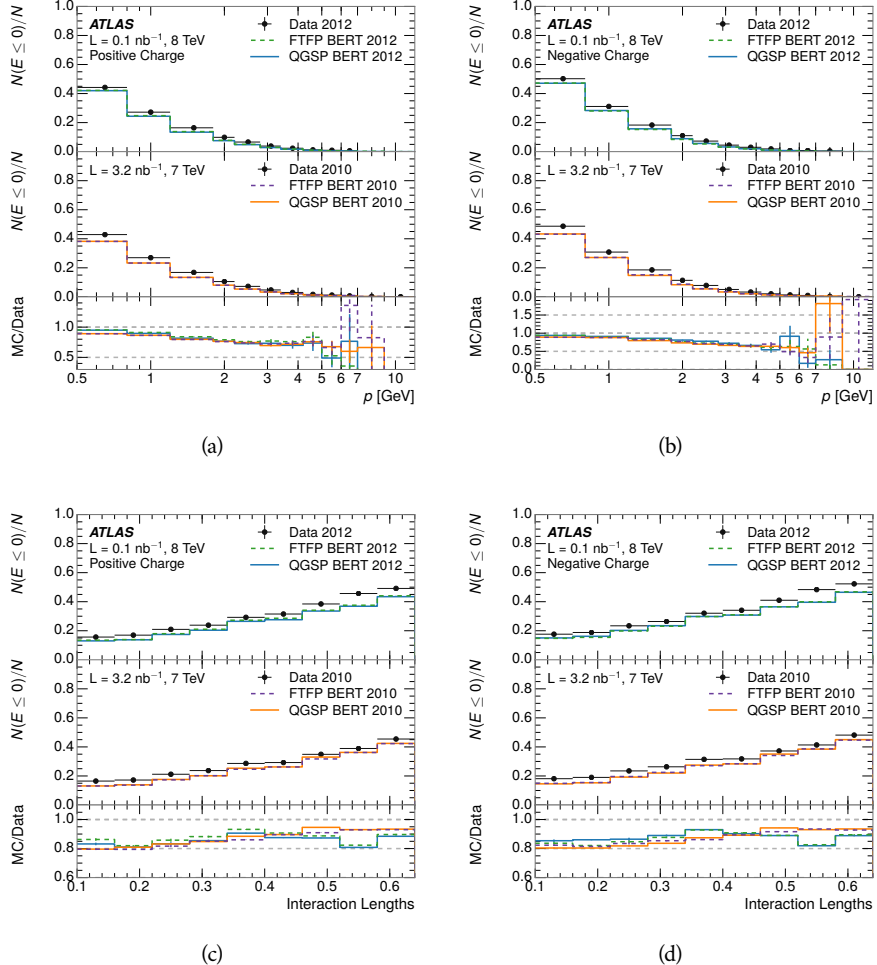


Figure 51: The fraction of tracks as a function (a, b) of momentum, (c, d) of interaction lengths with  $E \leq 0$  for tracks with positive (on the left) and negative (on the right) charge.

## 7.2.3 NEUTRAL BACKGROUND SUBTRACTION

The isolation requirement on hadrons is only effective in removing an energy contribution from nearby charged particles. Nearby neutral particles, predominantly photons from  $\pi^0$  decays, also add their energy to the calorimeter clusters, but mostly in the electromagnetic calorimeter. The arrangement of energy deposits is shown in Figure 52, which illustrates both energy deposits from the hadronic particle and additional deposits from neutral particles. It is possible to measure this contribution, on average, using late-showering hadrons that minimally ionize in the electromagnetic calorimeter. Such particles are selected by requiring that they deposit less than 1.1 GeV in the EM calorimeter within a cone of  $\Delta R < 0.1$  around the track. To ensure that these particles are well measured, they are additionally required to deposit between 40% and 90% of their energy in the hadronic calorimeter within a cone of  $\Delta R < 0.1$ .

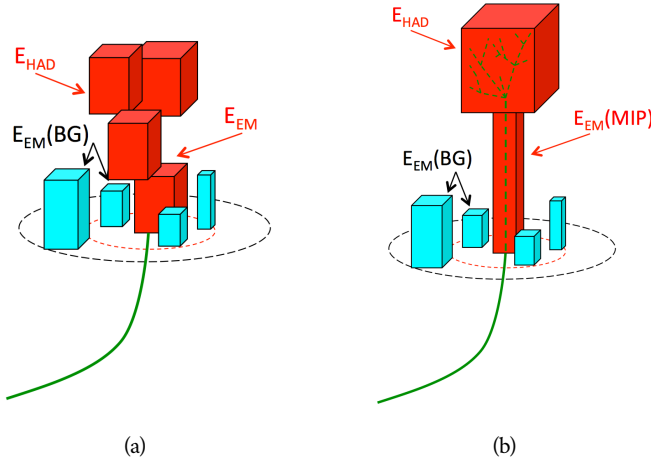


Figure 52: An illustration (a) of the geometry of energy deposits in the calorimeter. The red energy deposits come from the charged particle targeted for measurement, while the blue energy deposits are from nearby neutral particles and must be subtracted. The same diagram (b) for the neutral-background selection, described in Section 7.2.3.

These particles provide a clean sample to measure the nearby neutral background because they do not deposit energy in the area immediately surrounding them in the EM calorimeter, as shown in Figure 52. So, the energy deposits in the region  $0.1 < \Delta R < 0.2$  can be attributed to neutral particles alone. To estimate the contribution to the whole cone considered for the response measurement, that energy is scaled by a geometric factor of  $4/3$ . This quantity,  $\langle E/p \rangle_{BG}$ , measured in aggregate over a number of particles, gives the contribution to  $\langle E/p \rangle$  from neutral particles in the EM calorimeter. Similar techniques were used in the individual layers of the hadronic calorimeters to show that the background from neutrals is negligible in those layers [47].

The distribution of this background estimate is shown in Figure 53 for data and simulation with the two different physics lists. The contribution from neu-

tral particles falls from 0.1 at low momentum to around 0.03 for particles above 7 GeV. Although the simulation captures the overall trend, it significantly overestimates the neutral contribution for tracks with momentum between 2 and 8 GeV. This effect was also seen in the tails of the  $E/p$  distributions in Figure 50. This difference is likely due to modeling of coherent neutral particle radiation in Pythia8 that overestimates the production of  $\pi^0$  near the production of the charged particles. The discrepancy does not depend on  $\eta$  and thus is unlikely to be a mismodeling of the detector. This difference can be subtracted to form a corrected average of  $E/p$ .

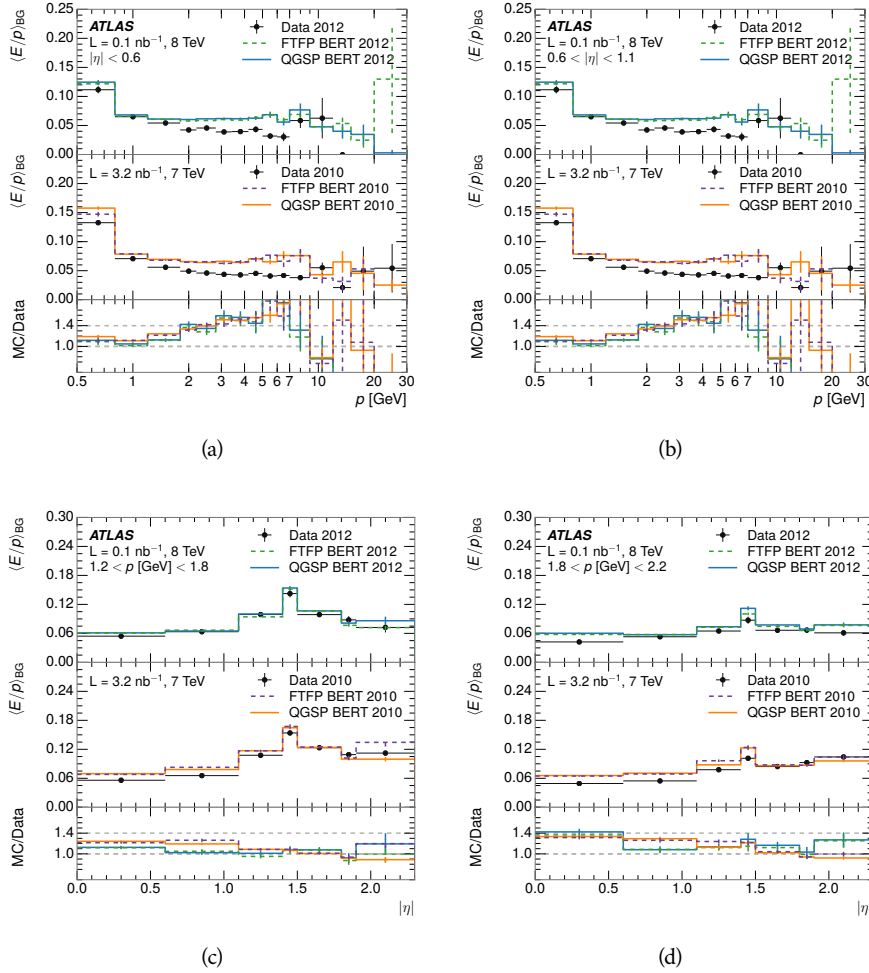


Figure 53:  $\langle E/p \rangle_{\text{BG}}$  as a function of the track momentum for tracks with (a)  $|\eta| < 0.6$ , (b)  $0.6 < |\eta| < 1.1$ , and as a function of the track pseudorapidity for tracks with (c)  $1.2 < p/\text{GeV} < 1.8$ , (d)  $1.8 < p/\text{GeV} < 2.2$ .

#### 7.2.4 CORRECTED RESPONSE

Figure 54 shows  $\langle E/p \rangle_{\text{COR}}$  as a function of momentum for several bins of pseudorapidity. This corrected  $\langle E/p \rangle_{\text{COR}} \equiv \langle E/p \rangle - \langle E/p \rangle_{\text{BG}}$  measures the average calorimeter response without the contamination of neutral particles. It is the

most direct measurement of calorimeter response in that it is the energy measured for fully isolated hadrons. The correction is performed separately in data and simulation, so that the mismodeling of the neutral background in simulation is removed from the comparison of response. The simulation overestimates the response at low momentum by about 5%, an effect that can be mostly attributed to the underestimation of the zero fraction mentioned previously. For  $|\eta| < 0.6$ , the data-simulation agreement has a larger discrepancy by about 5% for 2010 than 2012, although this is not reproduced in at higher pseudorapidity.

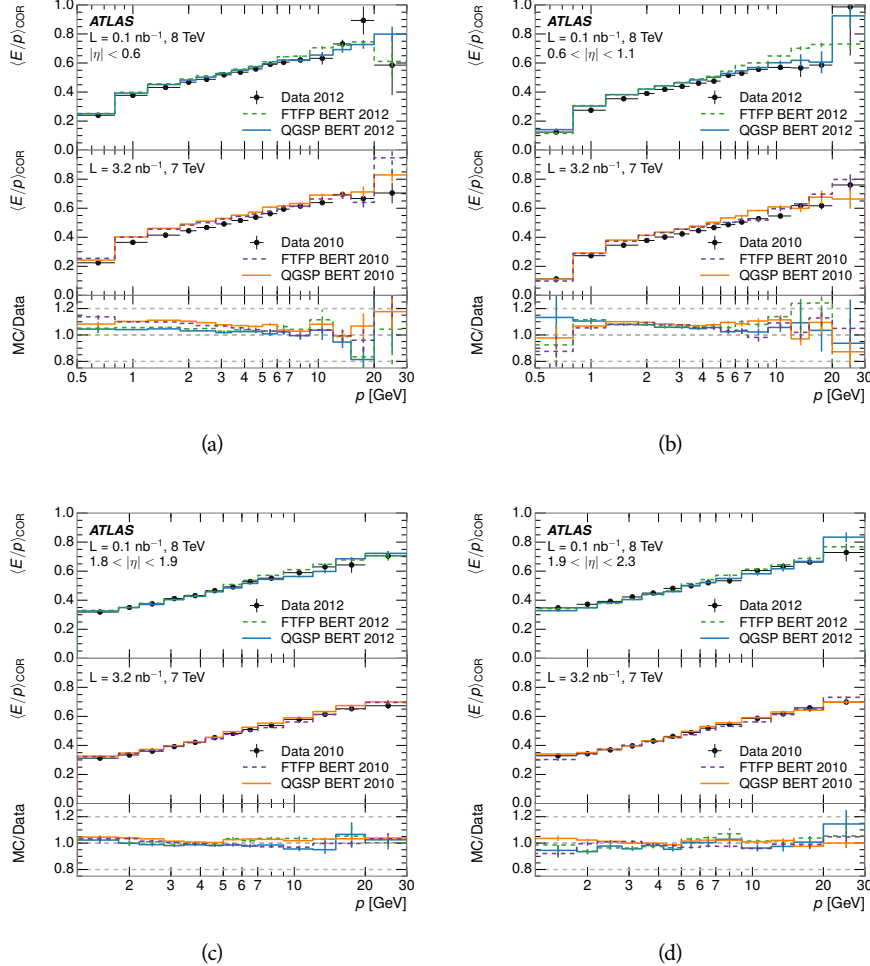


Figure 54:  $\langle E/p \rangle_{\text{COR}}$  as a function of track momentum, for tracks with (a)  $|\eta| < 0.6$ , (b)  $0.6 < |\eta| < 1.1$ , (c)  $1.8 < |\eta| < 1.9$ , and (d)  $1.9 < |\eta| < 2.3$ .

The response measurement above used topological clustering at the EM scale, that is clusters were formed to measure energy but no corrections were applied to correct for expected effects like energy lost outside of the cluster or in uninstrumented material. It is also interesting to measure  $\langle E/p \rangle_{\text{COR}}$  using LCW energies, which accounts for those effects by calibrating the energy based on the properties of the cluster such as energy density and depth in the calorimeter. Figure 55 shows these distributions for tracks with zero or more clusters and separately for tracks with one or more clusters. The calibration moves the mean

value of  $\langle E/p \rangle_{\text{COR}}$  significantly closer to 1.0 as desired, but the discrepancy between data and simulation remains in the comparison that includes tracks with zero associated clusters. The agreement between data and simulation improves noticeably when at least one cluster is required, as this removes the contribution from the mismodeling of the zero fraction.

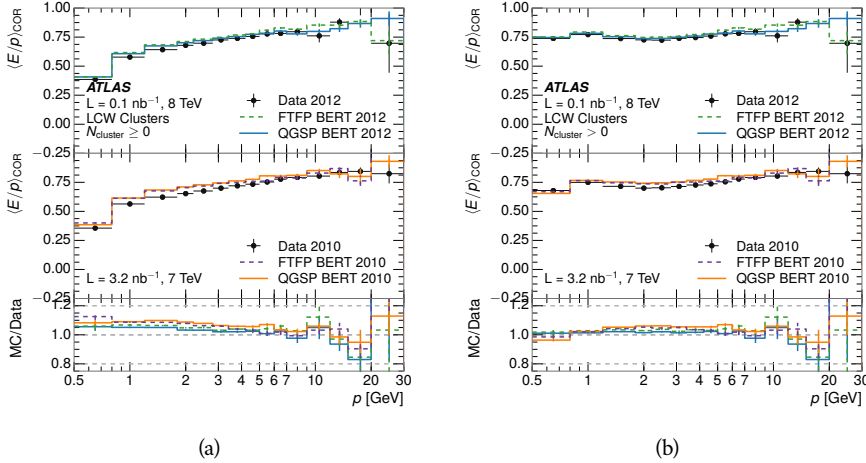


Figure 55:  $\langle E/p \rangle_{\text{COR}}$  calculated using LCW-calibrated topological clusters as a function of track momentum for tracks with (a) zero or more associated topological clusters or (b) one or more associated topological clusters.

### 7.2.5 ADDITIONAL STUDIES

As has been seen in several measurements in previous sections, the simulation does not correctly model the chance of a low momentum hadron to reach the calorimeter. Because of the consistent discrepancy across pseudorapidity and interaction lengths, this can be best explained by incomplete understanding of hadronic interactions with the detector [46]. For example, a hadron that scatters off of a nucleus in the inner detector can be deflected through a significant angle and not reach the expected location in the calorimeter. In addition, these interactions can produce secondary particles that are difficult to model.

The requirement used throughout the previous sections on the number of hits in the `TRT` reduces these effects by preferentially selecting tracks that do not undergo nuclear interactions. It is interesting to check how well the simulation models tracks with low numbers of `TRT` hits, which selects tracks that are more likely to have undergone a hadronic interaction. Figure 56 compares the distributions with  $N_{\text{TRT}} < 20$  to  $N_{\text{TRT}} > 20$  for real and simulated particles<sup>1</sup>. As expected, the tracks with fewer hits are poorly modeled in the simulation as  $\langle E/p \rangle_{\text{COR}}$  differs by as much as 25% at low momentum. They also have significantly lower  $\langle E/p \rangle_{\text{COR}}$  on average, because they are much less likely to have an associated cluster.

<sup>1</sup> The distribution with  $N_{\text{TRT}} > 20$  is the same as shown in Figure 54 (a) and is included again here for the comparison.

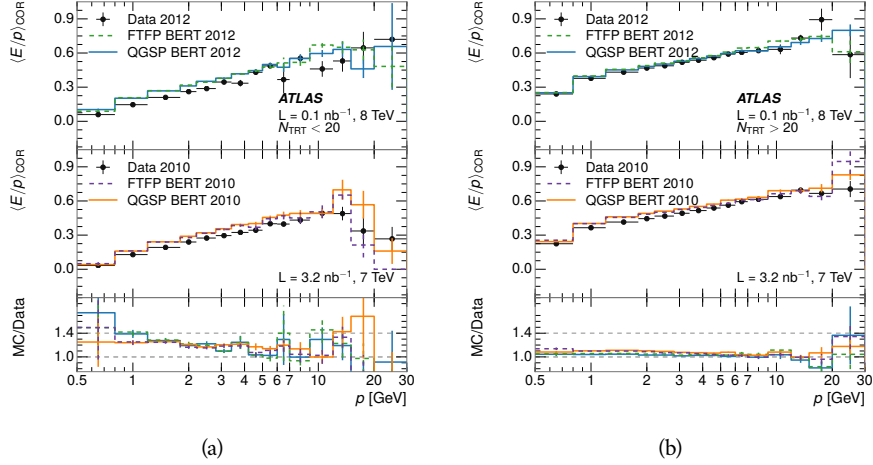


Figure 56: Comparison of the  $\langle E/p \rangle_{\text{COR}}$  for tracks with (a) less than and (b) greater than 20 hits in the TRT.

Another interesting aspect of the simulation is the description of antiprotons at low momentum, where QGSP\_BERT and FTFP\_BERT have significant differences. This can be seen to have an effect in the inclusive response measurement when separated into positive and negative charge. The  $\langle E/p \rangle_{\text{COR}}$  distributions for positive and negative particles are shown in Figure 57, where a small difference between QGSP\_BERT and FTFP\_BERT can be seen in the distribution for negative tracks. The figure also includes data, and the simulation overestimates  $\langle E/p \rangle_{\text{COR}}$  mostly due to an underestimation in zero fraction. There is an approximately 5% difference between the 2010 and 2012 simulated events. The difference between positive and negative particles is demonstrated more clearly in Figure 58, which shows the  $E/p$  distribution in the two simulations separated by charge. There is a small difference around  $E/p > 1.0$ , which can be explained by the additional energy deposited by the annihilation of the antiproton in the calorimeter that is modeled well only in FTFP\_BERT. This is also explored with data using identified antiprotons in Section 7.3.

The  $\langle E/p \rangle$  results in previous sections have considered the electromagnetic and hadronic calorimeters together as a single energy measurement, to emphasize the total energy deposited for a given particle. However, the deposits in each calorimeter are measured separately and  $\langle E/p \rangle$  can be constructed for each layer separately. As the layers are composed of different materials and are modeled separately in the detector geometry, confirmation that the simulation matches the data well in each layer adds confidence in both the description of hadronic interactions with the two different materials and also the geometric description of each.

The technique discussed in Section 7.2.3 for selecting MIPs in the electromagnetic calorimeter is also useful in studying deposits in the hadronic calorimeter. The tracks selected with the MIP requirements deposit almost all of their energy exclusively in the hadronic calorimeter. Figure 59 shows  $\langle E/p \rangle_{\text{Had}}^{\text{RAW}}$ , where RAW indicates that no correction has been applied for neutral backgrounds and

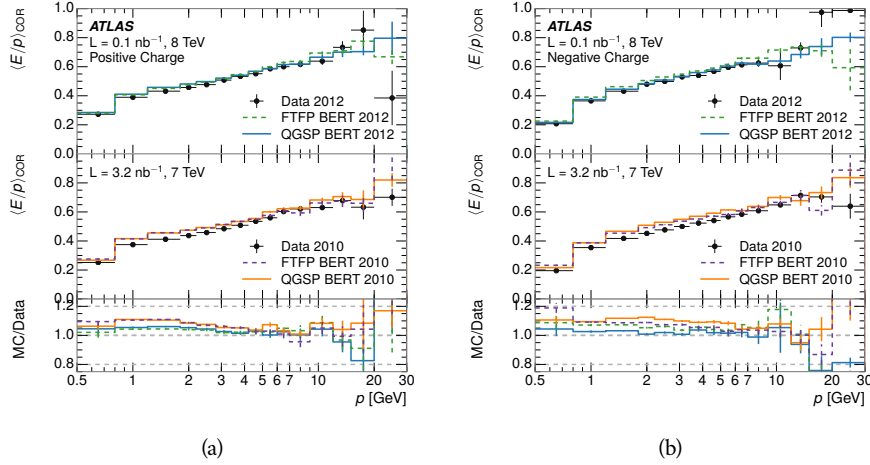


Figure 57: Comparison of the  $\langle E/p \rangle_{\text{COR}}$  for (a) positive and (b) negative tracks as a function of track momentum for tracks with  $|\eta| < 0.6$ .

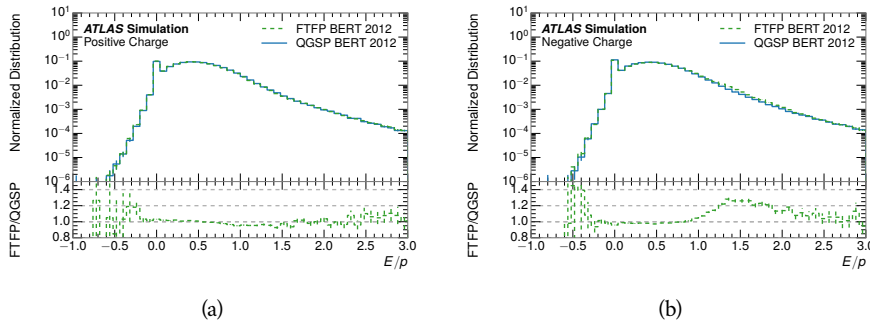


Figure 58: Comparison of the  $E/p$  distributions for (a) positive and (b) negative tracks with  $0.8 < p/\text{GeV} < 1.2$  and  $|\eta| < 0.6$ , in simulation with the FTFP\_BERT and QGSP\_BERT physics lists.

Had indicates that only clusters for the hadronic calorimeter are included<sup>2</sup>. The distributions are shown both for the original EM scale calibration and after LCW calibration. The data and simulation agree very well in this comparison, except in the lowest momentum bin where there is a 5% discrepancy that has already been seen in the measurements in Section 7.2.4.

A similar comparison can be made in the electromagnetic calorimeter by selecting particles which have no associated energy in the hadronic calorimeter. These results are measured in terms of  $\langle E/p \rangle_{\text{COR}}^{\text{EM}}$ , where EM designates that only clusters in the electromagnetic calorimeter are included and COR designates that the neutral background is subtracted as the neutral background is present in this case. Figure 60 shows the analogous comparisons to Figure 59 in the electromagnetic calorimeter. The  $\langle E/p \rangle_{\text{COR}}$  values are lower on average in the EM calorimeter than in the hadronic calorimeter, which is an expected conse-

<sup>2</sup> The RAW and COR versions of  $\langle E/p \rangle$  in this case are the same, as the neutral background is negligible in that calorimeter layer.

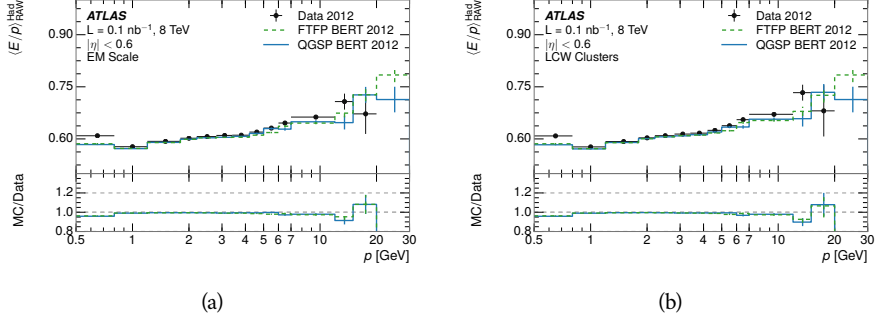


Figure 59: Comparison of the response of the hadronic calorimeter as a function of track momentum (a) at the EM-scale and (b) after the LCW calibration.

quence of their different material types (discussed in Section 5.4). In this case the disagreement between data and simulation is more pronounced, with discrepancies as high as 5% over a larger range of momenta. This level of discrepancy indicates that the description of the electromagnetic calorimeter is actually the dominant source of discrepancy in the combined distributions in Section 7.2.4.

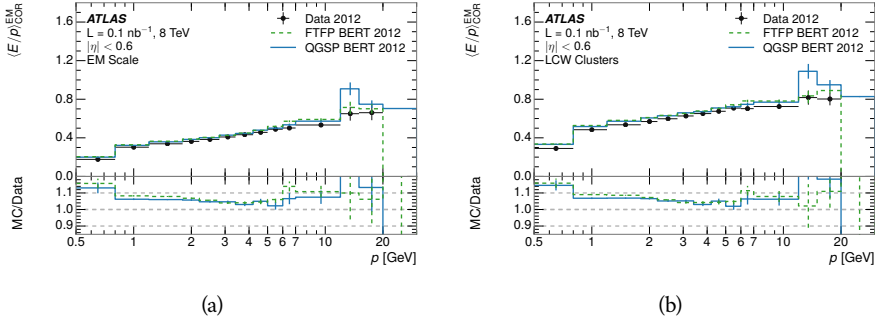


Figure 60: Comparison of the response of the EM calorimeter as a function of track momentum (a) at the EM-scale and (b) with the LCW calibration.

### 7.3 IDENTIFIED PARTICLE RESPONSE

The inclusive response measurement for hadrons can be augmented by measuring the response for specific particle species. The simulation models each particle type separately, and understanding the properties of each is important in constraining the uncertainty on jets. In order to select and measure specific hadrons, this section relies on the displaced decays of long-lived particles. Such decays can be identified by reconstructing secondary vertices with a requirement on mass. In particular,  $\Lambda$ ,  $\bar{\Lambda}$ , and  $K_S^0$  can be used to select a pure sample of protons, antiprotons, and pions, respectively.

## 7.3.1 DECAY RECONSTRUCTION

The measurement of the response for identified particles uses the same selection as for inclusive particles (Section 7.1.3) with a few additions. Each event used is required to have at least one secondary vertex, as described in Section 6.1.3, and the tracks are required to match to that vertex rather than the primary vertex. Pions are selected from decays of  $K_S^0 \rightarrow \pi^+ \pi^-$ , which is the dominant decay for  $K_S^0$  to charged particles. Protons are selected from decays of  $\Lambda \rightarrow \pi^- p$  and antiprotons from  $\bar{\Lambda} \rightarrow \pi^+ \bar{p}$ , which are similarly the dominant decays of  $\Lambda$  and  $\bar{\Lambda}$  to charged particles. The species of parent hadron in these decays is determined by reconstructing the mass of the tracks associated to the secondary vertex. The sign of the higher momentum decay particle can distinguish between  $\Lambda$  and  $\bar{\Lambda}$ , which of course have the same mass, as the proton or antiproton is kinematically favored to have higher momentum. The proton or antiproton will carry the higher momentum above 95% of the time. Examples of the reconstructed masses used to select these decays are shown in Figure 61. The mass peaks in data and both simulation models are very similar.

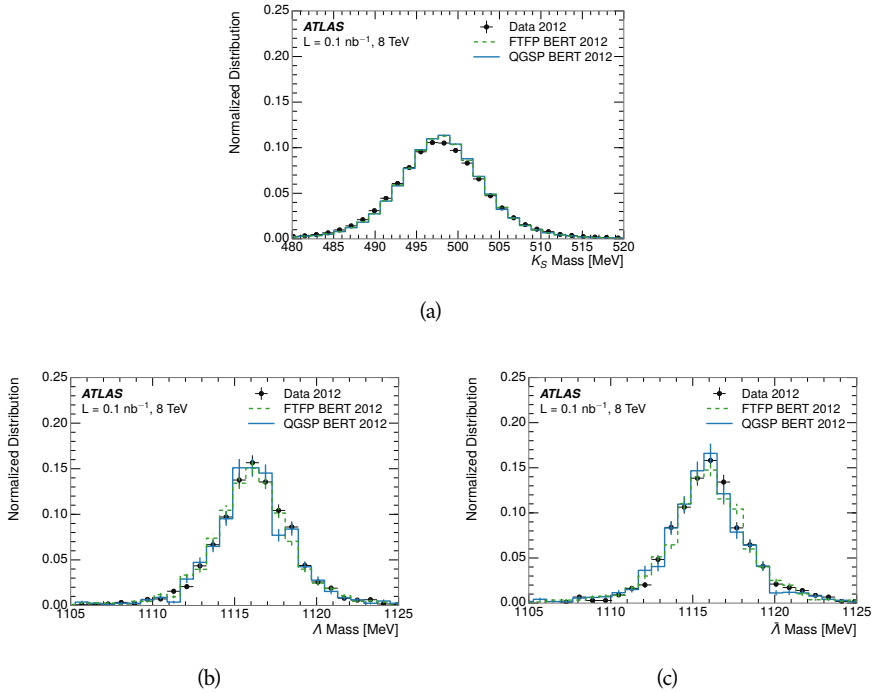


Figure 61: The reconstructed mass peaks of (a)  $K_S^0$ , (b)  $\Lambda$ , and (c)  $\bar{\Lambda}$  candidates.

The dominant backgrounds for the identified particle decays are nuclear interactions and combinatoric sources. These are suppressed by the kinematic requirements on the tracks as well as an additional veto which removes candidates that are consistent with both a  $\Lambda$  or  $\bar{\Lambda}$  and a  $K_S^0$  hypothesis, which is possible because of the different assumptions on particle mass in each case [47]. After these requirements, the backgrounds are found to be negligible compared to the statistical errors on these measurements.

## 7.3.2 IDENTIFIED RESPONSE

With these techniques the  $E/p$  distributions are extracted in data and simulation for each particle species and shown in Figure 62. These distributions are shown for a particular bin of  $E_a$  ( $2.2 < E_a/\text{GeV} < 2.8$ ), rather than  $p$ .  $E_a$  is the energy available to be deposited in the calorimeter: for pions  $E_a = \sqrt{p^2 + m_\pi^2}$ , for protons  $E_a = \sqrt{p^2 + m_p^2} - m_p$ , and for antiprotons  $E_a = \sqrt{p^2 + m_p^2} + m_p$ . In the pion case, the entire energy of the pion is deposited in the calorimeter, so  $E_a$  is just the usual energy. For protons, the proton remains after depositing its energy in the calorimeter, so its mass is not available and must be subtracted from  $E_a$ . And for antiprotons, the antiproton constituents annihilate with the quarks in the protons and neutrons of the calorimeter material, so it deposits its entire energy as well as an the additional energy from the annihilation; this extra energy is equal to the mass of the antiproton and is added to the available energy. The features of the  $E/p$  distributions are similar to the inclusive case, with a peak around 0.5 at low momentum. The zero fraction is not as pronounced as in the inclusive case. There is a small negative tail from noise and a large fraction of tracks with zero energy from particles which do not reach the calorimeter. The long positive tail is noticeably more pronounced for antiprotons because of the additional energy generated by the annihilation of the antiproton with the material of the detector, and the peak of the distribution is also increased for the same reason. The simulation correctly captures these features, and the agreement between data and simulation is good to within the available statistical limitations.

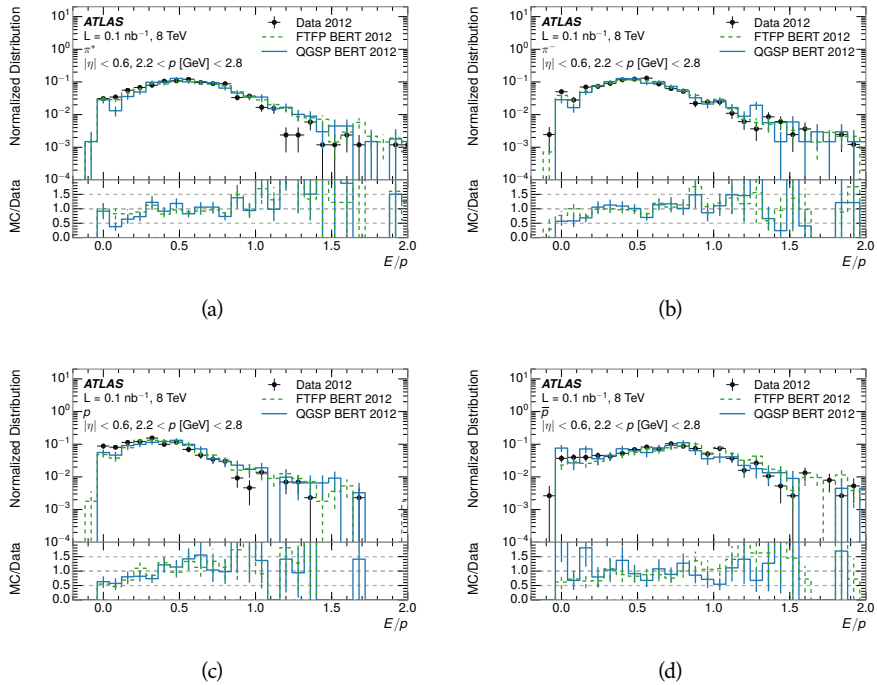


Figure 62: The  $E/p$  distribution for isolated (a)  $\pi^+$ , (b)  $\pi^-$ , (c) proton, and (d) anti-proton tracks.

The zero fraction is further explored in Figure 63 for pions and protons in data and simulation. The simulation consistently underestimates the zero fraction independent of particle species, which implies that this discrepancy is not caused by the model of a particular species but rather a feature common to all. The zero fraction is larger for  $\pi^-$  than  $\pi^+$ , which is evident in both data and simulation. However there is some suggestion that this increase in zero fraction leads to an even larger discrepancy in the modeling of  $\pi^-$  in simulation.

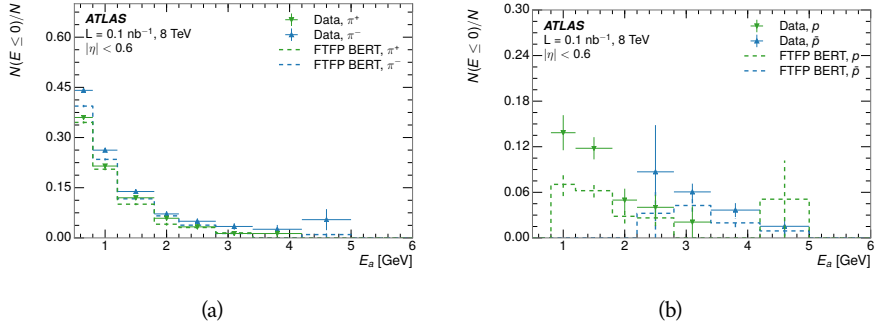


Figure 63: The fraction of tracks with  $E \leq 0$  for identified (a)  $\pi^+$  and  $\pi^-$ , and (b) proton and anti-proton tracks

It is also interesting to compare the response between the different particle species. One approach to do this is to measure the difference in  $\langle E/p \rangle$  between two types, which has the advantage of removing the neutral background. These differences are shown in various combinations in Figure 64. The response for  $\pi^+$  is greater on average than the response to  $\pi^-$  because of a charge-exchange effect which causes the production of additional neutral pions in the showers of  $\pi^+$  [69]. This effect becomes less significant as the  $\langle E/p \rangle$  increases, and the difference approaches zero. Both version of the simulation correctly model this trend. The response for  $\pi^+$  is also greater on average than the response to  $p$ , because a large fraction of the energy of  $\pi^+$  hadrons is converted to an electromagnetic shower [70, 71]. This effect is again reproduced by both simulations. The  $\bar{p}$  response, however, is significantly higher than the response to  $\pi^-$  because of the annihilation of the antiproton, but the difference decreases at higher energies where the additional energy has less relative importance. FTFP\_BERT models this effect more accurately than QGSP\_BERT because of their different descriptions of  $\bar{p}$  interactions with material.

It is also possible to remove the neutral background from these response distributions using the same technique as in Section 7.2.3. The technique is largely independent of the particle species and so can be directly applied to  $\langle E/p \rangle$  for pions. The  $\langle E/p \rangle_{\text{COR}}$  distributions for pions are shown in Figure 65, which are very similar to the inclusive results. The inclusive hadrons are comprised mostly of pions, so this similarity is not surprising. It is also possible to see the small differences between  $\pi^+$  and  $\pi^-$  response here, where  $\langle E/p \rangle_{\text{COR}}$  is higher on average for  $\pi^+$ . The agreement between data and simulation is significantly worse for the  $\pi^-$  distributions than for the  $\pi^+$ , with a discrepancy greater than 10% below 2-3 GeV.

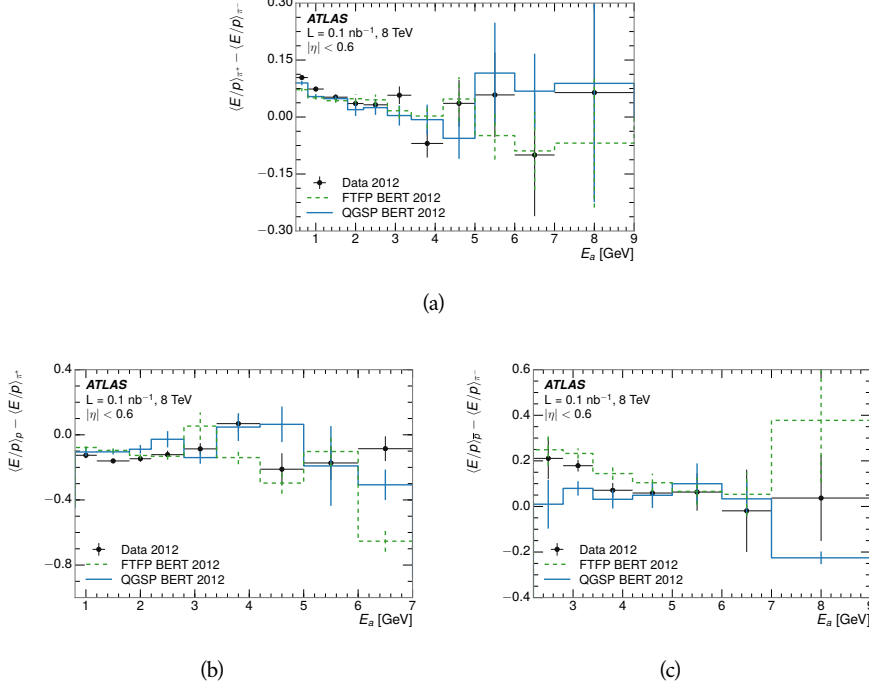


Figure 64: The difference in  $\langle E/p \rangle$  between (a)  $\pi^+$  and  $\pi^-$  (b)  $p$  and  $\pi^+$ , and (c)  $\bar{p}$  and  $\pi^-$ .

### 7.3.3 ADDITIONAL SPECIES IN SIMULATION

The techniques above provide a method to measure the response separately for only pions and protons. However the hadrons which forms jets include a number of additional species such as kaons and neutrons. The charged kaons are an important component of the inclusive charged hadron distribution, which is comprised of roughly 60-70% pions, 15-20% kaons, and 5-15% protons [46]. These fractions vary depending on the production mechanism, and the ranges are indicative of the variations between different events. These are difficult to measure in data at the ATLAS detector, as the particles which decay to kaons such as  $\phi$  and  $D$  mesons have shorter lifetimes and are comparatively rare. These properties make it impractical to identify a sufficient number of decays to make statistically meaningful measurements. The simulation of these particles includes noticeable differences in response between species at low energies, which are shown in Figure 66 for FTFP\_BERT. The significant differences in response between protons and antiprotons below 1 GeV are accounted for above in the definitions of  $E_a$ .

## 7.4 SUMMARY

These various measurements of calorimeter response shown above for data and simulation illuminate the accuracy of the simulation of hadronic interactions at the ATLAS detector. The results were obtained using 2010 and 2012 data at 7 and 8 TeV, but reflect the most current understanding of the detector alignment

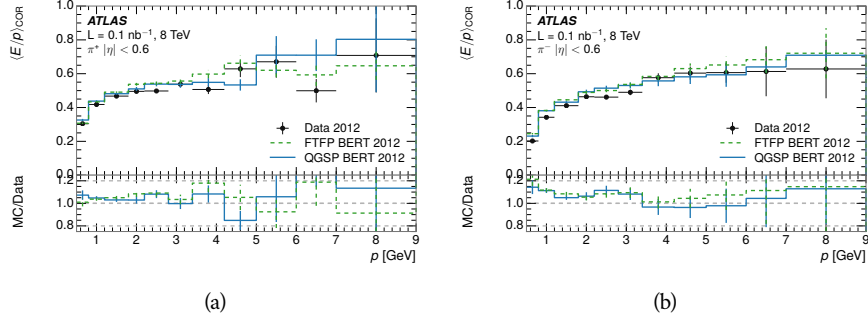


Figure 65:  $\langle E/p \rangle_{\text{COR}}$  as a function of track momentum for (a)  $\pi^+$  tracks and (b)  $\pi^-$  tracks.

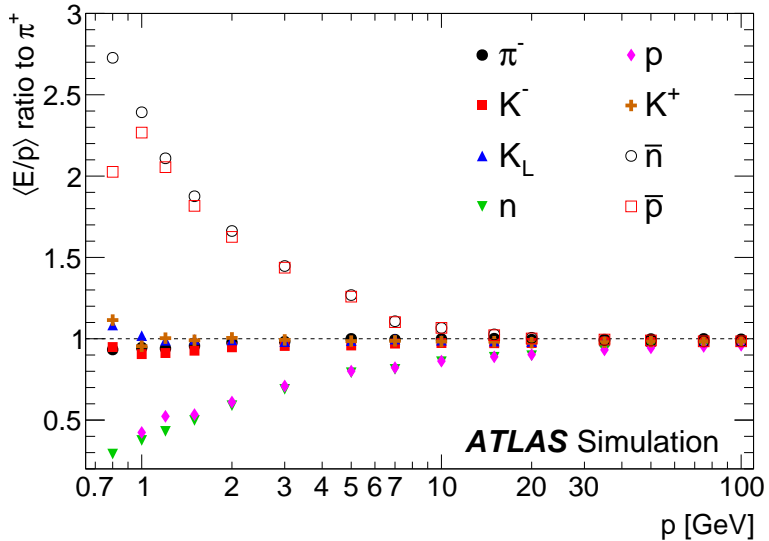


Figure 66: The ratio of the calorimeter response to single particles of various species to the calorimeter response to  $\pi^+$  with the physics list FTFP\_BERT.

and geometry. A number of measurements focusing on a comparison between protons and antiprotons suggest that FTFP\_BERT models those interactions more accurately than QGSP\_BERT. These measurements, among others, were the motivation to switch the default Geant4 simulation from QGSP\_BERT to FTFP\_BERT for all ATLAS samples.

Even with these updates, there are a number of approximately 5% discrepancies in response between the data and simulation. The differences result mostly from a difference in the modeling of the zero fraction, which is most significant at low energies. The difference in response without the zero fraction are primarily in the electromagnetic calorimeter, while the modeling of the hadronic calorimeter is accurate. At higher momenta the simulation of hadronic interactions is very consistent with data. Chapter 8 discusses how to use these observed differences to constrain the jet energy scale and its associated uncertainties.

## JET ENERGY RESPONSE AND UNCERTAINTY

---

### 8.1 MOTIVATION

As jets form a major component of many physics analyses at ATLAS, it is crucial to carefully calibrate the measurement of jet energies and to derive an uncertainty on that measurement. These uncertainties are often the dominant systematic uncertainty in high-energy analyses at the LHC. Jet balance techniques, as discussed in Section 6.4.3, provide a method to constrain the JES and its uncertainty in data, and provide the default values used for ATLAS jet measurements at most energies [72]. These techniques are limited by their reliance on measuring jets in data, so they are statistically limited in estimating the jet energy scale at the highest jet energies. This chapter presents another method for estimating the jet energy scale and its uncertainty which builds up a jet from its constituents and thus can be naturally extended to high jet momentum. Throughout this chapter the jets studied are simulated using Pythia8 with the CT10 parton distribution set [73] and the AU2 tune [50], and corrections are taken from the studies including data and simulation in Chapter 7.

As described in Section 6.4, jets are formed from topological clusters of energy in the calorimeters using the anti- $k_t$  algorithm. These clusters originate from a diverse spectrum of particles, in terms of both species and momentum, leading to significantly varied jet properties and response between jets of similar produced momentum. Figure 67 shows the momentum and particle distributions of simulated particles within jets at a few examples energies. Each bin for each distribution shows the fraction of jet constituents of that particle type and that truth energy for a jet of the specified energy. These show that majority of particles in jets are charged pions and photons, and the charged pions constituent carry the highest energies on average. The figure also demonstrates that the majority of the particles in a jet have much lower momentum than the jet itself; for example in 90-100 GeV jets less than 1% of particles have energies above 20 GeV. The  $E/p$  measurements provide a thorough understanding of the dominant particle content of jets, the charged hadrons.

### 8.2 UNCERTAINTY ESTIMATE

A correct modeling of jets in the data by simulation requires that both the particle production inside jets as well as the response of the calorimeter to particles are correctly modeled. Chapter 7 showed that the simulation does not perfectly model the calorimeter response, and provided measurements that can be used to correct for discrepancies. To determine the corrections appropriate for jets, that is to evaluate a jet energy response, the simulated jet energies are compared

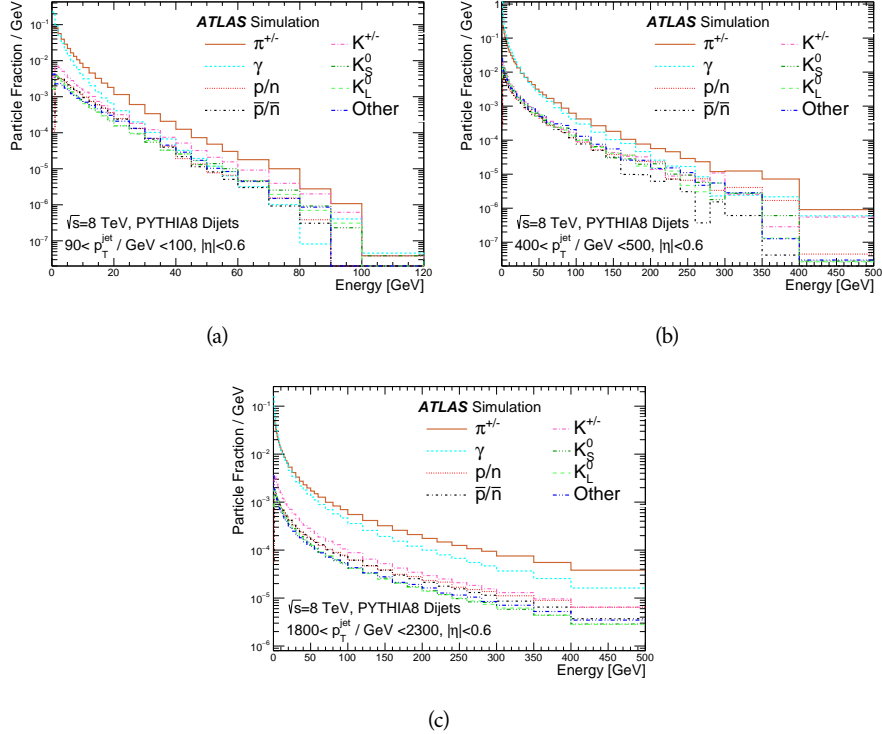


Figure 67: The spectra of true particles inside anti- $k_t$ ,  $R = 0.4$  jets with (a)  $90 < p_T/\text{GeV} < 100$ , (b)  $400 < p_T/\text{GeV} < 500$ , and (c)  $1800 < p_T/\text{GeV} < 2300$ .

to a corrected jet built up at the particle level. Each cluster in a jet is associated to the truth particle which deposited it, and the energy in that cluster is then corrected for a number of effects based on measurements in data. The primary corrections come from the single hadron response measurements in addition to response measured using the combined test beam which covers higher momentum particles [74]. These corrections include both a shift ( $\Delta$ ), in order to make the simulation match the average response in data, and an uncertainty ( $\sigma$ ) associated with the ability to constrain the difference between data and simulation. Some of the dominant sources of uncertainty are itemized in Table 7 with typical values, and the full list considered is described in detail in the associated paper [46]. These uncertainties cover differences between the data and simulation in the modeling of calorimeter response to a given particle. The typical values are listed as ranges to show the variation over momentum and pseudorapidity. For the in situ  $E/p$  term, for example,  $\Delta$  corresponds to the difference between data and simulation for  $\langle E/p \rangle_{\text{COR}}$  at the LCW scale (shown in Figure 55 (b)) and  $\sigma$  is the uncertainty on that difference including the statistical uncertainties of both the data and simulated events. No uncertainties are added for the difference between particle composition of jets in data and simulation, as this method focuses on providing a response correction for discrepancies of particle interactions rather than differences in particle composition.

From these terms, the jet energy scale and uncertainty is built up from individual energy deposits in simulation. Each uncertainty term is treated inde-

Abbrev.	Description	$\Delta$ (%)	$\sigma$ (%)
In situ $E/p$	The comparison of $\langle E/p \rangle_{\text{COR}}$ , at the <a href="#">LCW</a> scale, as described in Chapter 7 with statistical uncertainties from 500 MeV to 20 GeV.	0-3	1-5
CTB	The main $\langle E/p \rangle$ comparison uncertainties, binned in $p$ and $ \eta $ , as derived from the combined test beam results, from 20 to 350 GeV [74].	0-3	1-5
$E/p$ Zero Fraction	The difference in the zero-fraction between data and MC simulation from 500 MeV to 20 GeV.	5-25	1-5
$E/p$ Threshold	The uncertainty in the EM calorimeter response from the potential mismodeling of threshold effects in topological clustering.	0	0-10
Neutral	The uncertainty in the calorimeter response to neutral hadrons based on studies of physics model variations.	0	5-10
$K_L$	An additional uncertainty in the response to neutral $K_L$ in the calorimeter based on studies of physics model variations.	0	20
$E/p$ Misalignment	The uncertainty in the $p$ measurement from misalignment of the ID.	0	1
Hadrons, $p > 350$ GeV	An energy independent uncertainty for all particles above the energy range or outside the longitudinal range probed with the combined test beam.	0	10

Table 7: The dominant sources of corrections and systematic uncertainties in the [JES](#) estimation technique, including typical values for the correcting shift ( $\Delta$ ) and the associated uncertainty ( $\sigma$ ).

pendently, and is taken to be gaussian distributed. The resulting scale and uncertainty is shown in Figure 68, where the mean response is measured relative to the calibrated energy reported by simulation. The mean response is slightly below one, indicating that the simulation slightly overestimates the calorimeter response on average, and this response is relatively constant as a function of the jet  $p_T$ . The dominant uncertainties come from the statistical uncertainties on the  $E/p$  measurements at lower energies and the additional uncertainty for out of range measurements at higher energies. Combined the resulting uncertainty ranges from between 1.5% at low momentum and pseudorapidity to as much as 4% at higher momentum and pseudorapidity. The total uncertainty from this method at intermediate jet energies is comparable to other simulation-based methods [75] and is about twice as large as in-situ methods using data [72]. This method is the only one which provides an estimation above 1.8 TeV, however, and so is still a crucial technique in analyses that search for very energetic jets.

These techniques can also be used to measure the correlation between bins of average reconstructed jet momentum across a range of  $p_T$  and  $|\eta|$ , where correlations are expected because of a similarity in particle composition at similar energies. Figure 69 shows these correlations, where the uncertainties on jets in neighboring bins are typically between 30% and 60% correlated. The uncertainty on all jets becomes significantly correlated at high energies and larger pseudorapidities, when the uncertainty becomes dominated by the single term reflecting out of range particles.

### 8.3 SUMMARY

The technique described above provides a jet energy scale and uncertainty by building up jet corrections from the energy deposits of constituent particles. The  $E/p$  measurements are crucial in providing corrections for the majority of particles in the jets. The uncertainty derived this way is between 2 and 5% and is about twice as large at corresponding momentum than jet balance methods. However this is the only uncertainty available for very energetic jets using 2012 data and simulation, and repeating this method with Run 2 data and simulation will be important in providing an uncertainty for the most energetic jets in 13 TeV collisions.

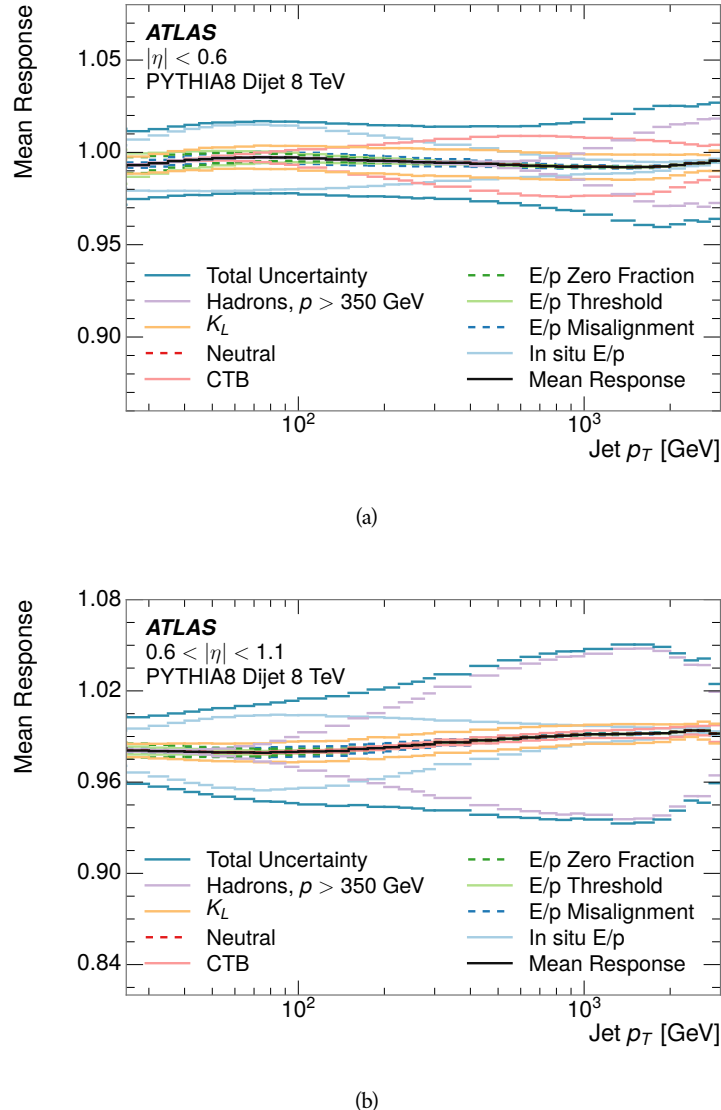


Figure 68: The JES response uncertainty contributions, as well as the total JES uncertainty, as a function of jet  $p_T$  for (a)  $|\eta| < 0.6$  and (b)  $0.6 < |\eta| < 1.1$ .

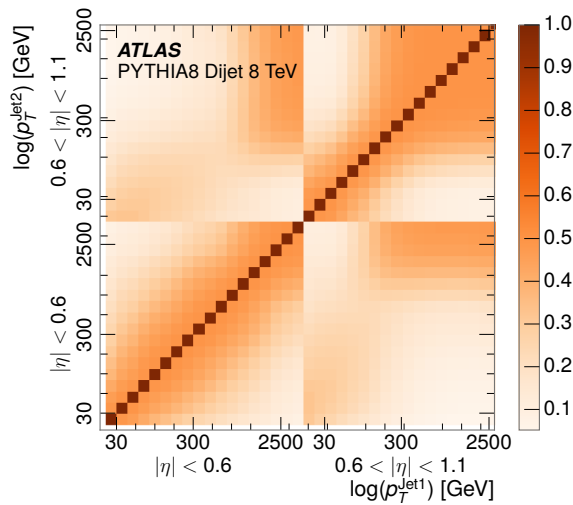


Figure 69: The correlations between bins of average reconstructed jet momentum as a function of jet  $p_T$  and  $|\eta|$  for jets in the central region of the detector.

PART IV  
SEARCH FOR LONG-LIVED PARTICLES

## LONG-LIVED PARTICLES IN ATLAS

---

As discussed in Section 2.6, various limitations in the SM suggest a need for new particles at the TeV scale. A wide range of extensions to the Standard Model predict that these new particles can have lifetimes greater than approximately one-hundredth of a nanosecond. These include theories with universal extra-dimensions [76, 77], with new fermions [78], and with leptoquarks [79]. As discussed in Section 3.4, many SUSY theories also produce these LLPs, in both R-Parity violating [80–82] and R-Parity conserving [83–86] formulations. Split supersymmetry [14, 15], for example, predicts long-lived gluinos with  $O(\text{TeV})$  masses. This search focuses specifically on the SUSY case, but many of the results are generic to any model with LLPs.

Long-lived gluinos or squarks carry color-charge and will thus hadronize into color neutral bound states called R-Hadrons. These are composit particles like the known hadrons but with one supersymmetric constituent, for example  $\tilde{g}q\bar{q}$  and  $\tilde{q}\bar{q}$ . In this hadronization process, the gluino can acquire an electric charge. Gluino pair production,  $pp \rightarrow \tilde{g}\tilde{g} + X$ , where  $X$  denotes the proton remnants, has the largest cross sectional increase with the increase in energy to 13 TeV, and so this search uses gluino R-Hadrons as its benchmark model. The features, techniques, and cross section limits discussed here are all largely independent of the model. Planned future updates will extend the case to include additional refinements for squark and chargino models, but the current method covers any long-lived, charged, massive particle.

### 9.1 EVENT TOPOLOGY

R-parity conserving SUSY models predict that gluinos will be produced in pairs at the LHC, through the processes shown in Figure 70, where the quarks and gluons are proton constituents. The gluon-initiated mode dominates for the collision energy and gluino masses considered for this search. During their production, the long-lived gluinos hadronize into color singlet bound states including  $\tilde{g}q\bar{q}$  and even  $\tilde{g}g$  [87]. The probability to form the gluon-only bound states is a free parameter usually taken to be 0.1, and 90% of the remaining R-Hadrons form meson states [88]. The charged and neutral states are approximately equally likely for mesons, so the R-Hadrons will be charged roughly 50% of the time.

These channels produce R-Hadrons with large  $p_T$ , but lower on average than their mass, so that they typically propagate with  $0.2 < \beta < 0.9$  [88]. Figure 71 shows the generated  $p_T$  and  $\beta$  distributions for a simulated example of R-Hadrons with a mass of 1600 GeV. The mean  $p_T$  is roughly half of the mass at 800 GeV, and so  $\beta$  peaks around 0.5. The fragmentation that produces these hadrons is very hard, so the jet structure around the R-Hadron is minimal, with less than 5 GeV of summed particle momentum expected in a cone of  $\Delta R < 0.25$  around

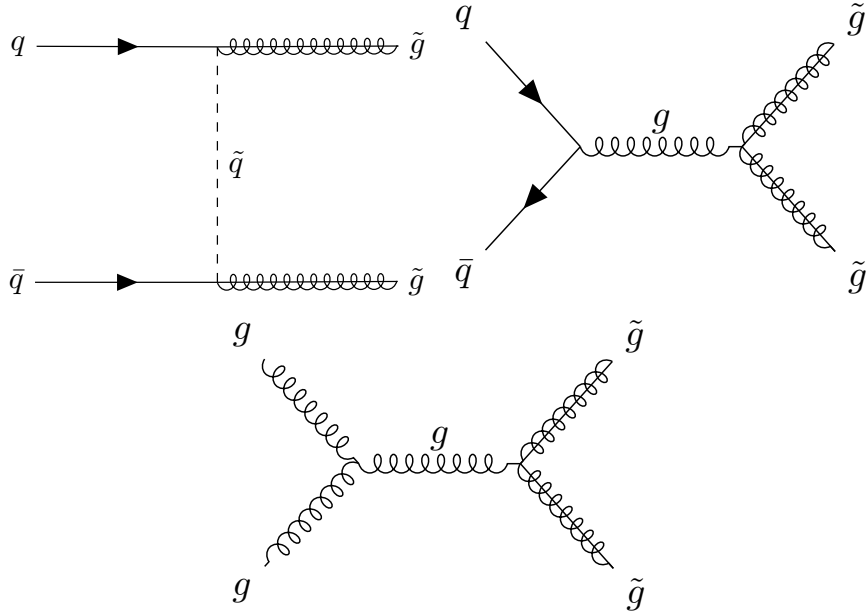


Figure 70: The processes which contribute to gluino pair production in the proton proton collisions, where the quarks and gluons are proton constituents.

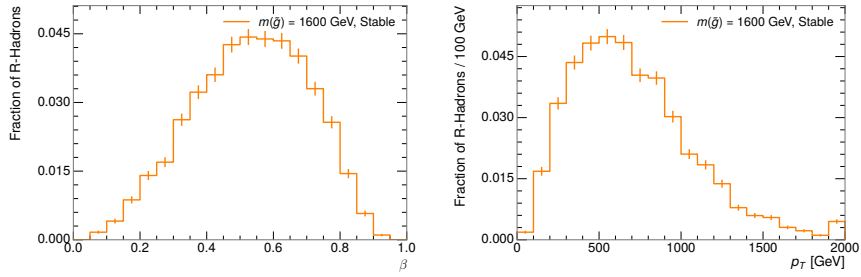


Figure 71: The generated  $p_T$  and  $\beta$  distributions for R-Hadrons with  $M = 1600$  GeV.

the R-Hadron [88]. After hadronization, depending on the gluino lifetime, the R-Hadrons then decay into hadrons and a LSP [87].

In summary, the expected event for pair-produced long-lived gluinos is very simple: two isolated, high-momentum R-Hadrons that propagate through the detector before decaying to jets. The observable features of such events depend strongly on the interaction of the R-Hadron with the material of the detector and also its lifetime. Section 9.1.1 describes the interactions of R-Hadrons which reach the various detector elements in ATLAS and Section 9.1.2 provides a summary of the observable event descriptions for R-Hadrons of various lifetimes.

### 9.1.1 DETECTOR INTERACTIONS

Although the distribution of decay times can be parametrized with a single parameter,  $\tau$ , the time before individual R-Hadrons decay follows an exponential distribution, leading to a range of decay times for any individual lifetime. This is

further confounded by the distribution of  $\beta$  as well as  $\eta$ , so that each R-Hadron propagates at a different velocity and travels a different distance before reaching each detector element. Therefore, the lifetime-dependent event topologies must be discussed as an average, and all times referred to within this section will assume  $\beta = 0.5$ , an  $\eta = 0$ , and that the particle decays after a time equal to its lifetime. Table 8 lists the distances of various subdetectors and the time after which a LLP will arrive at that subdetector for a few values of  $\beta$  and with  $\eta = 0$ .

Subdetector	Distance	$\tau$ at $\beta = 0.3$	$\tau$ at $\beta = 0.5$	$\tau$ at $\beta = 0.7$
Pixel	3.1 cm	0.35 ns	0.20 ns	0.15 ns
Calorimeter	1.5 m	17 ns	10 ns	7.2 ns
Muon System	5 m	56 ns	33 ns	24 ns

Table 8: The radial distances of each of the subdetectors and example arrival times for an R-Hadron with  $\eta = 0$  and the specified  $\beta$ .

After approximately 0.2 ns, the R-Hadron reaches the first layer of the pixel detector. If charged, it deposits energy into the material through repeated single collisions that result in ionization of the silicon substrate [3]. Because of its comparatively low  $\beta$ , the ionization energy can be significantly greater than expected for SM particles because the most-probable energy loss grows significantly as  $\beta$  decreases [3]. This large ionization can be measured through the ToT read out from the pixel detector as described in Section 6.1.2. Large ionization in the inner detector is one of the major characteristic features of LLPs. The particle propagates through all four layers of the pixel detector, where each provides a measurement of ionization, and then exits the pixel detector at 0.8 ns.

Throughout the next few nanoseconds, the R-Hadron propagates through the remainder of the inner detector. A charged R-Hadron will provide hits in each of these systems as would any other charged particle, and can be reconstructed as a track. The track reconstruction provides a measurement of its trajectory and thus its  $p$  as described in Section 6.1. The large  $p_T$ , shown in Figure 71, is another characteristic feature of massive particles produced at the LHC.

As of roughly 10 ns, the R-Hadron enters the calorimeter where it interacts hadronically with the material. Because of its large mass and  $p$ , the R-Hadron does not typically stop in the calorimeter, but rather deposits a small fraction of its energy through repeated interactions with nucleons. The probability of interaction between the gluino itself and a nucleon is low because the cross section drops off with the inverse square of its mass, so the interactions are primarily governed by the light constituents [89]. Each of these interactions can potentially change that quark content and thus change the sign of the R-Hadron, so that the charge at exit is typically uncorrelated with the charge at entry [88]. The total energy deposited in the calorimeters during the propagation is small compared to the kinetic energy of the R-Hadron, around 20-40 GeV, so that  $E/p$  is typically less than 0.1 [88].

Then, 30 ns after the collision, it reaches the muon system, where it again ionizes in the material if charged and can be reconstructed as a muon track. Because of the charge-flipping interactions in the calorimeter, this track may have

the opposite sign of the track reconstructed in the inner detector, or there may be a track present when there was none in the inner detector and vice-versa for those which are detected. The propagation time at the typically lower  $\beta$  results in a significant delay compared to muons, and a delay over 25 ns causes the muon signal to be lost outside the readout window. Between the probability of charge-flip and late arrival, there is a significant chance that an R-Hadron which was produced with a charge will not be identified as a muon. When it is reconstructed as a muon, that delay can be assessed in terms of a time-of-flight measurement, which is another characteristic feature of R-Hadrons.

## 9.1.2 LIFETIME DEPENDENCE

The above description assumed a lifetime long enough for the R-Hadron to exit the detector, which through this search is referred to as [VLL](#), as the particle may decay after exiting the detector. There are several unique signatures at shorter lifetimes where the R-Hadron decays in various parts of the inner detector; these lifetimes are referred to as [LL](#).

The shortest case where the R-Hadron is considered [LL](#) is for lifetimes around 0.01 ns, where the particle decays before reaching any of the detector elements. Although the R-Hadrons are produced opposite each other in the transverse plane, each R-Hadron decays to a jet and an [LSP](#). The two decays are uncorrelated, so the two [LSPs](#) carry different momenta and in different directions. And, since the [LSPs](#) are not measured, the produced jets can be significantly imbalanced in the transverse plane which results in large missing energy. That missing energy can be used to trigger candidate events, and provides the most efficient trigger option for shorter lifetimes. Additionally, the precision of the tracking system allows the displaced vertex of the R-Hadron decay to be reconstructed from the charged particles in the jet. The distance of that vertex from the interaction point can be used to distinguish R-Hadron decays from other processes. Figure 72 shows a schematic diagram of an example R-Hadron event with such a lifetime. The diagram is not to scale, but instead illustrates the detector interactions in the pixel detector, calorimeters, and muon system. It includes a representation of a charged R-Hadron and a neutral R-Hadron, as well as the [LSPs](#) and jets (shown as charged hadrons) produced in the decay. Neutral hadrons may also be produced in the decay but are not depicted. Previous searches on ATLAS have used the displaced vertex to target [LLP](#) decays [90].

The next distinguishable case occurs at lifetimes greater than 0.1 ns but less than 10 ns, where the R-Hadron forms a partial track in the inner detector. This forms a unique signature of a disappearing track. Two examples of such an event are illustrated in Figure 73 and Figure 74, which show the short track in the inner detector. The decay distance must be sufficiently long that it reaches the [SCT](#), or else the track will not be reconstructed at all. Depending on the mass difference between the R-Hadron and the [LSP](#), the decay products will either be a single, soft charged hadron and a [LSP](#) (Figure 73), or a jet and a [LSP](#) (Figure 74). A dedicated search on ATLAS used the disappearing track signature in the former case to search for [LLP](#) in Run 1 [91].

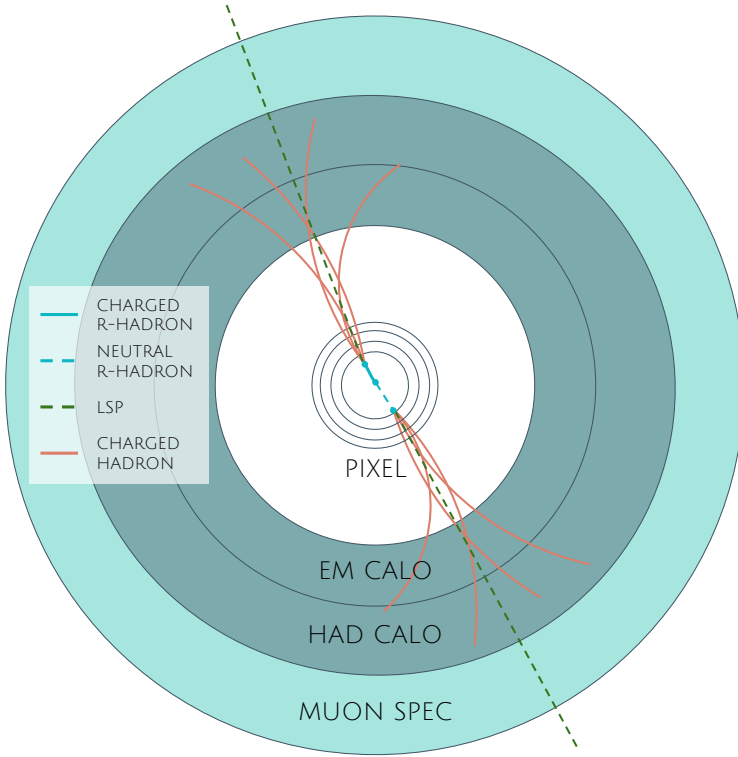


Figure 72: A schematic diagram of an R-Hadron event with a lifetime around 0.01 ns. The diagram includes one charged R-Hadron (solid blue), one neutral R-Hadron (dashed blue), LSPs (dashed green) and charged hadrons (solid orange). The pixel detector, calorimeters, and muon system are illustrated but not to scale.

In the latter case, the decays result in an event-level signature of up to two high- $p$  tracks, jets, and significant missing energy. The missing energy has the same origin as in the case of 0.01 ns lifetimes, from the decay to unmeasured particles, and again can be large. The high- $p$  tracks will also have the characteristically high-ionization of massive, long-lived particles in the Pixel detector. Figure 74 shows how the jets from the decay can still be reconstructed in the calorimeter. Several previous searches on ATLAS from Run 1 have used this signature to search for R-Hadrons [92, 93], including a dedicated search for LL particles [94].

If the lifetime is longer than several nanoseconds, in the range of 10–30 ns, the R-Hadron decay can occur in or after the calorimeters, but prior to reaching the muon system. In the case that the decays occur early enough within the calorimeters that the decay can be measured, the event topology is very similar to the above with jets originating in the inner detector. If the decay occurs after the calorimeter, jets may not be reconstructed at all. The events still often have large missing energy, although it is generated through different mechanisms, and so the same search strategy can be used. The R-Hadrons do not deposit much energy in the calorimeters, so a neutral R-Hadron will not enter into the missing energy calculation. A charged R-Hadron opposite a neutral R-Hadron will thus generate significant missing energy, and close to 50% of pair-produced R-Hadron events fall into this category. If both R-Hadrons are neutral then the

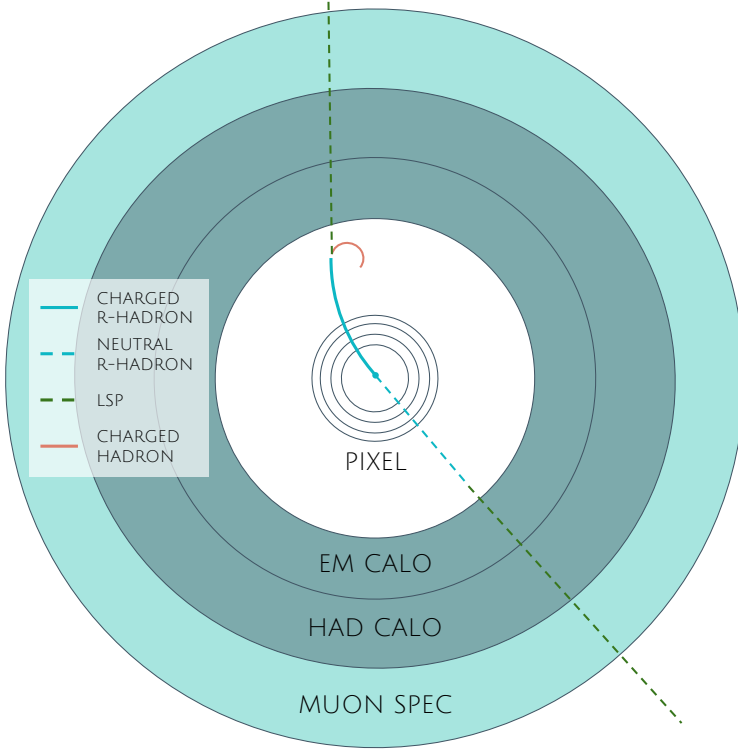


Figure 73: Schematic diagram of an R-Hadron event with a lifetime around 5 ns, where the masses of the R-Hadron and LSP are nearly degenerate. The diagram includes charged R-Hadrons (solid blue), neutral R-Hadrons (dashed blue), LSPs (dashed green) and charged hadrons (solid orange). The pixel detector, calorimeters, and muon system are illustrated but not to scale.

missing energy will be low because neither is detected. Two charged R-Hadrons will also result in low missing energy because both are reconstructed as tracks and will balance each other in the transverse plane. A small fraction of the time, one of the charged R-Hadron tracks may fail quality requirements and thus be excluded from the missing energy calculation and again result in significant missing energy. Figure 75 illustrates another example event with one charged R-Hadron which decays after approximately 20 ns, and shows how the jets from the decay might not be reconstructed.

The longest lifetimes, the VLL case, has all of the features of the 30-50 ns case but with the addition of muon tracks for any R-Hadrons that exit the calorimeter with a charge. That muon track can provide additional information from time-of-flight measurements to help identify LLPs. An example of the event topology for one charged and one neutral VLL R-Hadron is shown in Figure 76. Some searches on ATLAS have included this information to improve the search reach for VLL particles [93, 95].

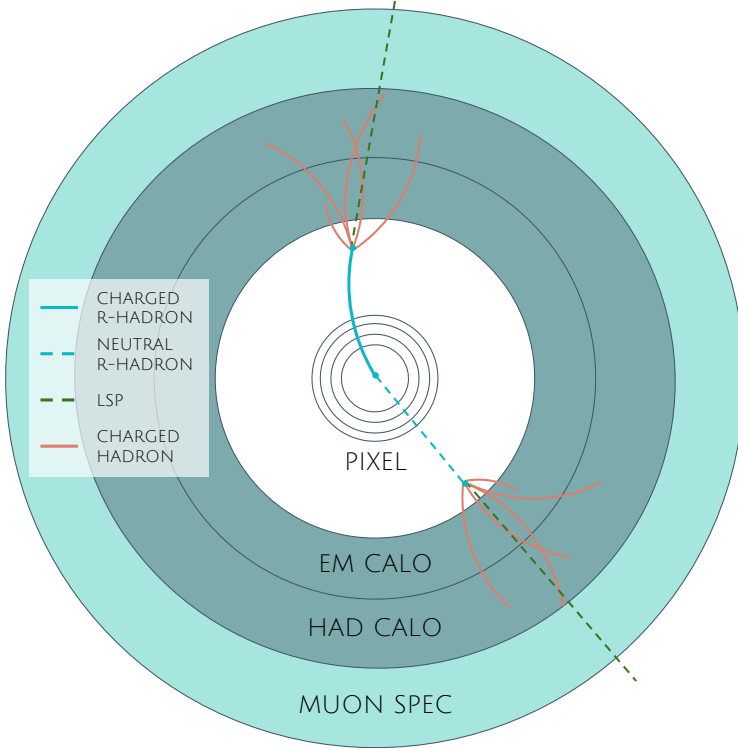


Figure 74: Schematic diagram of an R-Hadron event with a lifetime around 5 ns, where the masses of the R-Hadron and LSP are not degenerate. The diagram includes charged R-Hadrons (solid blue), neutral R-Hadrons (dashed blue), LSPs (dashed green) and charged hadrons (solid orange). The pixel detector, calorimeters, and muon system are illustrated but not to scale.

## 9.2 SIMULATION

All of the event topologies discussed above are modeled by simulations of R-Hadron events in the ATLAS detector. A large number of such samples are generated to determine efficiencies, to measure expected yields, and to estimate uncertainties. The primary interaction, pair production of gluinos with masses between 400 and 3000 GeV, is simulated using `Pythia 6.4.27` [5] with the AUET2B [96] set of tuned parameters for the underlying event and the CTEQ6L1 [73] PDF set. The simulated interactions include a modeling of pileup by adding secondary, minimum bias interactions from both the same (in-time pileup) and nearby (out-of-time pileup) bunch crossings. This event generation is then augmented with a dedicated hadronization routine to hadronize the long-lived gluinos into final states with R-Hadrons [97], with the probability to form a gluon-gluino bound set at 10% [98].

The cross sections used for these processes are calculated at `NLO` in the strong coupling constant with a resummation of soft-gluon emission at next-to-leading logarithmic (`NLL`) [99–103]. The nominal predictions and the uncertainties for each mass point are taken from an envelope of cross-section predictions using different PDF sets and factorization and renormalization scales [104]. As discussed in Section 2.5.4, the PDFs and scales determine the cross section by pro-

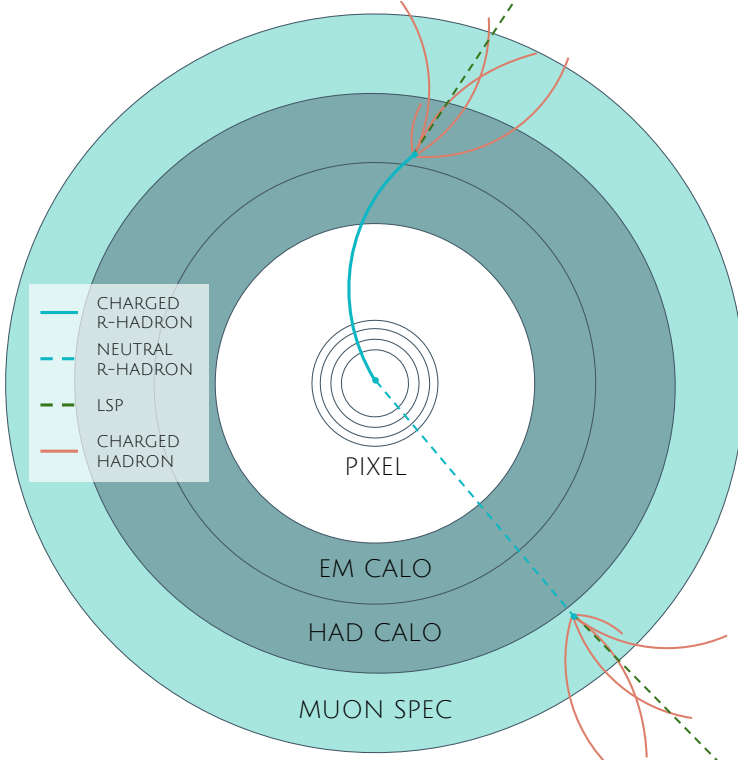


Figure 75: A schematic diagram of an R-Hadron event with a lifetime around 20 ns. The diagram includes one charged R-Hadron (solid blue), one neutral R-Hadron (dashed blue), LSPs (dashed green) and charged hadrons (solid orange). The pixel detector, calorimeters, and muon system are illustrated but not to scale.

viding the probabilities of the proton constituents to interact. Multiple estimates for the PDF and scales at 13 TeV can be used to provide an average cross section calculation and its uncertainty.

The R-Hadrons then undergo a full detector simulation [48], where the interactions of the R-Hadrons with the material of the detector are described by dedicated Geant4 [7] routines. These routines model the interactions described in Section 9.1.1, including the ionizing interactions in the silicon modules of the inner detector and the R-Hadron-nucleon interactions in the calorimeters [105, 106]. The specific routine chosen to describe the interactions of the R-Hadrons with nucleons, the “generic model”, uses a pragmatic approach where the scattering cross section is taken to be a constant 12 mb per light quark. In this model the gluino itself does not interact at all, although it carries most of the kinetic energy of the bound state.

The lifetimes of these R-Hadrons are then simulated at several working points,  $\tau = 0.1, 1.0, 3.0, 10, 30, 50$  and  $> 50\text{ns}$ . The actual decay times follow an exponential distribution, where  $\tau$  is the characteristic time. Only one decay mode is simulated for these benchmark samples,  $\tilde{g} \rightarrow q\bar{q}\tilde{\chi}_1^0$  with the neutralino mass set to 100 GeV. The search discussed here is also efficient for heavier neutralinos, which have very similar topologies but which generate less missing energy.

All of the simulated events are then reconstructed using the same software used for collision data. The fully reconstructed events are then reweighted to

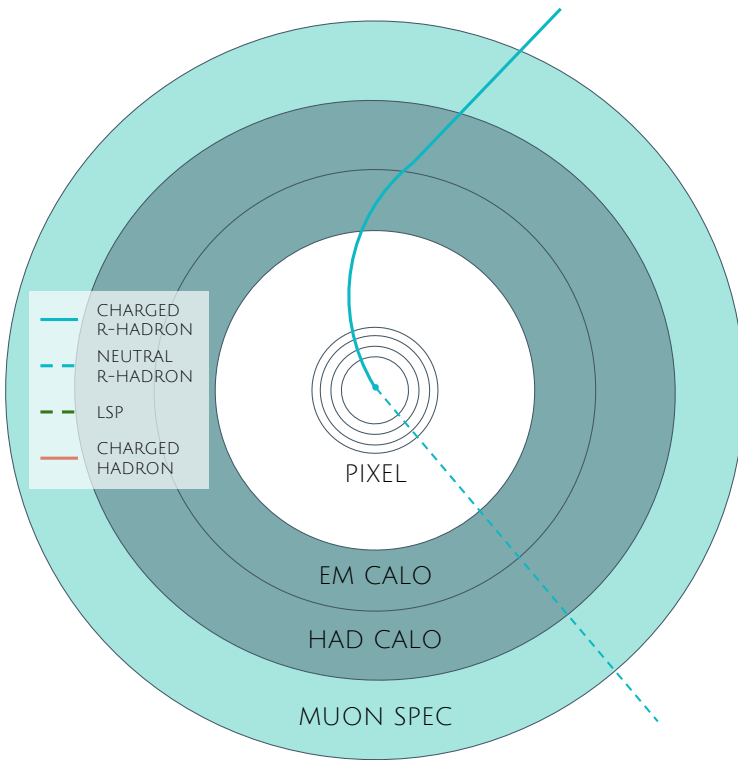


Figure 76: A schematic diagram of a [VLL](#) R-Hadron event. The diagram includes one charged R-Hadron (solid blue) and one neutral R-Hadron (dashed blue). The pixel detector, calorimeters, and muon system are illustrated but not to scale.

match the distribution of initial state radiation in an alternative sample of events, generated with MG5\_aMC@NLO [6], which has had a more accurate description of radiate effects than Pythia6 in previous iterations [94]. MG5\_aMC@NLO predicts a harder distribution of initial state radiation, where 28% more simulated events generate sufficient missing energy to trigger for [VLL](#) R-Hadrons. This reweighting provides a more accurate description of the  $p$  of the gluino-gluino system and is important in modeling the efficiency of triggering and offline event selection.

## EVENT SELECTION

---

The **LLPs** targeted by this search differ in their interactions with the detector from **SM** particles primarily because of their large mass. When produced at the energies available at the **LHC**, that large mass results in a low  $\beta$  (typically  $0.2 < \beta < 0.9$  as shown in Figure 71). Such slow-moving particles heavily ionize in detector material. Each layer of the pixel detector provides a measurement of that ionization, through **ToT**, as discussed in Section 6.1.2. The ionization in the pixel detector, quantified in terms of  $dE/dx$ , provides the major focus for this search technique, along with the momentum measured in the entire inner detector. It is effective both for its discriminating power and its use in reconstructing a particle's mass, and it can be used for a wide range of masses and lifetimes as discussed in Section 9.1.2. However  $dE/dx$  needs to be augmented with a few additional selection requirements to provide a mechanism for triggering and to further reduce backgrounds.

Ionization itself is not currently accessible for triggering, so this search instead relies on  $E_T^{\text{miss}}$  to trigger signal events. Although triggering on  $E_T^{\text{miss}}$  can be inefficient,  $E_T^{\text{miss}}$  is often large for many production mechanisms of **LLPs**, as discussed in Section 9.1.

The use of ionization to reject **SM** backgrounds relies on well-measured, high-momentum tracks, so some basic requirements on quality and kinematics are placed on the tracks considered in this search. A few additional requirements are placed on the tracks considered for **LLP** candidates that increase background rejection by targeting specific types of **SM** particles.

The ionization measurement with the Pixel detector can be calibrated to provide an estimator of  $\beta\gamma$ . That estimate, together with the momentum measurement provided by tracking, can be used to reconstruct a mass for each track which traverses the pixel detector,

$$m = \frac{p}{\beta\gamma} \quad (20)$$

That mass variable will be peaked at the **LLP** mass for any signal, and provides an additional tool to search for an excess. In addition to an explicit requirement on ionization, this search constructs a mass-window for each targeted signal mass in order to search for an excess of events.

The strategy discussed here is optimized for lifetimes of  $O(1) - O(10)$  ns. The specific values for each requirement in signal region were optimized considering the increase in discovery reach for tightening the requirement on each discriminating variable. Pixel ionization is especially useful in this regime as particles only need to propagate through the first seven layers of the inner detector, about 37 cm from the beam axis. The search is still competitive with other searches for **LLPs** at longer lifetimes, because the primary discriminating

variables are still applicable even for particles that do not decay within the detector [95]. Although the majority of the requirements will be the same for all lifetimes, two signal regions are defined to optimize separately for intermediate and long lifetime particles.

## 10.1 TRIGGER

Triggering remains a significant difficulty in defining an event selection with high signal efficiency in a search for [LLPs](#). There are no triggers available in the current ATLAS system that can fire directly from a high momentum track with large ionization, as tracking is not available at L1 (Section 5.6). Although in some configurations a charged [LLP](#) can fire muon triggers, this requirement introduces significant model dependence on both the allowed lifetimes and the interactions in the calorimeter [88], as discussed in Section 9.1.1.

For a search targeting particles which may decay prior to reaching the muon system, the most efficient available trigger is based on missing energy [88]. As discussed in Section 9.1, signal events can produce significant  $E_T^{\text{miss}}$  by a few mechanisms. At the trigger level however, the missing energy is only calculated using the calorimeters (Section 5.6) where the R-Hadrons deposit little energy. So, at short lifetimes,  $E_T^{\text{miss}}$  measured in the calorimeter is generated by an imbalance between the jets and undetected [LSPs](#) produced in R-Hadron decays. At longer lifetimes, without the decay products, missing energy is only produced in the calorimeters when the R-Hadrons recoil against an [ISR](#) jet.

These features are highlighted in Figure 77, which shows the  $E_T^{\text{miss}}$  distributions for simulated short lifetime (3 ns) and [VLL](#) R-Hadron events. The figure includes both the offline  $E_T^{\text{miss}}$ , the missing energy calculated with all available information, and Calorimeter  $E_T^{\text{miss}}$ , the missing energy calculated using only information available at the calorimeter which approximates the missing energy available at the trigger. The short lifetime sample has significantly greater  $E_T^{\text{miss}}$  and Calorimeter  $E_T^{\text{miss}}$  than the [VLL](#) sample as expected. For the [VLL](#) sample, a small fraction of events with very large  $E_T^{\text{miss}}$  (about 5%) migrate into the bin with very small Calorimeter  $E_T^{\text{miss}}$  because the  $E_T^{\text{miss}}$  produced by a charged R-Hadron track opposite a neutral R-Hadron track does not contribute any missing energy in the calorimeters.

So, either case to some extent relies on kinematic degrees of freedom to produce missing energy, as the pair-produced [LLPs](#) tend to balance each other in the transverse plain. For long lifetimes in particular, the presence of [ISR](#) is important in providing an imbalance in the transverse plane, and is an important aspect of modeling the selection efficiency for R-Hadron events. The missing energy trigger with the lowest threshold available is chosen for this selection in order to maximize the trigger efficiency. The formation of the trigger decision for missing energy was discussed in more detail in Section 5.6. During 2015 data collection this was the HLT\_xe70 trigger, which used a 50 GeV threshold on missing energy at L1 and a 70 GeV threshold on missing energy at the HLT which is nearly 100% efficient after the L1 requirement. With these thresholds, the incomplete balance of the [LSPs](#) results in a relatively low efficiency for long-

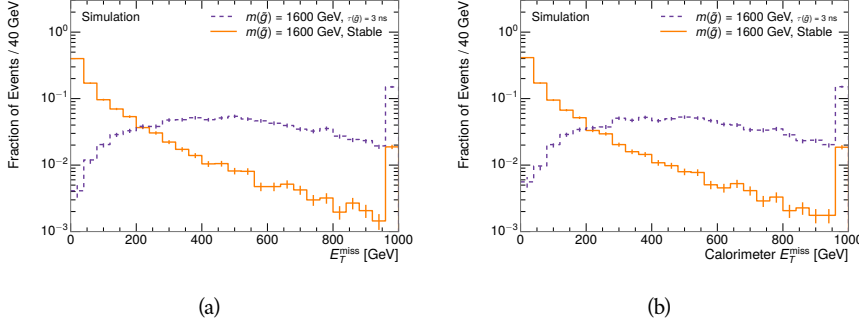


Figure 77: The distribution of (a)  $E_T^{\text{miss}}$  and (b) Calorimeter  $E_T^{\text{miss}}$  for simulated signal events before the trigger requirement. The final bin includes all events above the axis range.

lifetime particles, roughly 40%, and efficiencies between 65% and 95% for shorter lifetimes depending on both the mass and the lifetime.

## 10.2 KINEMATICS AND ISOLATION

After the trigger requirement, each event is required to have a primary vertex reconstructed from at least two well-measured tracks in the inner detector, each with  $p_T > 400 \text{ MeV}$ . If more than one such vertex exists, the primary vertex is taken to be the one with the largest summed  $p_T^2$  for all tracks associated to that vertex. The offline reconstructed  $E_T^{\text{miss}}$  is required to be above  $130 \text{ GeV}$  to additionally reject SM backgrounds. The transverse missing energy is calculated using fully reconstructed and calibrated offline objects, as described in Section 6.5. In particular the  $E_T^{\text{miss}}$  definition in this selection uses jets reconstructed with the anti- $k_t$  algorithm with radius  $R = 0.4$  from clusters of energy in the calorimeter (Section 6.4) and with  $p_T > 20 \text{ GeV}$ , as well as reconstructed muons, electrons, and tracks not identified as another object type.

The  $E_T^{\text{miss}}$  distributions are shown for data and a few simulated signals in Figure 78, after the trigger requirement. The data contains some events with  $E_T^{\text{miss}}$  below the nominal trigger threshold of  $70 \text{ GeV}$ , which can occur because  $E_T^{\text{miss}}$  at trigger level uses only calorimeter information while the full offline  $E_T^{\text{miss}}$  additionally includes tracks and muons which can balance the event. The cut placed at  $130 \text{ GeV}$  is 95% efficient for LL and 90% efficient for VLL particles, after the trigger requirement, because of the missing energy generating mechanisms discussed previously. The distribution of data in this figure and subsequent figures in this section can be interpreted as the distribution of backgrounds, as any signal contamination would be negligible if present at these early stages of the selection (prior to the final requirement on ionization). The background falls rapidly with missing energy, motivating the direct requirement on  $E_T^{\text{miss}}$  for the signal region.

It is typically the practice for searches for new physics on ATLAS to place an offline requirement on the triggering variable that is sufficiently tight to guar-

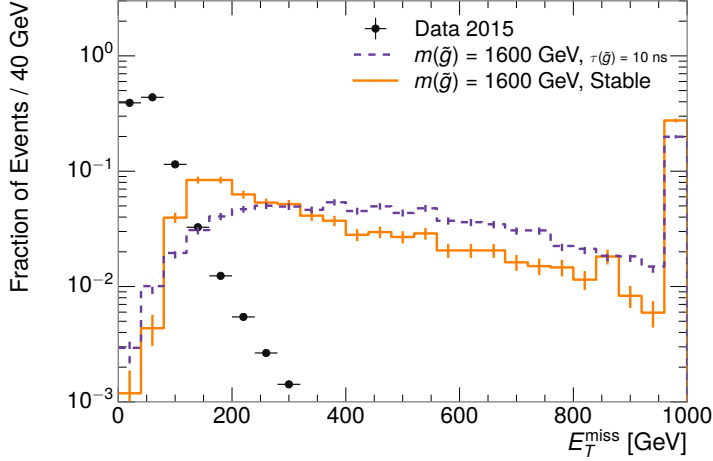


Figure 78: The distribution of  $E_T^{\text{miss}}$  for data and simulated signal events, after the trigger requirement. The final bin includes all events above the axis range.

antee that the event would pass the trigger. Such a tight requirement makes the uncertainty on the trigger efficiency of the simulation negligible, as modeling the regime where the trigger is only partially efficient can be difficult. In this analysis, however, because of the atypical interactions of R-Hadrons with the tracker and the calorimeter, the offline requirement on  $E_T^{\text{miss}}$  is not sufficient to guarantee a 100% trigger efficiency even at large values, as can be seen in Figure 79. This figure shows the efficiency for passing the HLT\_xe70 trigger as a function of the requirement on  $E_T^{\text{miss}}$ , which plateaus to roughly 85% even at large values. This plateau does not reach 100% because events which have large offline missing energy from a neutral R-Hadron produced opposite of a charged R-Hadron can have low missing energy in the calorimeters. The Calorimeter  $E_T^{\text{miss}}$ , on the other hand, does not have this effect and reaches 100% efficiency at large values because it is the quantity that directly corresponds to the trigger threshold. In both cases the efficiency of triggering is greater for the short lifetime sample because the late decays to hadrons and LSPs produce an imbalance in the calorimeters even though they may not be reconstructed offline as tracks or jets. For this reason, the requirement on  $E_T^{\text{miss}}$  is determined by optimizing the background rejection even though it corresponds to a value of trigger efficiency significantly below 1.0.

The events are then required to have at least one candidate LLP track. Although the LLPs are produced in pairs, many models do not consistently yield two charged particles, as discussed in Chapter 9. For example, in the R-Hadron model highlighted here, only 20% of events have two charged R-Hadrons while 47% of events have just one. A signal region requiring two charged particle candidates could be a powerful improvement in background rejection for a larger dataset, but it is not considered in this version of the analysis as it was found to be unnecessary to reject the majority of backgrounds.

For a track to be selected as a candidate, it must have  $p_T > 50 \text{ GeV}$  and pass basic quality requirements. The track must be associated to the primary vertex.

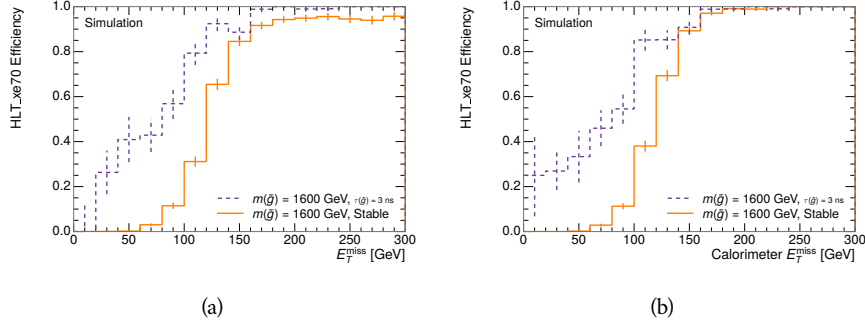


Figure 79: The trigger efficiency for the HLT\_xe70 trigger requirement as a function of (a)  $E_T^{\text{miss}}$  and (b) Calorimeter  $E_T^{\text{miss}}$  for simulated signal events.

It must also have at least seven clusters in the silicon layers in the inner detector to ensure an accurate measurement of momentum. Those clusters must include one in the innermost layer if the extrapolated track is expected to pass through that layer. And to ensure a reliable measurement of ionization, the track is required to have at least two clusters in the pixel detector that provide a measurement of  $dE/dx$ .

At this point in the selection, there is a significant high-ionization background from multiple tracks that significantly overlap in the Pixel detector. Previous versions of this analysis have rejected these overlaps by an explicit overlap rejection between pairs of fully reconstructed tracks, typically by requiring no additional tracks within a cone around the candidate. This technique, however, fails to remove the background from tracks that overlap so precisely that the tracks cannot be separately resolved, which can be produced in very collimated photon conversions.

Another observable, which more directly targets track overlaps, identifies cluster shapes that are likely formed by multiple particles based on a neural network classification algorithm, as discussed in Section 6.1.1. The number of clusters on a given track that are estimated to have contributions from more than one particle is called  $N_{\text{split}}$ . As the shape of clusters requires significantly less spatial separation to identify overlaps than it does to reconstruct two fully resolved tracks, this variable is more effective at rejecting backgrounds from overlaps. Figure 80 shows the dependence of ionization on  $N_{\text{split}}$ ; as  $N_{\text{split}}$  increases the most probable value of  $dE/dx$  grows significantly up to twice the expected value when  $N_{\text{split}} = 4$ .

A requirement of  $N_{\text{split}} = 0$  is very successful in reducing the long positive tail of the  $dE/dx$  distributions, as can be seen in Figure 81. Comparing the distribution for “baseline tracks”, tracks with only the above requirements on clusters applied and before the requirement on  $N_{\text{split}}$ , to the distribution with  $N_{\text{split}} = 0$ , it is clear that the fraction of tracks with large  $dE/dx$  is reduced by several orders of magnitude. The tracks without split hits are very close to the  $dE/dx$  distribution of identified muons, which are usually well isolated. Figure 81 also includes the distribution of  $dE/dx$  in an example signal simulation to demonstrate how effective  $dE/dx$  is as a discriminating variable with this isolation applied. The

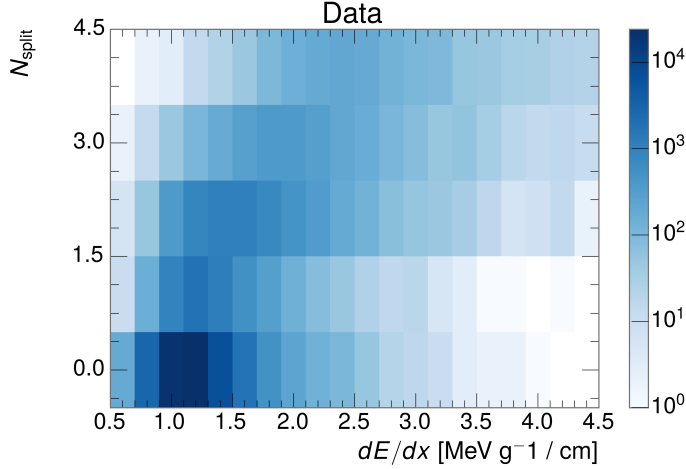


Figure 80: The dependence of  $dE/dx$  on  $N_{\text{split}}$  in data after basic track hit requirements have been applied.

background falls rapidly for  $dE/dx > 1.8 \text{ MeV g}^{-1} \text{cm}^2$  while the majority of the signal, approximately 90% depending on the mass, falls above that threshold. Over 90% of [LLP](#) tracks in simulated signal events pass the  $N_{\text{split}}$ -based isolation requirement.

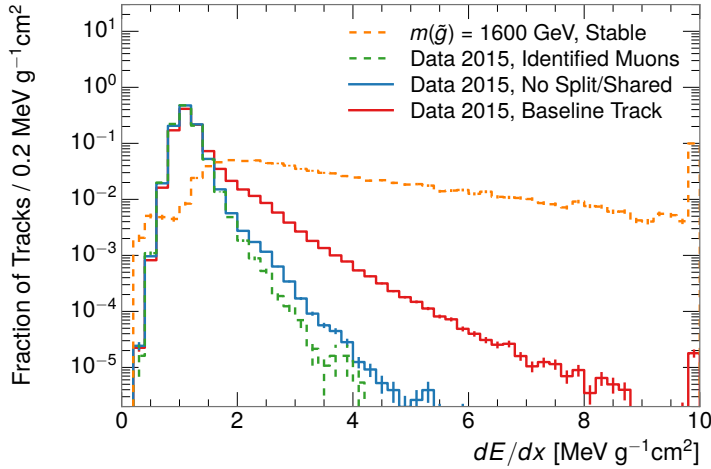


Figure 81: The distribution of  $dE/dx$  with various selections applied in data and simulated signal events. The final bin includes all tracks above the axis range.

A few additional kinematic requirements are imposed to help reduce [SM](#) backgrounds. The momentum of the candidate track must be at least 150 GeV, and the uncertainty on that measurement must be less than 50%. The distribution of momentum is shown in Figure 82 for tracks in data and simulated signal events after the previously discussed requirements on clusters, transverse momentum, and isolation have been imposed. The signal particles are much harder on av-

erage than their backgrounds as shown in Figure 71. The transverse mass,  $M_T$ , defined as

$$M_T = \sqrt{2p_T E_T^{\text{miss}}(1 - \cos(\Delta\phi(E_T^{\text{miss}}, \text{track})))} \quad (21)$$

estimates the mass of a decay of to a single charged particle and an undetected particle and is required to be greater than 130 GeV to reject contributions from the decay of W bosons. Figure 83 shows the distribution of  $M_T$  for data and simulated signal events. The signal is distributed over a wide range of  $M_T$ , with about 90% above the threshold value of 130 GeV. The data has a large number of contributions below 100 GeV from W boson decays and an additional peak from a kinematic shaping imposed by the requirements on  $E_T^{\text{miss}}$  and the track  $p_T$  in dijet events.

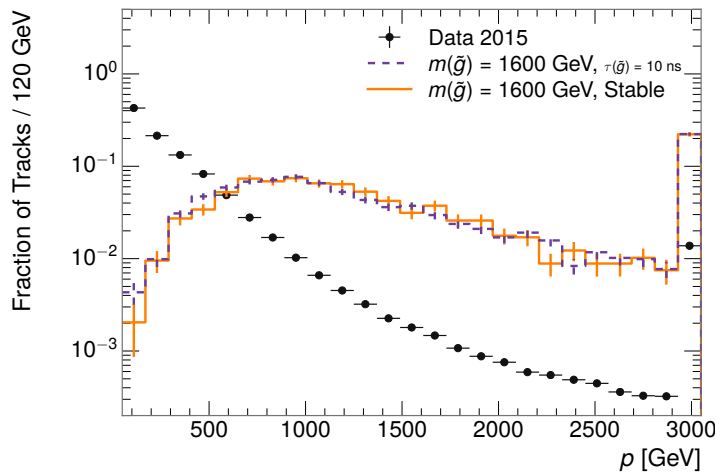


Figure 82: The distribution of track momentum for data and simulated signal events, after previous selection requirements have been applied. The final bin includes all tracks above the axis range.

### 10.3 PARTICLE SPECIES REJECTION

The amount of ionization deposited by particles with low mass and high momentum has a large positive tail [3], so backgrounds can be formed by a wide variety of SM processes when various charged particles have a few randomly large deposits of energy in the pixel detector. Those backgrounds can be additionally reduced by targeting other interactions with the detector where they are expected to have different behavior than R-Hadrons. The interactions with the detector depend on the types of particles produced rather than the processes which produce them, so this search forms a series of rejections to remove backgrounds from individual particle species. These rejections focus on using additional features of the event, other than the kinematics of the candidate track, as they can provide a powerful source of background rejection with very high signal efficiency. However, the lifetime of an R-Hadron can significantly change

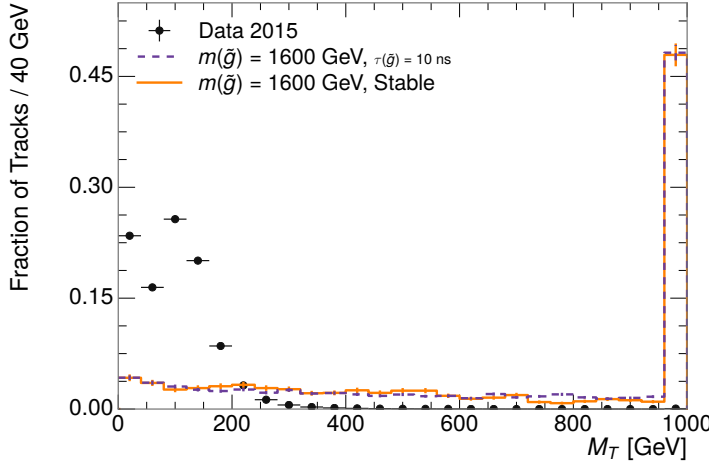


Figure 83: The distribution of  $M_T$  for data and simulated signal events, after previous selection requirements have been applied. The final bin includes all tracks above the axis range.

its detector characteristics, as discussed in Section 9.1.2. To accommodate these differences, the **SM** rejections defined in this section are split to form two signal regions, one for long-lifetimes particles, the **VLL** region ( $\tau[\text{ns}] \geq 50 \text{ ns}$ ), and one for intermediate lifetime particles, the **LL** region ( $0.4 < \tau[\text{ns}] < 50$ ).

Jets can contribute high momentum track backgrounds when an individual jet constituent carries large  $p_T$ . These tracks can be sufficiently well isolated from the other constituents that they are separately reconstructed and pass the  $N_{\text{split}}$  requirement. However, jets can be very effectively rejected by considering the larger-scale isolation of the candidate track. In this case the isolation focuses on the production of nearby particles as a jet-veto, rather than the isolation from overlapping tracks based on  $N_{\text{split}}$  that was used to reduce high-ionization backgrounds. As explained in Section 9.1, the fragmentation process which produces an R-Hadron is very hard and thus is not expected to produce additional particles with a summed momentum of more than 5 GeV. Nearby particles may be produced in the decay of the R-Hadron, but they will be significantly displaced, so the jet-veto only considers tracks associated to the primary vertex. The jet-veto uses the summed momentum of tracks with a cone of  $\Delta R < 0.25$ , referred to as  $p_T^{\text{Cone}}$ , which is shown in Figure 84 for data and simulated signal events. In the data this value has a peak at zero from isolated tracks such as leptons, and a long tail from jets which contains as much as 80% of the background above 20 GeV at this stage of the selection. In signal events  $p_T^{\text{Cone}}$  is strongly peaked at zero and significantly less than 1% of signal events have  $p_T^{\text{Cone}}$  above 20 GeV. This makes a requirement of  $p_T^{\text{Cone}} < 20 \text{ GeV}$  a very effective method to reject background without losing signal efficiency. For the **VLL** signal region, this cut is further tightened to  $p_T^{\text{Cone}} < 5 \text{ GeV}$  as it is the most effective variable remaining to extend the search reach for long lifetimes.

Even for fully isolated particles, there are additional methods to reject each type of particle using information in the muon system and calorimeters. Muons

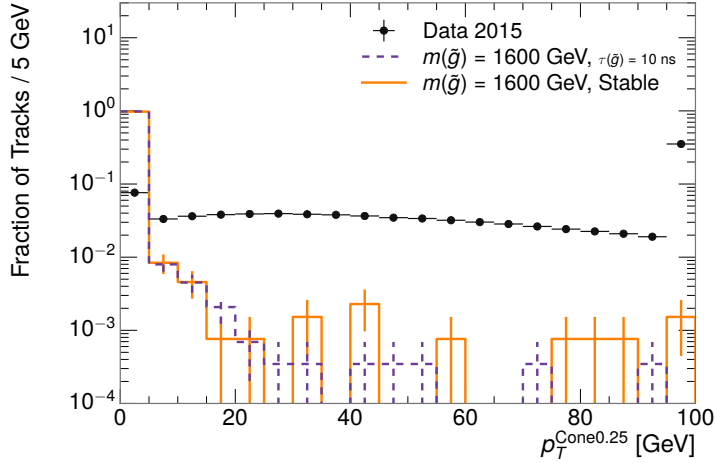


Figure 84: The distribution of summed tracked momentum within a cone of  $\Delta R < 0.25$  around the candidate track for data and simulated signal events, after previous selection requirements have been applied. The final bin includes all tracks above the axis range.

can be identified very reliably using the tracks in the muon system, as described in Section 6.3. For intermediate lifetimes ( $0.4 < \tau[\text{ns}] < 30$ ), the LLPs do not survive long enough to reach the muon system, and so muons are vetoed by rejecting tracks that associate to a muon with medium muon identification requirements (Section 6.3). For longer lifetimes ( $\tau > 30$  ns), this rejection is not applied because LLPs which reach the muon system can be identified as muons as often as 30% of the time in simulated samples.

Calorimeter-based particle rejection relies on the expected small deposits of energy from LLPs. When the lifetime is long enough to reach the calorimeter, a LLP deposits little of its energy as it traverses the material, as discussed in Section 9.1. Even when the particle does decay before the calorimeter, the majority of its energy is carried away by the LSP and not deposited in the calorimeter. In both cases the energy is expected to be distributed across the layers of the calorimeters and not peaked in just one layer. This can be quantified in terms of  $E/p$ , the ratio of calorimeter energy of a nearby jet to the track momentum, and  $f_{\text{EM}}$ , the fraction of energy in that jet within the electromagnetic calorimeter. When no jets fall within a cone of 0.05 of the particle,  $E/p$  and  $f_{\text{EM}}$  are both defined as zero.  $E/p$  is expected to be above 1.0 for electrons and hadrons because of the contributions from other nearby particles. At these momenta there is no significant fraction of tracks with no associated clusters due to interactions with the detector or insufficient energy deposits (see Section 7.2.2).  $f_{\text{EM}}$  is peaked close to 1.0 for electrons, and distributed between 10% and 90% for hadrons.

These trends can be seen in the two dimensional distribution for signal in Figure 85 for VLL and LL (10 ns) signal events. The majority of R-Hadrons in both samples fall into the bin for  $E/p = 0$  and  $f_{\text{EM}} = 0$  because the majority of the time there is no associated jet. In the VLL sample, when there is an associated jet,  $E/p$  is typically still below 0.1, and the  $f_{\text{EM}}$  is predominantly less than 0.8.

In the [LL](#) sample, on the other hand,  $E/p$  is larger on average because of the jets produced in the R-Hadron decay. It is still typically below 0.1, however, because most of the energy of the R-Hadron is carried by the [LSP](#) and not the jet. The  $f_{\text{EM}}$  is much lower on average in this case, below 0.1, because the 10 ns lifetime particles rarely decay before passing through the electromagnetic calorimeter. Figure 85 also includes simulated Z decays to electrons or tau leptons. From the decays to electrons it is clear that the majority of electrons have  $f_{\text{EM}}$  above 0.9. The  $\tau$  decays include a variety of products. Muons can be seen in the bin where  $E/p = 0$  and  $f_{\text{EM}} = 0$  because they do not have an associated jet. Electrons fall into the range where  $E/p > 1$  and  $f_{\text{EM}} > 0.9$ . Hadronic tau decays are the most common, and fall in the range of  $0.1 < f_{\text{EM}} < 0.9$  and  $E/p > 1.0$ .

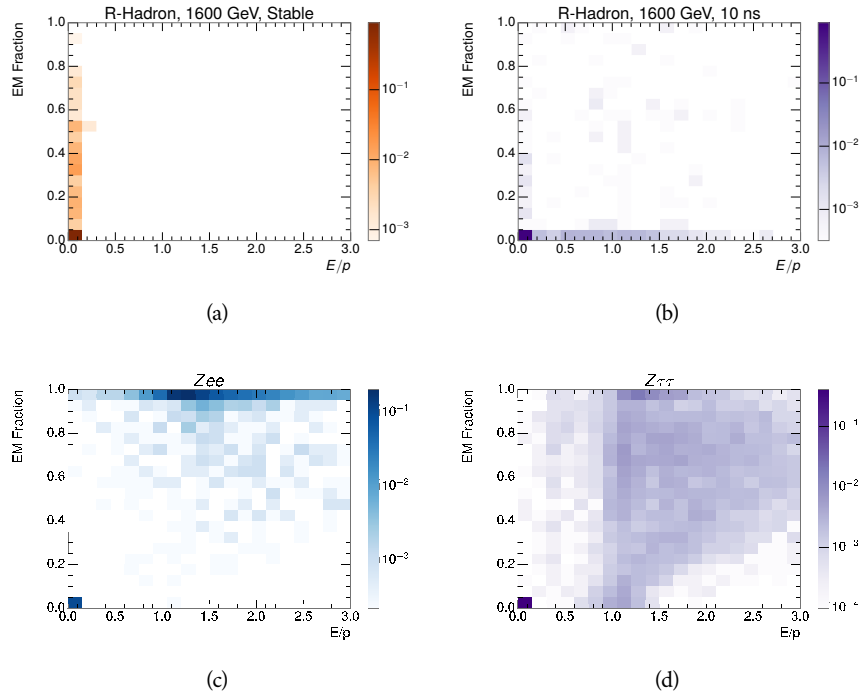


Figure 85: The normalized, two-dimensional distribution of  $E/p$  and  $f_{\text{EM}}$  for simulated (a) 1200 GeV [VLL](#) R-Hadron, and (b) 1200 GeV, 10 ns R-Hadron, (c)  $Z \rightarrow ee$ , and (d)  $Z \rightarrow \tau\tau$  events.

The differences motivate an electron rejection by requiring  $f_{\text{EM}} < 0.9$ . Similarly, isolated hadrons are rejected by requiring  $E/p < 1.0$ . These requirements combine to remove the majority of isolated electrons and hadrons but retain over 95% of the simulated signal across a range of masses and lifetimes. The suite of particle species rejection techniques provide a significant analysis improvement over previous iterations of ionization-based searches on ATLAS by providing additional background rejection with minimal loss in signal efficiency.

## 10.4 IONIZATION

The final requirement on the candidate track is the primary discriminating variable, the ionization in the pixel detector. That ionization is measured in terms of  $dE/dx$ , which was shown for data and simulated signal events in Figure 81.  $dE/dx$  is dramatically greater for the high mass signal particles than the backgrounds, which start to fall immediately after the minimally ionizing peak at 1.1 MeVg $^{-1}$ cm $^2$ . The  $dE/dx$  for candidate tracks must be greater than a pseudorapidity dependent threshold, specifically  $1.80 - 0.11|\eta| + 0.17\eta^2 - 0.05|\eta|^3$  MeV g $^{-1}$  cm $^{-2}$ , in order to correct for an approximately 5% dependence of the MIP peak position on  $\eta$ . The requirement was chosen as part of the signal region optimization, and reduces the backgrounds by a factor of 100 while remaining 70-90% efficient for simulated signal events depending on the mass.

### 10.4.1 MASS ESTIMATION

The mean value of ionization in silicon is governed by the Bethe equation and the most probable value follows a Landau-Vavilov distribution [3]. Those forms inspire a parametric description of  $dE/dx$  in terms of  $\beta\gamma$ ,

$$(dE/dx)_{\text{MPV}}(\beta\gamma) = \frac{p_1}{\beta^{p_3}} \ln(1 + [p_2\beta\gamma]^{p_5}) - p_4 \quad (22)$$

which performs well in the range  $0.3 < \beta\gamma < 1.5$ . This range includes the expected range of  $\beta\gamma$  for the particles targeted for this search, with  $\beta\gamma \approx 2.0$  for lower mass particles (O(100 GeV)) and  $\beta\gamma \approx 0.5$  for higher mass particles (O(1000 GeV)). The parameters,  $p_i$ , are fit using a 2015 data sample of low-momentum pions, kaons, and protons as described in Ref. [107]. Figure 86 shows the two-dimensional distribution of  $dE/dx$  and momentum along with the above fitted values for  $(dE/dx)_{\text{MPV}}$ .

The above equation (22) is then numerically inverted to estimate  $\beta\gamma$  and the mass for each candidate track. In simulated signal events, the mean of this mass value reproduces the generated mass up to around 1800 GeV to within 3%. The mass distributions are shown for a few VLL mass points in Figure 87. The large widths of these distributions come from the high variability in energy deposits in the pixel detector as well as the uncertainty on momentum measurements at high momentum, but the means converge to the expected values. A constant shift of 3% is observed between the mean of the reconstructed mass distribution and the generated mass, which is then corrected by applying a 3% shift in the opposite direction.

This analysis evaluates expected yields and the resulting cross sectional limits using windows in this mass variable. The windows are formed by fitting mass distributions in simulated signal events like those in Figure 87 to Gaussian distributions and taking all events that fall within  $\pm 1.4\sigma$  of the mean. As can be seen in Figure 87, typical values for this width are  $\sigma \approx 300 - 500$  GeV depending on the generated mass.

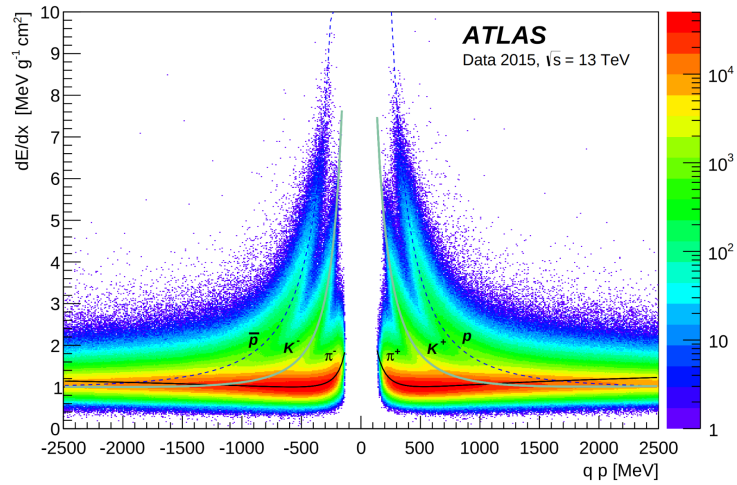


Figure 86: Two-dimensional distribution of  $dE/dx$  versus charge signed momentum ( $qp$ ) for minimum-bias tracks. The fitted distributions of the most probable values for pions, kaons and protons are superimposed.

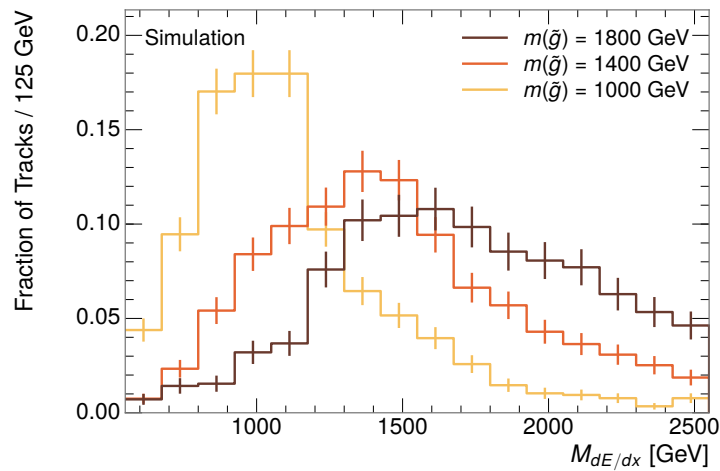


Figure 87: The distribution of mass estimated using  $dE/dx$  for simulated VLL R-Hadrons with masses between 1000 and 1600 GeV.

## 10.5 EVENT SELECTION

The numbers of events passing each requirement are shown in Table 9 for the full 2015 dataset and a simulated 1600 GeV, 10 ns lifetime R-Hadron sample. The table highlights the overall acceptance  $\times$  efficiency for signal events, which for this example is 19%. Between SM rejection and ionization, the selection requirements reduce the background of tracks which pass the kinematic requirements down by an additional factor of almost 2000.

Selection	Signal Events (%)	Data Events	Rejection
Generated	$26.0 \pm 0.3$		
$E_T^{\text{miss}}$ Trigger	$24.8 \pm 0.3$ (95%)		
$E_T^{\text{miss}} > 130$ GeV	$23.9 \pm 0.3$ (92%)		
Track Quality and $p_T$	$10.7 \pm 0.2$ (41%)	368324	1.0
Isolation Requirement	$9.0 \pm 0.2$ (35%)	108079	3.4
Track $p > 150$ GeV	$6.6 \pm 0.2$ (25%)	47463	7.8
$M_T > 130$ GeV	$5.8 \pm 0.2$ (22%)	18746	20
Electron/Hadron Veto	$5.5 \pm 0.2$ (21%)	3612	100
Muon Veto	$5.5 \pm 0.2$ (21%)	1668	220
Ionization Requirement	$5.0 \pm 0.1$ (19%)	11	33000

Table 9: The expected number of events at each level of the selection for LL 1600 GeV, 10 ns R-Hadrons, along with the number of events observed in data, for  $3.2 \text{ fb}^{-1}$ . The simulated yields are shown with statistical uncertainties only. The total efficiency  $\times$  acceptance is also shown for the signal and the rejection factor relative to initial track requirement is shown for data.

There is a strong dependence of this efficiency on lifetime and mass, with efficiencies dropping to under 1% at low lifetimes. Figure 88 shows the dependence on both mass and lifetime for all signal samples considered in this search. The dependence on mass is relatively slight and comes predominantly from the increasing fraction of R-Hadrons which pass the ionization cut with increasing mass. The trigger and  $E_T^{\text{miss}}$  requirements are most efficient for particles that decay before reaching the calorimeters. However, the chance of a particle to be reconstructed as a high-quality track decreases significantly at low lifetimes as the particle does not propagate sufficiently through the inner detector. These effects lead to a maximum in the selection efficiency for lifetimes around 10-30 ns. The lifetimes up to and including 30 ns are shown with the LL selection and the 50 ns and stable points are shown with the VLL selection.

The inefficiency of this signal region at short lifetimes comes almost exclusively from an acceptance effect, in that the particles do not reach the necessary layers of the SCT. This can be seen more clearly by defining a fiducial region which includes events with at least one R-Hadron that is produced with non-zero charge,  $p_T > 50$  GeV,  $p > 150$  GeV,  $|\eta| < 2.5$ , and a decay distance greater than 30 cm in the transverse plane. At short (1 ns) lifetimes, the acceptance into

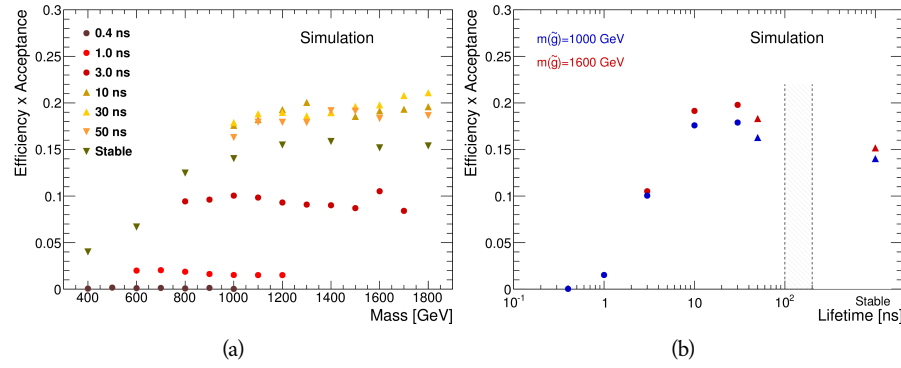


Figure 88: The acceptance  $\times$  efficiency as a function of R-Hadron (a) mass and (b) lifetime. (a) shows all of the combinations of mass and lifetime considered in this search, and (b) highlights the lifetime dependence for 1000 GeV and 1600 GeV R-Hadrons.

this region is as low as 4%. Once this acceptance is accounted for, the selection efficiency ranges from 25% at lifetimes of 1 ns up to 45% at lifetimes of 10 ns.

## BACKGROUND ESTIMATION

---

The event selection discussed in the previous section focuses on detector signatures, emphasizing a single high-momentum, highly-ionizing track. That track is then required to be inconsistent with the expected properties of SM particles, with various requirements designed to reject jets, hadrons, electrons, and muons (Section 10.3). Therefore the background for this search comes entirely from backgrounds that are outliers of various distributions including  $dE/dx$ ,  $f_{EM}$ , and  $p_T^{\text{Cone}}$ . The simulation can be tuned in various ways to do an excellent job of modeling the average properties of each particle type [108], but it is not necessarily expected to accurately reproduce outliers. For this reason, the background estimation used for this search is estimated entirely using data.

### 11.1 BACKGROUND SOURCES

SM charged particles with lifetimes long enough to form tracks in the inner detector can be grouped into three major categories based on their detector interactions: hadrons, electrons, and muons. Every particle that contributes to the background for this search belongs to one of these types. Relatively pure samples of tracks from each of these types can be formed in data by inverting the various rejection techniques in Section 10.3. Specifically, muons are selected requiring medium muon identification, electrons requiring  $E/p > 1.0$  and  $f_{EM} > 0.95$ , and hadrons requiring  $E/p > 1.0$  and  $f_{EM} < 0.95$ .

Figure 89 shows the distributions of momentum and  $dE/dx$  for these categories in data, after requiring the event level selection as well as the track requirements on  $p_T$ , hits, and  $N_{\text{split}}$ , as discussed in Section 10.2. Simulated signal events are included for reference. These distributions are only illustrative of the differences between types, as the rejection requirements could alter their shape. This is especially significant for momentum which enters directly into  $E/p$  and can indirectly affect muon identification. However it is clear that there are some differences between types in both distributions, even though the trends are similar. The distributions of momentum are not necessarily expected to match between the various types because the production mechanisms for each type result in different kinematic distributions.  $dE/dx$  is also different between types because of incomplete isolation; although the requirement on  $N_{\text{split}}$  helps to reduce the contribution of nearby particles it does not completely remove the effect of overlaps. Muons are better isolated because they do not have the additional particle from hadronization present for hadrons and they are significantly less likely to interact with the detector and produce secondary particles compared to hadrons and electrons. Thus muons have the smallest fraction of  $dE/dx$  above the threshold of  $1.8 \text{ MeVg}^{-1}\text{cm}^2$ ; hadrons and electrons have a larger fraction above this threshold.

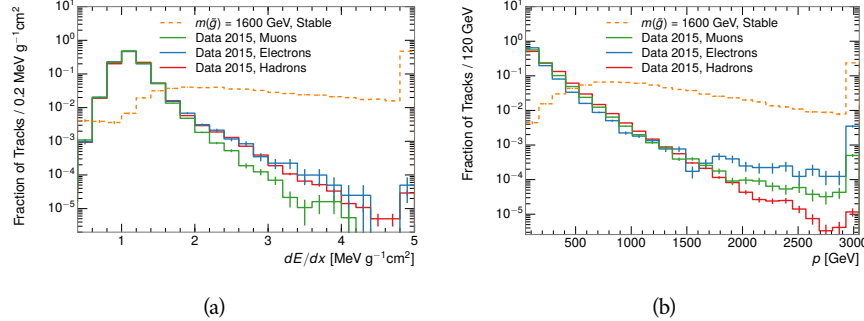


Figure 89: The distribution of (a)  $dE/dx$  and (b) momentum for tracks in data and simulated signal after requiring the event level selection and the track selection on  $p_T$ , hits, and  $N_{\text{split}}$ . Each sub-figure shows the normalized distributions for tracks classified as hadrons, electrons, and muons in data and R-Hadrons in the simulated signal.

It is difficult to determine what fraction of each particle type enters into the final signal region. The background method will not have significant dependence on the relative contributions of each species, but it is useful to understand the differences between each when considering the various tests of the method.

## 11.2 PREDICTION METHOD

The data-driven background estimation relies on the independence between the ionization measurement and other kinematic variables in the event. For standard model particles with momenta above 50 GeV,  $dE/dx$  is not correlated with momentum; though there is a slight relativistic rise as momentum increases, the effect is small compared to the width of the distribution of ionization energy deposits.. So, the proposed method to estimate the mass distribution of the signal region is to use the momentum from a track with low  $dE/dx$  (below the threshold value) and to combine it with a random  $dE/dx$  value from a  $dE/dx$  template. The resulting track is just as likely as the original, so a large set of random generations provide the expected distributions of momentum and ionization. These are then combined using the parametrization described in Section 10.4.1 to estimate  $\beta\gamma$  and then form a distribution of mass for the signal region using Equation 20.

Algorithmically this method is implemented by forming two distinct Control Regions (**CRs**). The first **CR**, CR1, is formed by applying the entire event selection from Chapter 10 apart from the  $dE/dx$  and mass requirements. The  $dE/dx$  requirement is instead inverted for this region. Because of the independence of  $dE/dx$  and  $p$ , the tracks in this control region have the same kinematic distribution as the tracks in the signal region, and are used to measure a two-dimensional template of  $p$  and  $\eta$ . The second **CR**, CR2, is formed from the event selection through the  $dE/dx$  requirement, but with an inverted  $E_T^{\text{miss}}$  requirement. The tracks in this control region are expected to have similar  $dE/dx$  distributions as the signal region before the ionization requirement, and so this region is used to measure a two-dimensional template of  $dE/dx$  and  $\eta$ .

The contribution of any signal to the control regions is minimized by the inverted selection requirements. Only less than 10% of simulated signal events have either  $dE/dx$  or  $E_T^{\text{miss}}$  below the threshold values in the original signal region, while the backgrounds are significantly enhanced by inverting those requirements. The signal contamination is less than 1% in both control regions for all of the simulated masses and lifetimes considered in this analysis.

With those measured templates, the shape of the mass estimation is generated by first selecting a random  $(p, \eta)$  combination from CR1. This momentum value is combined with a  $dE/dx$  value taken from the appropriate distribution of  $dE/dx$  for the selected  $\eta$  from CR2. The use of  $\eta$  in both random samplings controls for any correlation between  $p$ ,  $dE/dx$ , and  $\eta$ . Those values are then used to calculate a mass in the same way that is done for regular tracks in data, see Section 10.4.1. As this procedure includes all  $dE/dx$  values, the cut at 1.8 MeVg $^{-1}$ cm $^2$  is then enforced to fully model the signal region. The generated mass distribution is then normalized by scaling the background estimate to the data in the region  $M < 160$  GeV, where signals of this type have already been excluded [94]. This normalization uses the distributions of mass generated without the ionization requirement.

The statistical uncertainties on these background distributions are calculated by independently fluctuating each bin of the input templates according to their Poisson uncertainties. These fluctuations are repeated a large number of times, and the uncertainty on the resulting distribution is taken as the root mean square (RMS) deviation of the fluctuations from the average. As the procedure uses one million random combinations to generate the distributions, The statistical uncertainty from the actual random generations is negligible compared to the uncertainty from measuring the templates.

## 11.3 VALIDATION

The validity of the background estimation technique can be evaluated in both data and simulation. The underlying assumption that random combinations of  $dE/dx$  and momentum can predict a mass distribution in an orthogonal region can be tested using simulated samples where concerns like multiple particle types can be controlled. Using the same technique in another set of signal-depleted regions in data then extends this confidence to the more complicated case where several particle species are inherently included.

### 11.3.1 CLOSURE IN SIMULATION

The first test of the procedure is done using a simulated sample of  $W \rightarrow \mu\nu$  decays. These types of events provide the ingredients required to test the background estimate,  $E_T^{\text{miss}}$  and isolated tracks, with high statistics. In this example there is no signal, so simulated events in the orthogonal CRs are used to estimate the shape of the mass distribution of the simulated events in the signal region. To reflect the different topology for W boson decays, the CRs use slightly modified definitions. In all CRs, the requirement of  $p > 150$  GeV and the SM rejection

requirements are removed. Additionally, for the signal region the requirement on  $E_T^{\text{miss}}$  is relaxed to 30 GeV and the corresponding inverted requirement on CR2 is also set at 30 GeV.

With these modified selections, the simulated and randomly generated distributions of  $M_{dE/dx}$  are shown in Figure 90. This figure includes the mass distributions before and after the requirement on  $dE/dx$ , which significantly shapes the distributions. In both cases the background estimation technique reproduces the shape of  $M_{dE/dx}$  in the signal region. There is a small difference in the positive tail of the mass distribution prior to the ionization cut, where the random events underestimate the fraction of tracks with mass above 150 GeV by about 20%. After the ionization requirement, however, this discrepancy is not present and the two distributions agree to within statistical uncertainties in the positive tail.

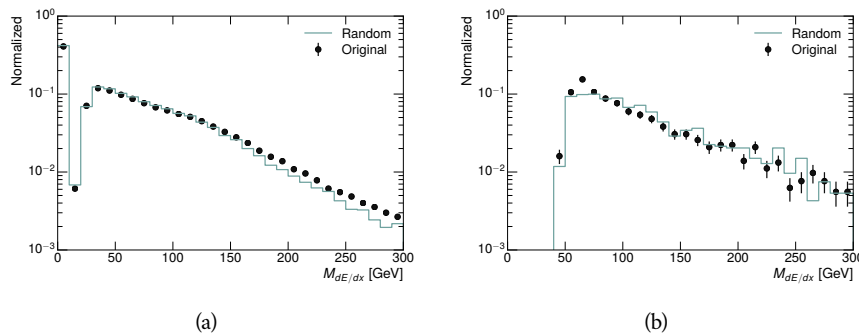


Figure 90: The distribution of  $M_{dE/dx}$  (a) before and (b) after the ionization requirement for tracks in simulated W boson decays and for the randomly generated background estimate.

This ability to reproduce the shape of the mass distribution in simulated events shows that the technique works as expected. No significant biases are acquired in using low  $dE/dx$  events to select kinematic templates or in using low  $E_T^{\text{miss}}$  events to select ionization templates, as either would result in a mismodeling of the shape of the mass distribution. The simulated events contain only one particle type, however, so this test only establishes that the technique works well when the the CRs are populated by exactly the same species.

### 11.3.2 VALIDATION REGION IN DATA

The second test of the background estimate is performed using data in an orthogonal validation region. The validation region, and the corresponding CRs, are formed using the same selection requirements as in the nominal method but with a modified requirement on momentum,  $50 < p[\text{GeV}] < 150$ . This allows the technique to be checked in a region with very similar properties but where the signal is depleted, as the majority of the signal has momentum above 150 GeV while the backgrounds are enhanced below that threshold. Any biases on the particle composition of the CRs for the signal region will be reflected in the CRs used to estimate the mass distribution in the validation region.

Figure 91 shows the measured and randomly generated mass distributions for data before and after the ionization requirement. The background estimate models the actual background before the ionization requirement very well, with good agreement to within the statistical uncertainties out to the limit of the mass distribution. There are very few events in the validation region after the ionization requirement, but the few observed events are consistent with the background prediction. The good agreement in this validation region provides a confirmation that the technique works even in the full-complexity case with multiple particle types entering the distributions. Any bias from changes in particle composition between regions is small compared to statistical uncertainties.

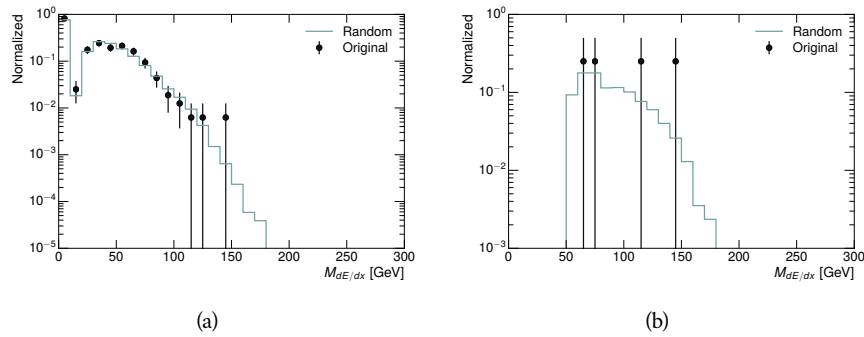


Figure 91: The distribution of  $M_{dE/dx}$  (a) before and (b) after the ionization requirement for tracks in the validation region and for the randomly generated background estimate.

## 11.4 EXPECTED BACKGROUND

Using the full technique in the primary regions described in Section 11.2 provides a final background estimate for the signal region of this search. It predicts a total background of  $11.1 \pm 1.7$  events in the **LL** region and  $17.2 \pm 2.6$  events in the **VLL** region. Table 10 shows the number of events predicted in mass windows for the grid of mass points, for each of the **LL** and **VLL** signal regions. Only one to two events are expected in each mass window, as the background distribution falls with increasing mass.

Mass	Expected Background, <code>LL</code>	Expected Background, <code>VLL</code>
1000	$1.328 \pm 0.063$	$1.803 \pm 0.081$
1100	$1.255 \pm 0.060$	$1.409 \pm 0.069$
1200	$1.193 \pm 0.058$	$1.310 \pm 0.066$
1300	$0.997 \pm 0.051$	$1.431 \pm 0.069$
1400	$1.131 \pm 0.056$	$1.273 \pm 0.065$
1500	$1.111 \pm 0.055$	$1.115 \pm 0.059$
1600	$1.193 \pm 0.058$	$1.041 \pm 0.057$
1800	$1.138 \pm 0.056$	$0.918 \pm 0.053$

Table 10: The expected number of background events within each of the mass windows for the stable and metastable signal regions.

## SYSTEMATIC UNCERTAINTIES

---

A number of systematic uncertainties affect the interpretation of the results of the search. These uncertainties can be broken down into two major categories, those which affect the estimate of the background using data and those which affect the measurement of the signal yield estimated with simulated events. The total measured systematic uncertainties range between 6-7% for the background estimation and 29-33% for the signal yield depending on lifetime. These systematic uncertainties are expected to be small compared to the statistical fluctuations of the measured yields so that measured cross-sectional limits will be dominated by statistical uncertainties. Only the systematic uncertainties on the background estimation are relevant for the search for LLPs, as the systematics on the signal yield enter only into the calculation of limits in the absence of a signal. The following sections describe each source of systematic uncertainty for each of the two types.

### 12.1 BACKGROUND ESTIMATE

The systematic uncertainties on the background estimate come primarily from considering alternative methods for generating the background distributions. These uncertainties are small compared to the statistical uncertainties on the background estimate which come from the limited statistics in measuring the template distributions, as described in Section 11.2. They are summarized in Table 11.

Source of Uncertainty:	Value [%]
Analytic Description of $dE/dx$	4.0
Muon Fraction ( <a>VLL</a> Region only)	3.0
IBL Ionization Correction	3.8
Normalization	3.0
Total ( <a>LL</a> Region):	6.3
Total ( <a>VLL</a> Region):	7.0

Table 11: A summary of the sources of systematic uncertainty for the data-driven background in the signal region. If the uncertainty depends on the mass, the maximum values are reported.

### 12.1.1 ANALYTIC DESCRIPTION OF $dE/dx$

The background estimate uses a binned template distribution to estimate the  $dE/dx$  of tracks in the signal region, as described in Section 11.2. It is also possible to fit that measured distribution to a functional form to help smooth the distribution in the tails of  $dE/dx$  where the template is driven by a small number of tracks. Both Landau convolved with a Gaussian and Crystal Ball functions are considered as the functional form and used to re-estimate the background distribution. The deviations compared to the nominal method are found to be 4%, and this is taken as a systematic uncertainty to cover the inability to carefully predict the contribution from the long tail of  $dE/dx$  where there are few measurements available in data.

### 12.1.2 MUON FRACTION

The signal region for **VLL** R-Hadrons explicitly includes tracks identified as muons, which have a known difference in their  $dE/dx$  distributions compared to non-muon tracks (Section 11.1). To account for a difference in muon fraction between the background region and the signal region for this selection, the  $dE/dx$  templates for muons and non-muons are measured separately and then the relative fraction of each is varied in the random generation. The muon fraction is varied by its statistical uncertainty and the resulting difference of 3% in background yield is taken as the systematic uncertainty.

### 12.1.3 **IBL** CORRECTIONS

The **IBL**, described in Section 5.3.1, received a significant dose of radiation during the data collection in 2015. The irradiation can cause a drift in the **ToT** calibration of the frontend electronics and thus alter the  $dE/dx$  measurement which includes the **ToT** output by the **IBL**. These effects are corrected for in the nominal analysis by scaling the  $dE/dx$  measurements by a constant factor derived for each run to match the average  $dE/dx$  value to a reference run. However, this corrective factor does not account for inter-run variations. To account for the potential drift of  $dE/dx$  within a single run, the correction procedure is repeated by varying the corrections up and down by the maximal run-to-run variation from the full data-taking period, which results in an uncertainty of 3.8%.

### 12.1.4 NORMALIZATION

As described in Section 11.2, the generated distribution of masses is normalized in a shoulder region ( $M < 160$  GeV) where signals have been excluded by previous analyses. That normalization factor is varied by its statistical uncertainty and the resulting fluctuation in the mass distribution of 3% is taken as a systematic uncertainty on the background estimate.

## 12.2 SIGNAL YIELD

The systematic uncertainties on the signal yield can be divided into three categories; those on the simulation process, those on the modeling of the detector efficiency or calibration, and those affecting the overall signal yield. They are summarized in Table 11. The largest uncertainty comes from the uncertainty on the production cross section for gluinos.

Source of Uncertainty	-[%]	+[%]
ISR Modeling ( <a href="#">LL</a> Region)	1.5	1.5
ISR Modeling ( <a href="#">VLL</a> Region)	14	14
Pile-up Reweighting	1.1	1.1
Trigger Efficiency Reweighting	0.9	0.9
$E_T^{\text{miss}}$ Scale	1.1	2.2
Ionization Parametrization	7.1	0
$\mu$ Identification	4.3	4.3
Luminosity	5	5
Signal size uncertainty	28	28
Total ( <a href="#">LL</a> Region)	30	29
Total ( <a href="#">VLL</a> Region)	33	32

Table 12: A summary of the sources of systematic uncertainty for the simulated signal yield. The uncertainty depends on the mass and lifetime, and the maximum negative and positive values are reported in the table.

### 12.2.1 ISR MODELING

As discussed in Section 9.2, MadGraph is expected to reproduce the distribution of [ISR](#) in signal events more accurately than the nominal Pythia samples [94]. The analysis reweights the distribution of [ISR](#) in the simulated signal events to match the distribution found in generated MadGraph samples. This has an effect on the selection efficiency in the signal samples, where [ISR](#) contributes to the generation of  $E_T^{\text{miss}}$ . To account for the potential inaccuracy on the simulation of [ISR](#) at high energies, half of the difference between the signal efficiency with the reweighted distribution and the original distribution is taken as a systematic uncertainty.

### 12.2.2 PILEUP REWEIGHTING

The simulated events were generated prior to data collection with an estimate of the average number of interactions per bunch crossing. This estimate does not match the value of pileup during actual data collection, but a large fraction of the

simulated events would be discarded in order to match the distribution in data. Therefore the simulated signal events are not reweighted for pileup by default in the analysis. The effect of the pileup on signal efficiency is not expected to depend on the mass or lifetime of the generated signal events, which allows all of the generated signal events to be used together to assess the pileup dependence. To account for the potential effect of the difference in the number of interactions per bunch crossing between data and simulation, the difference in yield between the nominal signal events and the reweighted events averaged over all masses and lifetimes is taken as a systematic uncertainty on the yield for each mass and lifetime (1.1%).

### 12.2.3 TRIGGER EFFICIENCY REWEIGHTING

As described in Section 10.2, the selection for this analysis does not require a sufficiently large value of  $E_T^{\text{miss}}$  to be above the plateau of trigger efficiency. Therefore, some signal events which would otherwise pass the event selection can be excluded because of the trigger requirement. These effects can be difficult to estimate in simulation, and thus are constrained by comparing data and simulated events in an alternative W boson region which uses decays to muons to find a relatively pure sample of events with missing energy. The trigger efficiencies for data and simulated W events are shown in Figure 92. The comparison between data and MC in this region constrains the simulation of the trigger efficiency. The simulated signal events are reweighted by the ratio of data to simulation in the W boson decays, while the difference between the data and simulation in those decays is taken as a systematic uncertainty. This results in an uncertainty of only 0.9% as the majority of events are well above the plateau and the disagreement between data and simulation is small even below that plateau.

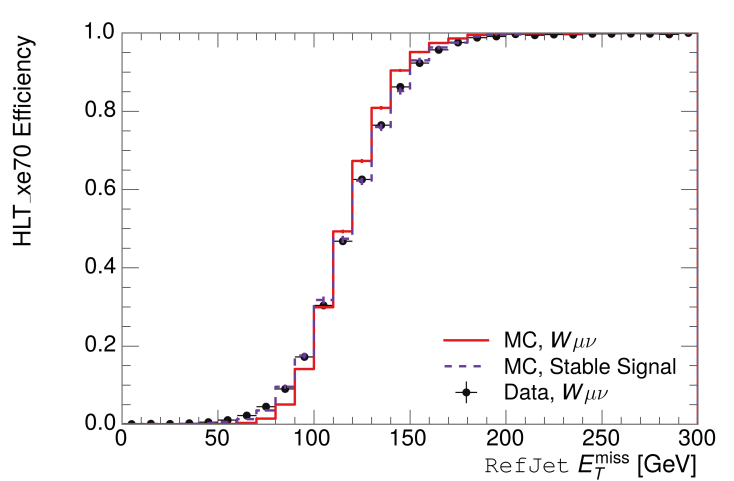


Figure 92: The trigger efficiency for the HLT\_xe70 trigger requirement as a function of Calorimeter  $E_T^{\text{miss}}$  for simulated data events with a W boson selection. Simulated signal events and simulated W boson events are also included.

Systematic Variation	-[%]	+[%]
JET_GroupedNP_1	-0.7	1.3
JET_GroupedNP_2	-0.7	1.2
JET_GroupedNP_3	-0.5	1.3

Table 13: Example of the contributing systematic variations to the total systematic for the  $E_T^{\text{miss}}$  Scale, as measured in a 1200 GeV, VLL R-Hadron signal sample.

#### 12.2.4 MISSING TRANSVERSE MOMENTUM SCALE

Variations on the JES enter into this analysis only in the requirement on  $E_T^{\text{miss}}$ , as variations on individual jets can alter the reconstructed  $E_T^{\text{miss}}$  in signal events. The effect of the measured  $E_T^{\text{miss}}$  is evaluated by varying the  $E_T^{\text{miss}}$  scale according to the one sigma variations on objects affecting event kinematics in simulated signal events. Missing energy is reconstructed from fully reconstructed objects so any systematic uncertainties affecting jets, muons, electrons, or the  $E_T^{\text{miss}}$  soft terms are included. The variations on these objects are taken from measurements in data using balance techniques as discussed in Section 6.4.3. The resulting difference in selection efficiency is expected to be small, because the jet variations only alter energies by a few percent. The only non-negligible contributions found using this method are itemized in Table 13 for an example signal sample (1200 GeV, VLL R-Hadron), where the systematic is measured as the relative difference in the final signal efficiency after applying the associated variation through the CP tools. The only variations that are significant are the grouped jet systematic variations, which combine recommended jet systematic uncertainties into linearly independent variations.

As the peak of the reconstructed  $E_T^{\text{miss}}$  distribution in the signal is significantly above the current threshold for events which pass the trigger requirement, the effect of scale variation is expected to be small, which is consistent with the measured systematic error of approximately 2%. Events which do not pass the trigger requirement usually fail because there are no ISR jets in the event to balance the R-hadrons' transverse momentum, so the reconstructed  $E_T^{\text{miss}}$  is low and therefore also expected to be not very sensitive to scale changes.

#### 12.2.5 MOMENTUM PARAMETRIZATION

The uncertainty on the signal efficiency from track momentum is calculated using the sagitta bias for  $q/P_{\gamma}$ , the only systematic variation of tracking that effects track momentum. The systematic is only important for tracks that are near the 150 GeV momentum threshold, as the variation may push these tracks above or below the selection requirement. Because the majority of R-Hadron tracks are well above this value (Figure 82), the resulting uncertainty is expected to be small. This uncertainty is propagated to the final selection efficiency by varying

the track momentum by the measured one sigma variations from tracking measurements [32], and the associated uncertainty is found to be negligible (0.3%).

#### 12.2.6 IONIZATION REQUIREMENT

The  $dE/dx$  distributions in data and simulated events have different most probable values, which is due in part to radiation effects in the detector that are not fully accounted for in the simulation. The difference does not affect the mass measurement used in this analysis, as independent calibrations are done in simulation and in data. However, it does affect the efficiency of the high  $dE/dx$  selection requirement. To calculate the size of the effect on the signal efficiency, the  $dE/dx$  distribution in signal simulation is scaled by a factor obtained from comparing the  $dE/dx$  distribution of inclusive tracks in data and in simulation. The difference in efficiency for this sample with a scaled  $dE/dx$  distribution, relative to the nominal case, is taken as a systematic uncertainty on signal efficiency. The uncertainty is as large as 7% for low masses and falls to a negligible effect for large masses.

#### 12.2.7 ELECTRON AND JET REJECTION

The systematic uncertainty on the electron rejection is measured by varying the EM fraction requirement significantly, from 0.95 to 0.9. This is found to have a less than 0.04% effect on signal acceptance, on average, and so is completely negligible. Similarly, the uncertainty on jet rejection is measured by tightening the  $E/p$  requirement from 0.5 to 0.4. This is found to have no effect on signal acceptance, so again the systematic is again negligible.

#### 12.2.8 MUON VETO

The signal region for [LL](#) particles has a requirement that the candidate tracks are not identified as medium muons because the majority of R-Hadrons in the lifetime range included in that region do not reach the muon spectrometers before they decay. However, the exponential tail of the R-Hadron lifetime distribution results in some R-Hadrons traversing the muon spectrometer. Even these R-Hadrons can still fail the muon medium identification some of the time, because they may arrive late to the muon spectrometer as discussed in Section 9.1.1. The hits generated by a R-Hadron will not be readout if it arrives 25 ns after the bunch crossing, causing it to fail the loose muon selection (Section 6.3.1). This can be seen in Figure 93, which shows the efficiency of the muon veto as a function of  $1/\beta$ , for two simulated [VLL](#) R-Hadron samples.

Thus, the efficiency of the muon veto depends on the timing resolution of the spectrometer, so an uncertainty is applied to the signal efficiency to cover differences in timing resolution between data and simulation. First, a sample of  $Z \rightarrow \mu\mu$  events is selected in data in which one of the muons has a late arrival time measured in the [MDT](#). Then the reconstructed  $\beta$  distribution is compared to the distribution in simulated  $Z \rightarrow \mu\mu$  events; the difference between these

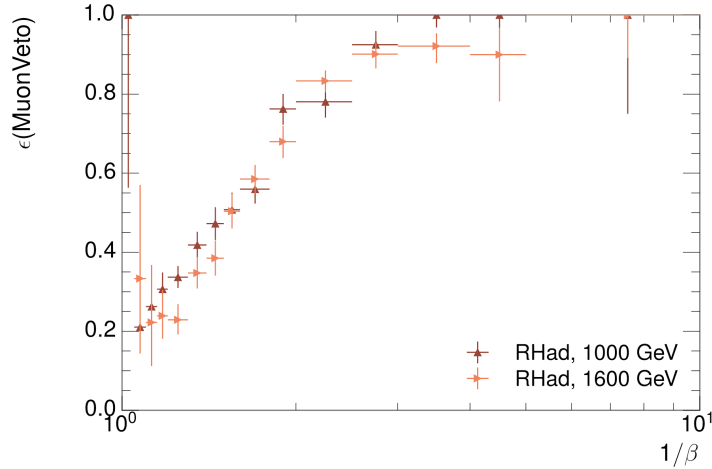


Figure 93: The efficiency of the muon veto for  $R$ -hadrons of two different masses, as a function of  $\frac{1}{\beta}$  for simulated R-Hadron tracks.

two distributions reflects the difference in timing resolution between data and simulation. To emulate this difference in simulated signal events, the magnitude of the difference is used to scale and shift the true  $\beta$  distribution of R-Hadrons in simulation. Signal events are then reweighted based on this varied  $\beta$  distribution, and the difference in the efficiency of the muon veto selection is compared with the nominal and reweighted true  $\beta$  distributions. The difference in muon veto efficiency is taken as a systematic uncertainty of the muon veto.

The comparison of reconstructed  $\beta$  between data and simulation is performed separately in the barrel, transition, and endcap regions of the spectrometer, and the reweighting of the true  $\beta$  distribution in signal is done per region. The comparison of average reconstructed MDT  $\beta$  between data and simulation for the barrel region is shown in Figure 94 for  $Z \rightarrow \mu\mu$  events. As expected, The uncertainty is found to be negligible for  $R$ -hadrons with short lifetimes, and is only significant for lifetimes above 30 ns.

#### 12.2.9 LUMINOSITY

The luminosity uncertainty is provided by a luminosity measurement on ATLAS and was measured to be 5% at the time of the publication of this analysis. The uncertainty is estimated by comparing luminosity measurements using several independent luminometers [109].

#### 12.2.10 SIGNAL CROSS SECTION

As discussed in Section 9.2, the signal cross sections are calculated at NLO in the strong coupling constant with a resummation of soft-gluon emission at NLL. The nominal predictions and the uncertainties for each mass point are taken from an envelope of cross-section predictions using different PDF sets and factorization

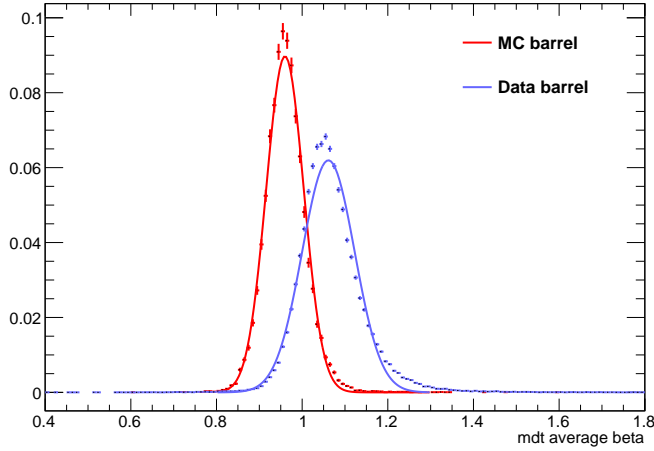


Figure 94: The average reconstructed MDT  $\beta$  distribution for  $Z \rightarrow \mu\mu$  events in which one of the muons has a late arrival time in the [MDT](#), for both data and simulation. A gaussian fit is superimposed.

and renormalization scales [104], as discussed in Section 9.2. The uncertainties on those cross sections range between 14% and 28% for R-Hadrons in the range of 400 to 1800 GeV [105, 106]. The uncertainty increases with the mass.

## RESULTS

---

Sixteen events were observed in the **VLL** signal region and eleven events were observed in the **LL** signal region, prior to requirements on the candidate track mass. The background estimate predicts  $17 \pm 2.6(\text{stat}) \pm 1.2(\text{syst})$  events for the **VLL** region and  $11.1 \pm 1.7(\text{stat}) \pm 0.7(\text{syst})$  events for the **LL** region. These counts are summarized in Table 14.

The mass estimated using  $dE/dx$  (Section 10.4.1) provides the final discriminating variable, where the signal would be expected as an excess in the falling exponential tail of the expected background. The observed distribution of masses is shown in Figure 95, along with the predicted distribution from the background estimate for each signal region. Both include a few example simulated signal distributions, which show the scale of an excess were the R-Hadron signals present. There is no statistically significant evidence of an excess in the data over the background estimation. From this distribution it is clearly possible to rule out signals with lower masses, around 1200 GeV, which have larger cross sections.

### 13.1 CROSS SECTION LIMITS

Because there is no significant excess of events observed in the signal region, this analysis sets upper limits on the allowed cross section for R-Hadron production. These limits are set for each mass point by counting the observed events in data, along with the expected background and simulated signal events, in windows of mass. The mass windows are formed by fitting the distribution of signal events to a Gaussian distribution, and the window is then  $\pm 1.4\sigma$  around the center of that Gaussian. Two examples of the windows formed by this procedure are shown in Tables 15-16, for the **VLL** and 10 ns working points. The corresponding counts of observed data, expected background, and simulated signal for those same working points are shown in Tables 17-18. Appendix A includes the mass windows and counts for all of the considered signal points.

The 95% confidence level upper limits on the cross sections for a large grid of masses (between 800 and 1800 GeV) and lifetimes (between 0.4 and **VLL**) are

Selection Region	Expected Background	Data
<b>VLL</b>	$17.2 \pm 2.6 \pm 1.2$	16
<b>LL</b>	$11.1 \pm 1.7 \pm 0.7$	11

Table 14: The estimated number of background events and the number of observed events in data for the specified selection regions prior to the requirement on mass. The background estimates show statistical and systematic uncertainties.

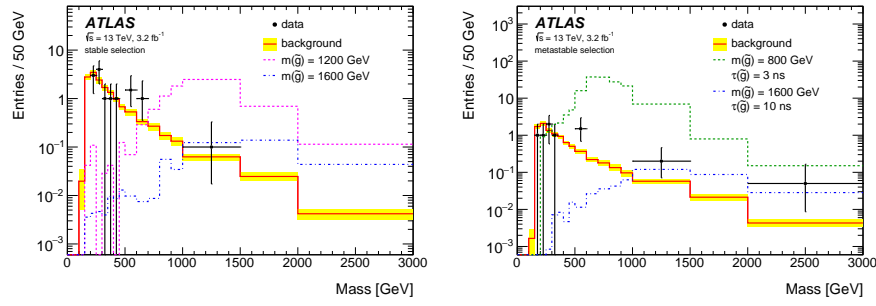


Figure 95: The observed mass distribution of events in data and the generated background distribution in (a) the [VLL](#) and (b) the [LL](#) signal region. A few example simulated signal distributions are superimposed.

$m(\tilde{g})$ [GeV]	Left Extremum [GeV]	Right Extremum [GeV]
1000	655	1349
1100	734	1455
1200	712	1631
1300	792	1737
1400	717	1926
1500	815	2117
1600	824	2122
1700	900	2274
1800	919	2344

Table 15: The left and right extremum of the mass window for each generated mass point with a 10 ns lifetime.

$m(\tilde{g})$ [GeV]	Left Extremum [GeV]	Right Extremum [GeV]
800	627	1053
1000	726	1277
1200	857	1584
1400	924	1937
1600	993	2308
1800	1004	2554

Table 16: The left and right extremum of the mass window used for each generated [VLL](#) mass point.

$m(\tilde{g})$ [GeV]	Expected Signal	Expected Background	Observed Data
800	$462.83 \pm 14.86$	$1.764 \pm 0.080$	2
1000	$108.73 \pm 3.38$	$1.458 \pm 0.070$	1
1200	$31.74 \pm 0.95$	$1.137 \pm 0.060$	1
1400	$10.22 \pm 0.29$	$1.058 \pm 0.058$	1
1600	$3.07 \pm 0.09$	$0.947 \pm 0.054$	1
1800	$1.08 \pm 0.05$	$0.940 \pm 0.054$	1

Table 17: The expected number of signal events, the expected number of background events, and the observed number of events in data with their respective statistical errors within the respective mass window for each generated `VLL` mass point

$m(\tilde{g})$ [GeV]	Expected Signal	Expected Background	Observed Data
1000	$144.48 \pm 5.14$	$1.499 \pm 0.069$	2
1100	$73.19 \pm 2.61$	$1.260 \pm 0.060$	2
1200	$41.54 \pm 1.41$	$1.456 \pm 0.067$	2
1300	$22.58 \pm 0.77$	$1.201 \pm 0.058$	2
1400	$12.70 \pm 0.42$	$1.558 \pm 0.071$	2
1500	$6.73 \pm 0.24$	$1.237 \pm 0.060$	2
1600	$3.90 \pm 0.13$	$1.201 \pm 0.058$	2
1700	$2.27 \pm 0.07$	$1.027 \pm 0.052$	2
1800	$1.34 \pm 0.04$	$1.019 \pm 0.052$	2

Table 18: The expected number of signal events, the expected number of background events, and the observed number of events in data with their respective statistical errors within the respective mass window for each generated mass point with a lifetime of 10 ns.

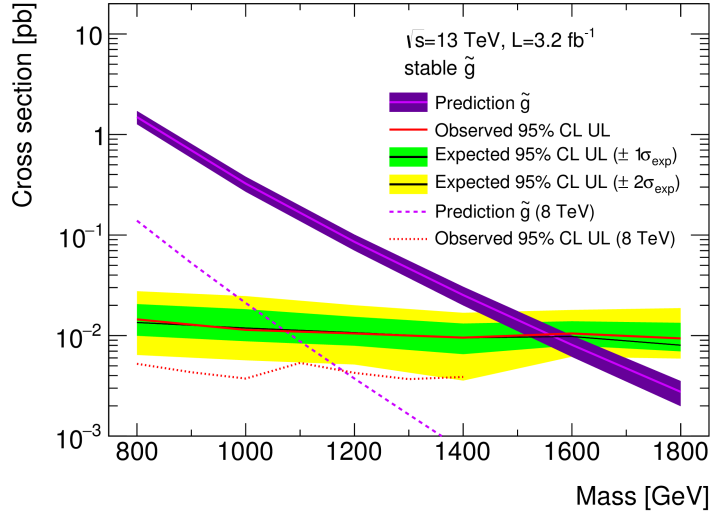


Figure 96: The observed and expected cross section limits as a function of mass for the [VLL](#) simulated signal. The predicted cross section values for the corresponding signals are also shown.

extracted from these counts with the  $CL_S$  method using the profile likelihood ratio as a test statistic [110]. For this procedure, the systematic uncertainties estimated for the signal and background yields are treated as Gaussian-distributed nuisance parameters. The uncertainty on the normalization of the expected background distribution is included in the expected background events. At this point the expected cross section limit is calculated for both the [LL](#) and [VLL](#) signal region for each lifetime point, and the region with the best expected limit is selected for each lifetime. Using that procedure, the [LL](#) region is used for lifetimes up to and including 30 ns, and the [VLL](#) region for lifetimes above it.

The resulting upper limits on the cross sections are shown as a function of mass in Figure 96 and Figure 97 for each lifetime considered. The limits are interpolated linearly between each mass point, and the dependence of the limit on the mass is small as the efficiency is relatively constant for large R-Hadron masses. There is however a strong dependence on lifetime, as discussed in Section 10.5, where the probability to form a fully reconstructed track and the kinematic freedom to produce  $E_T^{\text{miss}}$  result in a local maximum in the limit at 10-30 ns. The figures also include the expected cross section for pair-produced gluino R-Hadrons for reference. For the 10 ns and [VLL](#) cross section limits, both the observed limit and expected cross section for the Run 1, 8 TeV version of this analysis are also shown. There the cross section limits are lower because of the larger available luminosity. The signal cross sections are also much lower because of the lower collision energy.

## 13.2 MASS LIMITS

The cross section limits can then be used to derive a lower mass limit for gluino R-Hadrons by comparing them to the theoretically predicted production cross

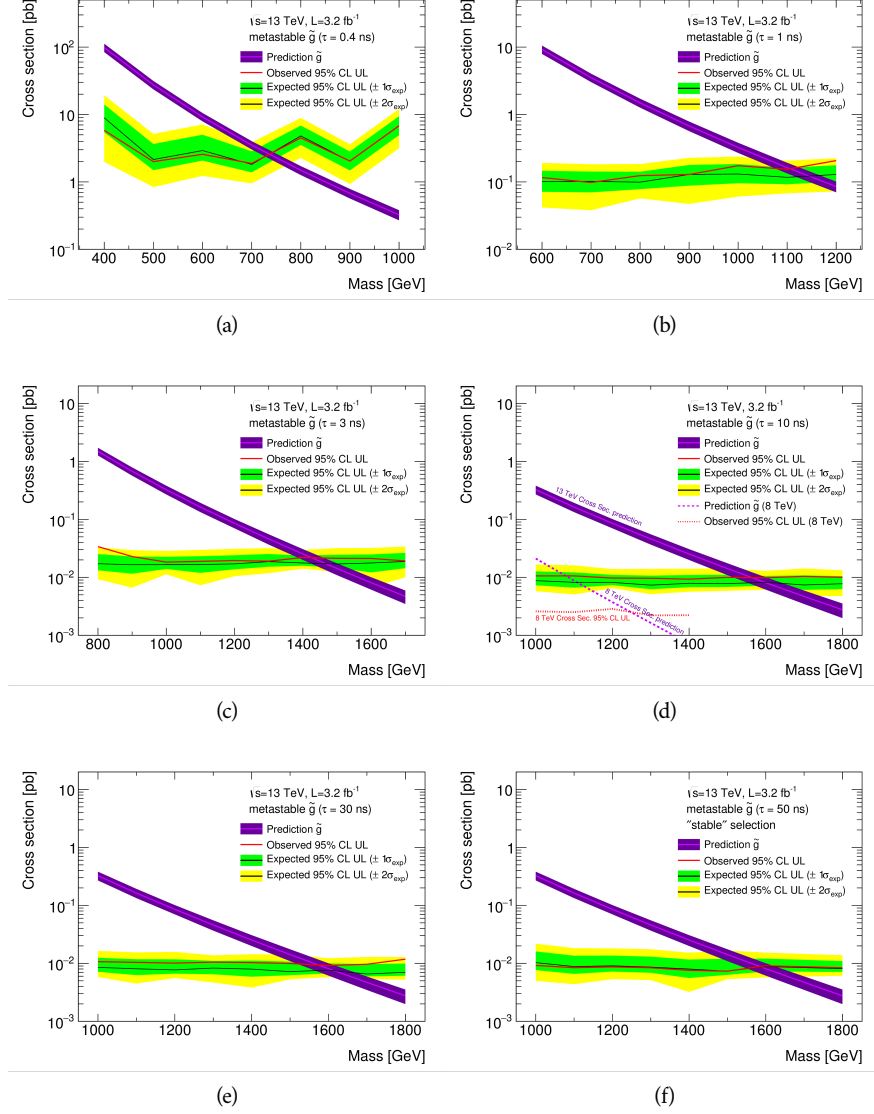


Figure 97: The observed and expected cross section limits as a function of mass for each generated lifetime. The predicted cross section values for the corresponding signals are also shown. An example of Run 1 cross section limits and predicted cross sections are shown in (d) for comparison.

sections. These mass limits range from only 740 GeV at the lowest lifetimes considered, where the selection efficiency is very low, to up to 1580 GeV at 30 ns where the selection efficiency is maximized. The observed and expected mass limits for each lifetime point are detailed in Table 19, which also lists which selection region was used for each lifetime. These excluded range of masses as a function of lifetime is also shown in Figure 98. The Run 1 limits are included for comparison; the limits have increased by about 200 GeV on average. The search has also improved since the previous incarnation from Run 1 in optimizing the region between 30 GeV and detector-stable lifetimes by introducing the second signal region. The definition of the **VLL** region prevents the significant drop in mass limit that occurred above 30 GeV in the Run 1 analysis.

Selection	$\tau$ [ns]	$M_{\text{obs}} > [\text{GeV}]$	$M_{\text{exp}} > [\text{GeV}]$
<b>LL</b>	0.4	740	730
"	1.0	1110	1150
"	3.0	1430	1470
"	10	1570	1600
"	30	1580	1620
<b>VLL</b>	50	1590	1590
"	<b>VLL</b>	1570	1580

Table 19: The observed and expected 95% CL lower limit on mass for gluino R-Hadrons for each considered lifetime.

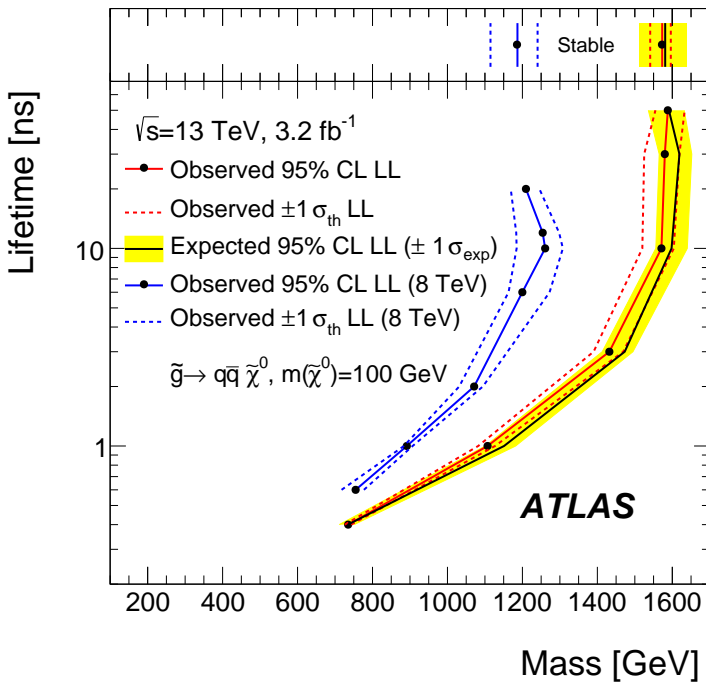


Figure 98: The excluded range of masses as a function of gluino lifetime. The expected lower limit (LL), with its experimental  $\pm 1\sigma$  band, is given with respect to the nominal theoretical cross section. The observed 95% LL obtained at  $\sqrt{s} = 8 \text{ TeV}$  [94] is also shown for comparison.

## SUMMARY AND OUTLOOK

---

The search described herein targetted the unique signature of TeV-scale, charged **LLPs**, which are predicted in a variety of extensions to the **SM** including some versions of **SUSY**. The dataset of 13 TeV proton-proton collisions was collected during 2015 by the ATLAS detector at the **LHC**, with an integrated luminosity of  $3.2 \text{ fb}^{-1}$ . The specific search strategy focused on identifying massive, charged particles which propagate through the Pixel detector in ATLAS by their characteristically large ionization. Recent updates to the strategy also include a number of rejection techniques that significantly reduce **SM** backgrounds compared to previous iterations. The analysis also provided a data-driven background estimation method that was shown to be effective with validation tests in both simulation and actual data.

No significant excesses above the background prediction were found in the data, and so limits were placed on the production of massive, charged, **LLPs**. Using a benchmark model of simulated R-Hadrons, cross sections above 10-100  $\text{fb}$  were excluded at 95% confidence level, depending on the lifetime of the R-Hadron. Together with the predicted gluino pair-production cross sections, these lead to mass limits on R-Hadrons up to 1600 GeV where the search is most sensitive. Though these specific values assume an R-Hadron **LLP**, the search strategy accomodates a number of other species and the limits can be interpreted for other models.

This search plays an important role in the current, combined ATLAS search for long lived particles. The mass limits provided by various ATLAS searches for long-lived gluino R-Hadrons can be seen in Figure 99. This search provides the strongest limit for lifetimes between 3 ns up through very long lifetimes, where it is still competitive with dedicated searches for **VLL** particles. The limits placed on gluino production are very similar to the limits on promptly decaying models.

These results are expected to be significantly improved in the following years, primarily because of continuing data collection at 13 TeV at the **LHC**. During 2016, but after the release of this analysis, ATLAS recorded an additional  $35.5 \text{ fb}^{-1}$  of collisions, and analysis of this data will significantly extend the limits presented here. The next iteration of the analysis can also provide additional interpretations of the search, by explicitly including other models like stop R-Hadrons and charginos in the limit calculations, as has been done in previous searches [94]. This strategy will continue to provide a competitive approach to discovering new **LLPs** throughout the lifetime of the **LHC**.

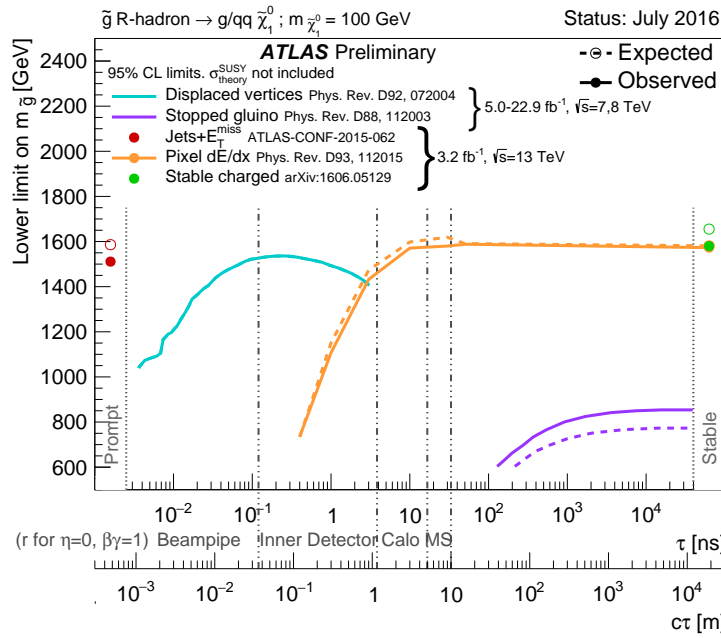


Figure 99: The constraints on the gluino mass as a function of lifetime for a split-supersymmetry model with the gluino R-Hadrons decaying into a gluon or light quarks and a neutralino with mass of 100 GeV. The solid lines indicate the observed limits, while the dashed lines indicate the expected limits. The area below the curves is excluded. The dots represent results for which the particle is assumed to be prompt or VLL. This curve representing this analysis is shown in orange.

PART V

APPENDIX

# A

## EXPANDED R-HADRON YIELDS AND LIMITS

---

$m(\tilde{g})$ [GeV]	Left Extremum [GeV]	Right Extremum [GeV]
1000	682	1387
1100	763	1478
1200	801	1606
1300	809	1841
1400	861	2011
1500	920	2032
1600	952	2173
1800	1017	2422

Table 20: The left and right extremum of the mass window for each generated mass point with a 50 ns lifetime.

$m(\tilde{g})$ [GeV]	Left Extremum [GeV]	Right Extremum [GeV]
1000	689	1321
1100	746	1513
1200	788	1670
1300	860	1734
1400	833	1925
1500	852	2048
1600	833	2283
1700	946	2379
1800	869	2505

Table 21: The left and right extremum of the mass window for each generated mass point with a 30 ns lifetime.

$m(\tilde{g})$ [GeV]	Left Extremum [GeV]	Right Extremum [GeV]
1000	655	1349
1100	734	1455
1200	712	1631
1300	792	1737
1400	717	1926
1500	815	2117
1600	824	2122
1700	900	2274
1800	919	2344

Table 22: The left and right extremum of the mass window for each generated mass point with a 10 ns lifetime.

$m(\tilde{g})$ [GeV]	Left Extremum [GeV]	Right Extremum [GeV]
800	531	1065
900	576	1165
1000	610	1345
1100	635	1432
1200	663	1563
1300	620	1667
1400	742	1727
1500	761	1937
1600	573	2000
1700	621	2182

Table 23: The left and right extremum of the mass window used for each generated mass point with a lifetime of 3 ns.

$m(\tilde{g})$ [GeV]	Left Extremum [GeV]	Right Extremum [GeV]
600	411	758
700	385	876
800	486	970
900	406	987
1000	408	1136
1100	555	1196
1200	516	1378

Table 24: The left and right extremum of the mass window used for each mass point with a lifetime of 1 ns.

$m(\tilde{g})$ [GeV]	Left Extremum [GeV]	Right Extremum [GeV]
400	204	510
500	295	639
600	288	702
700	323	701
800	190	771
900	277	677
1000	249	688

Table 25: The left and right extremum of the mass window for each generated mass point with a lifetime of 0.4 ns.

$m(\tilde{g})$ [GeV]	Left Extremum [GeV]	Right Extremum [GeV]
800	627	1053
1000	726	1277
1200	857	1584
1400	924	1937
1600	993	2308
1800	1004	2554

Table 26: The left and right extremum of the mass window used for each generated stable mass point.

$m(\tilde{g})$ [GeV]	Expected Signal	Expected Background	Observed Data
1000	$131.18 \pm 6.35$	$1.803 \pm 0.081$	1
1100	$71.11 \pm 3.35$	$1.409 \pm 0.069$	1
1200	$37.18 \pm 1.75$	$1.310 \pm 0.066$	1
1300	$20.76 \pm 0.95$	$1.431 \pm 0.069$	1
1400	$12.63 \pm 0.57$	$1.273 \pm 0.065$	1
1500	$6.57 \pm 0.29$	$1.115 \pm 0.059$	1
1600	$3.56 \pm 0.16$	$1.041 \pm 0.057$	1
1800	$1.27 \pm 0.05$	$0.918 \pm 0.053$	1

Table 27: The expected number of signal events, the expected number of background events, and the observed number of events in data with their respective statistical errors within the respective mass window for each generated mass point with a lifetime of 50 ns.

$m(\tilde{g})$ [GeV]	Expected Signal	Expected Background	Observed Data
1000	$144.65 \pm 6.34$	$1.328 \pm 0.063$	2
1100	$75.28 \pm 3.27$	$1.255 \pm 0.060$	2
1200	$40.51 \pm 1.75$	$1.193 \pm 0.058$	2
1300	$20.91 \pm 0.93$	$0.997 \pm 0.051$	2
1400	$11.97 \pm 0.51$	$1.131 \pm 0.056$	2
1500	$6.81 \pm 0.28$	$1.111 \pm 0.055$	2
1600	$4.19 \pm 0.16$	$1.193 \pm 0.058$	2
1700	$2.42 \pm 0.09$	$0.963 \pm 0.050$	2
1800	$1.46 \pm 0.05$	$1.138 \pm 0.056$	3

Table 28: The expected number of signal events, the expected number of background events, and the observed number of events in data with their respective statistical errors within the respective mass window for each generated mass point with a lifetime of 30 ns.

$m(\tilde{g})$ [GeV]	Expected Signal	Expected Background	Observed Data
1000	$144.48 \pm 5.14$	$1.499 \pm 0.069$	2
1100	$73.19 \pm 2.61$	$1.260 \pm 0.060$	2
1200	$41.54 \pm 1.41$	$1.456 \pm 0.067$	2
1300	$22.58 \pm 0.77$	$1.201 \pm 0.058$	2
1400	$12.70 \pm 0.42$	$1.558 \pm 0.071$	2
1500	$6.73 \pm 0.24$	$1.237 \pm 0.060$	2
1600	$3.90 \pm 0.13$	$1.201 \pm 0.058$	2
1700	$2.27 \pm 0.07$	$1.027 \pm 0.052$	2
1800	$1.34 \pm 0.04$	$1.019 \pm 0.052$	2

Table 29: The expected number of signal events, the expected number of background events, and the observed number of events in data with their respective statistical errors within the respective mass window for each generated mass point with a lifetime of 10 ns.

$m(\tilde{g})$ [GeV]	Expected Signal	Expected Background	Observed Data
800	$362.97 \pm 14.68$	$1.841 \pm 0.080$	5
900	$169.20 \pm 6.69$	$1.710 \pm 0.076$	3
1000	$84.78 \pm 3.23$	$1.727 \pm 0.076$	2
1100	$40.06 \pm 1.60$	$1.679 \pm 0.075$	2
1200	$20.06 \pm 0.81$	$1.598 \pm 0.072$	2
1300	$10.76 \pm 0.43$	$1.851 \pm 0.080$	2
1400	$5.52 \pm 0.22$	$1.374 \pm 0.064$	2
1500	$3.16 \pm 0.13$	$1.355 \pm 0.064$	2
1600	$2.13 \pm 0.11$	$2.235 \pm 0.093$	3
1700	$1.10 \pm 0.06$	$1.995 \pm 0.085$	2

Table 30: The expected number of signal events, the expected number of background events, and the observed number of events in data with their respective statistical errors within the respective mass window for each generated mass point with a lifetime of 3 ns.

$m(\tilde{g})$ [GeV]	Expected Signal	Expected Background	Observed Data
600	$431.80 \pm 36.60$	$2.418 \pm 0.099$	3
700	$192.77 \pm 15.28$	$3.267 \pm 0.126$	3
800	$69.63 \pm 5.90$	$2.125 \pm 0.089$	3
900	$28.91 \pm 2.59$	$3.114 \pm 0.121$	3
1000	$13.64 \pm 1.22$	$3.359 \pm 0.129$	5
1100	$6.13 \pm 0.57$	$1.879 \pm 0.081$	3
1200	$3.24 \pm 0.30$	$2.387 \pm 0.098$	5

Table 31: The expected number of signal events, the expected number of background events, and the observed number of events in data with their respective statistical errors within the respective mass window for each generated mass point with a lifetime of 1 ns.

$m(\tilde{g})$ [GeV]	Expected Signal	Expected Background	Observed Data
400	$181.71 \pm 75.59$	$6.780 \pm 0.238$	4
500	$103.88 \pm 30.05$	$4.310 \pm 0.160$	4
600	$28.34 \pm 9.34$	$4.868 \pm 0.177$	4
700	$13.62 \pm 4.00$	$3.908 \pm 0.147$	4
800	$2.75 \pm 1.15$	$9.001 \pm 0.308$	8
900	$2.25 \pm 0.71$	$5.045 \pm 0.183$	5
1000	$0.34 \pm 0.19$	$6.026 \pm 0.214$	6

Table 32: The expected number of signal events, the expected number of background events, and the observed number of events in data with their respective statistical errors within the respective mass window for each generated mass point with a lifetime of p4 ns.

$m(\tilde{g})$ [GeV]	Expected Signal	Expected Background	Observed Data
800	$462.83 \pm 14.86$	$1.764 \pm 0.080$	2
1000	$108.73 \pm 3.38$	$1.458 \pm 0.070$	1
1200	$31.74 \pm 0.95$	$1.137 \pm 0.060$	1
1400	$10.22 \pm 0.29$	$1.058 \pm 0.058$	1
1600	$3.07 \pm 0.09$	$0.947 \pm 0.054$	1
1800	$1.08 \pm 0.05$	$0.940 \pm 0.054$	1

Table 33: The expected number of signal events, the expected number of background events, and the observed number of events in data with their respective statistical errors within the respective mass window for each generated stable mass point

## BIBLIOGRAPHY

---

- [1] Michael E Peskin and Daniel V Schroeder. “An Introduction to Quantum Field Theory; 1995 ed.” Boulder, CO: Westview, 1995. URL: <https://cds.cern.ch/record/257493>.
- [2] Nobelprize.org. “The 2004 Nobel Prize in Physics - Popular Information”. 2014. URL: <https://cds.cern.ch/record/1165534>.
- [3] K. A. Olive et al. “Review of Particle Physics”. In: *Chin. Phys.* **C38**: (2014), p. 090001.
- [4] A. D. Martin, W. J. Stirling, R. S. Thorne, and G. Watt. “Parton distributions for the LHC”. In: *Eur. Phys. J.* **C63**: (2009), pp. 189–285. arXiv: [0901.0002 \[hep-ph\]](https://arxiv.org/abs/0901.0002).
- [5] Torbjorn Sjöstrand, Stephen Mrenna, and Peter Skands. “PYTHIA 6.4 Physics and Manual”. In: *JHEP* **0605**: (2006), p. 026. arXiv: [hep-ph / 0603175](https://arxiv.org/abs/hep-ph/0603175).
- [6] J. Alwall, R. Frederix, S. Frixione, V. Hirschi, F. Maltoni, O. Mattelaer, H. S. Shao, T. Stelzer, P. Torrielli, and M. Zaro. “The automated computation of tree-level and next-to-leading order differential cross sections, and their matching to parton shower simulations”. In: *JHEP* **07**: (2014), p. 079. arXiv: [1405.0301 \[hep-ph\]](https://arxiv.org/abs/1405.0301).
- [7] S. Agostinelli et al. “GEANT4: A simulation toolkit”. In: *Nucl. Instrum. Meth. A* **506**: (2003), pp. 250–303.
- [8] Prajwal Raj Kafle, Sanjib Sharma, Geraint F. Lewis, and Joss Bland-Hawthorn. “On the Shoulders of Giants: Properties of the Stellar Halo and the Milky Way Mass Distribution”. In: *Astrophys. J.* **794**:1 (2014), p. 59. arXiv: [1408.1787 \[astro-ph.GA\]](https://arxiv.org/abs/1408.1787).
- [9] Savas Dimopoulos and Howard Georgi. “Softly broken supersymmetry and SU(5)”. In: *Nuclear Physics B* **193**:1 (1981), pp. 150 – 162. ISSN: 0550-3213.
- [10] A. Djouadi et al. “The Minimal supersymmetric standard model: Group summary report”. In: *GDR (Groupement De Recherche) - Supersymetrie Montpellier, France, April 15-17, 1998*. 1998. arXiv: [hep-ph/9901246 \[hep-ph\]](https://arxiv.org/abs/hep-ph/9901246). URL: [https://inspirehep.net/record/481987/files/arXiv:hep-ph\\_9901246.pdf](https://inspirehep.net/record/481987/files/arXiv:hep-ph_9901246.pdf).
- [11] Stephen P. Martin. “A Supersymmetry primer”. In: (1997). [Adv. Ser. Direct. High Energy Phys.18,1(1998)]. arXiv: [hep-ph/9709356 \[hep-ph\]](https://arxiv.org/abs/hep-ph/9709356).
- [12] Gilly Elor, Lawrence J. Hall, David Pinner, and Joshua T. Ruderman. “Yukawa Unification and the Superpartner Mass Scale”. In: *JHEP* **10**: (2012), p. 111. arXiv: [1206.5301 \[hep-ph\]](https://arxiv.org/abs/1206.5301).

- [13] ATLAS Collaboration. “ATLAS SUSY Summary”. 2015. URL: [https://atlas.web.cern.ch/Atlas/GROUPS/PHYSICS/CombinedSummaryPlots/SUSY/ATLAS\\_SUSY\\_Summary/history.html](https://atlas.web.cern.ch/Atlas/GROUPS/PHYSICS/CombinedSummaryPlots/SUSY/ATLAS_SUSY_Summary/history.html).
- [14] G. F. Giudice and A. Romanino. “Split supersymmetry”. In: *Nucl. Phys. B* **699**: (2004), p. 65. arXiv: [hep-ph/0406088](https://arxiv.org/abs/hep-ph/0406088).
- [15] N. Arkani-Hamed, S. Dimopoulos, G. F. Giudice, and A. Romanino. “Aspects of split supersymmetry”. In: *Nucl. Phys. B* **709**: (2005), p. 3. arXiv: [hep-ph/0409232](https://arxiv.org/abs/hep-ph/0409232).
- [16] Lawrence J. Hall, Yasunori Nomura, and Satoshi Shirai. “Spread Supersymmetry with Wino LSP: Gluino and Dark Matter Signals”. In: *JHEP* **01**: (2013), p. 036. arXiv: [1210.2395 \[hep-ph\]](https://arxiv.org/abs/1210.2395).
- [17] Lyndon Evans and Philip Bryant. “LHC Machine”. In: *JINST* **3**: (2008), S08001.
- [18] C Lefevre. “LHC: the guide (English version). Guide du LHC (version anglaise)”. 2009. URL: <https://cds.cern.ch/record/1165534>.
- [19] ATLAS Collaboration. “The ATLAS Experiment at the CERN Large Hadron Collider”. In: *JINST* **3**: (2008), S08003.
- [20] S. Chatrchyan et al. “The CMS experiment at the CERN LHC”. In: *JINST* **3**: (2008), S08004.
- [21] A. Augusto Alves Jr. et al. “The LHCb Detector at the LHC”. In: *JINST* **3**: (2008), S08005.
- [22] K. Aamodt et al. “The ALICE experiment at the CERN LHC”. In: *JINST* **3**: (2008), S08002.
- [23] Collaboration LHCb. “For LHCb Talks”. 2012. URL: <http://cds.cern.ch/record/1463546>.
- [24] ATLAS Collaboration. “Luminosity Public Results”. 2016. URL: <https://twiki.cern.ch/twiki/bin/view/AtlasPublic/LuminosityPublicResultsRun2>.
- [25] Ars Technica. “Following protons on a trip to (and through) the LHC”. 2010. URL: <http://arstechnica.com/science/2010/08/following-protons-on-a-trip-to-and-through-the-lhc/>.
- [26] M Capeans, G Darbo, K Einsweiler, M Elsing, T Flick, M Garcia-Sciveres, C Gemme, H Pernegger, O Rohne, and R Vuillermet. “ATLAS Insertable B-Layer Technical Design Report”. Tech. rep. CERN-LHCC-2010-013. ATLAS-TDR-19. 2010. URL: <https://cds.cern.ch/record/1291633>.
- [27] ATLAS Collaboration. “A New Sub Detector for ATLAS”. 2014. URL: <http://atlasexperiment.org/news/2014/a-new-sub-detector-for-ATLAS.html>.
- [28] ATLAS Collaboration. “2015 start-up trigger menu and initial performance assessment of the ATLAS trigger using Run-2 data”. ATL-DAQ-PUB-2016-001. 2016. URL: <https://cds.cern.ch/record/2136007/>.

- [29] T. Cornelissen, M. Elsing, S. Fleischmann, W. Liebig, and E. Moyse. “Concepts, Design and Implementation of the ATLAS New Tracking (NEWT)”. In: (2007). Ed. by A. Salzburger.
- [30] ATLAS Collaboration. “Performance of the ATLAS Inner Detector Track and Vertex Reconstruction in High Pile-Up LHC Environment”. ATLAS-CONF-2012-042. 2012. URL: <https://cds.cern.ch/record/1435196>.
- [31] A. Salzburger. “The ATLAS Track Extrapolation Package”. In: (2007).
- [32] ATLAS Collaboration. “Early Inner Detector Tracking Performance in the 2015 Data at  $\sqrt{s} = 13$  TeV”. ATL-PHYS-PUB-2015-051. 2015. URL: <https://cds.cern.ch/record/2110140>.
- [33] ATLAS Collaboration. “A neural network clustering algorithm for the ATLAS silicon pixel detector”. In: *JINST* **9**: (2014), P09009. arXiv: [1406.7690 \[hep-ex\]](https://arxiv.org/abs/1406.7690).
- [34] ATLAS Collaboration. “Performance of primary vertex reconstruction in proton–proton collisions at  $\sqrt{s} = 7$  TeV in the ATLAS experiment”. ATLAS-CONF-2010-069. 2010. URL: <https://cds.cern.ch/record/1281344>.
- [35] ATLAS Collaboration. “Vertex Reconstruction Performance of the ATLAS Detector at  $\sqrt{s} = 13$  TeV”. ATL-PHYS-PUB-2015-026. 2015. URL: <https://cds.cern.ch/record/2037717>.
- [36] ATLAS Collaboration. “Electron reconstruction and identification efficiency measurements with the ATLAS detector using the 2011 LHC proton–proton collision data”. In: *Eur. Phys. J. C* **74**: (2014), p. 2941. arXiv: [1404.2240 \[hep-ex\]](https://arxiv.org/abs/1404.2240). PERF-2013-03.
- [37] ATLAS Collaboration. “Electron efficiency measurements with the ATLAS detector using the 2012 LHC proton–proton collision data”. ATLAS-CONF-2014-032. 2014. URL: <https://cds.cern.ch/record/1706245>.
- [38] ATLAS Collaboration. “Measurements of the photon identification efficiency with the ATLAS detector using  $4.9 \text{ fb}^{-1}$  of  $pp$  collision data collected in 2011”. ATLAS-CONF-2012-123. 2012. URL: <https://cds.cern.ch/record/1473426>.
- [39] ATLAS Collaboration. “Muon reconstruction performance of the ATLAS detector in proton–proton collision data at  $\sqrt{s} = 13$  TeV”. In: (2016). arXiv: [1603.05598 \[hep-ex\]](https://arxiv.org/abs/1603.05598). PERF-2015-10.
- [40] ATLAS Collaboration. “Topological cell clustering in the ATLAS calorimeters and its performance in LHC Run 1”. In: (2016). arXiv: [1603.02934 \[hep-ex\]](https://arxiv.org/abs/1603.02934). PERF-2014-07.
- [41] ATLAS Collaboration. “Properties of jets and inputs to jet reconstruction and calibration with the ATLAS detector using proton–proton collisions at  $\sqrt{s} = 13$  TeV”. ATL-PHYS-PUB-2015-036. 2015. URL: <https://cds.cern.ch/record/2044564>.

- [42] Matteo Cacciari, Gavin P. Salam, and Gregory Soyez. “The anti- $k_t$  jet clustering algorithm”. In: *JHEP* **04**: (2008), p. 063. arXiv: [0802 . 1189 \[hep-ph\]](#).
- [43] ATLAS Collaboration. “Jet global sequential corrections with the ATLAS detector in proton–proton collisions at  $\sqrt{s} = 8$  TeV”. ATLAS-CONF-2015-002. 2015. URL: <https://cds.cern.ch/record/2001682>.
- [44] ATLAS Collaboration. “A study of the material in the ATLAS inner detector using secondary hadronic interactions”. In: *JINST* **7**: (2012), P01013. arXiv: [1110 . 6191 \[hep-ex\]](#). PERF-2011-08.
- [45] ATLAS Collaboration. “Electron and photon energy calibration with the ATLAS detector using LHC Run 1 data”. In: *Eur. Phys. J. C* **74**: (2014), p. 3071. arXiv: [1407 . 5063 \[hep-ex\]](#). PERF-2013-05.
- [46] ATLAS Collaboration. “A measurement of the calorimeter response to single hadrons and determination of the jet energy scale uncertainty using LHC Run-1  $p\bar{p}$ -collision data with the ATLAS detector”. In: (2016). arXiv: [1607 . 08842 \[hep-ex\]](#). PERF-2015-05.
- [47] ATLAS Collaboration. “Single hadron response measurement and calorimeter jet energy scale uncertainty with the ATLAS detector at the LHC”. In: *Eur. Phys. J. C* **73**: (2013), p. 2305. arXiv: [1203 . 1302 \[hep-ex\]](#). PERF-2011-05.
- [48] ATLAS Collaboration. “The ATLAS Simulation Infrastructure”. In: *Eur. Phys. J. C* **70**: (2010), p. 823. arXiv: [1005 . 4568 \[hep-ex\]](#). SOFT-2010-01.
- [49] T. Sjöstrand, S. Mrenna, and P. Skands. “A Brief Introduction to PYTHIA 8.1”. In: *Comput. Phys. Commun.* **178**: (2008), pp. 852–867. arXiv: [0710 . 3820](#).
- [50] ATLAS Collaboration. “Summary of ATLAS Pythia 8 tunes”. ATL-PHYS-PUB-2012-003. 2012. URL: <http://cds.cern.ch/record/1474107>.
- [51] A.D. Martin, W.J. Stirling, R.S. Thorne, and G. Watt. “Parton distributions for the LHC”. In: *Eur. Phys. J. C* **63**: (2009). Figures from the [MSTW Website](#), pp. 189–285. arXiv: [0901 . 0002](#).
- [52] A. Sherstnev and R.S. Thorne. “Parton Distributions for LO Generators”. In: *Eur. Phys. J. C* **55**: (2008), pp. 553–575. arXiv: [0711 . 2473](#).
- [53] A. Ribon et al. “Status of Geant4 hadronic physics for the simulation of LHC experiments at the start of LHC physics program”. CERN-LCGAPP-2010-02. 2010. URL: <http://lcgapp.cern.ch/project/docs/noteStatusHadronic2010.pdf>.
- [54] M. P. Guthrie, R. G. Alsmiller, and H. W. Bertini. “Calculation of the capture of negative pions in light elements and comparison with experiments pertaining to cancer radiotherapy”. In: *Nucl. Instrum. Meth.* **66**: (1968), pp. 29–36.

- [55] H. W. Bertini and P. Guthrie. “News item results from medium-energy intranuclear-cascade calculation”. In: *Nucl. Instr. and Meth. A* **169**: (1971), p. 670.
- [56] V.A. Karmanov. “Light Front Wave Function of Relativistic Composite System in Explicitly Solvable Model”. In: *Nucl. Phys. B* **166**: (1980), p. 378.
- [57] H. S. Fesefeldt. “GHEISHA program”. Pitha-85-02, Aachen. 1985.
- [58] G. Folger and J.P. Wellisch. “String parton models in Geant4”. In: (2003). arXiv: [nucl-th/0306007](https://arxiv.org/abs/nucl-th/0306007).
- [59] N. S. Amelin et al. “Transverse flow and collectivity in ultrarelativistic heavy-ion collisions”. In: *Phys. Rev. Lett.* **67**: (1991), p. 1523.
- [60] N. S. Amelin et al. “Collectivity in ultrarelativistic heavy ion collisions”. In: *Nucl. Phys. A* **544**: (1992), p. 463.
- [61] L. V. Bravina et al. “Fluid dynamics and Quark Gluon string model - What we can expect for Au+Au collisions at 11.6 AGeV/c”. In: *Nucl. Phys. A* **566**: (1994), p. 461.
- [62] L. V. Bravin et al. “Scaling violation of transverse flow in heavy ion collisions at AGS energies”. In: *Phys. Lett. B* **344**: (1995), p. 49.
- [63] B. Andersson et al. “A model for low- $p_T$  hadronic reactions with generalizations to hadron-nucleus and nucleus-nucleus collisions”. In: *Nucl. Phys. B* **281**: (1987), p. 289.
- [64] B. Andersson, A. Tai, and B. H. Sa. “Final state interactions in the (nuclear) FRITIOF string interaction scenario”. In: *Z. Phys. C* **70**: (1996), pp. 499–506.
- [65] B. Nilsson-Almqvist and E. Stenlund. “Interactions Between Hadrons and Nuclei: The Lund Monte Carlo, Fritiof Version 1.6”. In: *Comput. Phys. Commun.* **43**: (1987), p. 387.
- [66] B. Ganhuyag and V. Uzhinsky. “Modified FRITIOF code: Negative charged particle production in high energy nucleus nucleus interactions”. In: *Czech. J. Phys.* **47**: (1997), pp. 913–918.
- [67] ATLAS Collaboration. “Topological cell clustering in the ATLAS calorimeters and its performance in LHC Run 1”. In: (2016). arXiv: [1603.02934 \[hep-ex\]](https://arxiv.org/abs/1603.02934).
- [68] Peter Speckmayer. “Energy Measurement of Hadrons with the CERN ATLAS Calorimeter”. Presented on 18 Jun 2008. PhD thesis. Vienna: Vienna, Tech. U., 2008. URL: <http://cds.cern.ch/record/1112036>.
- [69] CMS Collaboration. “The CMS barrel calorimeter response to particle beams from 2 to 350 GeV/c”. In: *Eur. Phys. J. C* **60**:3 (2009).
- [70] J. Beringer et al. (Particle Data Group). “Review of Particle Physics”. In: *Chin. Phys. C* **38**: (2014), p. 090001. URL: <http://pdg.lbl.gov>.

- [71] P. Adragna et al. “Measurement of Pion and Proton Response and Longitudinal Shower Profiles up to 20 Nuclear Interaction Lengths with the ATLAS Tile Calorimeter”. In: *Nucl. Instrum. Meth. A* **615**: (2010), pp. 158–181.
- [72] ATLAS Collaboration. “Jet energy measurement and its systematic uncertainty in proton–proton collisions at  $\sqrt{s} = 7$  TeV with the ATLAS detector”. In: *Eur. Phys. J. C* **75**: (2015), p. 17. arXiv: [1406.0076 \[hep-ex\]](#). PERF-2012-01.
- [73] Hung-Liang Lai, Marco Guzzi, Joey Huston, Zhao Li, Pavel M. Nadolsky, et al. “New parton distributions for collider physics”. In: *Phys. Rev. D* **82**: (2010), p. 074024. arXiv: [1007.2241 \[hep-ph\]](#).
- [74] E. Abat et al. “Study of energy response and resolution of the ATLAS barrel calorimeter to hadrons of energies from 20 to 350 GeV”. In: *Nucl. Instrum. Meth. A* **621**:1-3 (2010), pp. 134 – 150.
- [75] ATLAS Collaboration. “Jet energy measurement with the ATLAS detector in proton–proton collisions at  $\sqrt{s} = 7$  TeV”. In: *Eur. Phys. J. C* **73**: (2013), p. 2304. arXiv: [1112.6426 \[hep-ex\]](#). PERF-2011-03.
- [76] Nausheen R. Shah and Carlos E. M. Wagner. “Gravitons and dark matter in universal extra dimensions”. In: *Phys. Rev. D* **74**: (2006), p. 104008. arXiv: [hep-ph/0608140 \[hep-ph\]](#).
- [77] Jonathan L. Feng, Arvind Rajaraman, and Fumihiro Takayama. “Graviton cosmology in universal extra dimensions”. In: *Phys. Rev. D* **68**: (2003), p. 085018. arXiv: [hep-ph/0307375 \[hep-ph\]](#).
- [78] Paul H. Frampton and Pham Quang Hung. “Long-lived quarks?” In: *Phys. Rev. D* **58**: (5 1998), p. 057704. URL: <http://link.aps.org/doi/10.1103/PhysRevD.58.057704>.
- [79] C. Friberg, E. Norrbin, and T. Sjostrand. “QCD aspects of leptoquark production at HERA”. In: *Phys. Lett. B* **403**: (1997), pp. 329–334. arXiv: [hep-ph/9704214 \[hep-ph\]](#).
- [80] Herbert K. Dreiner. “An introduction to explicit R-parity violation”. In: (1997). arXiv: [hep-ph/9707435](#).
- [81] Edmond L. Berger and Zack Sullivan. “Lower limits on R-parity-violating couplings in supersymmetry”. In: *Phys. Rev. Lett.* **92**: (2004), p. 201801. arXiv: [hep-ph/0310001](#).
- [82] R. Barbieri et al. “R-parity violating supersymmetry”. In: *Phys. Rept.* **420**: (2005), p. 1. arXiv: [hep-ph/0406039](#).
- [83] M. Fairbairn et al. “Stable massive particles at colliders”. In: *Phys. Rept.* **438**: (2007), p. 1. arXiv: [hep-ph/0611040](#).
- [84] Christopher F. Kolda. “Gauge-mediated supersymmetry breaking: Introduction, review and update”. In: *Nucl. Phys. Proc. Suppl.* **62**: (1998), p. 266. arXiv: [hep-ph/9707450](#).

- [85] Howard Baer, Kingman Cheung, and John F. Gunion. “A Heavy gluino as the lightest supersymmetric particle”. In: *Phys. Rev. D* **59**: (1999), p. 075002. arXiv: [hep-ph/9806361](#).
- [86] S. James Gates Jr. and Oleg Lebedev. “Searching for supersymmetry in hadrons”. In: *Phys. Lett. B* **477**: (2000), p. 216. arXiv: [hep-ph/9912362](#).
- [87] Glennys R. Farrar and Pierre Fayet. “Phenomenology of the Production, Decay, and Detection of New Hadronic States Associated with Supersymmetry”. In: *Phys. Lett. B* **76**: (1978), pp. 575–579.
- [88] A. C. Kraan, J. B. Hansen, and P. Nevski. “Discovery potential of R-hadrons with the ATLAS detector”. In: *Eur. Phys. J.* **C49**: (2007), pp. 623–640. arXiv: [hep-ex/0511014 \[hep-ex\]](#).
- [89] Rasmus Mackeprang and David Milstead. “An Updated Description of Heavy-Hadron Interactions in GEANT-4”. In: *Eur. Phys. J.* **C66**: (2010), pp. 493–501. arXiv: [0908.1868 \[hep-ph\]](#).
- [90] ATLAS Collaboration. “Search for massive, long-lived particles using multitrack displaced vertices or displaced lepton pairs in  $pp$  collisions at  $\sqrt{s} = 8$  TeV with the ATLAS detector”. In: *Phys. Rev. D* **92**: (2015), p. 072004. arXiv: [1504.05162 \[hep-ex\]](#). SUSY-2014-02.
- [91] ATLAS Collaboration. “Search for charginos nearly mass degenerate with the lightest neutralino based on a disappearing-track signature in  $pp$  collisions at  $\sqrt{s} = 8$  TeV with the ATLAS detector”. In: *Phys. Rev. D* **88**: (2013), p. 112006. arXiv: [1310.3675 \[hep-ex\]](#). SUSY-2013-01.
- [92] ATLAS Collaboration. “Searches for heavy long-lived sleptons and R-Hadrons with the ATLAS detector in  $pp$  collisions at  $\sqrt{s} = 7$  TeV”. In: *Phys. Lett. B* **720**: (2013), p. 277. arXiv: [1211.1597 \[hep-ex\]](#). SUSY-2012-01.
- [93] ATLAS Collaboration. “Searches for heavy long-lived charged particles with the ATLAS detector in proton–proton collisions at  $\sqrt{s} = 8$  TeV”. In: *JHEP* **01**: (2015), p. 068. arXiv: [1411.6795 \[hep-ex\]](#). SUSY-2013-22.
- [94] ATLAS Collaboration. “Search for metastable heavy charged particles with large ionisation energy loss in  $pp$  collisions at  $\sqrt{s} = 8$  TeV using the ATLAS experiment”. In: *Eur. Phys. J. C* **75**: (2015), p. 407. arXiv: [1506.05332 \[hep-ex\]](#). SUSY-2014-09.
- [95] ATLAS Collaboration. “Search for heavy long-lived charged R-hadrons with the ATLAS detector in  $3.2 \text{ fb}^{-1}$  of proton–proton collision data at  $\sqrt{s} = 13$  TeV”. In: *Phys. Lett. B* **760**: (2016), pp. 647–665. arXiv: [1606.05129 \[hep-ex\]](#).
- [96] ATLAS Collaboration. “Further ATLAS tunes of PYTHIA 6 and Pythia 8”. ATL-PHYS-PUB-2011-014. 2011. URL: <https://cds.cern.ch/record/1400677>.
- [97] Aafke Christine Kraan. “Interactions of heavy stable hadronizing particles”. In: *Eur. Phys. J.* **C37**: (2004), pp. 91–104. arXiv: [hep-ex/0404001 \[hep-ex\]](#).

- [98] M. Fairbairn et al. “Stable massive particles at colliders”. In: *Phys. Rept.* **438**: (2007), p. 1. arXiv: [hep-ph/0611040](#).
- [99] W. Beenakker, R. Hopker, M. Spira, and P. M. Zerwas. “Squark and gluino production at hadron colliders”. In: *Nucl. Phys. B* **492**: (1997), p. 51. arXiv: [hep-ph/9610490](#).
- [100] A. Kulesza and L. Motyka. “Threshold resummation for squark-antisquark and gluino-pair production at the LHC”. In: *Phys. Rev. Lett.* **102**: (2009), p. 111802. arXiv: [0807.2405 \[hep-ph\]](#).
- [101] A. Kulesza and L. Motyka. “Soft gluon resummation for the production of gluino-gluino and squark-antisquark pairs at the LHC”. In: *Phys. Rev. D* **80**: (2009), p. 095004. arXiv: [0905.4749 \[hep-ph\]](#).
- [102] Wim Beenakker, Silja Brensing, Michael Kramer, Anna Kulesza, Eric Laenen, et al. “Soft-gluon resummation for squark and gluino hadroproduction”. In: *JHEP* **0912**: (2009), p. 041. arXiv: [0909.4418 \[hep-ph\]](#).
- [103] W. Beenakker, S. Brensing, M.n Kramer, A. Kulesza, E. Laenen, et al. “Squark and Gluino Hadroproduction”. In: *Int. J. Mod. Phys. A* **26**: (2011), p. 2637. arXiv: [1105.1110 \[hep-ph\]](#).
- [104] Michael Krämer et al. “Supersymmetry production cross sections in pp collisions at  $\sqrt{s} = 7$  TeV”. 2012. arXiv: [1206.2892 \[hep-ph\]](#).
- [105] Rasmus Mackeprang and Andrea Rizzi. “Interactions of Coloured Heavy Stable Particles in Matter”. In: *Eur. Phys. J.* **C50**: (2007), pp. 353–362. arXiv: [hep-ph/0612161 \[hep-ph\]](#).
- [106] Rasmus Mackeprang and David Milstead. “An Updated Description of Heavy-Hadron Interactions in GEANT-4”. In: *Eur. Phys. J.* **C66**: (2010), pp. 493–501. arXiv: [0908.1868 \[hep-ph\]](#).
- [107] ATLAS Collaboration. “ $dE/dx$  measurement in the ATLAS Pixel Detector and its use for particle identification”. ATLAS-CONF-2011-016. 2011. URL: <https://cds.cern.ch/record/1336519>.
- [108] ATLAS Collaboration. “The ATLAS Simulation Infrastructure”. In: *Eur. Phys. J.* **C70**: (2010), pp. 823–874. arXiv: [1005.4568 \[physics.ins-det\]](#).
- [109] ATLAS Collaboration. “Luminosity determination in pp collisions at  $\sqrt{s} = 8$  TeV using the ATLAS detector at the LHC”. In: (2016). arXiv: [1608.03953 \[hep-ex\]](#).
- [110] Alexander L. Read. “Presentation of search results: The CL(s) technique”. In: *J. Phys. G* **28**: (2002). [,11(2002)], pp. 2693–2704.